



**ZÁPADOČESKÁ UNIVERZITA V PLZNI
FAKULTA STROJNÍ
MATERIÁLOVÉ INŽENÝRSTVÍ A STROJÍRENSKÁ
METALURGIE**

DISERTAČNÍ PRÁCE

Wilayat Khan

předložena v souladu s požadavky pro titul

Doctor of Philosophy

Doktorský studijní program P 2301

**Study programme details: Materials Engineering and Engineering
Metallurgy**

**Theoretical investigations of spectroscopic, electronic and magnetic
properties of new low dimensional systems**

**Teoretický výzkum spektroskopických, elektronických a magnetických
vlastností nových nízkodimensionálních systémů**

Školitel: Doc. Dr. Ján Minár

Dedicated
to
my family

for their endless love, support and encouragement

A special dedication to
my late mother, my honorable father, my brother and
sisters, my sweet daughters and lovely, caring wife

and . . .

To whom it may concern

PROHLÁŠENÍ

Prohlašuji, že práce, která je uvedena v diplomové práci “Teoretické zkoumání spektroskopických, elektronických a magnetických vlastností nových nízkorozměrových systémů” při částečném splnění požadavků na udělování titulu Ph.D, předložené na Fakultě mechanické Inženýrství, Západočeské univerzity, Plzeň, je autentickým záznamem mé práce pod vedením Doc. Dr. Jana. Minára. Nepoužil jsem obsah v této diplomové práci pro udlení jakéhokoli jiného titulu nebo diplomu univerzity nebo jiného institutu.

2. října, 2017

Wilayat Khan

Contents

| | |
|--|-------------|
| List of Figures | xiii |
| List of Tables | xiv |
| Abbreviations | xv |
| 1 Introduction | 1 |
| 1.1 Aim of the Thesis | 8 |
| 1.2 Outline of the Thesis | 9 |
| 2 Density Functional Theory | 13 |
| 2.1 Theoretical Background | 14 |
| 2.2 Kohn–Sham equations | 16 |
| 2.3 The Exchange–Correlation Functionals | 16 |
| 2.3.1 The Local (spin) Density Approximation (L(S)DA) | 17 |
| 2.3.2 The Generalized Gradient Approximation (GGA) | 18 |
| 2.3.3 Trans–Blaha Modified Becke Johnson Approximation (TB–mBJ) | 19 |
| 2.3.4 On–site Hubbard interaction with DFT (DFT+U) | 20 |
| 3 Electronic Structure Methods | 24 |
| 3.1 The Augmented Plane Wave (APW) method | 26 |
| 3.2 The Linearized APW (LAPW) method | 27 |
| 3.3 The Linearized/Augmented Plane Wave plus Local Orbital (L/APW+lo) method | 29 |
| 3.4 Full Potential Linearized Augmented Plane Wave (FP–LAPW) method | 31 |
| 3.5 Optical Properties | 31 |
| 3.6 X–rays Absorption (XAS) and Electron Energy Loss (EELS) spectroscopy | 34 |
| 3.7 Thermoelectric Properties | 35 |
| 3.7.1 Electrical Conductivity | 37 |

| | | |
|----------|--|-----------|
| 4 | Materials Selection | 43 |
| 4.1 | Metal Oxides for Water Splitting Process | 43 |
| 4.1.1 | Hematite | 44 |
| 4.1.2 | Niobium Oxide | 45 |
| 5 | Theoretical and Experimental Study on the Optoelectronic Properties of $\text{Nb}_3\text{O}_7(\text{OH})$ and Nb_2O_5 Photoelectrodes | 51 |
| 5.1 | Introduction | 52 |
| 5.2 | Computational and experimental methodology | 53 |
| 5.2.1 | Calculation details | 53 |
| 5.2.2 | Experimental details | 54 |
| 5.3 | Results and discussion | 55 |
| 5.3.1 | Structural optimization | 55 |
| 5.3.2 | Electronic band structures | 56 |
| 5.3.3 | Optical properties | 59 |
| 5.3.4 | Comparison of the calculation with experimental EELS data . | 64 |
| 5.3.5 | Transport properties | 66 |
| 5.4 | Conclusion | 68 |
| 6 | Tuning the electronic structure of $\text{Nb}_3\text{O}_7(\text{OH})$ by titanium doping for enhanced light-induced water splitting | 73 |
| 6.1 | Introduction | 74 |
| 6.2 | Computational and experimental methodology | 75 |
| 6.2.1 | Computational details | 75 |
| 6.2.2 | Experimental details | 76 |
| 6.3 | Results and discussion | 77 |
| 6.3.1 | Structural properties | 77 |
| 6.3.2 | Formation energy | 79 |
| 6.3.3 | Band Structures and Density of States | 79 |
| 6.3.4 | Optical properties | 83 |
| 6.3.5 | Spectroscopic properties | 87 |
| 6.4 | Conclusion | 90 |
| 7 | Theoretical analysis of an Intermediate Band in Sn-doped Hematite with Wide-spectrum Solar Response | 94 |
| 7.1 | Introduction | 95 |
| 7.2 | Theoretical details | 96 |
| 7.3 | Results and Discussion | 98 |
| 7.3.1 | Structural Properties | 98 |
| 7.3.2 | Electronic structure | 99 |
| 7.3.3 | Magnetic properties | 105 |

| | | |
|--|---|------------|
| 7.3.4 | Optical properties | 107 |
| 7.4 | Conclusion | 110 |
| 8 | Local vs non-local states in FeTiO₃ probed with 1s2pRIXS: implications for photochemistry | 114 |
| 8.1 | Introduction | 115 |
| 8.2 | Materials and Methods | 116 |
| 8.2.1 | Samples | 116 |
| 8.2.2 | RIXS measurements | 117 |
| 8.3 | Calculations | 118 |
| 8.3.1 | Density functional theory calculations | 118 |
| 8.4 | Crystal field multiplet calculations | 118 |
| 8.5 | Results and discussions | 119 |
| 8.5.1 | Experimental 1s2pRIXS results | 119 |
| 8.5.2 | Crystal field multiplet analysis of the pre-edge features (A), (B) and (C) | 122 |
| 8.5.3 | First-principle computed band-structure analysis of the non-local features (D) and (E) | 125 |
| 8.5.4 | Implications for photocatalysis | 129 |
| 8.6 | Conclusion | 130 |
| 9 | Summary and Conclusions | 137 |
| Appendix A Tuning the electronic structure of Nb₃O₇(OH) by titanium doping for enhanced light-induced water splitting | | |
| | | 139 |
| A.1 | Detailed orbital resolved DOS of Nb-s/p/d orbitals Ti-s/p/d orbitals, O-s/p orbitals and H-s orbitals | 139 |
| Appendix B Local vs non-local states in FeTiO₃ probed with 1s2pRIXS: implications for photochemistry | | |
| | | 141 |
| B.1 | DFT calculation results | 141 |
| B.1.1 | Effect of the Hubbard U | 141 |
| B.1.2 | Detailed 3d orbitals pDOS | 141 |
| Acknowledgment | | 143 |
| Curriculum vitae | | 145 |
| 10 | Curriculum vitae | 145 |

List of Figures

| | | |
|-----|--|----|
| 1.1 | One-step and two-step photoexcitation process in water splitting. Conduction band (CB); valence band (VB); band gap (E_g). taken from [13] | 2 |
| 1.2 | Schematics of the relevant mechanism involved in the photocatalysis of water using a photoanode made of n -type semiconductor. Different steps labeled by number from 1-5 are discussed in the related text. taken from [16] | 3 |
| 1.3 | (a) Schematic view of energy band diagram of photoelectrochemical water splitting using Hematite as n -type semiconductor. Here the symbols E_g , V_{fb} , V_b stands for the photoanode bandgap, flat band potential and the applied bias. (b) Conceptual water splitting tandem cell using photoanode plus a dye-sensitized solar cell (DSC). taken from [12] | 5 |
| 1.4 | Schematic view of the dye-sensitized electrochemical photovoltaic cell and its constituents i.e. it consist of mesoporous semiconductor photoanode, the dye oxidized delivers electrons to semiconductor when it is photoexcited, and as a consequence oxidizes the mediator, a redox reaction completed in the electrolyte. The reduction (regeneration by mediator) of the oxidized dye <i>via</i> circulating through external circuit. taken from [11] | 7 |
| 2.1 | Schematic diagram of " Jacobs ladder " of exchange-correlation functionals proposed by J. P. Perdew. | 17 |
| 2.2 | Theoretical and experimental band gap values for some selected semiconductors. taken from [23] | 21 |
| 3.1 | Unit cell is decomposed into muffin-tin spheres and interstitial regions. | 28 |
| 3.2 | The basis functions (LAPW) created for $\mathbf{k}(\mathbf{G}=0)$ (a) at the M-point and (b) M-point of the Brillouin zone of a 3-layer thin film of Cu(100). The basis function selected here are Cu-4s(a)/4p states (b). taken from [13] | 29 |
| 3.3 | The radial solution u_l are augmented at MT sphere boundary for Ce for different orbital quantum number of an LAPW basis function. . . | 30 |

| | | |
|-----|--|----|
| 3.4 | Schematic representation of conduction band and valence band. It shows the energy versus the in plane carrier momentum (a) it describes the direct band transition and (b) describes the indirect band transition. | 32 |
| 3.5 | Sketch showing (a) the core band electron, Fermi level, valence and conduction bands (b) and the core electron excitation to the available unoccupied state above the Fermi level. | 34 |
| 3.6 | Upper part of the figure represents the electrical/thermal conductivity, Seebeck coefficient, power factor versus carrier concentration, while the lower part represents the electronic and lattice thermal conductivity against the $\ln(n)$. taken from [37] | 38 |
| 4.1 | Schematic representations of α -Fe ₂ O ₃ along different crystallographic axes. | 44 |
| 4.2 | Transformation of Nb ₂ O ₅ crystal phase versus temperature starting from 200 °C to 1200 °C. | 46 |
| 4.3 | Schematic representations of (a) TT-phase (pseudo-hexagonal), (b) T-phase (orthorhombic), (c) H-phase (monoclinic) and 3D crystal structures of (d) T-phase (orthorhombic) and (e) H-phase (monoclinic) of Nb ₂ O ₅ . [21] | 47 |
| 4.4 | Schematic representations of (a) Nb ₃ O ₈ and Nb ₃ O ₇ (OH) and (b) Nb ₂ O ₅ and in both figures the O and Nb atoms are marked by numbers according to their position in the crystal. | 47 |
| 5.1 | Schematic representation of the crystal structures of the artificial reference compound Nb ₃ O ₈ (left part (a)) and Nb ₃ O ₇ (OH) (right part (a)) and monoclinic H-Nb ₂ O ₅ (b). Black, red and green spheres represent Nb, O, and H atoms, respectively. | 56 |
| 5.2 | Calculated band structure of Nb ₃ O ₈ (left side of (a)), Nb ₃ O ₇ (OH) (b) and monoclinic H-Nb ₂ O ₅ (c). In addition the density of states is given for Nb ₃ O ₈ on the right side of (a). | 58 |
| 5.3 | The partial density of states were calculated using the TB-mBJ approach. In (a) the PDOS of Nb, O and H atoms are shown for Nb ₃ O ₇ (OH) in (b) for monoclinic H-Nb ₂ O ₅ . Solid (black, red, blue and green) lines represent <i>s</i> , <i>p</i> and <i>d</i> states, respectively. The Fermi level (E_F) is set to zero. | 60 |
| 5.4 | The real and imaginary part of the dielectric function. The peaks result from various transitions. The imaginary $\varepsilon_2(\omega)$ and real part $\varepsilon_1(\omega)$ of the DF calculated for Nb ₃ O ₇ (OH) and monoclinic H-Nb ₂ O ₅ | 61 |
| 5.5 | Calculated optical conductivity $\sigma(\omega)$ of Nb ₃ O ₇ (OH) and monoclinic H-Nb ₂ O ₅ | 63 |

| | | |
|-----|---|----|
| 5.6 | Comparison of the calculated energy loss functions $L(\omega)$ with experimental low loss EEL spectra for $\text{Nb}_3\text{O}_7(\text{OH})$ and $\text{H-Nb}_2\text{O}_5$ | 65 |
| 5.7 | Calculated and measured EELS edges of $\text{Nb}_3\text{O}_7(\text{OH})$. (a) Nb-M ₃ and (b) O-K edge. | 67 |
| 5.8 | Calculated thermoelectric conductivity for $\text{Nb}_3\text{O}_7(\text{OH})$ (black) and monoclinic $\text{H-Nb}_2\text{O}_5$ (red)calculated using the BoltsTraP code. Please note the different vertical axis values. | 69 |
| 6.1 | Crystal structures of (a) $\text{Nb}_3\text{O}_7(\text{OH})$, (b) Ti-doped $\text{Nb}_3\text{O}_7(\text{OH})$ (Ti=4.16 %) and (c) Ti-doped $\text{Nb}_3\text{O}_7(\text{OH})$ (Ti=8.32 %). These structures are based on $1 \times 2 \times 2$ supercell. The numbers assigned to different Nb and O atoms indicate that there are three inequivalent Nb atoms and eight inequivalent O atoms in these structures. | 77 |
| 6.2 | Overview of the band structure of nanostructure $\text{Nb}_3\text{O}_7(\text{OH})$ and Ti-doped $\text{Nb}_3\text{O}_7(\text{OH})$ as calculated from DFT. The Dispersion curves are taken along the Z-S-Y- Γ -T-Z lines in the BZ of $\text{Nb}_3\text{O}_7(\text{OH})$ (unit cell)/supercell (a)/(b) and c & d indicate the dispersion curve of Ti-doped $\text{Nb}_3\text{O}_7(\text{OH})$. This smearing of bands is related to the Ti contents. | 80 |
| 6.3 | Calculated total and elemental resolved density of states for $\text{Nb}_3\text{O}_7(\text{OH})$ and Ti-doped $\text{Nb}_3\text{O}_7(\text{OH})$ as obtained from First principal calculations. (a) elemental resolved DOS for $\text{Nb}_3\text{O}_7(\text{OH})$, in which the black, red, blue (solid lines) and red (dotted line) represents total, Nb, O and H atoms. (b, c) elemental resolved DOS of Ti-doped systems, in which black, red, (solid lines) and blue/red (dotted lines) represents total, Nb, Ti, O and H atoms. | 81 |
| 6.4 | DFT calculated of optical properties. (a & b) the real and imaginary part of dielectric function of $\text{Nb}_3\text{O}_7(\text{OH})$ and Ti: $\text{Nb}_3\text{O}_7(\text{OH})$ along x-axis. Here Ti (8.32 %) show more absorption than Ti (0 % & 4.16 %) . Fig c & d show the same optical parameter along z-axis which appear due to intraband transitions (due to smearing of orbitals) in the infrared region and interband transitions in the ultraviolet region. | 84 |
| 6.5 | DFT simulated electron energy loss spectra (EELS) of $\text{Nb}_3\text{O}_7(\text{OH})$ (black), Ti: $\text{Nb}_3\text{O}_7(\text{OH})$ (Ti= 4.16 %) (red) and Ti: $\text{Nb}_3\text{O}_7(\text{OH})$ (Ti= 8.32 %) (blue), showing similar peaks except with the peak variations. (a) EELS spectra of the entire systems along x-axis and z-axis. | 86 |

| | | |
|-----|--|-----|
| 6.6 | Calculated Nb–M ₃ edges of Nb ₃ O ₇ (OH) and Ti:Nb ₃ O ₇ (OH) (Ti= 4.16 % and 8.32 %) along with the experimental data. (a) Different Nb atoms contribution to the spectra is also been shown. Schematic spectra of Nb–M ₃ edges of the corresponding Ti concentrations along with the exp. data are also shown in b and c. The Black and red are designated to the calc. and exp. data of the Nb ₃ O ₇ (OH) and Ti:Nb ₃ O ₇ (OH), respectively. | 88 |
| 6.7 | Calculated O–K edges of Nb ₃ O ₇ (OH) and Ti:Nb ₃ O ₇ (OH) (Ti= 4.16 % and 8.32 %) along with the experimental data. In (a), the calculated spectra constructed by different O atoms positioned at various lattice sites in the crystal structures. Fig b and c show the O–K edges of the corresponding Ti Nb ₃ O ₇ (OH) along with the exp. data. The Black and red are designated to the calc. and exp. data of the Nb ₃ O ₇ (OH) and Ti:Nb ₃ O ₇ (OH), respectively. | 89 |
| 7.1 | Schematic of of the unit cell of α -Fe ₂ O ₃ with spin down Fe atoms and spin up Fe atoms, and Sn–doped with the same spin configuration, respectively. | 99 |
| 7.2 | Band structures representation for α -Fe ₂ O ₃ and Fe _{2-x} Sn _x O ₃ ($x= 8$ % and 12 %) under the GGA+U approach at $U_{eff}=5.0$ eV. | 100 |
| 7.3 | The calculated total density of states (TDOS) of α -Fe ₂ O ₃ and Fe _{2-x} Sn _x O ₃ ($x= 8$ % and 12 %) under the GGA+U approach at $U_{eff}=5.0$ eV. . . | 101 |
| 7.4 | Averaged partial density of states (pDOS) images (a) α -Fe ₂ O ₃ and in (b, c) Fe _{2-x} Sn _x O ₃ ($x=8$ %, 12 %) for those Fe atoms which are 4.0 Å to 6.0 Å ($x=8$ %)/3.72 Å to 6.25 Å ($x=12$ %) and for those O atoms which are 3.78 Å to 6.25 Å ($x=8$ %)/3.78 Å to 6.6Å ($x=12$ %) away from Sn atoms. In (c), the pDOS of Fe–3d orbitals show filled intermediate band at -0.8 eV under the GGA+U approach at $U_{eff}=5.0$ eV. | 103 |
| 7.5 | Averaged partial density of states (pDOS) images of (a, b) Fe _{2-x} Sn _x O ₃ ($x=8$ %, 12 %) for those Fe atoms which are 2.68 Å to 3.59 Å ($x=8$ %)/2.84Å to 3.59 Å ($x=12$ %) and for those O atoms which are 2.09 Å to 2.14 Å ($x=8$ %)/2.13 Å to 2.15Å ($x=12$ %) close to Sn atoms. In (a), the pDOS of Fe–3d orbitals show partially filled intermediate band (I.B ₁) and filled intermediate band (I.B ₂) with O–2p orbitals at -0.8 eV and in (b) O–2p orbitals contribute to I.B ₂ under the GGA+U approach at $U_{eff}=5.0$ eV. | 104 |
| 7.6 | Partial density of states (pDOS) images of (a, b) Fe _{2-x} Sn _x O ₃ ($x=8$ %) and (a, b, c) Fe _{2-x} Sn _x O ₃ ($x=12$ %). Both shows the pDOS of Sn–5s/5p/4d orbitals which contribute to the filled intermediate band (I.B ₂) at -0.8 eV and partially filled intermediate band (I.B ₁), under the GGA+U approach at $U_{eff}=5.0$ eV. | 106 |

| | | |
|-----|--|-----|
| 7.7 | (a) Calculated optical spectra: (a) the imaginary and (b) the real part of dielectric function, (c) the electron energy loss function and (d) the reflectivity of α -Fe ₂ O ₃ and Fe _{2-x} Sn _x O ₃ ($x=8\%$ and 12%) in the energy window from 0.0 to 3.5 eV. The optical thresholds are compared to pure and different Sn concentration. The absorption edge of Fe ₂ O ₃ with Sn-doped lies in IR region and maximum peaks related to the transition of I.B. | 108 |
| 7.8 | Visual representation of photocatalytic activity of α -Fe ₂ O ₃ and Fe _{2-x} Sn _x O ₃ in the UV region extended to Infrared region (left side) and on the right side the I.Bs photocatalysis of Fe _{2-x} Sn _x O ₃ | 109 |
| 8.1 | Crystal structure of ilmenite FeTiO ₃ and zoom on the face sharing Fe and Ti octahedrons. | 117 |
| 8.2 | a) Fe K-edge XANES spectra of FeTiO ₃ in TFY detection compared with K α_1 -HERFD detection (red line), inset: full energy range spectra; b) 1s2pRIXS map of FeTiO ₃ showing the five features labeled from A to E; c) TFY and HERFD spectra of Fe ₂ O ₃ ; d) 1s2pRIXS map of Fe ₂ O ₃ . The diagonal lines serve as guides for the eye to show the constant emitted energies for non-resonant K α_1 emission (RIXS map color scale is the intensity normalized to the edge jump of the K α_1 -HERFD spectrum). | 120 |
| 8.3 | a) Experimental 1s2pRIXS plane of FeTiO ₃ zoomed on features (A), (B) and (C); b) Calculated 1s2pRIXS plane of the local Fe ²⁺ 1s \rightarrow 3d RIXS E2+E1 transitions. | 122 |
| 8.4 | (Bottom) Calculated features (A), (B) and (C) of the Fe K-edge HERFD-XANES: E2+E1 sum (black) and individual E2 (green) and E1 (violet) contributions compared to the experimental (red -) spectrum and the corrected (- -) spectrum from the tail of feature (D) (....). (Top) Assignment of the 1s ¹ 3d ⁷ multi-electronic states (in O _h symmetry for simplicity). | 124 |
| 8.5 | Experimental (top) and calculated (bottom) RIXS constant incident energy slices obtained at A (-) B (- -) and C (...), corresponding to the white lines drawn in Figure 3. | 126 |
| 8.6 | Calculated electric dipole absorption cross-section (red plain line) at the Fe K-edge (top panel) compared with the projected DOS (lower panels) on Fe, Ti and O (plain lines: β spin, dotted lines: α spin). The experimental HERFD-XANES is added for comparison (black dashed line, upper panel). Fe* denotes the Fe atom including the 1s core-hole | 128 |

| | | |
|-----|--|-----|
| A.1 | Calculated orbital resolved DOS of (a, b) $\text{Nb}_3\text{O}_7(\text{OH})$ and (c-f) $\text{Ti:Nb}_3\text{O}_7(\text{OH})$. In all cases, the VBM are dominated by O- $2p$ orbitals and CBM are dominated by Nb- $4d$ orbitals. But due to the addition of Ti atom, the O- $2p$ /Ti- px orbitals smears over the Fermi level and Nb- $4d$ orbitals coupled with Ti- $3d$ orbitals. | 140 |
| B.1 | Projected DOS of Fe, Ti and O atoms for various values of Hubbard U: a) 0 eV, b) 5 eV, c) 7 eV. | 142 |
| B.2 | Projected DOS on the 3d orbitals of Fe and Ti, calculated with DFT without core-hole. | 142 |

List of Tables

| | | |
|-----|---|----|
| 4.1 | Lattice parameters of different phases (TT, T, M and H phases) of Nb_2O_5 | 45 |
| 5.1 | Band gaps of $\text{Nb}_3\text{O}_7(\text{OH})$ and Nb_2O_5 determined experimentally and from calculation (in [eV]). | 57 |
| 6.1 | Calculated Interatomic Distances for $\text{Nb}_3\text{O}_7(\text{OH})$ (A1) and $\text{Ti:Nb}_3\text{O}_7(\text{OH})$ (A2, A3). | 78 |
| 6.2 | Ti dopant formation energies in $\text{Nb}_3\text{O}_7(\text{OH})$ | 79 |
| 7.1 | Results obtained for lattice parameters (a, c), volume (V_0) from calculations through the GGA method for $\alpha\text{-Fe}_2\text{O}_3$. (in \AA) | 98 |

Abbreviations

| | |
|--------|---------------------------------------|
| DSSC | Dye-sensitized solar cell |
| PS | Photosynthesis |
| CB | Conduction band |
| VB | Valence band |
| PEC | Photoelectrochemical |
| PC | Photocatalysis |
| IR | Infrared |
| VIS | Visible light |
| UV | Ultraviolet |
| DS | Dye-sensitized |
| DFT | Density functional theory |
| KS | Kohn Sham |
| SWE | Shrödinger wave equation |
| BO | Born Oppenheimer |
| RPA | Random phase approximation |
| LDA | Local density approximation |
| GGA | Generalized gradient approximation |
| OEP | Optimized effective approximation |
| BJ | Becke Johnson |
| TB-mBJ | Trans Blaha modified Becke Johnson |
| TMO | Transition metal oxide |
| OEP | Muffin tin |
| APW | Augmented plane wave |
| LAPW | Linearized augmented plane wave |
| LMTO | Linear muffin tin orbital |
| FP | Full potential |
| V | Potential |
| THz | Tetrahertz |
| P | Polarization vector |
| XAS | X-rays absorption |
| RIXS | Resonant inelastic X-rays scattering |
| EELS | Electron energy loss spectroscopy |
| ELNES | Energy loss near edge structure |
| XANS | X-rays absorption near edge structure |
| TE | Thermoelectric |
| BTT | Boltmann transport theory |
| SCF | Self consistent field |
| TEM | Transmission electron microscopy |
| IBZ | Irreducible Brillouin zone |

| | |
|--------------|---------------------------------|
| DOS | Density of states |
| TDOS | Total density of states |
| PDOS | Partial density of states |
| I.B | Intermediate band |
| MMCT | Metal metal charge transfer |
| TFY | Total fluorescence yield |
| FWHM | Full width half maximum |
| CFM | Crystal field multiplet |
| E_g | Band gap |
| α | Alpha (spin) |
| β | beta (spin) |
| \AA | Angstrom |
| Z | Atomic number |
| h^+ | Hole |
| \bar{e} | Electron |
| E_F | Fermi level |
| h | Plank constant |
| ϵ_0 | Permittivity of free space |
| n | Electron density |
| N | Number of electrons |
| ψ | Wave function |
| ϕ | Orbitals |
| ∇n | Density gradient |
| $F(x)$ | Enhancement factor |
| f^{GGA} | Exchange correlation functional |
| I | Ionization energy |
| A | Electron affinity |
| J | Hund's exchange parameter |
| l | Angular momentum |
| u_l | Radial function |
| m_e | Effective mass |
| ϵ | Dielectric function |
| ∇^2 | Laplace operator |
| f_k^a | Occupation probability |
| χ | Linear susceptibility |
| γ | Relativistic correction factor |
| T | Temperature |
| S | Seebeck coefficient |
| σ | Electrical conductivity |
| κ | Thermal conductivity |
| f_k | Distribution function |

| | |
|------------------|-------------------|
| v_α | Drift velocity |
| Ω | Volume |
| τ | Relaxation time |
| λ | Wavelength |
| R_{MT} | Muffin tin radius |
| R | Reflectivity |
| L | Energy loss |
| Δ | Difference |
| E_{form} | Formation energy |
| μ_B | Magnetic moment |

Chapter 1

Introduction

The consumption of fossil fuels faces our society to a new challenges and forces us to search for alternatives. Efficient harvesting of energy from the sun light by using solar cells can cover an important part of worldwide energy consumption. To balance out fluctuations in energy production, novel storage technologies need to be simultaneously developed and with this regard hydrogen is intensively discussed as a very promising material for energy storage.

To reduce the demand for fossil fuel, photovoltaic cells become more and more attractive as the sun continuously delivers 120000TW of solar energy to the Earth [1]. Nanostructured devices, like dye-sensitized solar cells (DSSC) and photocatalysis cell attract increasing attention [2]. Dye-sensitized solar cells and photocatalysis use semiconductors to generate charges which are either separated to produce current or used up for chemical reactions (e.g. the splitting of water to produce hydrogen gas). Solar light is absorbed by the semiconductor whereby an electron is excited from the valence to the conduction band leading to electron-hole pairs [3, 4]. The size of the band gap and energetic position of the conduction as well as valence band edges are crucial for the performance of a semiconductor in photochemistry. They determine the portion of the solar spectrum absorbable by the semiconductor, the potential of the electron-hole pair and the band alignment of the device [5, 6]. In addition to experimental studies, ab-initio calculation of the band edge energies of a high variety of oxides [7, 8, 9, 10] can predict the photocatalytic properties of electrode materials.

Currently, the most efficient solar cells are made of III/IV group materials and copper/indium-sulphide/selenide thin film [11]. These are used in aerospace components in the form of chemical energy. Similar to natural photosynthesis (PS) phenomenon, there are many smart, realistic and effective schemes for storage of electrical energy deduced from the conversion of electromagnetic radiation. The photosynthesis retrieves carbohydrates from effective rearrangements of electrons in H_2O and CO_2 . However it has very low efficiency and the energy obtained from it is not sufficient to cover all needs of our daily life. Due to this reason, from the

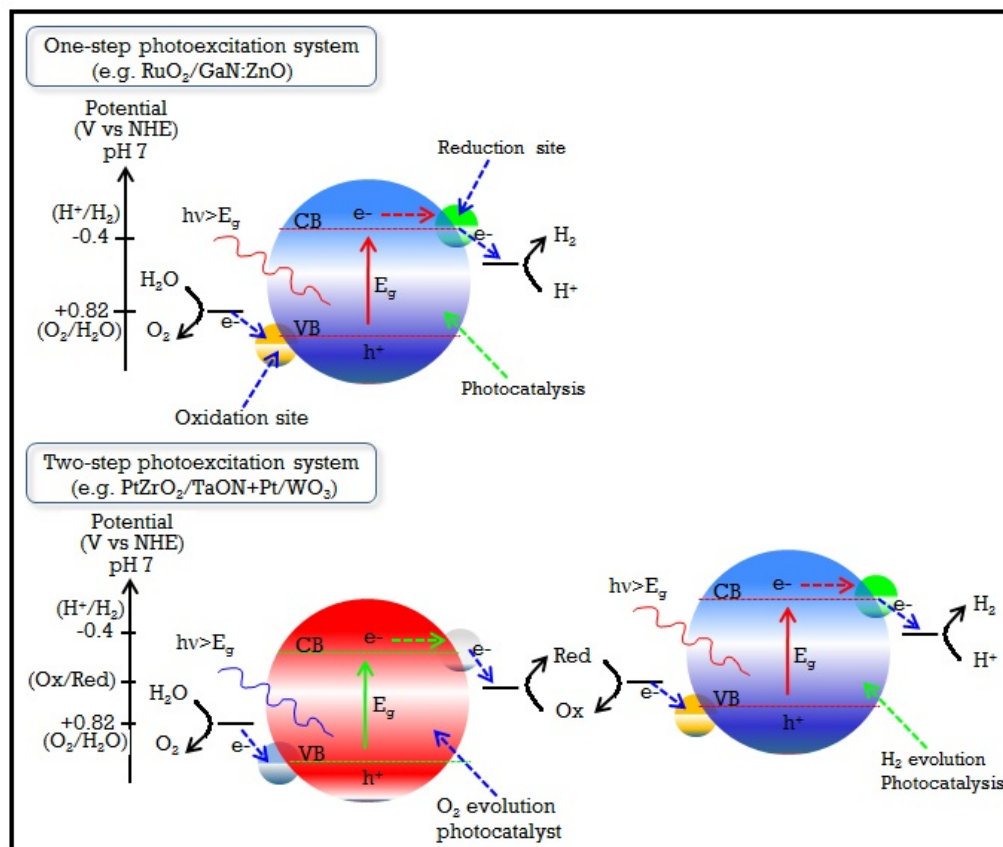


Figure 1.1: One-step and two-step photoexcitation process in water splitting. Conduction band (CB); valence band (VB); band gap (E_g). taken from [13]

last 40 years scientists have been significantly focus on the routes of converting sun light. The most interesting route for artificial photosynthesis is splitting H_2O into hydrogen and oxygen ($H_2O \rightarrow 1/2O_2 + H_2$ ($E^0 = 1.23$ V, where E^0 is the theoretical minimum band gap for water splitting)), i.e. the feasible source of energy is based on hydrogen.

There are two different processes, photoelectrochemical (PEC) and photocatalysis (PC), involved in the H_2 production. Photocatalysis water splitting got an intensive attention as a production of H_2 and O_2 resulting from the chemical reaction of H_2O with dispersive materials; inorganic (collide materials) [13, 14] and organic (molecular complex) materials [15]. Fig. 1.1 illustrates photocatalytic water splitting by two elementary approaches. In the first approach, the entire water splitting into its constituents under the illumination of visible (VIS) light is performed in a single step. Maeda [13] reported a shortcoming of this mechanism, namely the availability of proper materials with small energy gap and stability for functional appliances.

In the second type, the irradiation causes two step pumping of electrons in two different photocatalytic materials, that is named the Z-scheme (encouraged by natural photosynthesis). In this process, the variation in the Gibb's free energy

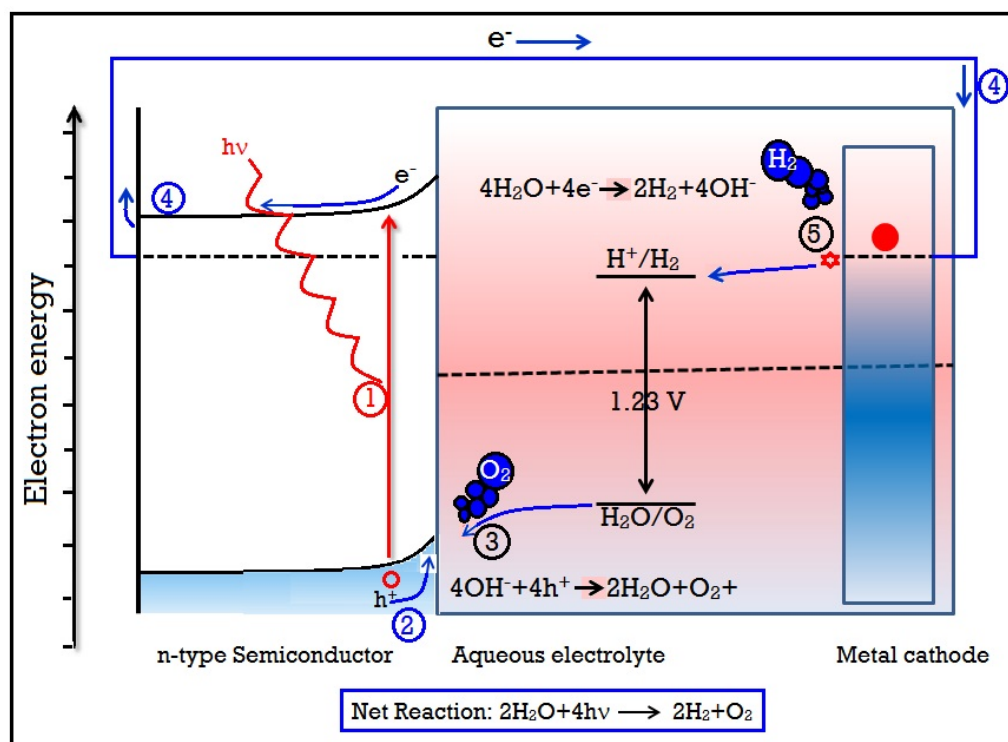


Figure 1.2: Schematics of the relevant mechanism involved in the photocatalysis of water using a photoanode made of n -type semiconductor. Different steps labeled by number from 1–5 are discussed in the related text. taken from [16]

(ΔG), used to carry the photocatalytic reaction, is reduced in comparison to the one-step water splitting process leading to the production of H_2 and O_2 , respectively. In this approach a semiconductor is used either as a reducing or an oxidizing material at one side of the photocatalytic system.

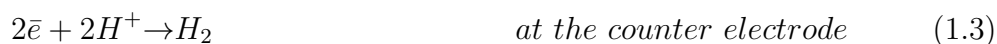
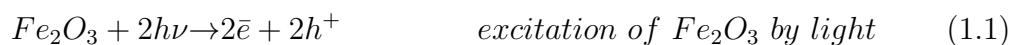
Alternative to the photocatalysis, PEC uses photosensitive semiconducting materials as electrodes and is similar to the normal well known water electrolysis. The O_2 and H_2 are produced at different electrodes i.e. cathode and anode. It consists of two electrodes made of either photovoltaic semiconducting materials (p -type or n -type) and metallic materials or both electrodes correspond to n/p -types materials. When semiconductor/electrolyte is immersed in a solution then a depletion region (junction) appears at the surface of semiconductor/electrolyte. At junction point, exciton creation takes place upon irradiation and travels in opposite direction to each other which finally accumulate at electrolyte/semiconductor (n/p -type) to obtain one half of the water splitting process.

Fig. 1.2 illustrates the procedure of water splitting with n -type semiconductors as electrode material in the following steps: (1) Electron-hole pair (exciton) is produced in a material due to irradiation. (2) The hole moves toward the interface of semiconductor/electrolyte where oxidation occurs at step 3. It means that the hole has reduced the water and produced O_2 . Step (4) describes the motion of electrons

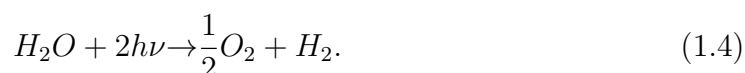
within the semiconductor and proceed to external circuit. Finally in step (5) the water is reduced to H_2 by electron at metal surface. The efficiency of a semiconductor can be improved in water by changing some parameters due to the addition of catalyst and other intrinsic properties parameters of materials.

To demonstrate the physical and chemical mechanisms appearing in the PEC, we would like to discuss hematite as a photoanode. These processes are depicted in Fig. 1.3a. Photons of greater energy than that of the band gap are observed and electron/hole pairs are formed. These electron/hole pairs are separated in general by the electric field at the depletion region. The system consists of two electrodes: a semiconductor electrode and a counter electrode. The electrons move through the semiconductor and reach the counter electrode *via* the external circuit, where hydrogen production occurs. The hole reacts with the semiconductor electrode (at the surface), where they contribute to oxidation reaction: $h^+ + R \rightarrow O$ (R is redox specie). The electrons re-enter in the cell by the external circuit and reduce back the oxidized O. Substantial work has been performed to optimize the efficiency of redox couples made of II/VI or III/VI compounds (*n*-type semiconductor) and sulphide/polysulphide, vanadium(II)/vanadium(III) or I_2/I electrolytes. For such a regenerative cell the efficiency was found up to 19.6 % [17]. Fig. 1.3b shows two photosystems connected in series. At first, the thin nanostructure α - Fe_2O_3 absorbs the visible part of the solar spectrum. Upon irradiation, a hole is produced in the valence band which oxidizes the water to oxygen, while the electron excited to conduction band moves through second photosystem (here consisting of dye-sensitized nanostructure TiO_2), which is placed directly under the α - Fe_2O_3 . Then TiO_2 harvests very low energy photons not absorbed by the top electrode. The photovoltage generated by the TiO_2 produces hydrogen due to the CB electrons. The entire water splitting process is done under visible light.

Mathematically the water splitting process in α - Fe_2O_3 photoelectrode under the visible light is shown by the following equations:



Total process can be written as:



Regardless of the difference in PC and PEC phenomena, both require the same type of materials. In 1972, titania was reported for the first time [18] as a good

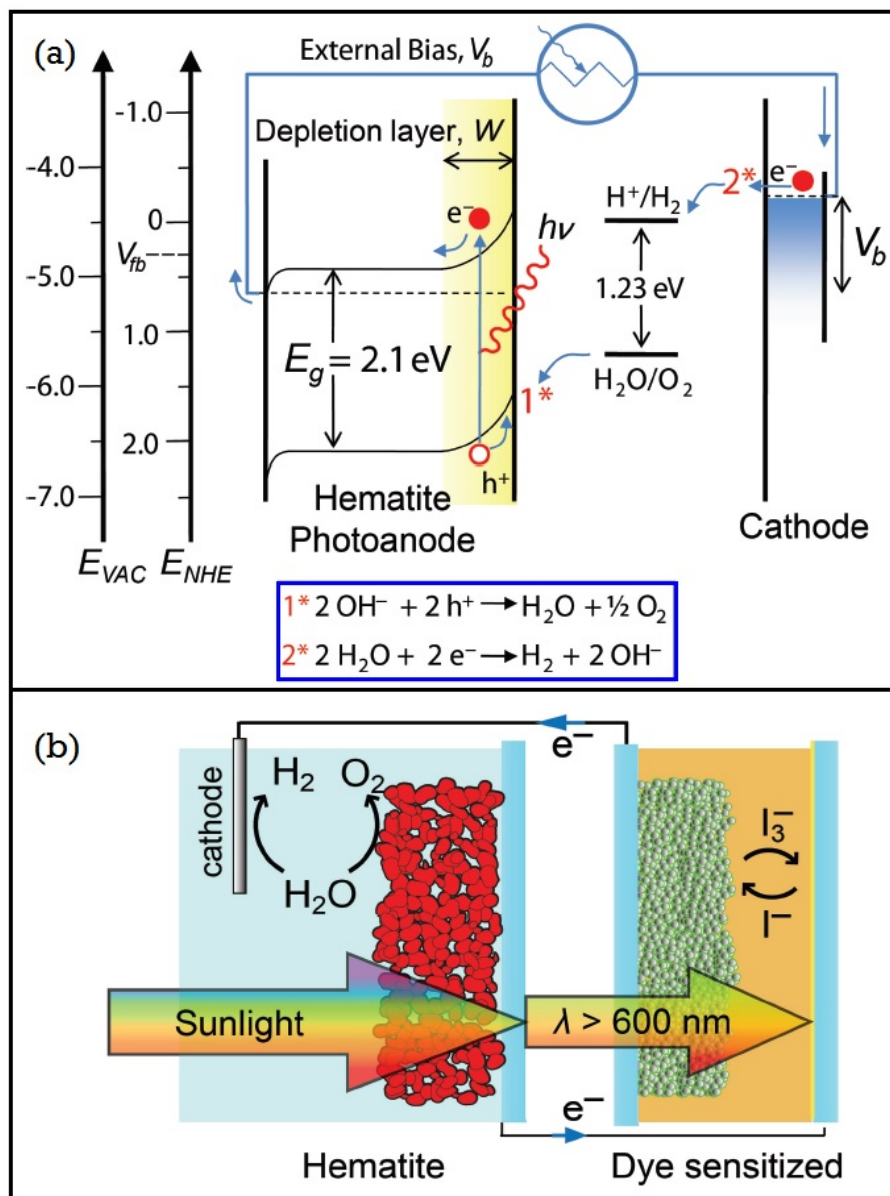


Figure 1.3: (a) Schematic view of energy band diagram of photoelectrochemical water splitting using Hematite as n -type semiconductor. Here the symbols E_g , V_{fb} , V_b stands for the photoanode bandgap, flat band potential and the applied bias. (b) Conceptual water splitting tandem cell using photoanode plus a dye-sensitized solar cell (DSC). taken from [12]

semiconductor for photocatalysis. But it absorbs the solar spectrum in the ultraviolet (UV) regime due to its large band gap (3.0–3.2 eV) and as a result it exhibits low efficiency with respect to light conversion. Many efforts have been devoted to the reduction of the absorption edge of titania to visible regime, or to synthesize novel material alternative to titania performing photocatalysis in the said regime. In view of these numerous efforts, narrow band gap semiconductors were suggested to absorb visible solar light. The main disappointment appears in the prospect of PEC due to instability of these materials under irradiation. Recently, new metal oxide semiconductors like Nb_2O_5 has a wide band gap, is stable under illumination and its threshold energy has been proposed in the UV regime and predicts sensitivity to VIS light.

This problem was resolved by introducing the dye-sensitized (DS) electrochemical photovoltaic cell illustrated in Fig. 1.4. The dye is in general got more attention in the solar cell and a short description on the working procedure of DSSC can be explained as: firstly, the dye is photoexcited due to the incident photon and injects an electron into the semiconductor (here TiO_2) as a result of oxidizing the dye. At this stage a separation in the exciton (semiconductor(electron)/dye (hole)) occurs at the interface of the semiconductor. Secondly, the electron is extracted by the external circuit that contributes to electrical energy and then reaches the counter electrode, where it reduces to redox mediator. The redox mediator exists in the DS solar cell in the form of liquid electrolyte, which consists of the redox couple I^-/I_3^- . The circuit completes at the redox electrolyte (liquid) and again oxidizes the dye.

Recently, nanostructured and large surface area mesoscopic semiconducting materials [19] have received great attention as DS solar cells that allow wide spectrum absorption. For example TiO_2 , Nb_2O_5 , SnO_2 (metal oxide) and CdSe (chalcogenides) are several ideal mesoporous nanostructure compounds and their interconnection allows for carriers (holes/electrons) transport. The dye-sensitized solar cell is grown as a heterojunction of large surface area between p -type semiconductor and n -type polymer transmit hole and large surface area mainly used for effective charge separation. Generally, dye-sensitized heterojunction relaxes the condition in selecting the photo-absorber and charges transport materials to obtain maximal efficiency of photo-current. It has great preference over other phenomena due to greater charge separation (after the photo-generation by the dye) at the space charge region and now a days the most extensive studying system.

Fujishima et al., [18] developed the water splitting process at the TiO_2 photoelectrodes. It opens a pathway for engineers and scientists to fabricate new materials with small band gap, able to absorb light in the visible region and use as an oxidizing and reducing agents in water. In addition these novel materials would also be cheap, and have tunability of carriers upon irradiation and show stability in water. Up to now, there is no single semiconductor that meets all the key properties (discussed above) i.e. some compounds are stable in water but absorbing small amount of light

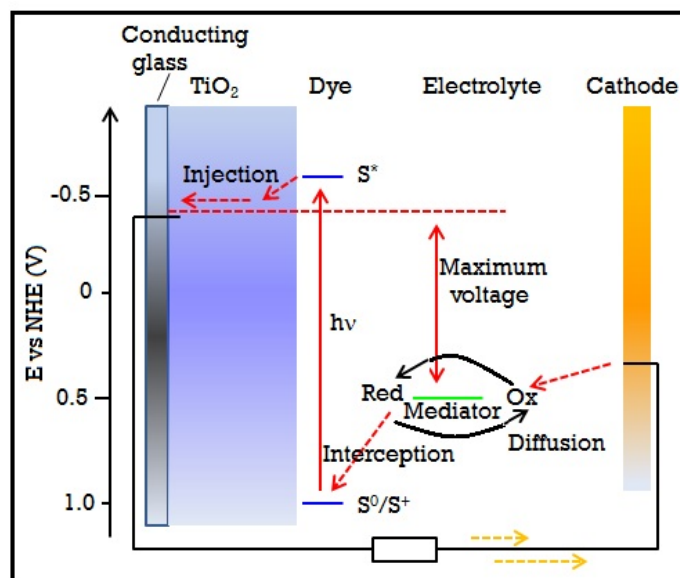


Figure 1.4: Schematic view of the dye-sensitized electrochemical photovoltaic cell and its constituents i.e. it consist of mesoporous semiconductor photoanode, the dye oxidized delivers electrons to semiconductor when it is photoexcited, and as a consequence oxidizes the mediator, a redox reaction completed in the electrolyte. The reduction (regeneration by mediator) of the oxidized dye *via* circulating through external circuit. taken from [11]

due to their large band gap like TiO_2 (anatase). On the other hand, some materials have small band gap but show instability in water, such as InP ($E_g=1.3$ eV) reported by Szklarczyk et al., [20]. The research community is trying continuously to develop an ideal material using experiments [21] and first principle studies [22, 23]. Therefore, large efforts have been performed to promote narrow band gap semiconductors absorbing light in VIS region used as promising photovoltaic devices but these are unstable under light illumination. The synthesis of nanostructure semiconductor has renovated importance in the tandem cells for photocatalysis under visible light, which represents the most appreciable steps in the PEC research. Silicon (Si) based systems offer 7 % efficiency when they are connected in series (four Si) to produce electricity. Tandem cells consisting of III-V semiconductors [17, 24] deliver higher efficiency from 12–20 % during light to H_2 conversion but have some major disadvantages like cost and stability. Recently, a tandem cell of low cost was developed from the nanostructure photoanodes WO_3 ($E_g=2.6$ eV) [25, 26] or $\alpha\text{-Fe}_2\text{O}_3$ (2.01 eV) [27] which serve as a known electrodes (see Fig. 1.3b) harvesting light in the VIS regime. Murphy et al., in 2006 reported maximum efficiencies of 8.0 % for WO_3 and $\alpha\text{-Fe}_2\text{O}_3$ is the most promising candidate with efficiency of 16.8 % solar to energy (H_2). But there is still some limitation in $\alpha\text{-Fe}_2\text{O}_3$ like rapid recombination rate, small electrical conduction etc. Therefore, we focus on novel nanostructure materials and also modify the efficiency of Fe_2O_3 electrode *via* doping.

1.1 Aim of the Thesis

Photocatalytic reaction arises from the interaction between sun light and the semiconductor in the water electrolyte. Semiconductors have many potential applications in photocatalysis among others due to their low cost, stability. In particular the flexible possibility to tune their properties by preparing novel hetrostructures. This leads to the unique structural, optoelectronic and spectroscopic properties. Nevertheless, often measured physical properties of these photocatalytic materials are very difficult to understand, and there is still a need for intensive theoretical analysis. In this thesis, we would like to present recent theoretical investigations in this area. Our calculations about these systems give detailed information about the structure, optoelectronic and spectroscopic properties, using the density functional theory. We focus here on two classes of promising photocatalytic materials, namely various Nb oxides and doped hematite.

$\text{Nb}_3\text{O}_7(\text{OH})$ and Nb_2O_5 nanostructures are promising alternative materials to conventionally used oxides, e.g. TiO_2 , in the field of photoelectrodes in dye-sensitized solar cells and photo-electrochemical cells. Despite this important future application, some of their central electronic properties such as the density of states, band gap and dielectric function are not well understood. In this work, we present combined theoretical and experimental studies on $\text{Nb}_3\text{O}_7(\text{OH})$ and $\text{H-Nb}_2\text{O}_5$ to elucidate their spectroscopic, electronic and transport properties. In particular we show that the structural position of the H-atom in $\text{Nb}_3\text{O}_7(\text{OH})$ has an important effect on its electronic properties. To verify the predicted model, we calculated electron energy-loss spectra in the low loss region, as well as, the O-K and Nb-M₃ element-specific edges. These results are compared with corresponding experimental electron energy loss function. In addition, our calculations of thermoelectric conductivity show that $\text{Nb}_3\text{O}_7(\text{OH})$ has more suitable optoelectronic and transport properties for photochemical application than the calcinated $\text{H-Nb}_2\text{O}_5$ phase. To improve further the performance of $\text{Nb}_3\text{O}_7(\text{OH})$, we functionalised it by doping with Ti. Titanium doping contributed to the modifications of the structure and optoelectronic properties of $\text{Nb}_3\text{O}_7(\text{OH})$. The bond lengths varied by Ti doping confirmed from the structural properties. The presence of Ti in the crystal structure does not alter the optical band gap energy, but the amount of photoabsorption drastically increased with increased contents of Ti. Theoretical study is accompanied by a corresponding detailed experimental electron energy loss spectra and electron energy loss near edge structure study.

Next class of materials is based on hematite $\alpha\text{-Fe}_2\text{O}_3$ and related materials, which are shown to be efficient photocatalytic materials for water splitting process under visible light. We have further improved the photocatalytic activity of hematite by varying tin concentration which substitutes Fe in pristine hematite. Here we show the most stable doping is connected with the octahedral vacancies. To gain

insight into the optoelectronic properties of pure and doped-hematite, we employed the on-site Hubbard interaction and generalized gradient approximation. In this way we obtained the accurate band gap and optoelectronic properties of Sn-doped Fe_2O_3 . The presence of Sn introduced sub-band gaps into the original gap and their catalysis activities are shifted to the infrared region due to an intermediate band. Here, we demonstrate the idea of intermediate bands in hematite for distinctive device applications. Last but not the least, metal-metal charge transfer is expected to be the main mechanism that enables the harvesting of solar light by iron-titanium oxides for photocatalysis. We have studied ilmenite FeTiO_3 as a model compound for metal-metal charge transfer with 1s2pRIXS at the Fe K-edge. The contribution of electric dipole transitions due to local p - d mixing allowed by the trigonal distortion of the cation site is supported by WIEN2k and crystal field multiplet calculations. Non-local features of RIXS are assigned to electric dipole transitions to excited Fe^* $4p$ states mixed with the neighboring Ti $3d$ states. The comparison with calculations enables to demonstrate that metal-metal charge transfer in ilmenite is favored by the hybridization between the Fe $4p$ and delocalized Ti $3d$ orbitals via the O $2p$ orbitals.

1.2 Outline of the Thesis

The present thesis consists of eight chapters. Chapter 1 contains a literature survey, which includes an overview on basic features of artificial photosynthesis like photocatalysis, including a discussion on water splitting materials used for photocatalysis and DSSCs. Chapters 2 and 3 are dedicated to the basic idea of DFT and electronic band structure methods, which follow as: a brief overview of many body interacting systems, KS equations, exchange correlation functions, electronic structure methods mainly on full potential linearized augmented plane wave (FP-LAPW) method, and finally a short introduction to some physical properties and BoltzTraP code. Chapter 4 presents a description on the structures and the properties of Niobium systems and hematite. In Chapter 5, we report on theoretical study of the $\text{Nb}_3\text{O}_7(\text{OH})$ and Nb_2O_5 nanostructural materials. The electronic structure, optical and spectroscopic properties of $\text{Nb}_3\text{O}_7(\text{OH})$ and Nb_2O_5 was determined from the FP-LAPW method employed in WIEN2k code. Secondly, we modeled $\text{Nb}_3\text{O}_7(\text{OH})$ by placing H atom at accurate position and found that it has a promising effect on the electronic structure of $\text{Nb}_3\text{O}_7(\text{OH})$. In this chapter we further calculated EELS and ELNES have nice agreement with Exp. data, which proved the validity of our suggested model. In Chapter 6, the effect of Ti on the structural, optoelectronic and spectroscopic properties of $\text{Nb}_3\text{O}_7(\text{OH})$ is described in detail. Interestingly, Ti replaced Nb confirmed from the formation energy. Doping of Ti revealed the harvesting of more light exposed by the $\varepsilon(\omega)$ spectra. The effect of the Sn dopant in hematite (α - Fe_2O_3) on the electronic structure and optical properties of hematite is investigated

in Chapter 7. It also contains a detailed discussion on intermediate bands and their effect on the optoelectronic properties. In addition, the performance of FeTiO_3 as photocatalyst for photochemistry was studied, which is a model compound for metal metal charge transfer with 1s2pRIXS at the Fe–K edge is described in Chapter 8. Here we described that both quadrupole and electric dipole contributions to RIXS, whereas electric dipole was calculated from WIEN2k code, which represents the local part of the RIXS. At the end, in chapter 9 the results of this work are concluded and provide the future plan for these materials. The appendices contain the supporting information for this study.

Bibliography

- [1] K. Yu, J. Chen, *Nanoscale Res. Lett.* 2008, 4, 1.
- [2] A. Hagfeldt, G. Boschloo, L. Sun, L. Kloo, H. Pettersson, *Chem. Rev.* 2010, 110, 6595.
- [3] M. Grätzel, *J. Photochem. Photobio. C* 4, 145 (2003).
- [4] A. Kudo and Y. Miseki, *Chem. Soc. Rev.* 38, 253 (2009).
- [5] K. Maeda and K. Domen, *Journal of Physical Chemistry C* 111, 7851 (2007).
- [6] P. Cendula, S. D. Tilley, S. Gimenez, J. Bisquert, M. Schmid, M. Grtzel, and J. O. Schumacher, *J. Phys. Chem. C* 118, 29599 (2014).
- [7] Y. Matsumoto, *J. Solid State Chem.* 126, 227 (1996).
- [8] X. Yong and M. A. A. Schoonen, *Am. Mineral.* 85, 543 (2000).
- [9] I. E. Castelli, T. Olsen, S. Datta, D. D. Landis, S. Dahl, K. S. Thygesen, and K. W. Jacobsen, *Energy Environ. Sci.* 5, 5814 (2012).
- [10] L. Yang, H. Zhou, T. Fan, and D. Zhang, *Phys. Chem. Chem. Phys.* 16, 6810 (2014).
- [11] M. Grätzel, *NATURE.* 414, 338, (2001).
- [12] K. Sivula, F. L. Formal, and M. Gratzel, *ChemSusChem*, 4, 432, (2011).
- [13] K. Maeda, K. Domen, *J. Phys. Chem. Lett.* 1, 2655, (2010).
- [14] M. D. Hernandez-Alonso, F. Fresno, S. Suarez, J. M. Coronado, *Energy Environ. Sci.* 2, 1231, (2009).
- [15] A. J. Esswein, D. G. Nocera, *Chem. Rev.* 107, 4022, (2007).
- [16] F. L. Formal, *On the Morphology and Interfaces of Nanostructured Hematite Photoanodes for Solar-Driven Water Splitting (thesis)*, (2011).
- [17] S. Licht, *J. Phys. Chem.* 105, 6281 (2001).

-
- [18] A. Fujishima, K. Honda, *Nature*. 238, 37 (1972).
- [19] O'Regan, B. Grätzel, M. *Nature* 353, 737, (1991).
- [20] M. Szklarczyk, J. O. Bockris, *J. Phys. Chem.* 88, 5241, (1984).
- [21] M. Woodhouse, B. A. Parkinson, *Chem. Soc., Rev.* 38, 197, (2009).
- [22] A. Walsh, S. H. Wei, Y. Yan, M. M. Al-Jassim, J. A. Turner, *Phys. Rev. B* 76, 165119, (2007).
- [23] J. Greeley, T. F. Jaramillo, J. Bonde, I. B. Chorkendorff, J. K. Norskov, *Nat. Mater.* 5, 909, (2006).
- [24] O. Khaselev, J. A. Turner, *Science* 280, 425, (1998).
- [25] M. Ni, M. K. H. Leung, D. Y. C. Leung, K. Sumathy, *Renewable Sustainable Energy Rev.* 11, 401, (2007).
- [26] C. Santato, M. Ulmann, J. Augustynski, *J. Phys. Chem. B* 105, 936, (2001).
- [27] S. U. M. Khan, J. Akikusa, *J. Phys. Chem. B* 103, 7184, (1999).
- [28] S. B. Betzler, A. Wisnet, B. Breitbach, C. Mitterbauer, J. Weickert, L. Schmidt-Mended and C. Scheu, *J. Mater. Chem. A*, 2, 12005, (2014).

Chapter 2

Density Functional Theory

This chapter of the thesis mainly demonstrates the theoretical background of techniques used to solve many body problem. We will start here with a sentence that *"In science and technology, condensed matter physics act as an important input and it is one of the largest research fields that analyzes nano and macroscopic properties of the materials both experimentally as well as theoretically"*.

So in this regard, the available modern and experimental techniques have the ability to investigate materials with respect to their size, composition and functionality, and those methods can characterize more accurately their physical and chemical properties. Meanwhile, progress in theoretical methodologies based on quantum mechanics and available computational resources inspires the researchers to model and predict an electronic properties of finite and extended materials. Principally, the solution to these theoretical problems are very challenging and require high computational power. Sometimes, it is difficult to understand experimental results and computational methods turn out to be extremely useful, and are able to explain, predict and guide the experimental techniques.

The first principles electronic structure techniques are an emerging approach in science for the description of the ground-state as well as spectroscopic properties. The main aim of the first principle calculations is to describe many body problem *via* Schrödinger wave equation to get the desired wave function, which is then used as a starting point for calculations of physical observables of the materials. However, the use of many-body wave function, turned out to be not practicable approach for description of bigger systems. Fortunately, in 1964, Hohenberg and Kohn gave a rigorous proof that instead of many-body wave function, simpler object, e.g. electronic density can be used instead [1]. This approach is called nowadays as density functional theory (DFT). Later on, Kohn and Sham [2] introduced a way how to find an energy functional of density, by mapping of the many-body problem onto the simpler effective one-electron problem, known as a Kohn-Sham system. DFT calculations provide a deep insight into the solid state physics, chemistry, biology and material science. Furthermore, DFT also treats traditionally all kind of systems

like the superconducting materials, organic materials (used in solar cells), magnetic materials (alloys), proteins, mesoscopic materials and layered–quasi structure and surfaces. In this chapter of the thesis, we will briefly introduce the basic idea of DFT, and provide a guidance on the improvements of the approximations for the electron density. We will also expose the role of DFT in solving the problems. At the end we close this chapter with short description of methods that study the valuable properties, like optical and spectroscopic properties.

2.1 Theoretical Background

In order to know about DFT, it is necessary that we should evoke some basics of the quantum mechanics. In quantum mechanics the dynamics of the wave function ψ is carried out by the Schrödinger wave equation (SWE), $i\hbar\partial_t|\psi\rangle = \hat{H}|\psi\rangle$. Here \hat{H} is many particle Hamiltonian. Our main aim is to describe systems in which electrons move in the external potential of the fixed nuclei. Hamiltonian for electrons in external field $v_{ext}(\vec{r}_j)$ is:

$$\hat{H} = \sum_{j=1}^N \left[\left(\frac{-\hbar^2}{2m_e} \nabla^2 + v_{ext}(\vec{r}_j) \right) \right] + \frac{1}{2} \sum_{i \neq j}^N \frac{e^2}{4\pi\epsilon_0 |\vec{r}_i - \vec{r}_j|}. \quad (2.1)$$

The mass and fundamental charge of electron are characterized by m_e and e . The conventional fundamental constants are characterized by \hbar (Planck constant/ 2π), ϵ_0 , e and π , respectively. The second term $v_{ext}(\vec{r}_j)$ in Eq. 2.1 defines the external potential that consists of the entire Coulomb potentials of the M –nuclei on N –electrons and can be expressed as:

$$v_{ext}(\vec{r}_j) = \sum_{j=1}^M \frac{-\hbar}{2M_j} \nabla^2 + \frac{1}{2} \sum_{i \neq j}^M \frac{e^2 Z_i Z_j}{4\pi\epsilon_0 |\vec{R}_i - \vec{R}_j|} - \sum_{i=1}^N \sum_{j=1}^M \frac{e^2 Z_j}{4\pi\epsilon_0 |\vec{r}_i - \vec{R}_j|}. \quad (2.2)$$

Here, the masses and their respective positions of nuclei are characterized by M_j and \vec{R}_j , while the electronic positions are symbolized by \vec{r} . The wave function for the entire electrons ($\psi(x_1, \dots, x_N)$) obey the Pauli exclusion principle and denotes combined space and spin variables. In first view, Eq. 2.1 seems very simple but in reality it is impossible to solve because we deal with highly correlated system in the order of 10^{23} particles.

In order to get improvements we acquire to streamline the problems and for that we will consider some approximations, by reducing the complexity of SWE. In the following discussion, we will consider some common approximations.

First of all, we consider the Born Oppenheimer (BO) approximation, which fixes the nucleus to be at rest at its equilibrium position. BO approximation stems from the fact that the mass of nuclei is 2000 times greater than that of electron mass. This leads a separation between the electrostatic interaction between the nuclei and

nuclei/electrons and electronic interactions. Based on BO, we remove the terms in Eqs. (2.1, 2.2) that corresponds to the momenta of the nuclei and Eq. 2.1 takes the shape as:

$$\hat{H} = \sum_{j=1}^N \frac{-\hbar^2}{2m_e} \nabla^2 - \sum_{i=1}^N \sum_{j=1}^M \frac{e^2 Z_j}{4\pi\epsilon_0 |\vec{r}_i - \vec{R}_j|} + \frac{1}{2} \sum_{i \neq j}^N \frac{e^2}{4\pi\epsilon_0 |\vec{r}_i - \vec{r}_j|}. \quad (2.3)$$

Eq. 2.3 includes only the electronic coordinates and interestingly, these terms deal with many particles system. The kinetic energy term of the nuclei in the $v_{ext}(\vec{r}_j)$ are excluded from Eq. 2.3 based on the BO approximation. Parametrically, the BO Hamiltonian depends on the position of nuclei and remains in the Hilbert space of $\psi_e(\vec{r})$. Nowadays there are many quantum chemical methods that can be used for solving this Schrödinger equation. However, the most important aspect of solving the Schrödinger equation is the selection of an appropriate method. In case of the solid state materials the Density Functional Theory (DFT) is applied which in comparison with other wave function based methods offers flexibility and reasonable computational effort. The key idea of DFT is using the particle density $n(\vec{r})$ for interpretation of the many-body problem and transforming it into a single-body problem. According to the Hohenberg-Kohn Theorem [1] the ground state wave function ψ_0 is a unique functional of $n(\vec{r})$ and there is a direct correlation between the v_{ext} and the density of electron at ground state (n_0). It is known that many-body Hamiltonian is developed by $v_{ext}(\vec{r})$ and in principle: it is possible that n_0 determines the ground state wave function (ψ) of the respective system, and n_0 follows uniquely the ψ . This demonstrates a one to one correlation between them and leads to an assumption that n preside over the entire properties of the system. As a result, the expectation value for any observable \hat{P} is a unique functional of n at ground state, which can be written as:

$$\langle \psi | \hat{P} | \psi \rangle = P[n]. \quad (2.4)$$

According to the second theorem, the total energy functional at ground state under any $v_{ext}(\vec{r})$ applied to many electrons system, can be expressed as:

$$E[n(\vec{r})] = F_{HK}[n(\vec{r})] + \int n(\vec{r}) v_{ext}(\vec{r}) d(\vec{r}), \quad (2.5)$$

where, $v_{ext}(\vec{r})$ is the external potential which comes from many nuclei. The first term ($F_{HK}[n(\vec{r})]$) on the right-hand side is a universal functional of the electron gas system, independent of $v_{ext}(\vec{r})$. Following the variational principle, $E[n(\vec{r})]$ tuned to its minimal value regarding to the ground state density of the respective system associated to $v_{ext}(\vec{r})$.

2.2 Kohn–Sham equations

Though, the H–K theorems strongly correlate the density and the external potential (1st theorem) and correlate total energy to external potential (2nd theorem), but it is failed to find the concrete solution. In 1965, Kohn and Sham published their equations and switched DFT to practical applications [2], like e.g. electronic band structure of solids. Kohn and Sham replaced many–body system (interacting) to single particle system (non–interacting), leading to the accurate total energy functional $E[n(\vec{r})]$ of the non–interacting system [2, 3]. The $E[n(\vec{r})]$ can be expressed as:

$$E[n(\vec{r})] = T_s[n(\vec{r})] + \int v_{eff}(\vec{r})n(\vec{r})d^3\vec{r}. \quad (2.6)$$

In Eq. 2.6, the first term $T_s[n(\vec{r})]$ can be elaborated as kinetic energy of the non–interacting electrons with $n(\vec{r})$. The single particle KS equation for electrons moving in an effective $v_{ext}(\vec{r})$ can be written as:

$$\left[\frac{-\hbar^2}{2m_e}\vec{\nabla}^2 + v_{eff}(\vec{r}) - \varepsilon_j\right]\phi_j(\vec{r}) = 0, \quad (2.7)$$

where the KS energy eigenvalues (the diagonal members of the Lagrangian multiplier) and the wave functions of a single particle (also called KS orbitals) are represented by ε_j and $\phi_j(\vec{r})$, respectively. The density of the interacting particles can then be defined as by using the KS orbitals ϕ_j :

$$n_s(\vec{r}) = \sum_{j=1}^N |\phi_j(\vec{r})|^2. \quad (2.8)$$

The $v_{eff}(\vec{r})$ mentioned in Eqs. (2.6, 2.7) can be written as:

$$v_{eff}(\vec{r}) = v(\vec{r}) + \int \frac{n(\vec{r}')}{|\vec{r} - \vec{r}'|} d\vec{r}' + v_{xc}(\vec{r}). \quad (2.9)$$

Now it is obvious from these equations that the non–interacting electrons are moving in $v_{eff}(\vec{r})$ rather than in $v(\vec{r})$. The $v_{xc}(\vec{r})$ = the exchange correlation potential = $\frac{\delta E_{xc}}{\delta n(\vec{r})}$. The entire K–S equations can be solved by self consistent field approach. The accurate density and total energy of the system at the ground state can be calculated if v_{xc} is known.

2.3 The Exchange–Correlation Functionals

The KS equations mentioned in the previous section are exact, irrespective of the BO approximation. However, the exact form of $v_{xc}[(n)]$ is not known and we need some approximations for xc functional. For this purpose a large number of functionals have been recommended. According to complexity, they were categorized by J. P. Perdew and K. Schmidt, in a scheme named as Jacob’s ladder [5], shown in

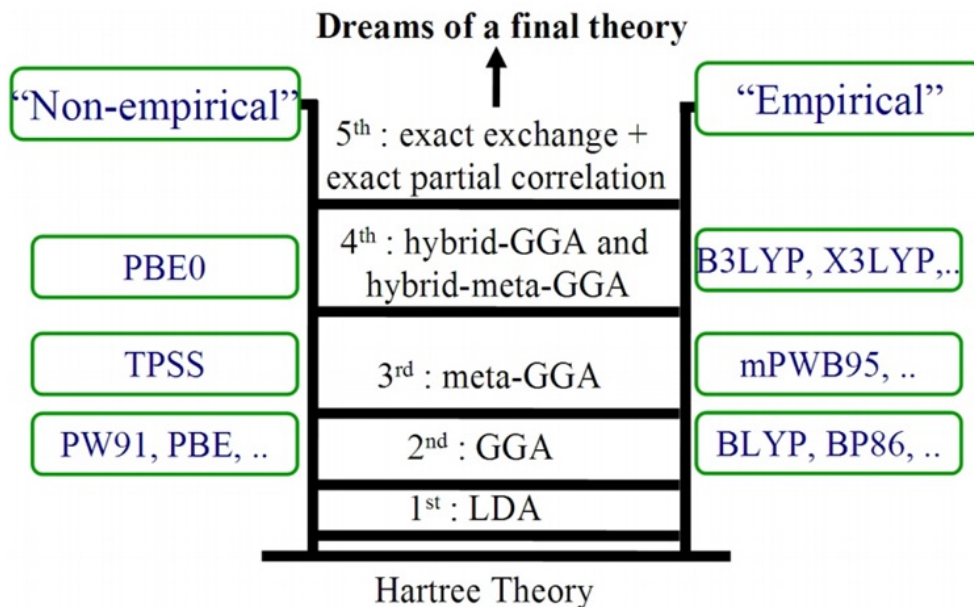


Figure 2.1: Schematic diagram of " Jacobs ladder " of exchange-correlation functionals proposed by J. P. Perdew.

Fig. 2.1. It starts from local density approximation and ends with the accurate xc functional. There are two kinds of functionals. (1) Non-empirical functionals were developed in the frame of some physical criteria. (2) Empirical functionals were developed following by the known outcomes of atomic/molecule characteristics. These functionals will be introduced in the following section in detail.

From the last few years, many approximations have been introduced, but we describe here only a few of them (listed below) used in our calculations for the specific features of water splitting materials.

- **Local (spin) density approximations (L(S)DA)**
- **Generalized gradient approximation (GGA)**
- **Trans Blaha–modified Becke Johnson approximation (TB–mBJ)**
- **On–site Hubbard interaction with DFT (DFT+U)**

2.3.1 The Local (spin) Density Approximation (L(S)DA)

In the LDA approximation [2, 6], a real system is decomposed into small volumes and the density of electrons ($n(\vec{r})$) is assumed to be homogeneous within each small volume. So, the xc energy can be extracted from the homogeneous electronic density. Mathematical expression for the total xc energy is given by:

$$E_{xc}^{LDA}[n(\vec{r})] = \int d^3\vec{r} n(\vec{r}) \varepsilon_{xc}^{hom}, \quad (2.10)$$

here, the E_{xc} per particle of a uniform electron gas with density is symbolized as

ε_{xc}^{hom} [7]. Practically, E_x and E_c of a uniform electron gas with $n(\vec{r})$ are calculated separately i.e. an analytic relation for the E_x is used and a known expression of Volso, Wilk and Nusair (VWN) [8] on the basis of quantum Monte Carlo technique for electron gas [9] is used for the calculation of E_c , respectively. It should be noted that the VWN–LDA is used in SPR–KKR code by default, while the LDA proposed by Perdew and Wang [29] based on random phase approximation (RPA) is used in WIEN2k code by default.

Moreover, local spin density approximation (LSDA) [29, 11] is also commonly used approximation in the solid state physics to calculate E_{xc} per particle depends on $n_{\uparrow}(\vec{r})$ and $n_{\downarrow}(\vec{r})$. Hence, due to spin dependent density, the above equation takes the shape as:

$$E_{xc}^{LDA}[n_{\uparrow}(\vec{r}), n_{\downarrow}(\vec{r})] = \int d^3\vec{r} n(\vec{r}) \varepsilon_{xc}[n_{\uparrow}(\vec{r}), n_{\downarrow}(\vec{r})]. \quad (2.11)$$

The above equation is used to characterize the magnetic systems. For this, spin densities ($n(\vec{r}) = n_{\uparrow}(\vec{r}) + n_{\downarrow}(\vec{r})$) are used instead of total electron density. Due to this, one particle wave function with spin up and spin down and then two effective potentials (one for spin up and spin down) were obtained.

In fact, LDA works extremely well for metals in which the densities are varying very slowly. The idea behind this success in LDA is the systematic cancellation of error and the fulfilling of sum rules for any density during the cancellation. Besides, LDA does underestimate (overestimate) the correlation (exchange) in uniform systems, but generate nice results of E_{xc}^{LDA} . Furthermore, its recent results report overestimation in the cohesive energy (15–20 %) and underestimation in the lattice constant (2–3 %) of metals as well as insulators.

2.3.2 The Generalized Gradient Approximation (GGA)

In order to solve the problem of rapid variations of electron density in real materials, a density gradient ($\nabla n(\vec{r})$) is included as the next term of a Taylor expansion. First effort to include gradient of the density into the LDA functional failed completely. Perdew [13] pointed out the reason that it violates the basic sum rule and suggested the so-called generalized gradient approximation (GGA) [14, 15]. The generalized gradient approximation (GGA) [14] results from the cut-off appear in the curve at higher gradients for higher contributions of gradient.

Becke [16] explained the working procedures of the GGA's, which he explains by using the following expression:

$$E_{xc} = \int d^3\vec{r} A n(\vec{r}) F(x(\vec{r})). \quad (2.12)$$

The symbols $n(\vec{r})$ and $x = |\vec{\nabla} n|/n^{4/3}$ are standing for the local density and reduced gradient. In Eq. 2.12, the LDA expression and enhancement factor are symbolized by the letters A and $F(x(\vec{r}))$, respectively. The functional, here denoted by

enhancement factor $F(x)$, depends not only on the local $n(\vec{r})$ but also on the $\vec{\nabla}n(\vec{r})$ to evaluate the asymmetry of the xc between h^+ and reference \bar{e} 's. In this series, Kohn [17] introduced an equivalent formalism:

$$E_{xc}^{GGA} = \int f^{GGA}(n(\vec{r}), |\vec{\nabla}n(\vec{r})|) n(\vec{r}) d\vec{r}. \quad (2.13)$$

Irrespective of LDA, the GGA functional depends on two independently calculated variables like $x = n$ and $y = \vec{\nabla}n$, which are functions of \vec{r} by itself. The exchange–correlation functional f^{GGA} depends on x and y , respectively.

This functional positioning one step above from the LDA (known as second generation) on the Jacob's ladder (see Fig. 2.1). Different approaches have been introduced i.e. Becke (B88) [18], Perdew and Wang (PW91) [6], Lee–Yang–Parr (LYP) [19] and Perdew, Burke and Enzerhof (PBE) [20], to yield functionals up to corrected correlation. Finally, as a conclusion, GGA favored robust surfaces and reduces over–binding as compared to LDA. Introducing $\vec{\nabla}n(\vec{r})$, the ground state properties of molecule and solids calculating *via* GGA are found far better than LDA and close to the experiment.

2.3.3 Trans–Blaha Modified Becke Johnson Approximation (TB–mBJ)

The functionals (L(S)DA/GGA) (mentioned in Sec. 2.3.1 and 2.3.2) proposed specific approaches for the xc energy E_{xc} to calculate the electronic structure of the solid state materials within DFT based on KS method. The results obtained from these approximations (semi–local) have very good agreement with the experimental findings. Computationally, these approaches are less expensive than other suggested methods. In spite of all these qualities, both LDA/GGA functionals have drawbacks especially in semiconductors and insulators. They underestimate the band gaps [21] or falsely lead to metallic nature.

A. D. Becke and E. R. Johnson (BJ) in 2006 proposed an exchange potential that reproduced the accurate form of atomic OEP and improved results over LDA and PBE–GGA. Apart from this, BJ potential underestimates the band gaps and it is not precise; therefore some improvement is still needed. F. Trans and P. Blaha [23] modified the original BJ potential that to produce better band gaps. This interprets with the experimental results as well as with the results of other expensive methods. Mathematically, modified BJ (MBJ) can be written as (It should be noted that the subscript σ is used in the TB–mBJ approach is used for spin.):

$$v_{x,\sigma}^{MBJ}(\vec{r}) = cv_{x,\sigma}^{BJ}(\vec{r}) + (3 - c) \frac{1}{\pi} \sqrt{\frac{5}{12}} \sqrt{\frac{2t_{\sigma}(\vec{r})}{2n_{\sigma}(\vec{r})}}. \quad (2.14)$$

Here, n_{σ} is the electron density and (t_{σ}) is kinetic energy correction. $(\frac{1}{2}) \sum_{i=1}^{N_{\sigma}} \vec{\nabla} \psi_{i,\sigma}^* \cdot \psi_{i,\sigma}$.

The original exchange potential proposed by Becke and Roussel that model exchange hole Coulomb potential is:

$$v_{x,\sigma}^{BR}(\vec{r}) = -\frac{1}{b_\sigma(\vec{r})}(1 - e^{-x_\sigma(\vec{r})}) - \frac{1}{2}x_\sigma(\vec{r})e^{-x_\sigma(\vec{r})}. \quad (2.15)$$

The parameters x_σ to be calculated need some variables i.e. $\vec{\nabla}n_\sigma$, $\vec{\nabla}^2n_\sigma$ and t_σ for x_σ and b_σ from an equation $(\frac{x_\sigma^3 e^{-x_\sigma(\vec{r})}}{8\pi n_\sigma})^{\frac{1}{3}}$ is used. Basically, Becke and Johnson used the Slater potential ($v_{x,\sigma}^{Slater}$) rather than the BR potential ($v_{x,\sigma}^{BR}$) and they verified that both potentials are similar for atoms i.e. $v_{x,\sigma}^{Slater} = v_{x,\sigma}^{BR}$. In WIEN2k code, they modified t_σ that depend on the KS potential, is given by:

$$t_\sigma(\vec{r}) = \sum_{i=1}^{N_\sigma} \varepsilon_{i,\sigma} |\psi_{i,\sigma}|^2 - v_{effe,\sigma}^{KS}(\vec{r})n_\sigma + \frac{1}{2}\nabla^2 n_\sigma. \quad (2.16)$$

The parameter c in Eq. 2.14 has a linear relation with $|\vec{\nabla}n(\vec{r})/n(\vec{r})|^{1/2}$, which is shown in a relation:

$$c = \alpha + \beta \left(\frac{1}{v_{cell}} \int \frac{|\vec{\nabla}n(\vec{r}')|}{n(\vec{r}')} d^3\vec{r}' \right)^{\frac{1}{2}}, \quad (2.17)$$

α and β are two free parameters. In the WIEN2k code [42], the dimensionless quantity α having value is -0.012 and $\beta = 1.023 \text{ Bohr}^{1/2}$. To the exchange potential of mBJ ($v_{x,\sigma}^{MBJ}$), also include a correlation affect in the form of LDA correlation potential [20] i.e. mBJ-LDA. Under the condition of variant available possibilities, F. Tran et al., [41] got very satisfactory results using Eq. 2.14, and the results (band gaps of different semiconductors) obtained *via* LDA and mBJ-LDA functionals are plotted in Fig. 2.2, with the results obtained from HSE, G_0W_0 and GW.

2.3.4 On-site Hubbard interaction with DFT (DFT+U)

In this thesis, we treat transition metal oxides (TMO) [1, 2, 26] (with localized d states) for which traditional DFT approximations fail to determine the accurate gap of insulators and semiconductors especially in systems like bulk Silicon, ZnO and other correlated insulators [25]. The symbol Δ_C is defined as the difference between the ionization energy ($I^N = E_0^{N-1} - E_0^N$) and the electron affinity ($A^N = E_0^N - E_0^{N+1}$), where E_0^N indicates the ground states energy of N correlated system. In this context, it was found that narrowing band gaps of TMO are governed by the $3d$ localized states. So in order to overcome this error a deficiency of traditional DFT approximations, we apply a generalized Hubbard model to calculate the exact v_{xc} of a correlated system, as a consequence to get a stable ground state electronic structure. So, in 1991, Anisimov and his co-worker [22] developed a similar method to the hybrid functionals named as LDA+U to predict the insulating nature of the TMO rather than metallic one as predicted by LDA or GGA. The on-site Coulomb interaction in the localized states like d states deal with by Hubbard type term (U) is the main aim of DFT+U. To correct the double counting of the interactions, a

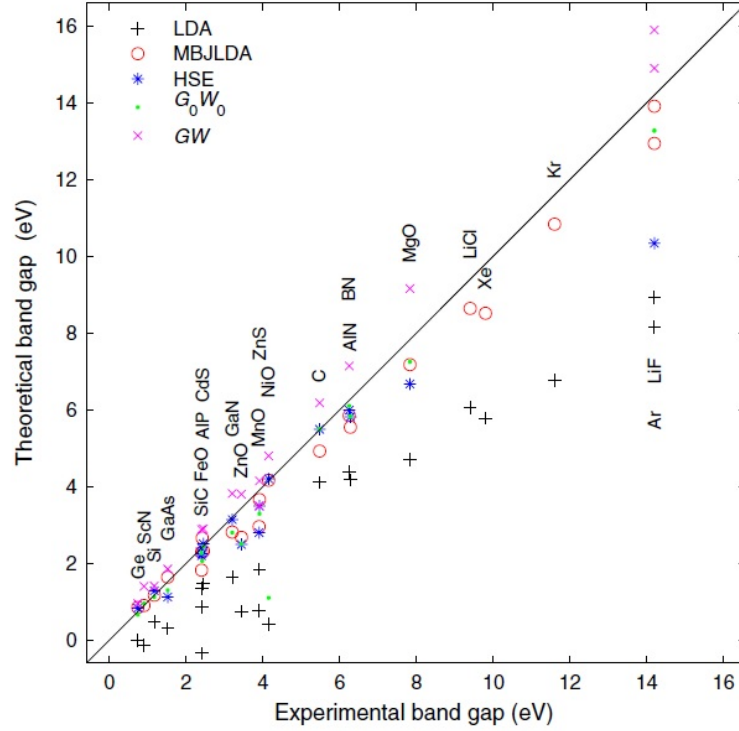


Figure 2.2: Theoretical and experimental band gap values for some selected semi-conductors. taken from [23]

correlation term was considered within the Hubbard model. The total energy at the level of LDA+U can be written as [26]:

$$E = E^{LDA} + \frac{1}{2} \sum_{m,m',\sigma} U(n_{im\sigma} - n^0)(n_{im'\sigma} - n^0) + \frac{1}{2} \sum_{\substack{m,m',\sigma \\ (m \neq m')}} (U - J)(n_{im\sigma} - n^0)(n_{im'\sigma} - n^0), \quad (2.18)$$

where m, m' and σ defining various d orbitals and spin (\uparrow, \downarrow), respectively, and J is used for Hund's rule exchange parameter. First term E^{LDA} is the spin-independent total energy term. Eq. 2.18 is defined in concurrence to the orthonormality of the localized orbital (strongly correlated electrons). The quantities $n^0 = n_d/10$ =mean occupancy of single d orbital, and $n_{im\sigma}$ =spin and orbital dependent of these localized orbitals. Due to on-site Coulomb interaction, these bands split into an upper Hubbard band (at $+U/2$) and lower Hubbard band (at $-U/2$) to obtain a desired band gaps (insulating gaps). These findings show nice agreement to the results obtained from the hybrid functionals reported by Tran et. al. [27] in TMO.

Bibliography

- [1] P. Hohenberg, W. Kohn, Phys. Rev. 136, B864, (1964)
- [2] W. Kohn, and L. J. Sham, Phys. Rev. 140, A1133, (1965)
- [3] P. Hohenberg and W. Kohn, Phys. Rev. 140, 1133, (1965)
- [4] P. E. Blöchl, Phys. Rev. B 50, 17953, (1994)
- [5] J. P. Perdew and K. Schmidt, AIP conf. Proc. 577, 1, (2001)
- [6] J. P. Perdew and Y. Wang, Phys. Rev. B 45, 13244, (1992)
- [7] W. Kohn and L. J. Sham, Phys. Rev. 140, A1133, (1965)
- [8] S. H. Vosko, L. Wilk and M. Nusair, Can. J. Phys. 58, 1200, (1980)
- [9] D. M. Ceperley and B. J. Alder, Phys. Rev. Lett. 45, 566, (1980)
- [10] J. P. Perdew, and Y. Wang, Physical Review B 45 (23), 13244, (1992).
- [11] D. M. Ceperley, and B. J. Alder, Physical Review Letters 45 (7), 566, (1980).
- [12] G. S. Painter, Phys. Rev. B 24, 4264, (1981)
- [13] J. P. Perdew, Phys. Rev. Lett. 55, 1665, (1985)
- [14] D.C. Langreth, M. Mehl, Phys. Rev. B 28, 1809, (1983).
- [15] J. P. Perdew, M. Ernzerhof, A. Zupan, and K. Burke, Journal of Chemical Physics 108 (4), 1522, 1998.
- [16] A.D. Becke, Phys. Rev. A 38, 3098, (1988)
- [17] W. Kohn, Reviews of Modern Physics, 71, 1253, (1999)
- [18] A. D. Beck, Phys. Rev. A 38, 3098, (1988)
- [19] W. Lee, C. Yang and R. G. Parr, Phys. Rev. B 37, 785, (1988)
- [20] J. P. Perdew, K. Burke, and M. Ernzerhof, Phys. Rev. B 45, 13244, (1996).

-
- [21] J. Heyd, J. E. Peralta, G. E. Scuseria, and R. L. Martin, *J. Chem. Phys.* 123, 174101, (2005).
- [22] V. I. Anisimov, J. Zaanen, and O. K. Andersen, *Phys. Rev. B* 44, 943, (1991).
- [23] F. Tran and P. Blaha, *PRL* 102, 226401, (2009).
- [24] W. Kohn, Nobel Lecture: 71, 1253, (1999).
- [25] V. Brosco, Z.-J. Ying and J. Lorenzana, *Sci. Rep.*, 3, 2172, (2013).
- [26] V. I. Anisimov, J. Zaanen and O. K. Andersen, *Phys. Rev. B* 44, 943, (1991)
- [27] F. Tran, P. Blaha, K. Schwarz, P. Novák, *Phys. Rev. B* 74, 155108, (2006).

Chapter 3

Electronic Structure Methods

In this chapter, we will focus on the solution of Kohn–Sham (KS) equation and related quantum mechanical problems i.e. total energy and other physical observables. We want to describe the single electron system as the vital role ingredient for the 3D electron systems. The Bloch theorem deals with the periodicity of a crystal that reduces infinite number of wavefunctions of a single electron to simple electrons of a unit cell, which is to be calculated. In terms of calculation, it describes the systems and their study is restricted to unit cell in a reciprocal space. So in order to evaluate the KS orbitals of a crystal, we need to apply the Bloch states to solve quantum mechanical wavefunction and energy of a system at ground states.

The sobering news after converting the many body interacting system to single electron interacting system, namely the KS equations, still presents numerous complications: In the atomic region it is found that the kinetic energy (K.E) leads to rapid oscillation near the nuclei due to its large value. With this large value of K.E, the ψ_n in the atomic region can be described by small basis set, because it is then hard to solve the SWE. While in between the atoms K.E and ψ_n behave oppositely i.e. K.E is small and ψ_n is smooth, and in addition the ψ_n acquire large basis sets.

These difficulties are non-trivial and different strategies have been introduced.

(1) The atomic point of view plays a central role in the quantum mechanics. Like atomic orbitals, the basis functions are selected. In contrast, the ψ_n can be characterized by small basis functions, while the chemical bonding is characterized by the overlapping tails of these basis functions. Many methods in this class are in accord of, (a) a well established basis set is included, where the basis function are difficult to manage and (b) mathematically and numerically proper basis functions are implemented, which reproduces the inadequacies. However, these inadequacies are then compensated by large basis sets.

(2) Pseudopotentials consider the free electrons in the valence shell in the external potential of the core electrons of an atom. Therefore, the plane-waves are always used for free electron gas in pseudopotential approximation. These plane-waves make the basis function smooth and suitable for computation. In contrast to the

computational efficiency, there are some disadvantages like it needs large basis sets and it completely ignores strong fluctuation near the nucleus.

(3) Augmented wave techniques represent a different approach in which a space composed of wave functions similar to atomic like wave inside the atomic regions and a set of envelope functions (plane waves) are considered in the bonding region. These waves are then augmented at the sphere boundary.

The projected plane wave method is a new version of augmented plane wave and pseudopotential methods, which takes the advantages of both methods into a merge electronic structure method. Based on these ideas, let us briefly describe the methods of our interest in recent research.

In 1937, Slater [1] introduced augmented wave method (APW). According to this method the potential inside the MT sphere is spherically symmetrical and constant in the interstitial region. Then O. K. Andersen [2] demonstrated that the energy dependent basis sets can be augmented with energy independent basis functions by linearization. In the APW method, the eigenfunction is evaluated at fixed energy by orbital solution of the radial function. Therefore, every time a new energy is required in the evaluation of new basis sets. The energy dependent matrix elements lead the secular equation will be non-linear problem in energy.

In the APW method, the basis set is constructed in the atomic region by radial solution to the Schrödinger equation for spherically symmetric effective potential as a function of energy

$$\left[\frac{-\hbar^2}{2m_e}\nabla^2 + v_{eff}(\vec{r}) - \varepsilon\right]\phi_{l,m}(\varepsilon, \vec{r}) = 0, \quad (3.1)$$

It should be remembered that the angular momentum eigenstates is $\phi_{l,m}$ (partial wave), which is expressed as a product of u_l and $Y_{l,m}$. The energy dependent $\phi_{l,m}$ can be expanded by Taylor series in the limit of energy $\varepsilon_{\nu,l}$.

$$\phi_{l,m}(\varepsilon, \vec{r}) = \phi_{\nu,l,m}(\vec{r}) + (\varepsilon - \varepsilon_{\nu,l})\dot{\phi}_{\nu,l,m}(\vec{r}) + O((\varepsilon - \varepsilon_{\nu,l})^2), \quad (3.2)$$

here both partial wave and energy derivative of partial wave are equal, while the energy derivative term is obtained from the energy derivative of SE

$$\left[\frac{-\hbar^2}{2m_e}\nabla^2 + v_{eff}(\vec{r}) - \varepsilon\right]\dot{\phi}_{\nu,l,m}(\varepsilon, \vec{r}) = \dot{\phi}_{\nu,l,m}(\varepsilon, \vec{r}). \quad (3.3)$$

Next to begin from the basis set (plane wave), also called envelope functions $|\tilde{\chi}_i\rangle$. These plane waves are replaced by partial waves/derivative partial waves inside the atomic region, in such a way that the envelope function is continuous and differentiable. The augmentation of these χ_i can be written as

$$\chi_i(\vec{r}) = \tilde{\chi}_i(\vec{r}) + \sum_R \theta_R(\vec{r})\tilde{\chi}_i(\vec{r}) + \sum_{R,l,m} \theta_R(\vec{r})[\phi_{\nu,R,m}(\vec{r})a_{R,l,m,i} + \dot{\phi}_{\nu,R,m}(\vec{r})b_{R,l,m,i}]. \quad (3.4)$$

The term θ_R (step function) in the augmented sphere of radius \vec{R}_R (which is \sim covalent radius) is equal to unity and zero outside. It may also be called the MT radius in the touching spheres of neighboring atoms. One therefore requires that the valence states determine by the basis functions. Here the core states denote the localized states in the augmentation sphere which can be determined from the radial solution to Schrödinger equation within the sphere. Both coefficients ($a_{R,l,m,i}$ and $b_{R,l,m,i}$) are obtained from the envelope functions, which are divided into spherical harmonics by radial functions around each atomic site

$$\tilde{\chi}_i(\vec{r}) = \sum_{l,m} u_{R,l,m,i}(|\vec{r} - \vec{R}_R|) Y_{l,m}(\vec{r} - \vec{R}) \quad (3.5)$$

The matching norm of $\phi_{R,l,m,i}$ and $\dot{\phi}_{R,l,m,i}$ and $u_{R,l,m,i}(|\vec{r}|)$ and its derivative, results in the expansion coefficients ($a_{R,l,m,i}$ and $b_{R,l,m,i}$).

If the basis functions (in Eq. 3.5) are plane waves, then the technique based on them is called linearized augmented plane wave (LAPW). Singh [3] presented a thorough review on LAPW method. Let us discuss shortly the improvements of the LAPW. The idea of augmentation was firstly introduced by Soler [4]. At the same time, the APW are discontinuous at the surface of augmented sphere. Soler used an expansion of the plane wave for the second term with the same dependency as in the third term, which faster the convergence of angular momentum. Based on this, Singh [5] introduced local orbitals (nonzero in the MT sphere), where they are superpositions of both partial waves from various expansion energies. Local orbital relaxes the variational flexibility in the energy. Further improvement comes from Sjöstedt [6], relaxing the condition for the basis function i.e. these are differentiated at the sphere boundary. According to her, the local orbital are enclosed in the sphere and put no extra condition on the APW basis set. The increased variational flexibility in the energy improved the convergence of PW.

Last but not the least, the full potential LAPW method provides well-define basis sets [7]. In this case, the shape approximation is used entirely to define the basis sets $|\chi_i\rangle$, whereas the matrix elements ($\langle \chi_i | H | \chi_i \rangle$) of the Hamiltonian are determined with FP-LPAW.

3.1 The Augmented Plane Wave (APW) method

In order to solve the KS equation, many possible methods have been developed. Frequently, Slater [1] approximated the solution of KS equation by developing the augmented plane wave method. Based on this method, one can identify two different classes of regions in space (single crystal): (1) type-1 with spheres centered at each sites, called muffin tin (MT) spheres (2) type-2 with free space between these spheres, named as interstitial region. The MT spheres are chosen so that they do not overlap and they approximately fill the possible space. In this respect, Slater [1]

distinguished the basis sets i.e. they behave as plane waves in the interstitial region, and are approximated to be spherically symmetric inside the MT spheres, which is shown in Fig. 3.1. These limitations to the potential are called MT approximation or shape approximation. Both basis functions are augmented into the radial solutions of the Schrödinger wave equation at the sphere boundary. The Bloch eigenfunctions near the atomic sites can be directly described from these radial functions. In this approximation, the single eigenfunction can be effectively expressed as:

$$\varphi_G^{APW}(\vec{r}, \vec{k}) = \begin{cases} e^{i((\vec{k}+\vec{G})\vec{r})} & I \text{ region} \\ \sum_L a_L^{\vec{k}+\vec{G}} u_l(\vec{r}, E_l) Y_L(\hat{r}) & MT \text{ region,} \end{cases} \quad (3.6)$$

where the reciprocal lattice vector, crystal momentum, angular momentum index (l, m) and spherical harmonic in this expression are given symbols as \vec{G} , \vec{k} , L and $Y_L(\hat{r})$. The coefficients $a_L^{\vec{k}+\vec{G}}$ are responsible for the matching norm. At this condition, the basis functions are acquired to be continuous at MT sphere boundaries and the coefficients $a_L^{\vec{k}+\vec{G}}$ are found from the plan wave expansion into Bessel function (which is replaced by radial function suggested by Slater) at the sphere boundary, while the plane waves are energy dependent. Where u_l depends on energy E_l represents the radial solution of the Schrödinger wave equation. Consequently, the APW explains very well that it uses very efficient basis functions and generally describes the entire quantities in both regions of space.

Nonetheless, disadvantages to the APW method exist. (1) The APW method does not allow sufficient variational freedom at fixed energy. Because each APW must be produced at a given fixed eigenenergy. (2) As the radial function u_l depends on energy, this leads a secular equation to non-linear problem, and makes the APW method very expensive. (3) In APW, there is another problem which is not overly important but has an impact on the calculations i.e. the radial function equal to zero at the boundary of MT sphere which could result in asymptotic behavior implies a decoupling of PW 's and radial function. (Note: For detailed discussion see the book by Loucks [8] and for the introduction point of view see the articles by L.F. Mattheis et al. and H. Ehrenreich et al., [9, 10]).

3.2 The Linearized APW (LAPW) method

As is well known, the augmented plane wave method does not provide correction to the non-linear as well as the asymptotic problems. However, some important formalism has been provided by APW to devise a different and improved method for this purpose, called the linearized augmented plane wave (LAPW) method [2, 11]. The energy dependent basis functions u_l inside the MT spheres were extended by

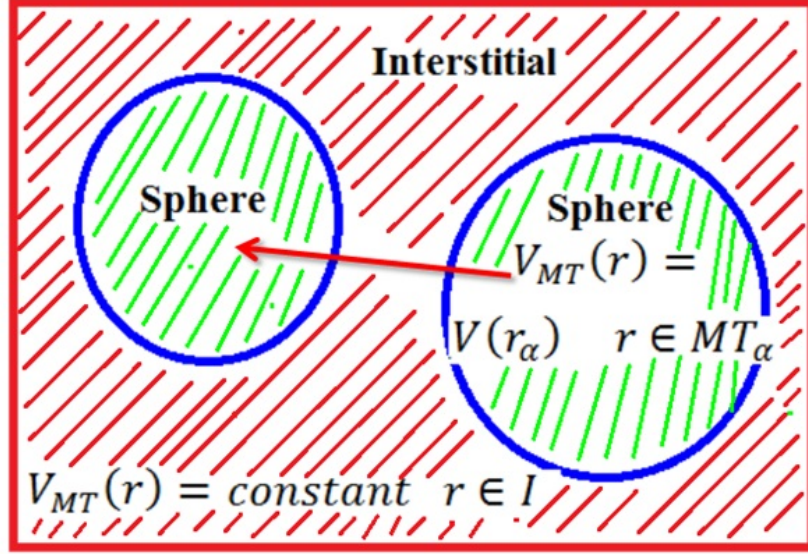


Figure 3.1: Unit cell is decomposed into muffin–tin spheres and interstitial regions.

their energy derivatives (\dot{u}_l) mentioned by Marcus [12]. Both u_l and \dot{u}_l are calculated at fixed energy E_l . So, the energies and wavefunctions are overwhelmed by an error, but the errors are only of the fourth and second order in the difference $E - E_l$. For this mechanism, the energy independent basis functions,

$$\varphi_G^{LAPW}(\vec{r}, \vec{k}) = \begin{cases} e^{i((\vec{k} + \vec{G})\vec{r})} & I \text{ region} \\ \sum_L R_L^{LAPW}(\vec{r}) Y_L(\hat{r}) & MT \text{ region.} \end{cases} \quad (3.7)$$

The basis functions of LAPW is shown schematically in Fig. 3.2. The value of coefficient $R_L^{LAPW}(\vec{r})$ is equal to the linear combination of $a_L^{\vec{k} + \vec{G}} u_l(\vec{r}, E_1)$ and $b_L^{\vec{k} + \vec{G}} \dot{u}_l(\vec{r}, E_1)$, where \dot{u}_l is the energy derivative of u_l . The continuity in the basis function with the first derivative of the basis function at the surface of the MT sphere are assured by the determined values of the coefficients ($a_L^{\vec{k} + \vec{G}} u_l(\vec{r}, E_1)$ and $b_L^{\vec{k} + \vec{G}} \dot{u}_l(\vec{r}, E_1)$).

The shape of the physical solution of the energy dependent radial function will not have similarities with u_l and \dot{u}_l , while the matching norms are strictly mathematical (see from the Fig. 3.3). The linearization in the basis sets of the APW method offer enough flexibility to represent valence electron states in the I region and localized electronic states close to nuclei around E_1 . The main importance in the LAPW method is to construct sufficient variational freedom that could solve exactly the single particle Schrödinger equation within the MT sphere. In LAPW, by linearization, two major problems were resolved: to eliminate the non-linear problem to secular equation and use single diagonalization of the secular equation to

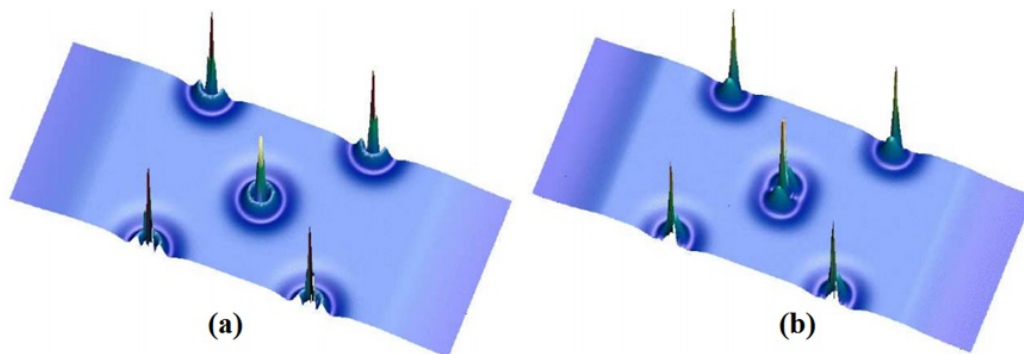


Figure 3.2: The basis functions (LAPW) created for $\mathbf{k}(\mathbf{G}=0)$ (a) at the M-point and (b) M-point of the Brillouin zone of a 3-layer thin film of Cu(100). The basis function selected here are Cu-4s(a)/4p states (b). taken from [13]

determine all energy eigenvalues. Especially more specific to calculation, the convergence in the LAPW method is merely less or equal than APW method with respect to basis functions [13] but without any doubt the LAPW is in practice an improved method over APW.

3.3 The Linearized/Augmented Plane Wave plus Local Orbital (L/APW+lo) method

Generally, electronic states are categorized into three parts: (1) core states completely localized inside the atomic sphere and treated fully relativistically, (2) valence states electrons are responsible to take part in chemical bonding, and (3) semi-core states present a problem to LAPW method. These states are described as core states because of the high delocalization in the MT sphere. Yet the energy parameter acquired to describe these states is already utilized for the description of the valence states. For example, the La-5p states lie in high energy, which is to be neglected in the total energy simulations [14]. This problem has been extensively resolved at different available schemes. As, in APW method, the lonely energy independent basis sets does not provide sufficient variational flexibility to find a solution at fixed energy. This problem was disposed of by introducing extra basis set containing local orbitals for $l \leq 3$. The addition of local orbitals did not affect the basis set (APW) and the no. of plane waves in I region.

So, in order to improve the variational flexibility, Singh [14] established the notion of the local orbitals (LOs) to deal with the semicore states in the LAPW method. The local orbitals presented extra basis sets, which are entirely confined in the MT spheres, are given by.

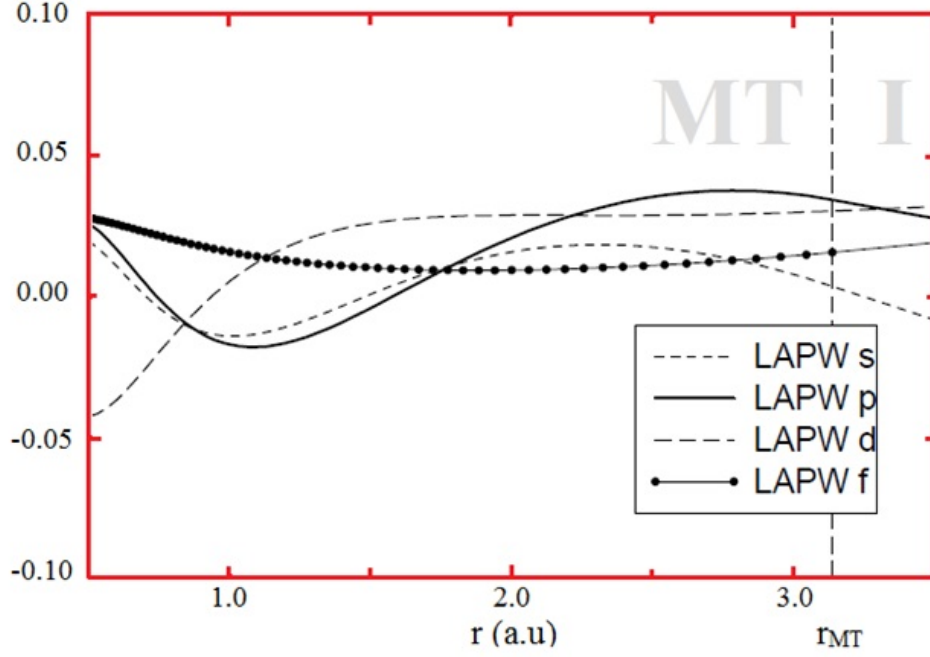


Figure 3.3: The radial solution u_l are augmented at MT sphere boundary for Ce for different orbital quantum number of an LAPW basis function.

$$\phi_L^{lo}(\vec{r}, \vec{k}) = \begin{cases} 0 & I \text{ region} \\ R_L^{lo}(\vec{r})Y_L(\hat{r}) & MT \text{ region,} \end{cases} \quad (3.8)$$

herein, the coefficient R_L^{lo} is equal to similar radial functions (see section 3.2) except lo replace $\vec{k} + \vec{G}$, which is the index for local orbitals i.e. $a_L^{lo}u_l(\vec{r}, E_1)$ and $b_L^{lo}\dot{u}_l(\vec{r}, E_1)$, and using the same linearization energy. The entire coefficients are found from the normalization of the basis function of the local orbital and have zero values at sphere boundary. Slight change in the linearization energy for the local orbitals cannot influence simulations. The linearization energy can easily be selected under certain condition like decoupling of basis functions and b_L^{lo} can be evaluated at the MT boundary with a limitation that $a_L^{lo}=1$ and $\phi_L^{lo}=0$. It should be noted that once LAPW code is modified using the local orbitals then it is very easy to turn it into APW+lo method.

The basis set of APW+lo include both respective radial functions; (1) $u_l(\vec{r}, E_1)$, which is used to describe efficiently the eigenfunction at fixed energy E_1 (in APW method) (2) and that of LAPW methods a linear combination of $u_l(\vec{r}, E_1)$ and $\dot{u}_l(\vec{r}, E_1)$, which is used to describe the states effectively away from E_1 . Furthermore, the inclusion of local orbitals in APW compared to the standard LAPW offers faster setup of matrix elements.

The APW+lo method leads to a small basis set similar to APW method and

same linearization energy, yielding the same accuracy as LAPW method but faster in convergence described by numbers of PWs [16]. Greater efficiency of APW+lo is based on mixed basis set that highlight the significance of the orbital quantum number (l), while higher l used for LAPW.

3.4 Full Potential Linearized Augmented Plane Wave (FP-LAPW) method

The APW method [1] based on MT approximation was regularly used in metallic systems (highly coordinated systems) e.g. face center cube metals. However, the MT approximation found a weak approximation in systems where solids are covalently bonded and in layered structures systems. This leads to a contradiction with experiments. So, the **full potential (FP)** method is introduced to enhance further accuracy in the results. For this no shape approximation was introduced, which is essential to treat these problems. According to FP-LAPW, which combines the basis set of LAPW method, the potential in the I region is not constant and non-spherical within MT sphere. On the basis of no-shape approximation, the V (maximum between two neighbor atoms) and n (minimum between two neighbor atoms) are augmented in to lattice harmonics within each individual MT sphere and (outside I region) as a Fourier series.

$$V(\vec{r}) = \begin{cases} \sum_G V_I^G e^{i\vec{G}r}(\hat{r}) & MT \text{ region} \\ \sum_L V_{MT}^L(\vec{r}) Y_L(\hat{r}) & I \text{ region.} \end{cases} \quad (3.9)$$

This general scheme is called as full potential calculation scheme. Due to no shape approximation, the choice of the MT radii is no more critical in this method. With the development of this method it is possible that one would achieve various radii (a maximum choice) depending on weather one would seek at the n (density) and V (potential). Comparatively, with implication of FP-LAPW method, it is very easy to handle the problem rather to make compromise with MT approximation.

3.5 Optical Properties

Linear optical properties based on linear optical response theory determine from OPTIC program [20] implemented in WIEN2k code [21], which we explain as: it is known that intrinsic semiconductors behave as insulator (at very low temperature), where the valence band maximum (VBM) (completely occupied by electrons) and conduction band minimum (CBM) (normally free or partially filled) are separated

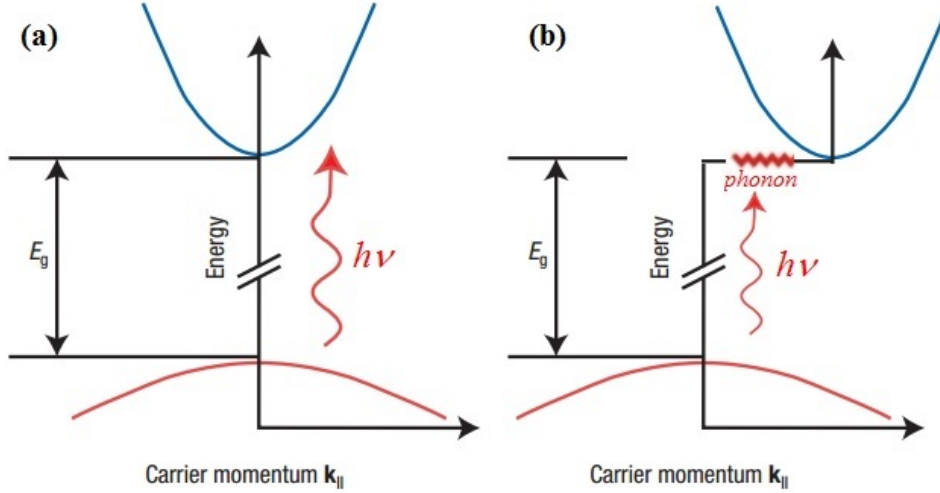


Figure 3.4: Schematic representation of conduction band and valence band. It shows the energy versus the in plane carrier momentum (a) it describes the direct band transition and (b) describes the indirect band transition.

by band gap. The semiconductors of direct band gap have zero momentum and vice versa (see Fig. 3.4).

Fig. 3.4 demonstrates that the electron from VB is optically excited and leaves the hole in the VB, referred to as optically induced transitions of exciton. Holes behave similar to electrons in spin, charge and effective mass but in opposite sign. Mathematically, the behavior of a single exciton is similar to H atom in parabolic band. The binding energy E_b of the lowest state is directly related to reduce effective mass μ and has an inverse relation with m_0 and square of dielectric constant ε [22]; $E_b = \mu/(m_0\varepsilon^2)$. This implies that smaller μ ($\approx 0.05m_0$) and larger ε (≈ 13) in case of GaAs produce E_b in the order of few meV, which is lying below VB to CB transition. Therefore, the natural level for internal exciton transitions is the far-infrared, terahertz (THz) on the spectral range and is equals to 4.1 meV (photon energy). In semiconductor physics, the SWE represents electrons and holes are the Wannier equation, while Wannier excitons stand for the solution of bound pair.

During the discussion, we will elaborate the excitons and their basic properties with some restriction i.e. the binding energy of small excitons need large Bohr radius implies large spatial separation of excitons lead non-bosonic behavior. Moreover, recombination of electron (excited) in CB whereas hole in VB happens in a short interval (10^{-9} s) in direct band gap semiconductors and emits the excess energy, usually referred as spontaneous emission. On the basis of these fermionic (electron/hole) excitations, semiconductors lead several insights e.g. exciton resonance (optical absorption), spontaneous emission, and photoluminescence [23, 24]. Here, we will briefly explain the main aspects of optical absorption (interband spectroscopy):

→ **Interband Spectroscopy :**

It is recognized that on the basis of Maxwell's equations, one can know some related features of semiclassical properties (optical) of semiconductors.

In semiclassical optics, Maxwell's wave equation (without free carriers) is given by:

$$[\nabla^2 + \frac{n^2}{c^2} \frac{\partial^2}{\partial t^2}]E = -\mu_0 \frac{\partial^2}{\partial t^2}P. \quad (3.10)$$

Here in, ∇^2 stands for Laplace operator, μ_0 is constant depending on the unit system and polarization vector is symbolized by P . The wave equation describes the interaction of classical electromagnetic field and matter, can be split into two parts e.g. resonant part (treated strongly on the basis of macroscopic optical polarization) and nonresonant part (taken into the refractive index). In this thesis, we neglect the polaritonic propagation effects, because we deal with nanostructural materials. In the case of crystalline materials (semiconductors), it is suitable to express P into Bloch basis [25] i.e. $P = \sum_k d_{cv} P_k + c.c.$, here P_k , D_{cv} describe polarization amplitude, optical dipole matrix element between CB and VB (interband transition) and \mathbf{k} is the carrier's crystal momentum, respectively. S. W. KOCH et al., [26] obtained the Bloch equations (for semiconductors) while introducing interband transition (optical) and Coulomb interaction between excitons that couple P_k and f_k^a (occupation probability). Here the Wannier equation is defined as the linear polarization equation in homogeneous form i.e. $f^e = 0 = f^h$ and has mathematical similarity to SE used for H problem, and it can be solved in two ways such as excitation states (bound solution) and Coulomb interacting ionized state (unbound solution). The electron-hole susceptibility is obtained from the inhomogeneous part, resulting in the Elliott formula [27] (linear susceptibility) as:

$$\chi(\omega) = 2|d_{cv}|^2 \sum_{\lambda} \frac{|\phi_{\lambda(r=0)}|^2}{E_{\lambda} - \hbar\omega - i\gamma_{\lambda}}. \quad (3.11)$$

This equation exposes the resonant contribution, a phenomenological dephasing factor γ_{λ} and also shows that the absorption resonance occurs at ω . The susceptibility exposes the degree of polarization of dielectric materials due to the application of external electric field i.e. greater the susceptibility larger will be the polarization in the material. Hence, it influences the electric permittivity, which in turn influences different mechanism. The optical behavior of an intrinsic semiconductor can be determined from the lattice, free carriers (mobile ions and holes) and the interband transitions, which ultimately lead to a dielectric function.

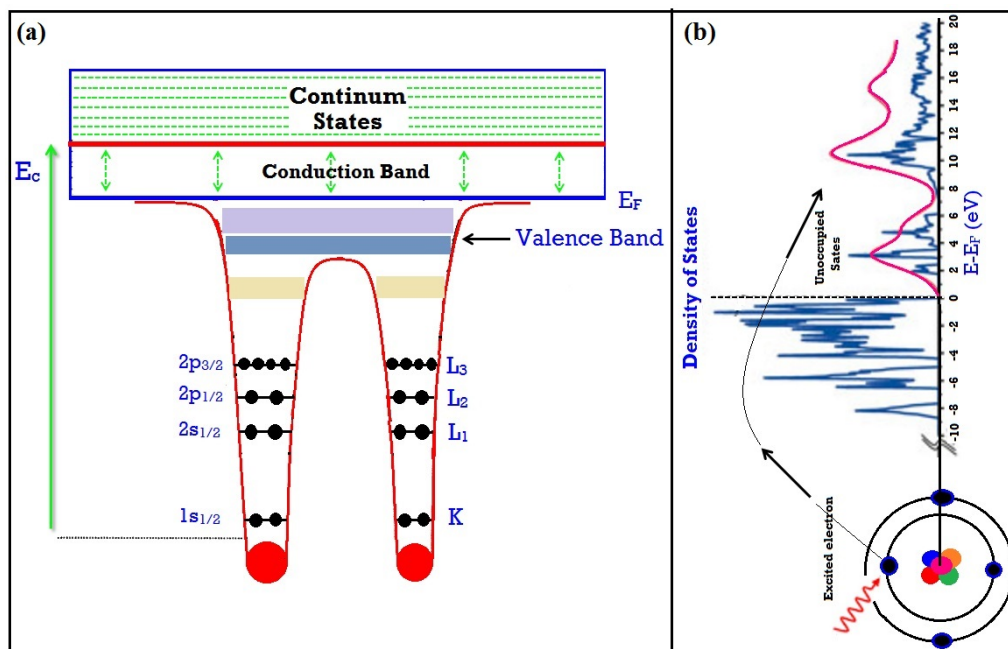


Figure 3.5: Sketch showing (a) the core band electron, Fermi level, valence and conduction bands (b) and the core electron excitation to the available unoccupied state above the Fermi level.

3.6 X-rays Absorption (XAS) and Electron Energy Loss (EELS) spectroscopy

X-rays absorption (XAS) and electron energy loss spectroscopy (EELS) are fundamental core level techniques for analyzing electronic properties; structural, chemical of a specific materials. XAS takes responsibility for the energy absorption of X-rays and EELS describes the energy loss of high energy electron propagating through a material [28]. The spectra obtained from both techniques include fine structure and edge structure in the case of extended energy loss and absorption denoted as (ELNES/XANES, EXELFS/EXAFS). Here, we focus on ELNES (energy loss near edge structure), accounts for the electron energy absorption near and above the core level energies of an atom. It corresponds to inelastic losses from the core states (deeply) electron excitation to unoccupied states (above the Fermi level) in a system and similar approach is also applied to XAS. As EELS is an absorption method and the deep core level present the electronic structure of excited electron (in empty states). Besides the fitting parameters, the shape of the spectra (edge) roughly proportional to unoccupied angular momentum partial density of states, followed by selection rules ($\Delta l = \pm 1$). Fig. 3.5 demonstrates the core electron bands (narrower and strongly bound to the nucleus) than valence band and conduction band.

According to an independent particle approximation [29], the screened core hole effect must be considered in the simulation of excited electron states. There are

many approaches working under different conditions to simulate core hole XAS and EELS of crystal, while the narration of excitation is upgrade in the electronic band structure methods. It is known from Fermi's Golden rule [30] that both X-rays absorption coefficient and transition rate are proportional to each other and mostly the one-electron approximation of the Golden's rule (equation is given below) is used for the calculations of XAS.

$$\mu \propto \sum_f | \langle \psi_f | \mathbf{p} \cdot \mathbf{A}(\mathbf{r}) | \psi_i \rangle |^2 \delta(\mathbf{E}_f - \mathbf{E}_i - \hbar\omega). \quad (3.12)$$

For the sake of fitting with the experimental data, some of the parameters like $e = \hbar = m = 1$, energy is taken in eV and distance in Å, respectively. The symbols ψ_i and ψ_f take care of initial and final states of the effective one electron H_i (i =initial) and H' for final state. The H' is used to simulate the ψ_f equals to "final-state rule". Final term ($\delta(E_f - E_i - \hbar\omega)$) stands for density of states. In case of deep-core excitations, $e^{ikr} = 1$ i.e. the magnetic vector potential is ignored (dipole approximation). Quadrupole correction is scaled as $(Z\alpha)^2$, where Z is the nuclear charge and α is fine structure constant ($\cong 1/37$). Moreover, Zangwill and Soven in 1980 reported a negligible effect of the local field to deep core excitation.

Now, suppose the core loss EELS, where the incident electron loses its energy during the interaction with the specimen's atomic electron and excite electron to unoccupied state from initial state. Double differential cross-section is considered during this transition probability that describes the scattering of electrons (fraction) into a solid angle $d\Omega$ in the energy rang from E to $E+dE$. It can be determined quantum mechanically using Fermi's Golden rule. According to one electron model, the double differential cross-section can be written as:

$$\frac{d^2\sigma}{dEd\Omega} \propto \frac{4\gamma^2}{a_0^2q^4} | \langle \psi_f | \underline{q} \cdot \underline{r} | \psi_i \rangle |^2 \rho E, \quad (3.13)$$

here the Bohr radius, relativistic correction factor, scattering vector and density of states are symbolized as a_0 , γ , \underline{q} , \underline{r} and ρE , respectively. It is clear from Eq. 3.12 and Eq. 3.13 that both electron-electron and photon-electron operators ($\underline{q} \cdot \underline{r}$) have the same dipole, and also have the same selection rule $\Delta l = \pm 1$. From the above discussion, we concluded that both XAS and EELS are the same.

3.7 Thermoelectric Properties

In this part of thesis, we will elaborate it in three steps going from Thermoelectric properties to BoltzTraP code [31] and Boltzmann transport theory.

→ **Thermoelectric properties**: Nowadays, solar photovoltaic and solar thermal phenomena are mainly used to convert solar energy for human use. The work-

ing principle of photovoltaic devices is to generate electricity from the electron hole pairs and can be used in houses and especially in solar farms, while the second one generates electricity from heat used in power plant and hot water systems. So, thermoelectric (TE) materials allow a direct conversion of temperature gradient (∇T) into thermoelectric power gradient (∇S) and vice versa. (TE) materials have potential applications like power generation and refrigeration technologies as well as their future advancements and in addition also have the capability in the technological areas e.g. sensors, energy harvesting, and the latest idea of thermopower wave sources.

Generally, the efficiency of (TE) devices is mainly governed by the figure of merit (dimensionless), i.e. $zT = S^2\sigma T/\kappa_E + \kappa_L$. Here, the terms S , σ , κ_E , κ_L and T stand for thermopower (Seebeck Co-efficient), electrical conductivity, electronic/lattice thermal conductivity and absolute temperature, respectively and all these parameters except T are interrelated to each other.

→ **Boltzmann Transport Theory** : The flowing of current (electrical/thermal current) applied fields (electric field/ ∇T) are termed as transport. As it is clear from the first sentence that there is a linear relationship between current and fields a step must be taken to calculate the transport coefficient from this linear behavior. Transport coefficients have been evaluated with the help of microscopic model of transport process. The Boltzmann transport formulation is used in this thesis, which governed the semi-classical approach in the limit of constant relaxation time approximation. The current is in general can be written as:

$$\vec{J} = e \sum_{\vec{k}} f_{\vec{k}} \vec{v}_{\vec{k}}, \quad (3.14)$$

where $\vec{v}_{\vec{k}}$, is the group velocity corresponds to state \vec{k} with population $f_{\vec{k}}$. The distribution function $f_{\vec{k}}$ (measure the number of carrier) can change *via* diffusion, external fields (electric/magnetic fields/ ∇T) and scattering of carriers by phonons/impurities/crystal defects. The Boltzmann equation carries the interactions between the entire mechanisms, which is obtain from the population of states [32], which can be expressed as:

$$\frac{\partial f_{\vec{k}}}{\partial t} + \vec{v}_{\vec{k}} \cdot \nabla_{\vec{r}} f_{\vec{k}} + \frac{e}{\hbar} (\vec{E} + \frac{1}{c} \vec{v}_{\vec{k}} \times \vec{H}) = \left(\frac{\partial f_{\vec{k}}}{\partial t} \right)_{scattering}. \quad (3.15)$$

For zero fields, the Boltzmann transport equations (BTE) are found to be Fermi-Dirac distribution function $f_0(\vec{k})$. Applying the condition of zero field plus constant relaxation time for scattering terms, the population in the state is:

$$f_{\vec{k}} = f_0(-\vec{k}) + e \left(-\frac{\partial f_{\vec{k}}}{\partial \varepsilon_{\vec{k}}} \right) \tau_{\vec{k}} \vec{v}_{\vec{k}} \cdot \vec{E}. \quad (3.16)$$

The Fermi distribution function at equilibrium position (zero fields) is:

$$f_0 \vec{k} = \frac{1}{e^{\frac{\varepsilon_{\vec{k}} - \mu}{k_B T}} + 1}, \quad (3.17)$$

the chemical potential in the above Eq. 3.17 is symbolized as μ , which possess high dependency on carrier concentration and low on temperature.

→ **BoltzTraP code**: It is a computer program that evaluate the semi-classic transport coefficients. It is compatible to the band structure code WIEN2k [21] and also can be easily interfaced to other available band structure codes like VASP [33, 34, 35], Quantum espresso [36] etc. BoltzTraP code [31] is reliable on the Fourier interpolation of energies of the bands $d\varepsilon$ calculated from WIEN2k code [21], and also resulting in the velocities as Fourier sums. The BoltzTraP code is based on the semi classical Boltzmann transport theory (BTT) under constant relaxation time approximation and rigid band approximation has been tested for many applications. These calculations need very dense \mathbf{k} -mesh, normally acquired for the band structure in **SCF** (self-consistent field) calculation.

Furthermore, it determines the applicability of materials as conductive materials. So, recent development in the nanostructured semiconducting materials has been found to solve the energy problem. These compounds are classified on the basis of low cost, high surface area, environmentally friendly and reliable. Normally the materials (insulators, semiconductors, and metals) are classified into good or bad criterion base on the figure of merit, power factor, Seebeck coefficient and electrical/thermal conductivity, which is labeled in Fig. 3.6. It can be seen in Fig. 3.6 that the materials have high electrical conductivity and high charge density leading to a high thermoelectric effect.

3.7.1 Electrical Conductivity

The rigid band approximation and BTT employed in BoltzTraP code [31] is used to calculate electrical conductivity tensor, which is a base for all transport coefficients. The passage of the electronic charges (electrons, holes) through crystal lattice of a material is called electrical conductivity. Mathematically it can be defined as the product of density of charge carriers (n) and their mobility (μ) i.e.

$$\sigma = n\mu e, \quad (3.18)$$

where

$$\sigma = \frac{e\tau}{m^*}. \quad (3.19)$$

Here μ depends on the relaxation time (τ) and effective mass (m^*), which is mainly determined from the band structure. As the mobility of charge carriers is treated semi-classically in BTT and their drift velocity in a specific band is given

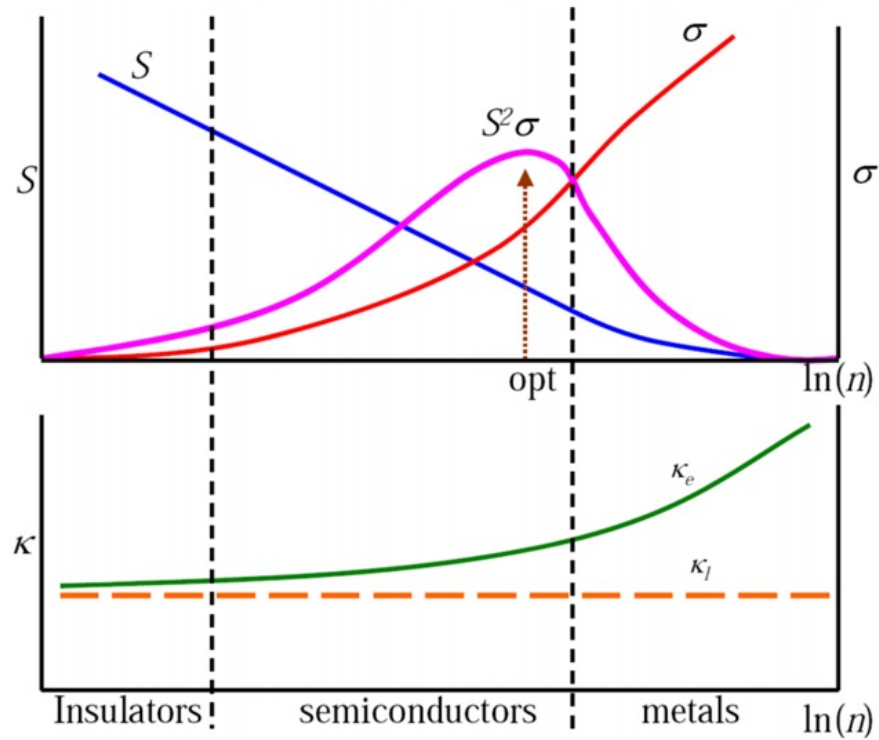


Figure 3.6: Upper part of the figure represents the electrical/thermal conductivity, Seebeck coefficient, power factor versus carrier concentration, while the lower part represents the electronic and lattice thermal conductivity against the $\ln(n)$. taken from [37]

by:

$$v_\alpha(i, \mathbf{k}) = \frac{1}{\hbar} \frac{\partial \varepsilon(i, \mathbf{k})}{\partial k_\alpha}, \quad (3.20)$$

where $\varepsilon(i, k)$, and k represent the i th band at point \mathbf{k} and component of the wave vector and subscript is the cartesian index. From the DFT band structure we calculate the group velocity and then we simulate energy dependent transport distribution tensor:

$$\sigma_{\alpha,\beta}(i, \mathbf{k}) = \frac{e^2}{N} \sum_{i,\mathbf{k}} \tau(i, \mathbf{k}) v_\alpha(i, \mathbf{k}) v_\beta(i, \mathbf{k}) \delta[\varepsilon - \varepsilon(i, \mathbf{k})], \quad (3.21)$$

and the electrical conductivity transport distribution tensor depends on temperature and chemical potential is define by [38]:

$$\sigma_{\alpha,\beta}(T, \mu) = \frac{1}{\Omega} \int \sigma_{\alpha,\beta}(\varepsilon) \left[-\frac{\partial f_0(T, \varepsilon, \mu)}{\partial \varepsilon} \right] d\varepsilon. \quad (3.22)$$

Here, the group velocity, relaxation time, volume of the unit cell, Fermi Dirac distribution function and equilibrium distribution function are represented symbolically by v , τ , Ω , f_μ and f_0 . Moreover, the number of \mathbf{k} -points and Cartesian axes are described by N and α/β .

Bibliography

- [1] J. C. Slater, Phys. Rev. 51, 846, (1937).
- [2] O. K. Andersen, Phys. Rev. B, 12, 3060, (1975).
- [3] D. J. Singh, Planewaves, pseudopotentials and the LAPW method (Kluwer, 1994).
- [4] J. Soler, A. R. Williams, Phys. Rev. B 40, 1560, (1989).
- [5] D. J. Singh, Phys. Rev. B 43, 6388, (1991).
- [6] E. Sjöstedt, L. Nordström, D. J. Singh, Solid State Commun. 113, 15 (2000).
- [7] H. Krakauer, M. Posternak, A. J. Freeman, Phys. Rev. B 19, 1706, (1979).
- [8] T. L. Loucks, Augmented Plane Wave method: a guide to performing electronic structure calculations, Benjamin, New York (1967)
- [9] L. F. Mattheis, J. H. Wood, A. C. Switendick, Methods in Computational Physics 8, 64 (1968)
- [10] H. Ehrenreich, F. Seitz, D. Turnbull (editors), the calculation of electronic energy bands by the augmented plane wave method J. O. Dimmock in Solid State Physics, volume 26, Academic Press, 103-273, (1971).
- [11] D. D. Koeling, G. O. Arbman, Journal of Physics F 5, 2041, (1975).
- [12] P. M. Marcus, Variational Methods in the Computation of Energy Bands, Int. J. Quantum Chem. Suppl. 1, 567 (1967).
- [13] S. Blügel and G. Bihlmayer Computational Nanoscience: J. Grotendorst, S. Blügel, D. Marx (Eds.), John von Neumann Institute for Computing, Jülich, NIC Series, Vol. 31, ISBN 3-00-017350-1, pp. 85-129, 2006.
- [14] D. Singh, Phys. Rev. B 43, 6388, (1991).
- [15] E. Sjöstedt, L. Nordström, D. J. Singh, Solid State Comm. 114, 15, (2000).
- [16] G. K. H. Madsen, P. Blaha, K. Schwarz, E. Sjöstedt, L. Nordström, Phys. Rev. B 6, 195134, (2001).

- [17] T. L. Loucks, *Augmented Plane Wave Method* (Benjamin, New York, 1967).
- [18] H. Bross, *Phys. Kondens. Mater.* 3, 119, (1964); *Z. Phys. B* 81, 233, (1990).
- [19] P. Marcus, *Int. J. Quantum. Chem. Suppl.* 1, 567, (1967).
- [20] D. J. Singh, S. S. A. Seo, and H. N. Lee, *Phys. Rev. B* 82, 180103, (2010).
- [21] P. Blaha, K. Schwarz, G. Madsen, D. Kvasnicka, and J. Luitz, *WIEN2k: An Augmented Plane Wave plus Local Orbitals Program for Calculating Crystal Properties* (Karlheinz Schwarz, Techn. Universität Wien, Austria, 2001).
- [22] R. A. Kaindl, M. A. Carnahan, D. Hägele, R. Lövenich and D. S. Chemla, *Nature*. 423, 734, (2003).
- [23] J. Shah, *Ultrafast Spectroscopy of Semiconductors and Semiconductor Nanostructures* (Springer, Berlin, 1999).
- [24] D. S. Chemla, and J. Shah, *Many-body and correlation effects in semiconductors*. *Nature* 411, 549, (2001).
- [25] H. Haug, and S. W. Koch, *Quantum Theory of the Optical and Electronic Properties of Semiconductors* 4th edn (World Scientific, Singapore, 2004).
- [26] S. W. Koch, M. Kira, G. Khaitrova and H. M. Gibbs, *nature materials*, 5, 523, (2006).
- [27] R. J. Elliott, in *Polarons and Excitons* (eds Kuper, C. G. and Whitefield, G. D.) 269, (Oliver and Boyd, Edinburgh, 1963).
- [28] R. F. Egerton, *Electron Energy-Loss Spectroscopy in the Electron Microscope* (Plenum Press, New York, 1996).
- [29] K. Jorissen and J. J. Rehr, *Phy. Rev. B* 81, 245124, (2010).
- [30] A. Messiah, 1966, *Quantum Mechanics* (Wiley, New York)
- [31] G. K. Madsen and D. J. Singh, *Computer Physics Communications* 175, 67, (2006).
- [32] J. M. Ziman, *Principles of the Theory of Solids*, chapter 7, (1972).
- [33] G. Kresse and J. Hafner, *Phys. Rev. B*, 47, 558, (1993); G. Kresse and J. Hafner, *Phys. Rev. B*, 49, 14251, (1994).
- [34] G. Kresse and J. Furthmüller, *Comput. Mater. Sci.*, 6, 15, (1996).
- [35] G. Kresse and J. Furthmüller, *Phys. Rev. B*, 54, 11169, (1996).

-
- [36] Paolo Giannozzi, et.al. Quantum ESPRESSO: a modular and open-source software project for quantum simulations of materials. *J.Phys: Condens matter*, 21, 395502, (2009).
- [37] Y. Saeed, Tuning the Transport Properties of Layered Materials for Thermoelectric Applications using First-Principles Calculations (thesis), (2014).
- [38] A. P. Nayak et. al., *Nature Communications* 5, 3731, (2014)

Chapter 4

Materials Selection

In this part of the thesis, a short description on metal oxides, most oftenly used for water splitting process, is presented. In addition, our discussion will be more specific to niobium oxide and hematite regarding their physical properties and crystal structures.

4.1 Metal Oxides for Water Splitting Process

The role of metal oxides in physics, chemistry and material science have been widely described [1, 2, 3, 4, 5]. Technologically, these systems are used in the manufacturing of different electronic devices and most significantly used as photocatalysts. Oxides in bulk size have strong stability with well established crystallographic structures. Though, the decrease in the particle size enhances the free surface energy. The varying thermodynamic stability corresponds to their respective size and can induce variation in the cell parameters and structural transformations [6, 7, 8]. But these nano particles disappear due to the high surface free energy and, secondly, an interaction with environment. So, the nanostructural materials possess small surface free energy, yet show stability i.e. mechanical and structural. As a conclusion, phases, which are stable in nanostructure, show less stability in bulk and such behavior has been observed in TiO_2 , VO_x , Al_2O_3 or MoO_x .

TiO_2 was the first nanostructure material, reported by Fujishima et al., [9], used as photocatalyst with the capability of producing H_2 and O_2 from water splitting. It was also reported as an innovative photoelectrode material in the DSSCs [10], more specifically to efficiency. Unfortunately, TiO_2 absorbs light from solar spectrum in the UV range with respect to its large band gap (3.4 eV) [11] that results a decrease in efficiency and less stability in aqueous solution [12]. Comparison with tin oxide SnO_2 (stable, n -type and large band gap ~ 3.6 eV semiconductor) [13] possess magnificent optoelectronic properties. Besides, it is less valuable as compared to TiO_2 and ZnO for DSSCs due to their fast exciton recombination. In the same manner, organolead trihalide perovskites having band gaps in the range from 1.5 eV

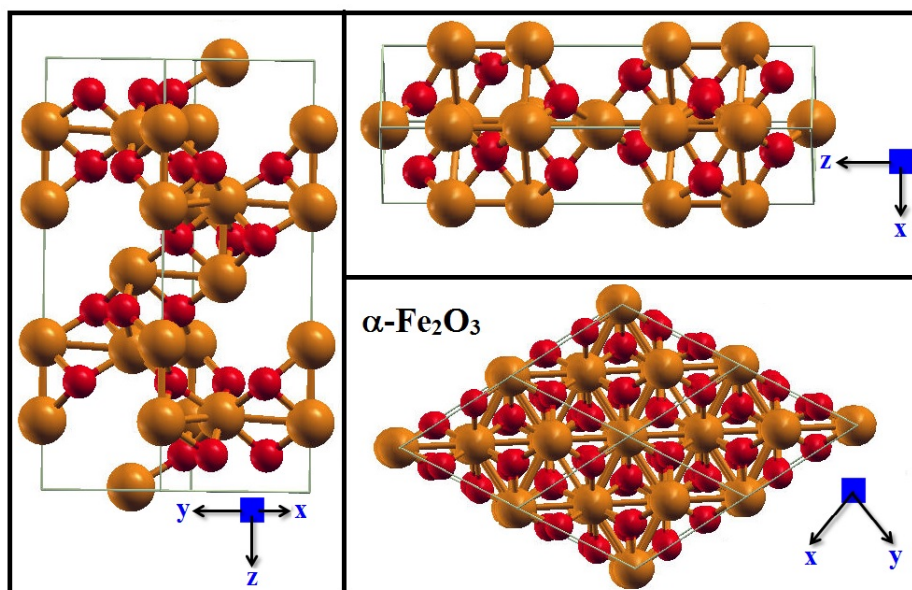


Figure 4.1: Schematic representations of $\alpha\text{-Fe}_2\text{O}_3$ along different crystallographic axes.

to 2.3 eV [14, 15] found as photoelectrode but unfortunately it shows instability, when exposed to air. Along with TiO_2 , the researcher paid much effort to prepare other photoanode materials like $\alpha\text{-Fe}_2\text{O}_3$, Nb_2O_5 etc.

4.1.1 Hematite

Iron presents 6.3 % by weight in the earth's crust and marks fourth in the most common elements; it becomes oxidized to ferrous (+2) and ferric (+3) in air. Iron oxide has the ability to absorb light in the VIS region. Among other iron oxides, hematite ($\alpha\text{-Fe}_2\text{O}_3$) demonstrates good photocatalytic activity and solar energy conversion. From the last few years, it has been paid most attention due to low cost, stability, and narrow band gap 2.1 eV [16] (convert solar radiation into useful energy upto 40 %) and split the water into H_2 and O_2 by PEC.

Under ambient conditions, it is the most stable and common crystalline form of iron oxide. The hematite, where iron Fe and oxygen O atoms arrange in the corundum structure (trigonal-hexagonal scalenohedral (class $\bar{3}2/m$)), has rhombohedral symmetry with space group $R\bar{3}c$. Lattice parameters of $\alpha\text{-Fe}_2\text{O}_3$ are $a = 5.0356 \text{ \AA}$, $c = 13.7489 \text{ \AA}$, and have six formula units/unit cell [17]. The structure of $\alpha\text{-Fe}_2\text{O}_3$ is very easy to understand and can be described as; the anions (O^{2-}) are organized in hexagonal close-packed lattice along the z -direction and cations (Fe^{3+}) hold two-thirds of octahedral aperture in the plane parallel to z -axis. Cations Fe^{3+} organize in such a way that it makes pairs of FeO_6 octahedra. Then, it shares their edges with three nearest octahedra in the same plane and one face with an octahedra along the z -direction in the adjacent plane, as illustrated in Fig. 4.1. The trigonal

Table 4.1: Lattice parameters of different phases (TT, T, M and H phases) of Nb₂O₅

| Crystal phase | Space groups | Lattice Constant | | | Temperature (C ⁰) | Refs |
|---------------------------|--------------|------------------|--------------|--------------|-------------------------------|----------------|
| | | <i>a</i> (Å) | <i>b</i> (Å) | <i>c</i> (Å) | | |
| Pseudo-hexagonal | P6/mmm | 3.60 | 3.61 | 3.92 | 500 | [22, 33, 34] |
| Orthorhombic | Pbam | 6.19 | 3.625 | 3.94 | - | [33, 35, 36] |
| Tetragonal | I4/mmm | 20.44 | 3.83 | 3.82 | 900 | [35, 27] |
| Monoclinic | P12/m1 | 21.14 | 3.82 | 19.45 | >1000 | [1, 3, 22, 35] |
| $\beta=119.9^0 \pm 0.4^0$ | P2, P2/m | | | | | and [37]-[47] |

distortion is caused by face sharing as the Fe atoms situated at the center repel to minimize the Modeling energy of the crystal. Accordingly, acquire C_{3v} symmetry and exhibits two different bond lengths of Fe–O (see Fig. 4.1). In short, α -Fe₂O₃ behaves as antiferromagnetic below 260 K, while at room temperature, it exhibits ferromagnetic nature.

4.1.2 Niobium Oxide

Niobium pentoxide Nb₂O₅ has been recently realized to be another nanostructure metal oxide semiconductor, that offers a variety of applications that enhance its importance and applicability in different research areas. Alternative to TiO₂, it has got much attention due to its appreciative properties like being non-toxic, highly chemically/thermodynamically stable, stable under light irradiation. It is non corrosive material. In 1940s, importance has been given to Nb₂O₅, when its polymorphs [18, 19] were synthesized and investigated as photocatalyst and photoelectrode materials in DSSCs. These extensive polymorphs are transparent because of their large band gap, stable in air and aqueous solution [20], with complex structure. These polymorphs are of different structural phases, which is in general based on NbO₆ octahedral groups and the entire phases consist of ReO₃-type structure. To date, 15 polymorphs have been reported, [21] among them the most common structures are: pseudo-hexagonal (TT-Nb₂O₅), orthorhombic (T-Nb₂O₅), and monoclinic (H-Nb₂O₅) [22, 23, 20, 24].

The crystal phases of Nb₂O₅ are shown in Fig. 4.2, that transform from amorphous to T-phase to M-phase and finally to H-phase [25] with respect to increase in temperature from 200 °C to ~1000 °C, respectively. The unit cell structures of these polymorphs are shown in Fig. 4.3. The crystallographic data of TT, T, M and H phases of niobium pentoxides are listed in Tab. 4.1.

Herein, four, five or six O atoms are connected to each Nb atom (which is in the center of all O atoms) on the *ab*-plane and chain exists between Nb/O atoms along

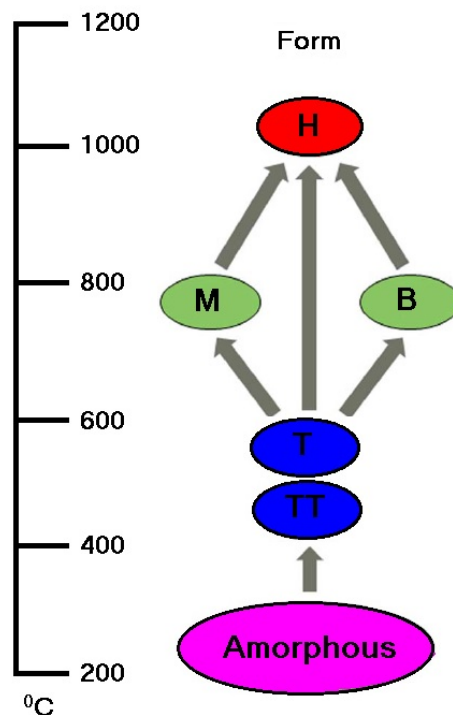


Figure 4.2: Transformation of Nb_2O_5 crystal phase versus temperature starting from 200 °C to 1200 °C.

the z -axis. T-phase of Nb_2O_5 is obtained in the form of orthorhombic symmetry, where six O atoms surround Nb atom (octahedral attachment). Also, thermodynamically stable polymorph is monoclinic phase (H- Nb_2O_5) with lattice parameters: $a = 21.15 \text{ \AA}$, $b = 3.82 \text{ \AA}$, $c = 19.36 \text{ \AA}$, $\beta = 119.80^\circ$ [26]. It consists of (3×4) and (3×5) blocks (ReO_3), coupled with NbO_6 octahedra *via* columns of tetrahedral sites. In addition to compensation of O deficiency, which is common in Nb_2O_5 structures, is the nonstoichiometric compensation *via* partially detaching cations from tetrahedron column. It can be obtained from shearing of crystal structure along $(1\ 0\ 0)$ and $(0\ 0\ 1)$ planes of ReO_3 blocks due to the rearrangement of these blocks. Similar to H- Nb_2O_5 , the M phase of Nb_2O_5 consists of 4×4 of ReO_3 blocks [23, 27].

3D hierarchical $\text{Nb}_3\text{O}_7(\text{OH})$ is a novel photocatalytic material used for photochemistry and it is used as photoanode material as DSSC based on its performance surpasses Nb_2O_5 . It is characterized by a smaller band gap 3.1 eV as compared to 3.40–3.85 eV for different phases of Nb_2O_5 , respectively [22]. $\text{Nb}_3\text{O}_7(\text{OH})$ orthorhombic phase (same as most binary Nb_2O_5) consists of $(3 \times \infty)$ blocks expanded infinitely along b - and c -directions. Its crystallographic data is given by: $a = 20.74 \text{ \AA}$, $b = 3.823 \text{ \AA}$ and $c = 3.936 \text{ \AA}$, [28] respectively. A phase transformation occurs in $\text{Nb}_3\text{O}_7(\text{OH})$ above 500 °C (calcinde temperature) and appears as Nb_2O_5 (monoclinic phase) [29, 30] the structure is similar to the latter compound [31] (see Fig. 5.1). Our theoretical simulation describes improvement in the electronic structure, optoelectronic and thermoelectric properties of $\text{Nb}_3\text{O}_7(\text{OH})$ over

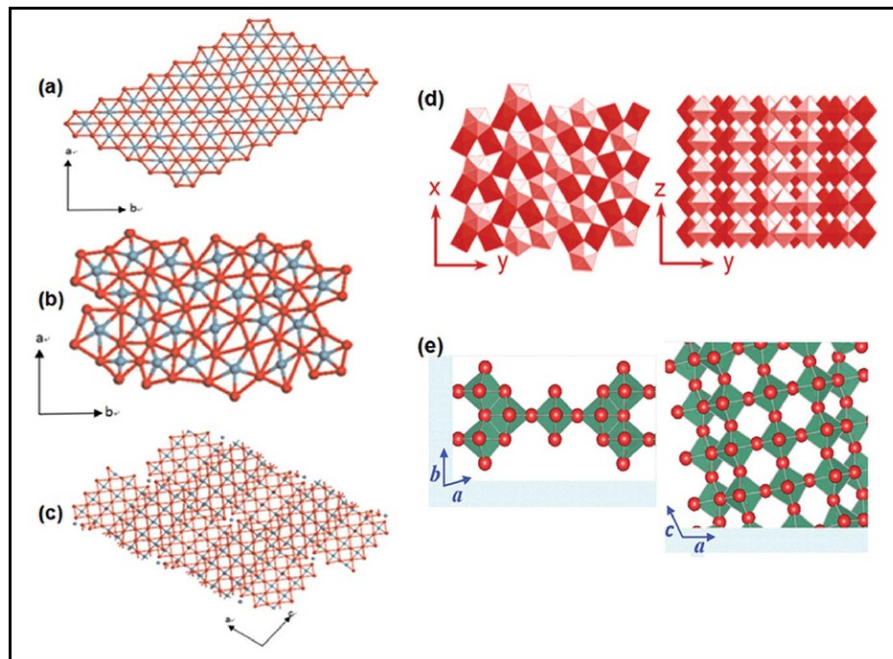


Figure 4.3: Schematic representations of (a) TT-phase (pseudo-hexagonal), (b) T-phase (orthorhombic), (c) H-phase (monoclinic) and 3D crystal structures of (d) T-phase (orthorhombic) and (e) H-phase (monoclinic) of Nb_2O_5 . [21]

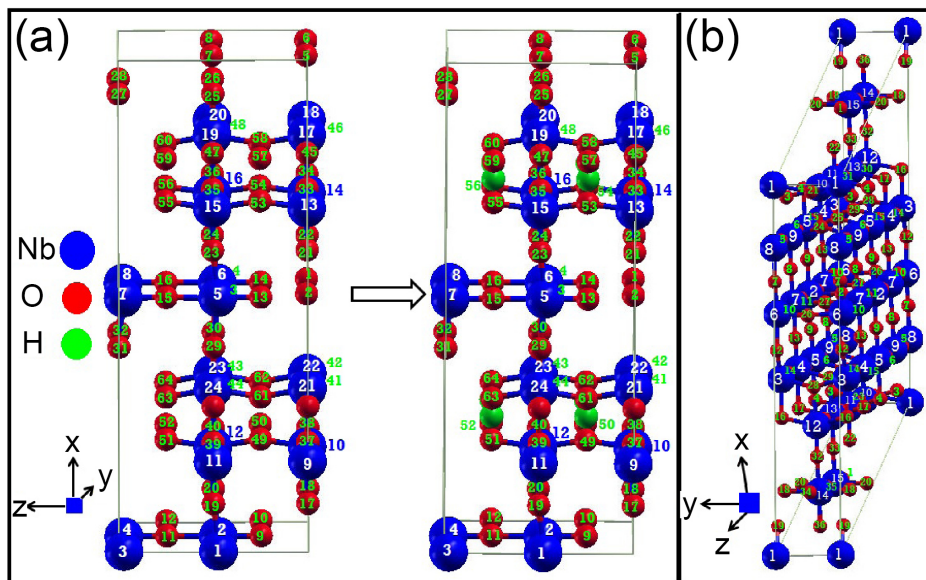


Figure 4.4: Schematic representations of (a) Nb_3O_8 and $\text{Nb}_3\text{O}_7(\text{OH})$ and (b) Nb_2O_5 and in both figures the O and Nb atoms are marked by numbers according to their position in the crystal.

Nb_2O_5 [32].

Bibliography

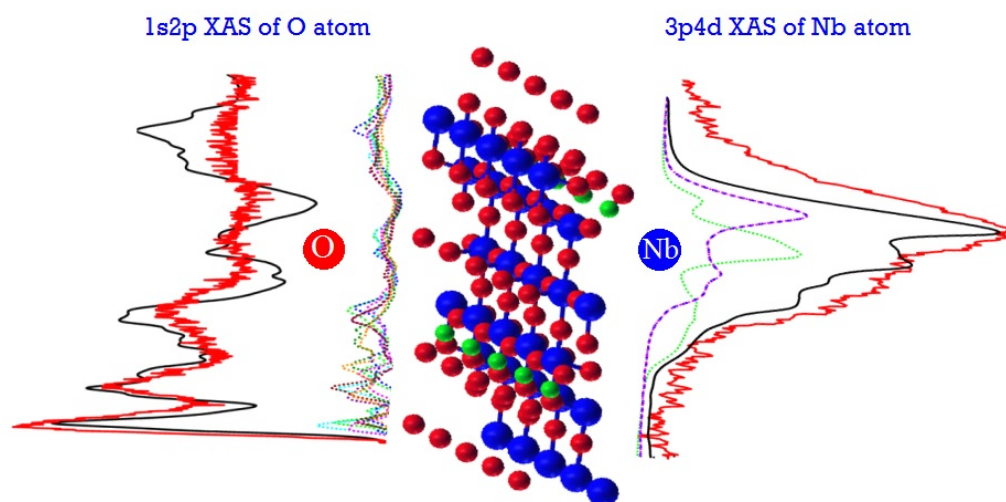
- [1] C. Noguera, *Physics and Chemistry at Oxide Surfaces*; Cambridge University Press:Cambridge, UK, (1996).
- [2] H. H. Kung, *Transition Metal Oxides: Surface Chemistry and Catalysis*; Elsevier: Amsterdam, (1989).
- [3] V. E. Henrich, P. A. Cox, *The Surface Chemistry of Metal Oxides*; Cambridge University Press: Cambridge, UK, (1994).
- [4] A. F. Wells, *Structural Inorganic Chemistry*, 6th ed; Oxford University Press: New York, (1987).
- [5] J. A. Rodriguez, M. F. García, (Eds.) *Synthesis, Properties and Applications of Oxide Nanoparticles*. Wiley: New Jersey, (2007).
- [6] J. Schoiswohl, G. Kresse, S. Surnev, M. Sock, M. G. Ramsey, F. P. Netzer, *Phys. Rev. Lett.* 92, 206103, (2004).
- [7] J. M. McHale, A. Auroux, A. J. Perrota, A. Navrotsky, *Science* 277, 788, (1997).
- [8] H. Zhang, J. F. Bandfield, *J. Mater. Chem.* 8, 2073, (1998).
- [9] A. Fujishima, K. Honda, *Nature.* 238, 37 (1972).
- [10] O'Regan, B. Grätzel, *M. Nature* 353, 737, (1991).
- [11] A. Janotti, C. Van de Walle, *Rep. Prog. Phys.* 72, 126501, (2009).
- [12] M. Liu, C.-Y. Nam, C. Black, J. Kamcev, L. Zhang, *J. Phys. Chem. C* 117, 13396, (2013).
- [13] W. Zhou, Y. Liu, Y. Yang, P. Wu, *J. Phys. Chem. C* 118, 6448, (2014).
- [14] J. Noh, S. Im, J. Heo, T. Mandal, S. Seok, *Nano Lett.* 13, 1764, (2013).
- [15] G. Eperon, S. Stranks, C. Menelaou, M. Johnston, L. Herz, H. Snaith, *Energy Environ. Sci.* 7, 982, (2014).
- [16] G. Rollmann, A. Rohrbach, P. Entel, and J. Hafner, *Phy. Rev. B* 69, 165107 (2004).

- [17] L. Pauling and S.B. Hendricks, *J. Am. Chem. Soc.* 47, 781, (1925).
- [18] F. Holtzberg, A. Reisman, M. Berry and M. Berkenblit, *J. Am. Chem. Soc.*, 79, 2039, (1957).
- [19] G. Brauer, *Z. Anorg. Allg. Chem.*, 248, 1, (1941).
- [20] I. Nowak and A. M. Ziolek, *Chem. Rev.*, 99, 3603, (1999).
- [21] A. R. Rozina, S. Z. Ahmad, et. al., *J. Mater. Chem. A*, 2, 15683 (2014).
- [22] A. Le Viet, R. Jose, M. V. Reddy, B. V. R. Chowdari and S. Ramakrishna, *J. Phys. Chem. C*, 114, 21795, (2010).
- [23] H. Schäfer, R. Gruehn and F. Schulte, *Angew. Chem., Int. Ed. Engl.*, 5, 40, (1966).
- [24] L. A. Reznichenko, V. V. Akhnazarova, L. A. Shilkina, O. N. Razumovskaya and S. I. Dudkina, *Crystallogr. Rep.*, 54, 483, (2009).
- [25] E. I. Ko and J. G. Weissman, *Catal. Today*, 8, 27, (1990).
- [26] K. Kato, S. Tamura, *Acta Crystallogr. B-Stru.* 31, 673, (1975).
- [27] W. Mertin, S. Andersson and R. Gruehn, *J. Solid State Chem.*, 1, 419, (1970).
- [28] F. Izumi, H. Kodama, *Z. Anorg. Allg. Chem.* 441, 8, (1978).
- [29] H. Zhang, Y. Wang, D. Yang, Y. Li, H. Liu, P. Liu, B. Wood, H. Zhao, *Adv. Mater.* 24, 1598 (2012).
- [30] S. B. Betzler, T. Harzer, J. Ciston, U. Dahmen, G. Dehm, and C. Scheu, *Cryst. Growth Des.*, 16, 4309–4317, (2016).
- [31] B. M. Gatehouse and A. D. Wadsley, *Acta Crystallogr.*, 17, 1545, (1964).
- [32] W. Khan, S. Betzler, O. Sipr, J. Ciston, P. Blaha, C. Scheu, J. Minar, *J. Phy. Che. C*, 120, 23329–23338, (2016).
- [33] M. Palatnikov, O. Shcherbina, N. Sidorov and K. Bormanis, *Ukr. J. Phys. Opt.*, 13, 207, (2012).
- [34] L. K. Frevel and H. W. Rinn, *Anal. Chem.*, 27, 1329, (1955).
- [35] O. Kubaschewski and B. E. Hopkins, *J. Less-Common Met.*, 2, 172, (1960).
- [36] W. T. Holser, *Acta Crystallogr.*, 9, 196, (1956).
- [37] R. Norin and A. Magnioli, *Naturwissenschaften*, 47, 354, (1960).
- [38] K. Kato, *Acta Crystallogr., Sect. B: Struct. Crystallogr. Cryst. Chem.*, 32, 764, (1976).

Chapter 5

Theoretical and Experimental Study on the Optoelectronic Properties of $\text{Nb}_3\text{O}_7(\text{OH})$ and Nb_2O_5 Photoelectrodes

This chapter is based on a manuscript by Wilayat Khan, Sophia B. Betzler, Ondřej Šipr, Jim Ciston, Peter Blaha, Christina Scheu, and Ján Minár, *J. Phys. Chem. C*, 2016, 120, 23329—23338. In this chapter, we did the electronic, optical, spectroscopic properties and thermoelectrical conductivity calculations. The spectroscopic properties are then compared to Exp. data.



5.1 Introduction

The consumption of fossil fuel stocks presents our society with a new challenge and forces the research for alternatives. Efficient harvesting of the power of the sun with solar cells would suffice to cover the world wide energy consumption. To balance out fluctuations in the energy production novel storage technologies need to be developed simultaneously and in this regard hydrogen is intensively discussed as a very promising material for energy storage. Dye-sensitized solar cells (DSSC) and photocatalysis both apply semiconductors to generate charges which are either separated to produce current or used up for chemical reactions (e.g. the splitting of water to produce hydrogen gas). The solar light is absorbed by the semiconductor whereby an electron is excited from the valence to the conduction band leading to electron-hole pairs [1, 2]. The band gap size and energy position of the conduction and valence band edges of the semiconductor are crucial for the performance of a semiconductor in photochemistry as they determine the portion of the solar spectrum absorbable by the semiconductor, the potential of the electron-hole pair and the band alignment of the device [3, 4]. Theoretical studies calculated the band edge energies of a high variety of oxides [5, 6, 7, 8] predicting their applicability as photocatalyst or electrode material. Subsequent to their separation the generated charges need to diffuse to the surface of the semiconductor. This process is endangered by charge recombination a major loss mechanism leading to reduced quantum yields. Consequently, both the charge transport properties and the energy position of the band gap of a material have to be taken into account at evaluating its applicability as photo-catalyst. Still, the ideal material system was not yet discovered [9] and research needs to go beyond established material systems. This study focuses on the prediction of material properties of a material class which was very recently discovered as new material with attractive properties for photochemistry: Several experimental studies show the applicability of $\text{Nb}_3\text{O}_7(\text{OH})$ [10, 11, 12, 13, 14, 15, 16] and Nb_2O_5 [10, 11, 16, 17, 18, 19, 20, 21, 22, 23] as photocatalyst and electrode material in DSSCs. $\text{Nb}_3\text{O}_7(\text{OH})$ can be transformed into monoclinic $\text{H-Nb}_2\text{O}_5$ by calcination. [10, 24] The changes of the material properties which go along with this phase-transformation will be investigated on a theoretical basis in this study.

Density functional theory (DFT) is widely used for ground-states calculations in physics, chemistry and material science. [25, 26] DFT is very useful to predict the exact ground state properties, but in particular electronic properties of semiconductors related to excited states such as e.g. size of the band gap, strongly depend on the choice of the exchange correlation functional. Recently, Zhang et al. [10] studied structural properties of $\text{Nb}_3\text{O}_7(\text{OH})$ and Nb_2O_5 oxides by means of generalized gradient approximation (GGA) [27], which is in general well suited to obtain accurate structural parameters [28]. Based on this functional, Zhang et al. discussed in detail the position of H-atoms in the hydroxide $\text{Nb}_3\text{O}_7(\text{OH})$. However, the calculations of

electronic structure properties of these materials such as the density of states, band gap and dielectric function are not well understood. As a first step of our study we have tested various exchange–correlation functionals such as i.e. the local density approximation (LDA) [29], the GGA [27], Engel Vosko (EVGGA) [30] and Tran and Blaha modified Becke Johnson (TB–mBJ) [31]. Here we show, that within the TB-mBJ functional predicted electronic and optical properties of $\text{Nb}_3\text{O}_7(\text{OH})$ and Nb_2O_5 agree very well with measured low–loss spectra, as well as the near edge fine structure of the O–K and Nb–M₃ edges of $\text{Nb}_3\text{O}_7(\text{OH})$. This gives new insights into the structure of the edge. The electronic structure furthermore forms the basis for the determination of the thermoelectric conductivity of the two compounds with the BolzTraP[32] code.

5.2 Computational and experimental methodology

5.2.1 Calculation details

All density functional theory based calculations were performed using the linearized augmented plane wave+local orbitals (LAPW+lo) method as implemented in the WIEN2k code [33]. The muffin tin radii R_{MT} for $\text{Nb}_3\text{O}_7(\text{OH})$ were set to 1.8, 1.3 and 0.55 Bohr for the niobium, oxygen and hydrogen atoms, respectively. The muffin tin radii for monoclinic H- Nb_2O_5 were set to 1.74 for niobium atoms and 1.58 Bohr for oxygen atoms. The wave functions in the atomic spheres were expanded up to an angular momentum of $l = 10$. The plane wave cutoff in the interstitial region was set so that $R_{MT} \cdot K_{MAX}=7$ for Nb_2O_5 and 3 for $\text{Nb}_3\text{O}_7(\text{OH})$, respectively, and was validated by convergence of the forces on the atoms. To obtain the electronic structure as well as optical properties, we used a k–point mesh of $16 \times 16 \times 15$ for $\text{Nb}_3\text{O}_7(\text{OH})$ and $3 \times 18 \times 4$ for Nb_2O_5 .

The structural relaxations were done using the GGA [27] functional. Since it is well known that local exchange correlation functionals underestimate band gaps, the electronic structure calculations were performed using the TB–mBJ approach. This functional usually predicts band gaps with higher accuracy [31] than GGA. However, we also performed all calculations with GGA and with LDA functionals so that a detailed comparison of the results obtained using different exchange–correlation functionals with the experiment is possible. This comparison demonstrated that the TB–mBJ approach is suitable for the Nb oxides studied here (see Sec. 5.3.4 below).

The linear optical properties of $\text{Nb}_3\text{O}_7(\text{OH})$ and H- Nb_2O_5 were derived from the OPTIC program[34] included in the WIEN2k simulation package. The imaginary part of the dielectric tensor (ε_2) was calculated according to Ref. [35]. The real part of the dielectric function (ε_1) is derived from the Kramers–Kronig relation[36].

Both, the optical conductivity $\sigma(\omega) = \frac{\omega}{2\pi} \varepsilon_2(\omega)$ and the energy loss function $L(\omega) = \frac{\varepsilon_2(\omega)}{[\varepsilon_1(\omega)]^2 + [\varepsilon_2(\omega)]^2}$ can be calculated directly from $\varepsilon_1(\omega)$ and $\varepsilon_2(\omega)$ [37].

Core loss electron energy-loss spectra of Nb–M₃ and O–K edges were calculated with the X-ray absorption module of the WIEN2k code. The application of Fermi's golden rule is possible for the used experimental scattering geometry as the dipole approximation is fairly valid [38]. We had to account for the core hole to achieve a satisfying agreement between theoretical and experimental core loss data at the O–K and Nb–M₃ edges. This was done using the static core hole approach. One of the relevant core electrons was removed, the number of valence electrons was increased by one and a self-consistent calculation was done so that the electrons adjust to the presence of the core hole. This calculation was done for every non-equivalent oxygen and niobium atom in the unit cell using a $2 \times 2 \times 1$ super-cell.

The BoltzTraP code[32] was used to calculate the electrical conductivity under constant relaxation time τ . [39, 40] These calculations are based on the Boltzmann transport theory and necessary information about the band dispersion is obtained by corresponding DFT calculation.

5.2.2 Experimental details

In addition to the theoretical calculations we performed electron energy-loss spectroscopy (EELS) measurements in a transmission electron microscope (TEM). The Nb₃O₇(OH) sample was synthesized according to the procedure described by Betzler et al. [14] Monoclinic H–Nb₂O₅ was obtained by calcination of Nb₃O₇(OH) at 850 °C [15]. Low loss data was acquired to get experimental information about the optical response of the samples. In addition, core loss data were recorded to investigate the coordination and bonding characteristic of the crystal lattices. The low loss spectra were detected using a double corrected FEI–TEAM 0.5 microscope operated at 300 kV. An energy resolution of 0.15 to 0.18 eV (determined by the full width at half maximum of the zero-loss peak) was achieved using a monochromator and a spectrometer entrance aperture of 1 mm under parallel illumination of the sample (convergence angle below 0.2 mrad). The linear fit method [41] enables the determination of the band gap of materials from the low-loss region (energy losses between 0 and 50 eV). In addition, optical extinction data were detected for a spectral region of 250 to 1200 nm. The Tauc method [42] was applied to determine the band gap based on optical data and it was used to compare to the band gaps measured by EELS. The element specific edges were measured using a Zeiss Libra microscope operated at 200 kV with parallel illumination (convergence angle about 0.2 mrad). An energy resolution of 0.3 to 0.4 eV was achieved for the determination of the O–K and Nb–M₃ edges using a monochromator and a collection angle of 17 mrad. The spectra were detected with a dispersion of 0.07 eV/channel.

5.3 Results and discussion

5.3.1 Structural optimization

We considered three systems in our study: monoclinic H-Nb₂O₅, orthorhombic Nb₃O₇(OH) and an auxiliary Nb₃O₈ system.

Nb₃O₇(OH) and Nb₃O₈

Nb₃O₇(OH) has an orthorhombic structure isomorphous with Nb₃O₇F, which crystallizes in *Cmmm* (number 65) space group [43, 44]. The experimental unit cell parameters are $a = 20.74$, $b = 3.823$, $c = 3.936$ Å. It is well known that it is very difficult to find the exact position of H-atoms by means of X-ray diffraction. Therefore, theoretical studies are important here. Zhang et al. [29] based their DFT calculations on a suggested position for the H-atom: Here the H-atom is attached to an oxygen atom O(8) between two Nb(3) sites (Nb(2) and (3) are situated in edge-sharing oxygen octahedra, while Nb(1) sits in a corner-sharing one). We used their structural model as starting point for our structure relaxation. The structure of Nb₃O₇(OH) which we obtained is quite similar to the structure of Zhang et al.; [10] a perspective diagram is shown Fig. 5.1a. The largest difference between our results and the structure found by Zhang et al. [10] concern the region close to the OH group: the O-H distance increased by 0.359 Å (1.07 in relaxed, -1.429 in unrelaxed structure model) and the Nb-O distance by 0.053 Å (2.030 in relaxed, -1.977 in unrelaxed state).

To study the bare effects of the hydrogen atom on the electronic structure, optoelectronic and transport properties, we also performed calculations for an artificial Nb₃O₈ reference compound. Nb₃O₈ is not known experimentally and was defined by removing the H-atom from the crystal lattice of Nb₃O₇(OH) while leaving all structural parameters as in the original Nb₃O₇(OH) compound.

H-Nb₂O₅

Nb₂O₅ exhibits more than 15 different polymorphs [45]. Monoclinic H-Nb₂O₅ is the thermodynamically stable polymorph which forms after calcination of Nb₃O₇(OH) at 500 °C [10]. Its crystal structure was determined experimentally by Gatehouse et al. [46] and Kato [47]. It crystallizes in the space group P2/m (number 10), with lattice parameters $a = 21.153$, $b = 3.823$ and $c = 19.356$ Å and $\gamma = 119.5^\circ$. There are 15 inequivalent Nb sites in this structure, one of them corresponds to a disordered position: the corresponding Nb atom occupies the $2i$ Wyckoff positions, each of the statistical displacements of $y = \pm 0.2285$ is occupied with concentration of 0.5. We ignored this partial fractional occupancy by occupying instead Wyckoff position $1a$ [at (0.0, 0.0, 0.0)] with occupation 1.0. This geometry was then optimized by

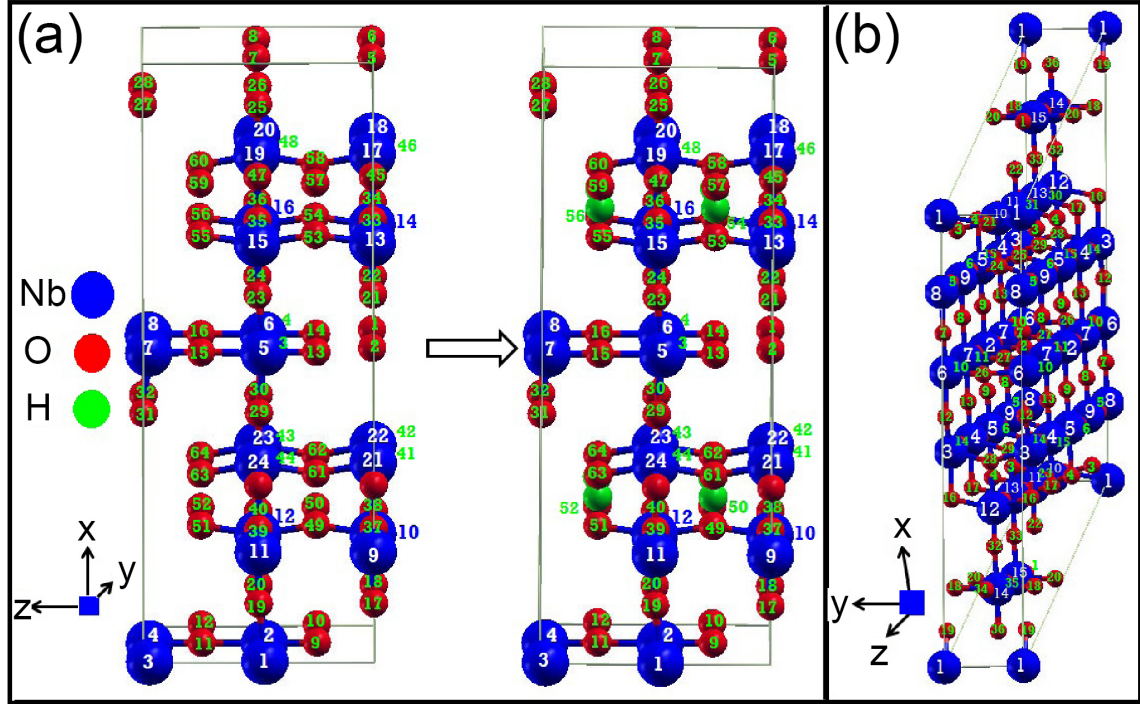


Figure 5.1: Schematic representation of the crystal structures of the artificial reference compound Nb_3O_8 (left part (a)) and $\text{Nb}_3\text{O}_7(\text{OH})$ (right part (a)) and monoclinic $\text{H-Nb}_2\text{O}_5$ (b). Black, red and green spheres represent Nb, O, and H atoms, respectively.

minimizing the forces exerted on the atoms, keeping the overall unit cell parameters constant. The relaxed structure of $\text{H-Nb}_2\text{O}_5$ we thereby obtained is shown in Fig. 5.1b. The changes with respect to the original experimental structure[46, 47] are generally small: the bond lengths typically changed by 0.001–0.050 Å, only in one case the Nb–Nb bond length increased by 0.20 Å and in one case the O–O bond length increase by 0.11 Å. The largest change of course concerns the Nb atom that was transferred from the $2i$ site to the $1a$ site. In the relaxed structure, all Nb atoms are coordinated octahedrally by oxygen.

5.3.2 Electronic band structures

The response range of a semiconductor in the visible light regime is determined by the size of its band gap and its band structure, while its ability to successfully participate at the chemical reaction depends on the energetic position of the gap. The electronic band dispersions of orthorhombic Nb_3O_8 and $\text{Nb}_3\text{O}_7(\text{OH})$ as well as monoclinic $\text{H-Nb}_2\text{O}_5$ are plotted in Figs. 5.2(a–c) along the high symmetry lines inside the irreducible Brillouin zone (IBZ). The band structure calculation of all three compounds was performed using the TB–mBJ [31] approach. It is very difficult to predict the accurate position of the H–atom in the crystal lattice of $\text{Nb}_3\text{O}_7(\text{OH})$ from

both experiment as well as theory. As described above we model the H positions following Zhang et al.[29]. The energetically lowest position for H-atom can be found in the octahedra of Nb(3) atom as it is shown in Fig. 5.1a. The use of the suggested relaxed crystal structure shows semiconducting properties with an indirect band gap for Nb₃O₇(OH) and a fundamental band gap of 1.70 eV. The comparison with the reference compound Nb₃O₈ exhibits that the presence of hydrogen in the crystal lattice shifts the Fermi energy to the top of the valence bands resulting in a change from metallic (Nb₃O₈) to semiconducting (Nb₃O₇(OH)) properties. In addition the uppermost valence band shows a much larger dispersion for Nb₃O₇(OH) than Nb₃O₈ and the conduction bands are shifted to lower energies by 0.5 eV in Nb₃O₇(OH). Apart from that, changes of the band structure due to the H-atom are small (Figs. 5.2(a, b)).

Like Nb₃O₇(OH) monoclinic H-Nb₂O₅ is also an indirect band gap semiconductor with a larger fundamental band gap of 2.56 eV (Fig. 5.2). The valence band maximum (VBM) and conduction band minimum (CBM) occur at R and Y symmetry points in Nb₃O₇(OH) while they appear at D, E, Z, C and B symmetry points of the IBZ in H-Nb₂O₅. Indirect transitions need a momentum transfer supplied by phonons to realize k-conservation. The calculated findings for the band gaps are summarized in Tab. 5.1. In addition experimentally determined values are given which were obtained using both absorption spectroscopy and electron energy-loss spectroscopy. Optical spectroscopy yields a band gap of 3.1 eV for both compounds, while a slightly larger band gap of 3.2 eV is determined for H-Nb₂O₅ from EEL spectra. This compares well with the calculated optical band gaps of the two compounds which were found to be 3.1 eV for Nb₃O₇(OH) and 3.0 eV for H-Nb₂O₅. The band gaps of the two niobium oxide phases are similar to TiO₂[48] and allow the absorption of light from the UV region ($\lambda < 390$ nm) of the solar spectrum.

Table 5.1: Band gaps of Nb₃O₇(OH) and Nb₂O₅ determined experimentally and from calculation (in [eV]).

| | Nb ₃ O ₇ (OH) | monoclinic H-Nb ₂ O ₅ |
|-------------|-------------------------------------|---|
| | experimental band gap | |
| optical | 3.09 (± 0.05) | 3.07 (± 0.05) |
| EELS | 3.1 (± 0.1) | 3.2 (± 0.1) |
| | theroretical band gap | |
| fundamental | 1.70 | 2.56 |
| optical | 3.1 | 3.0 |

The partial density of states (PDOS) reveal deeper insights into the band structure of Nb₃O₇(OH) and H-Nb₂O₅ (Figs. 5.3(a-b)). The partial DOS confirms that the top of the valence bands of both compounds primarily originate from the O-2p

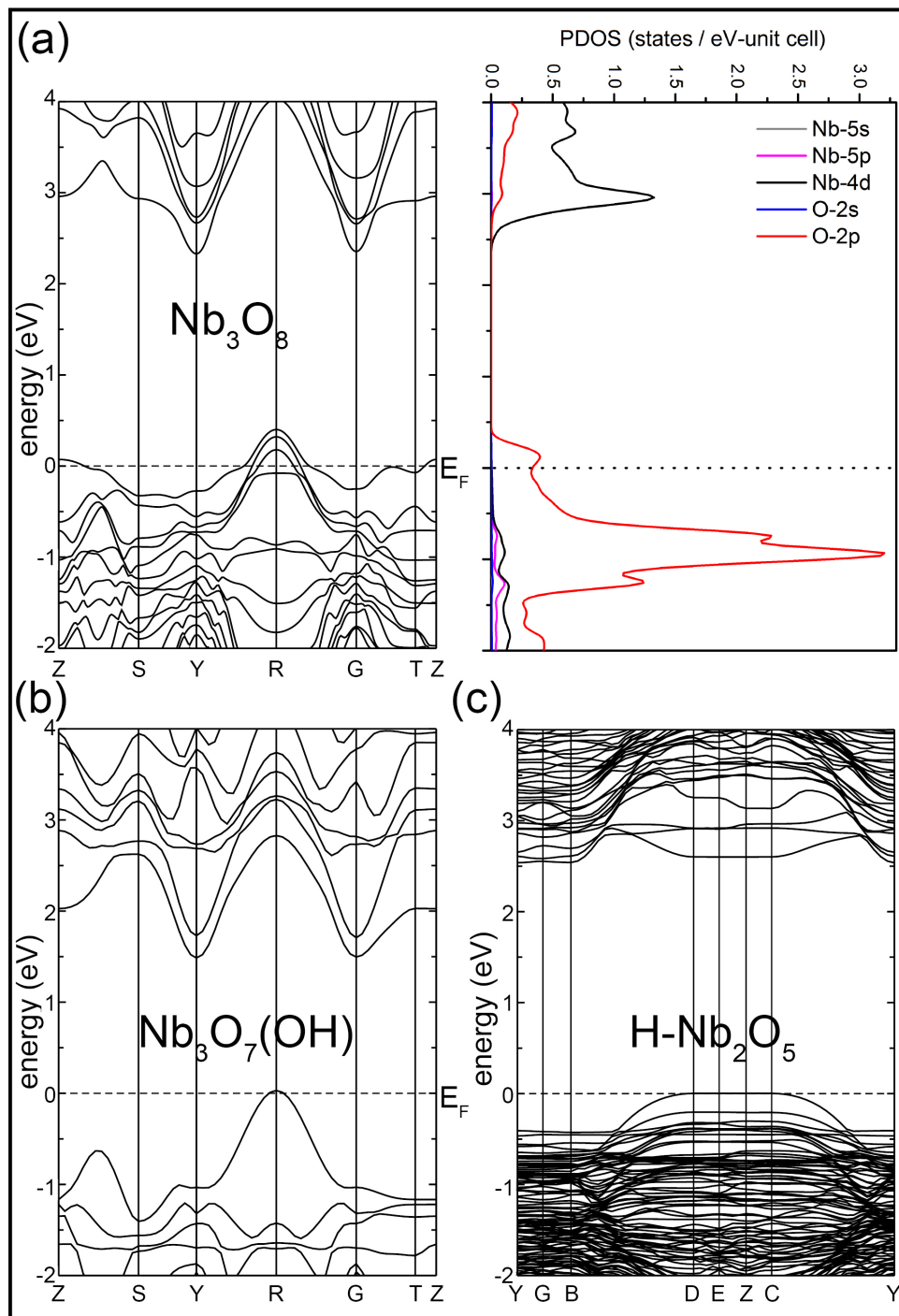


Figure 5.2: Calculated band structure of Nb_3O_8 (left side of (a)), $\text{Nb}_3\text{O}_7(\text{OH})$ (b) and monoclinic $\text{H-Nb}_2\text{O}_5$ (c). In addition the density of states is given for Nb_3O_8 on the right side of (a).

orbitals, and the bottom of the conduction band mainly from Nb-4d orbitals with a negligible contribution of H-1s orbitals. The valence band of both Nb₃O₇(OH) and H-Nb₂O₅ is divided into two distinct regions: The energy region at -6.0 eV to \sim -4.0 eV is dominated equally by the 4d/2p orbitals of Nb and O atoms, while small contributions of Nb-5s/5p orbitals and H-1s orbital are also observed. A strong overlap is observed for the O-2p and Nb-4d orbitals (below 6.0 eV) and the oxygen 2s orbitals with the 5s orbitals of Nb atoms also show strong interplay at 5.5 eV. The second energy region at -4.0 eV \sim 0.0 eV is mainly assigned to O-2p but the Nb-4d orbitals contribute significantly less along with minor participation of 2s/5s/5p/1s orbitals of O/Nb/H atoms. The 2s/5s orbitals of O/Nb atoms (from -3.7 eV to \sim 0.0 eV) and the 1s/2s orbitals of H/O atoms of Nb₃O₇(OH) present strong interaction with each other at -2.2 eV, while the 2s/5s of O/Nb atoms (from -1.30 eV to 0.0 eV) in Nb₂O₅ only partially interact. The H-1s orbitals are more than -3.0 eV deeper in energy than the VBM since the H-atom is coordinated solely by one O-atom leading to negligible hybridization over all other atoms. The bands above the Fermi level at energy 2.34 eV (Nb₃O₇(OH)) and 2.56 eV (Nb₂O₅) \sim 4.0 eV are robustly assigned to Nb-4d orbitals mixing with small contributions of s/p orbitals of O/Nb atoms. The region beyond 4.0 eV is still mainly composed of Nb-4d orbitals combined with O-2p orbitals and minor participation of the remaining orbitals of Nb/O/H atoms.

From the above discussion it becomes clear that the O-2p (VBM) and Nb-4d (CBM) orbitals are predominately responsible for optical excitations in Nb₃O₇(OH) and H-Nb₂O₅. Furthermore, the investigations show that doping with H-1s causes a shifting of all peaks at the VBM towards lower regions as well as a broadening of these peaks (Fig. 5.3(a-b)/5.2).

5.3.3 Optical properties

It is known that semiconductors play an important role in the field of optoelectronic devices where the band gap defines the threshold energy of electromagnetic radiation and differentiates between transparency and absorbing region. The optical properties of Nb₃O₇(OH) and H-Nb₂O₅ were calculated by linear response formalism and the complex dielectric function (namely $\varepsilon_1(\omega)$ and $\varepsilon_2(\omega)$) of Nb₃O₇(OH) and H-Nb₂O₅ are calculated.

In Fig. 5.4a the calculated frequency dependent perpendicular and parallel parts (defined along the crystallographic *c*-direction) of the imaginary $\varepsilon_2(\omega)$ dielectric function are shown for Nb₃O₇(OH) and H-Nb₂O₅. In Nb₃O₇(OH) the threshold energy for the perpendicular polarization is 3.19 eV and thus a bit smaller than the energy (3.33 eV) for parallel polarization while the threshold energy for both polarization axes is nearly the same for H-Nb₂O₅ (3.40 eV).

Furthermore, there are absorption peaks at 3.82/5.16 eV and around 5.81 eV

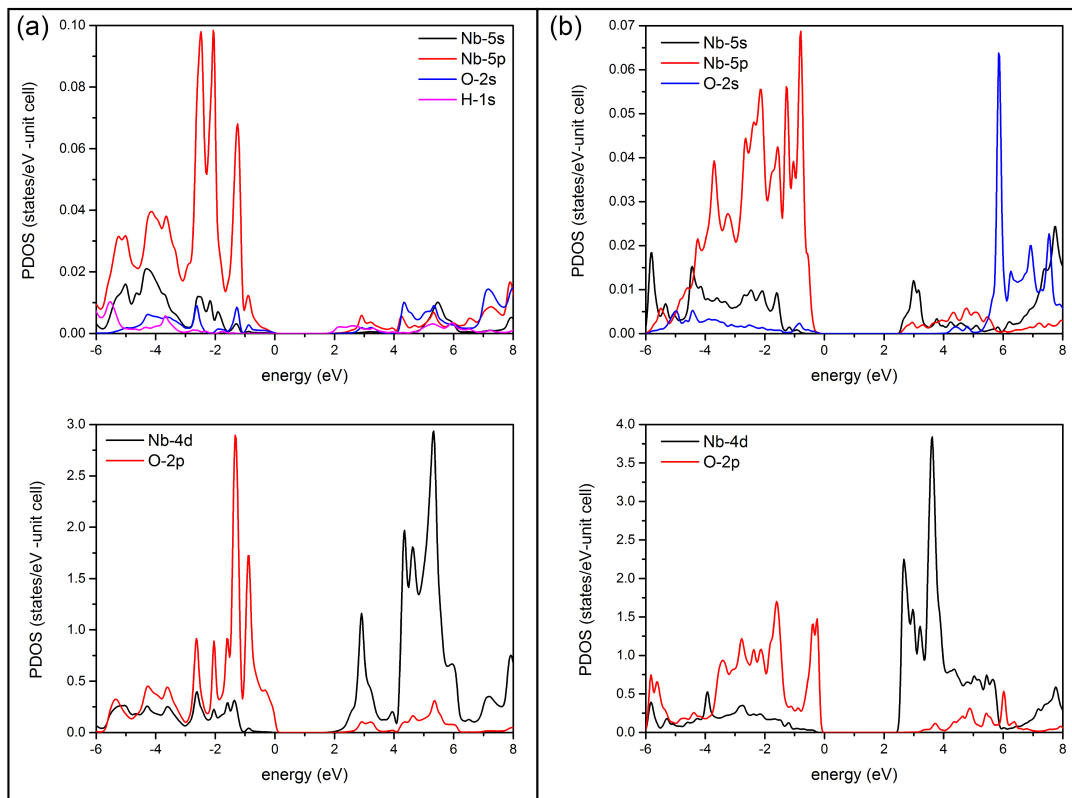


Figure 5.3: The partial density of states were calculated using the TB-mBJ approach. In (a) the PDOS of Nb, O and H atoms are shown for $\text{Nb}_3\text{O}_7(\text{OH})$ in (b) for monoclinic $\text{H-Nb}_2\text{O}_5$. Solid (black, red, blue and green) lines represent s , p and d states, respectively. The Fermi level (E_F) is set to zero.

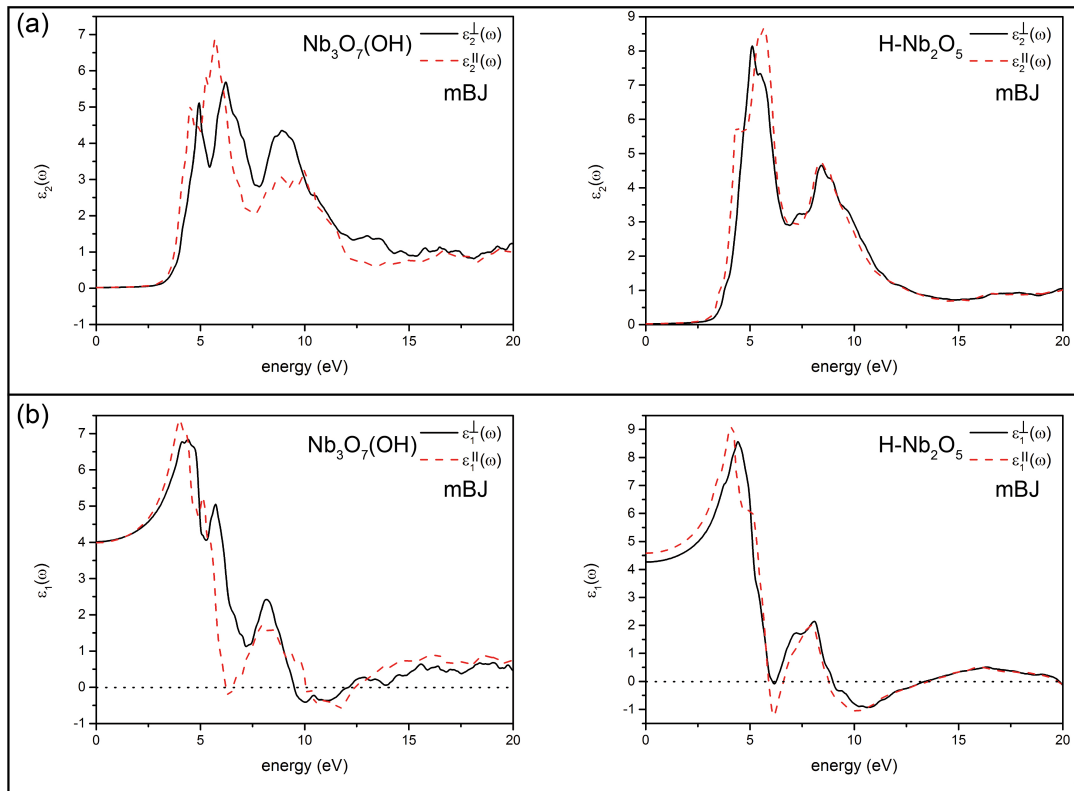


Figure 5.4: The real and imaginary part of the dielectric function. The peaks result from various transitions. The imaginary $\epsilon_2(\omega)$ and real part $\epsilon_1(\omega)$ of the DF calculated for $\text{Nb}_3\text{O}_7(\text{OH})$ and monoclinic $\text{H-Nb}_2\text{O}_5$.

($\varepsilon_2^\perp(\omega)$) and 4.53/5.70 eV ($\varepsilon_2^\parallel(\omega)$) in $\text{Nb}_3\text{O}_7(\text{OH})$ which are shifted to 5.83/5.67 eV for $\varepsilon_2^\perp(\omega)/\varepsilon_2^\parallel(\omega)$ in $\text{H-Nb}_2\text{O}_5$. These peaks are attributed to the allowed transitions of electrons from the VBM (O-2p orbitals) to CBM (Nb-4d orbitals).

Additional absorption peaks are situated at 9.10 eV ($\varepsilon_2^\perp(\omega)$) and 10.01 eV ($\varepsilon_2^\parallel(\omega)$) in $\text{Nb}_3\text{O}_7(\text{OH})$ and at 8.4 eV for both polarizations in Nb_2O_5 . These peaks result from transitions of electrons from the orbitals below -4.0 eV to orbitals above 4.0 eV. The difference of the absorption peaks observed for $\text{Nb}_3\text{O}_7(\text{OH})$ and Nb_2O_5 is attributed to their different crystal structures.

The calculated real part of the dielectric function, which describes the electronic polarizability of the material, were extracted from the imaginary part of the dielectric function using the Kramers–Kronig expression[36] for the perpendicular $\varepsilon_1^\perp(\omega)$ and parallel $\varepsilon_1^\parallel(\omega)$ polarization (Fig. 5.4b). $\varepsilon_1^\perp(\omega)$ shows three maxima at 3.74 eV, 4.72 eV and 5.54 eV and a smaller feature at 8.08 eV, while $\varepsilon_1^\parallel(\omega)$ exhibits two maxima at 4.01 eV and 5.10 eV for $\text{Nb}_3\text{O}_7(\text{OH})$ and a smaller peaks at 7.98 eV. The spectra of $\text{H-Nb}_2\text{O}_5$ shows one dominant peak at 4.04 eV and one smaller peak at 8.08 eV for $\varepsilon_1^\perp(\omega)$ respectively 4.18 eV and 7.98 eV for $\varepsilon_1^\parallel(\omega)$. Both optical components of $\varepsilon_1(\omega)$ in $\text{Nb}_3\text{O}_7(\text{OH})/\text{Nb}_2\text{O}_5$ are positive until 9.51/9.24 eV ($\varepsilon_1^\perp(\omega)$) and (6.21, 10.05)/(5.89, 8.77) eV ($\varepsilon_1^\parallel(\omega)$) and become negative beyond these energies. In addition, plasma frequencies are produced at the energy points 11.96 eV /(6.57, 12.45) eV ($\varepsilon_1^\perp(\omega)/\varepsilon_1^\parallel(\omega)$) in $\text{Nb}_3\text{O}_7(\text{OH})$ and 13.21 eV /(6.63, 13.59 eV) in $\text{H-Nb}_2\text{O}_5$ ($\varepsilon_1^\perp(\omega)/\varepsilon_1^\parallel(\omega)$) in the positive direction with $\varepsilon_1^\perp(\omega)/\varepsilon_1^\parallel(\omega)=0$. The static values of $\text{Nb}_3\text{O}_7(\text{OH})$ are 4.12 eV ($\varepsilon_1^\perp(0)$) and 3.98 eV ($\varepsilon_1^\parallel(0)$) while $\text{H-Nb}_2\text{O}_5$ is characterized by static values of 4.30 eV ($\varepsilon_1^\perp(0)$) and 4.58 eV ($\varepsilon_1^\parallel(0)$). This means that $\text{Nb}_3\text{O}_7(\text{OH})$ and $\text{H-Nb}_2\text{O}_5$ obey the Penn model [49] which states that larger optical band gaps results in smaller static values.

On the basis of the dielectric function the perpendicular $\sigma^\perp(\omega)$ and parallel $\sigma^\parallel(\omega)$ components of the optical conductivity were calculated for both compounds (Fig. 5.5). There is considerable more optical anisotropy in $\text{Nb}_3\text{O}_7(\text{OH})$ compared to $\text{H-Nb}_2\text{O}_5$ (almost isotropic) for both polarizations. For $\text{Nb}_3\text{O}_7(\text{OH})$ the maximum values of $\sigma^\perp(\omega)$ are situated around 5.83 eV ($4.33 \times 10^{15} \text{ s}^{-1}$) and 9.13 eV ($4.25 \times 10^{15} \text{ s}^{-1}$) and of $\sigma^\parallel(\omega)$ at 5.73 eV ($4.75 \times 10^{15} \text{ s}^{-1}$) and 10.01 eV ($3.95 \times 10^{15} \text{ s}^{-1}$). $\text{H-Nb}_2\text{O}_5$ expresses two peaks for both components; for $\sigma^\perp(\omega)$, these peaks are situated at 5.83 eV ($4.44 \times 10^{15} \text{ s}^{-1}$) and 8.96 eV ($4.08 \times 10^{15} \text{ s}^{-1}$) and for $\sigma^\parallel(\omega)$ at 5.70 eV ($5.96 \times 10^{15} \text{ s}^{-1}$) and 8.47 eV ($4.82 \times 10^{15} \text{ s}^{-1}$). The difference between the optical conductivity of the two compounds is attributed to their electronic structure as these peaks are mainly composed by the states close to the Fermi level.

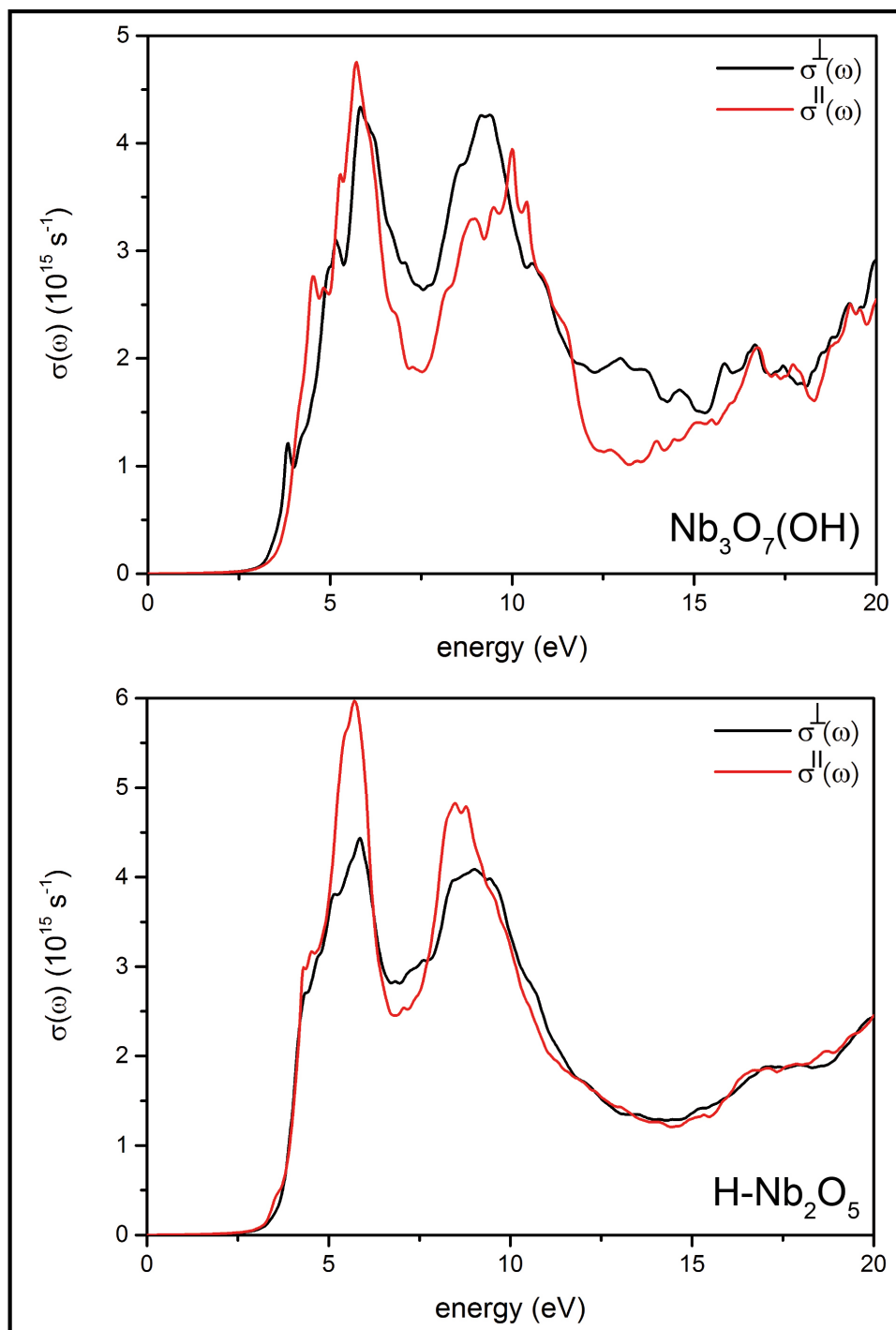


Figure 5.5: Calculated optical conductivity $\sigma(\omega)$ of $\text{Nb}_3\text{O}_7(\text{OH})$ and monoclinic $\text{H-Nb}_2\text{O}_5$.

5.3.4 Comparison of the calculation with experimental EELS data

The quality of the calculation was investigated using experimental low loss EEL spectra which were compared to theoretical spectral components of the energy loss function $L(\omega)$ for both compounds. Fig. 5.6 shows the spectra $L(\omega)$ which were calculated theoretically using the TB-mBJ functional[31]. The peaks in $L(\omega)$ have a direct proportionality to the energy loss of fast electrons which transmit through materials. A plasma frequency is produced for the energy points in $\varepsilon_1(\omega)$ for which $\varepsilon_1^\perp(\omega)/\varepsilon_1^\parallel(\omega)=0$ applies. These are then responsible for the plasmon resonance in $L(\omega)$. Due to the lack of interband transitions, the valence shell electrons are regarded as free which results in plasma peaks in both optical spectra of $L^\perp(\omega)/L^\parallel(\omega)$. The low-loss spectra were measured along [100] ($^\perp(\omega)$) and [001] ($^\parallel(\omega)$) direction for $\text{Nb}_3\text{O}_7(\text{OH})$ and off-zone axis for Nb_2O_5 . The experimental spectra for the two crystal directions of $\text{Nb}_3\text{O}_7(\text{OH})$ show broad features at 7 eV and a double peak structure between 12 eV and 15 eV. The first peak is similar for both crystal directions and can nicely be reproduced by theory which yields a value of 7.1 eV for $L^\perp(\omega)$ and $L^\parallel(\omega)$. The peak intensity of the experimentally observed double peak varies for the two crystal directions: The experimental $L^\parallel(\omega)$ exhibits an enhanced intensity for the first peak at 12 eV, while the second peak at 15 eV is more intense for the experimental $L^\perp(\omega)$. This is also nicely reproduced by theory which exhibits a maximum at 12.47 eV for ($L^\parallel(\omega)$) and 15.0 eV for ($L^\perp(\omega)$). The theoretical spectrum $L^\parallel(\omega)$ and $L^\perp(\omega)$ of H-Nb₂O₅ shows similar features which are positioned at 6.7 and 14.2 eV. Therefore, the experimental spectrum was not acquired along a certain crystal direction. The feature observed experimentally resemble the two dominant peaks in the theoretical spectra of $L^\perp(\omega)$ and $L^\parallel(\omega)$. There is a good agreement between experiment and calculated low-loss features for both compounds, which proves the validity of our structure models. Some finer details of the calculated spectrum could not be resolved experimentally. This might be due to the experimental point spread function which limits the energy resolution.

Element specific electron energy-loss edges give further insights into the local surrounding of the elements in the crystal structure. Both crystal structures $\text{Nb}_3\text{O}_7(\text{OH})$ and monoclinic H-Nb₂O₅ are composed of edge- and corner-sharing NbO₆ octahedra. This is why no significant differences were observed for the electron energy-loss near edge structure (ELNES) of the experimental Nb-M₃ and O-K edges of the two compounds. In this regard, the Nb-M₃ and O-K edge spectra were only calculated for $\text{Nb}_3\text{O}_7(\text{OH})$ to elucidate the contribution of the different lattice sites to the ELNES of the edges. The theoretical spectra were calculated using the WIEN2k code[33] as X-ray absorption spectra (XAS) assuming that EEL spectra are practically the same as XAS spectra for the investigated energy losses. This approximation is valid since the EELS data were acquired within the dipole regime,

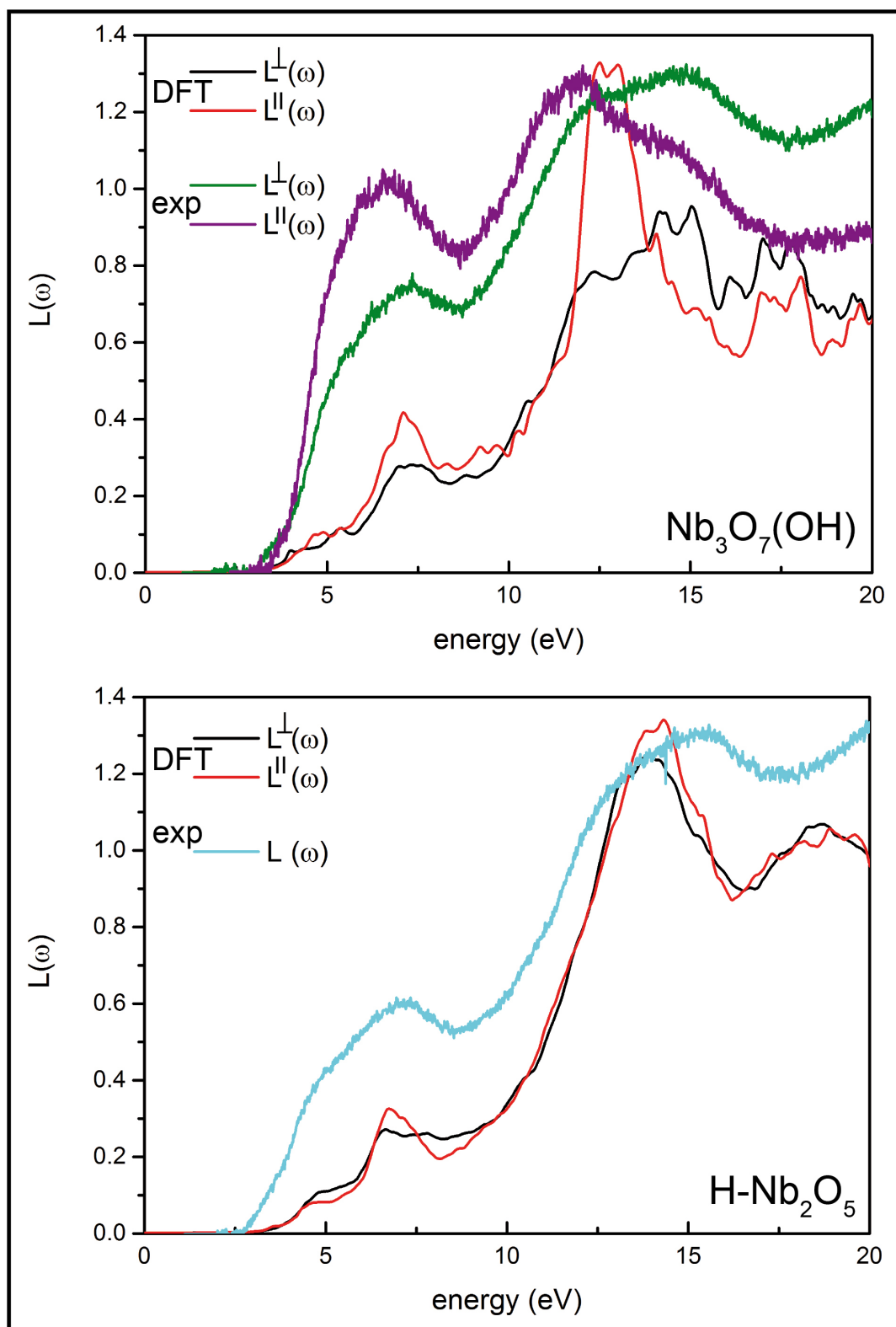


Figure 5.6: Comparison of the calculated energy loss functions $L(\omega)$ with experimental low loss EEL spectra for $\text{Nb}_3\text{O}_7(\text{OH})$ and $\text{H-Nb}_2\text{O}_5$.

i.e. small scattering angles. The spectra were obtained as weighted superpositions of spectra generated at each of the inequivalent atomic positions. Fig. 5.7 summarizes the experimental spectrum, the weighted superposition and the individual contributions of atoms in inequivalent lattice sites.

Pentavalent Nb_2O_5 is characterized by a Nb– $M_{2,3}$ edge which exhibits two white lines with high-energy shoulders and is consistent with previously reported ELNES data [50]. The experimental data of the Nb– M_3 edge of $\text{Nb}_3\text{O}_5(\text{OH})$ likewise shows one broad line with a maximum at about 3 eV above the onset and a shoulder around 4.2 eV. Our calculations which are based on the dipole selection rule ($\Delta l = \pm 1$) [51] nicely reproduce the ELNES of this edge, which is explained by excitations from the Nb– $3p_{3/2}$ level to unoccupied Nb– $4d$ states while dipole allowed transitions from $3p_{3/2}$ to Nb– $5s$ play a minor role. From the calculations it is obvious that the substructuring of the white line is related to the inequivalent Nb sites in either edge or corner-sharing NbO_6 octahedra. Niobium which sits in the center of edge-sharing NbO_6 octahedra (depicted as Nb(2) and Nb(3) in Fig. 5.7) mainly contributes to the main peak, while the share of the Nb(1) atoms which sit in corner-sharing octahedra dominates the shoulder of the Nb– M_3 spectrum.

The experimental O–K edge, which results from transitions of the $1s$ core electrons to unoccupied states with p character shows five dominant peaks at 2.0, 6.0, 14.0, 22.0 and 33.0 eV above the onset. The entire spectrum could be reproduced nicely by calculations as shown in Fig. 5.7b. This was achieved by including the core hole effect into the calculations using the final state rule. Doing so we performed eight supercell calculations for each inequivalent O–site. The calculations exhibit a huge difference between contributions stemming from different inequivalent oxygen atoms; The first three peaks at 2.0 eV, 6.0 eV and 13.0 eV at the theoretic scale mainly originates from the following O–atoms contributions as: (1) The first peak originates from O(1), O(3) and O(4) with minor contribution of O(2, 5–8); (2) the second peak appears mainly due to contributions from O(6) and O(3), and (3) the third peak is almost equally contributed by O(6), O(1) and O(3) with minor participation of other O–atoms. The remaining two peaks are produced by equal contribution of all O–atoms only O(2) participates more at the last peak. Fig. 5.7 shows a nice agreement between the theory and experiment for the O–K edge and Nb– M_3 edge, likewise proving our structure model for $\text{Nb}_3\text{O}_7(\text{OH})$.

5.3.5 Transport properties

The electronic transport properties are crucial for the performance of a material in functional devices as electrons and holes need to diffuse through the material subsequent to their generation. These properties are dominated by the effective masses of holes/electrons and their mobilities. The effective masses of electrons and holes were calculated for $\text{Nb}_3\text{O}_7(\text{OH})$ and $\text{H-Nb}_2\text{O}_5$ by fitting the electronic

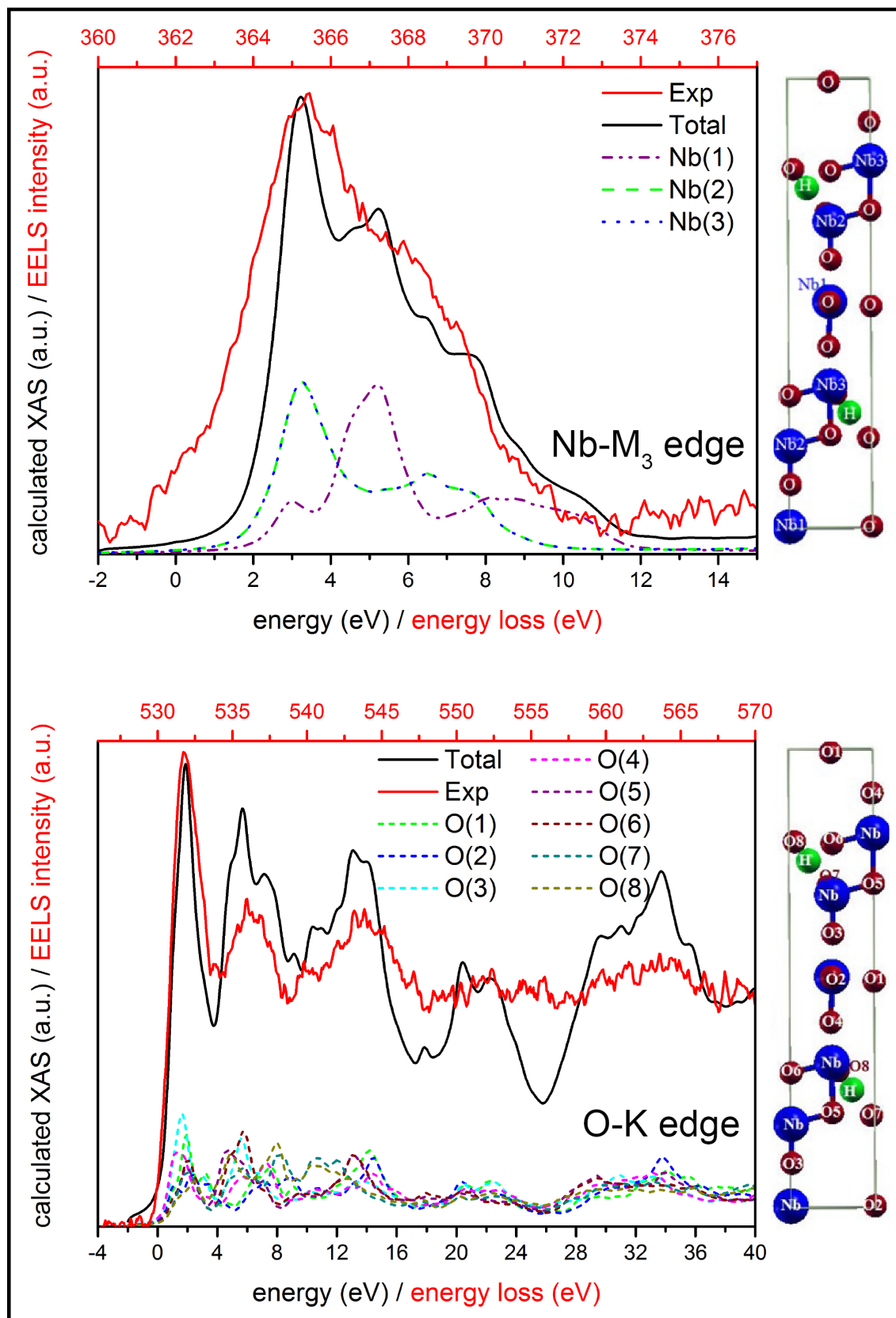


Figure 5.7: Calculated and measured EELS edges of $\text{Nb}_3\text{O}_7(\text{OH})$. (a) Nb-M₃ and (b) O-K edge.

dispersion curves (E–K curve) around the CBM and VBM niveau:

$$m^* = \hbar^2 \left(\frac{\partial^2 E}{\partial k^2} \right)^{-1} \quad (5.1)$$

where m^* and \hbar are the effective mass and reduced Planck constant. The calculated effective masses of electrons (m_e^*) are $0.147 m_e$ for $\text{Nb}_3\text{O}_7(\text{OH})$ and $0.112 m_e$ for $\text{H-Nb}_2\text{O}_5$. Values of $0.351 m_e$ and $0.959 m_e$ were found for the masses of holes (m_h^*) for $\text{Nb}_3\text{O}_7(\text{OH})$ and $\text{H-Nb}_2\text{O}_5$, respectively. The inverse relation of the effective mass with the mobility of carriers μ_e/μ_h is given by

$$\mu_e = \frac{e\tau}{m_e^*} \quad \text{and} \quad \mu_h = \frac{e\tau}{m_h^*} \quad (5.2)$$

with τ being the relaxation time and e the charge of an electron. Accordingly, greater effective mass of holes or electrons yield smaller mobilities and vice versa. Both compounds express a higher mobility of electrons resulting in n -type conductivity with $\text{Nb}_3\text{O}_7(\text{OH})$ exceeding $\text{H-Nb}_2\text{O}_5$.

To elucidate the prospects of $\text{Nb}_3\text{O}_7(\text{OH})$ and $\text{H-Nb}_2\text{O}_5$ in functional devices, the thermoelectric conductivity was calculated under constant relaxation time approximation using the BoltzTraP code[32]. In Fig. 5.8 the thermoelectric conductivity σ^{ave} is plotted as function of the chemical potential $\mu(\text{eV})$ at 300 K for both $\text{Nb}_3\text{O}_7(\text{OH})$ and $\text{H-Nb}_2\text{O}_5$. The $\sigma^{ave}(\mu, T = 300 \text{ K})$ plots are separated into a region below the Fermi level E_F , which is assigned to hole carriers (p -type), and a region above E_F assigned to electrons (n -type). For $\text{Nb}_3\text{O}_7(\text{OH})$ the $\sigma^{ave}(\mu, T = 300 \text{ K})$ plot shows a sharp increase in the n -type region with reaching a value of $1.26 \times 10^{20}(\Omega\text{ms})^{-1}$ compared to the p -type region ($0.57 \times 10^{20}(\Omega\text{ms})^{-1}$). The thermoelectric conductivity of $\text{H-Nb}_2\text{O}_5$ is likewise characterized by a greater value of $3.92 \times 10^{19}(\Omega\text{ms})^{-1}$ in the n -type region compared to the p -type region were $\sigma^{ave}(\mu, T = 300 \text{ K})$ equals $2.97 \times 10^{19}(\Omega\text{ms})^{-1}$.

It is worth to note, that even though both compounds behaves like n -type semiconductors, the thermoelectric conductivity of electrons is by factor of 3 higher in $\text{Nb}_3\text{O}_7(\text{OH})$ than in $\text{H-Nb}_2\text{O}_5$. This is in line with the high photochemical efficiency of $\text{Nb}_3\text{O}_7(\text{OH})$ observed experimentally.[10, 24]

5.4 Conclusion

In summary, we investigated the electronic structure, optical and electronic transport properties of $\text{Nb}_3\text{O}_7(\text{OH})$ and $\text{H-Nb}_2\text{O}_5$ using the TB–mBJ [31] functional and developed a model to simulate the presence of hydrogen in the crystal lattice of $\text{Nb}_3\text{O}_7(\text{OH})$. The calculated band structures showed that both compounds are wide and indirect band gap semiconductors, with the calculated optical band gaps being similar to the ones determined experimentally. For both compounds, mainly Nb–4d orbitals construct the CBM while O–2p orbitals form the VBM so that transitions

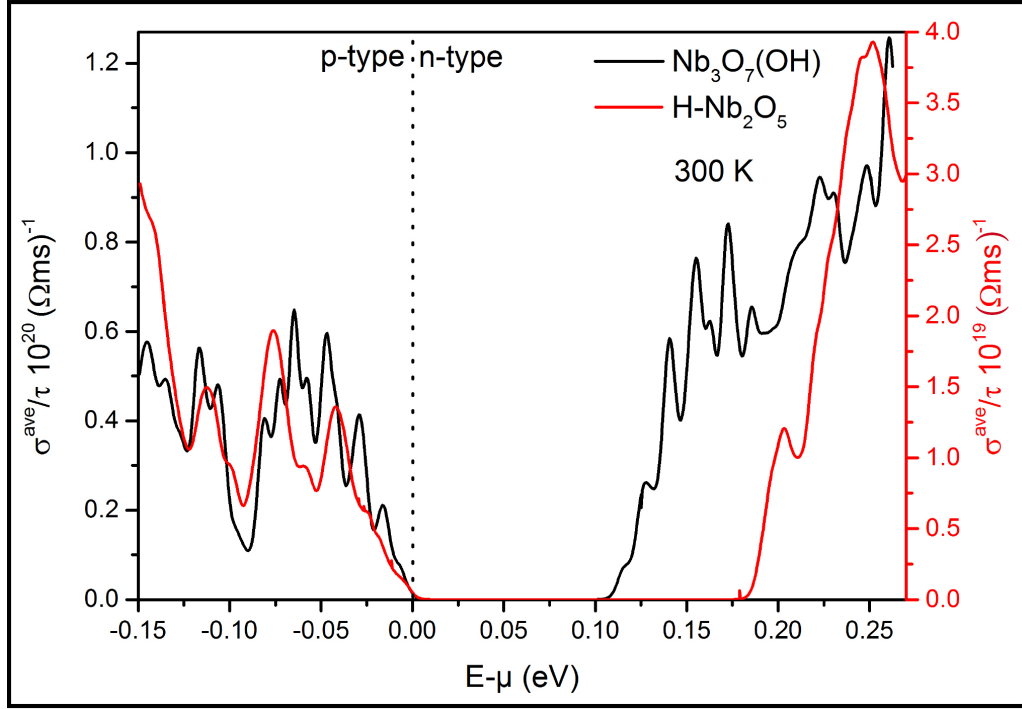


Figure 5.8: Calculated thermoelectric conductivity for $\text{Nb}_3\text{O}_7(\text{OH})$ (black) and monoclinic $\text{H-Nb}_2\text{O}_5$ (red) calculated using the BoltsTraP code. Please note the different vertical axis values.

between these orbitals are mainly responsible for optical transitions featuring sharp peaks in the dielectric function. Compared to $\text{H-Nb}_2\text{O}_5$, $\text{Nb}_3\text{O}_7(\text{OH})$ shows a greater optical anisotropy and a higher thermoelectric conductivity $\sigma^{ave}(\mu, T = 300\text{K})$. Both compounds express n -type conductivity, and the thermoelectric conductivity of electrons is by a factor of three higher in $\text{Nb}_3\text{O}_7(\text{OH})$ compared to $\text{H-Nb}_2\text{O}_5$. Similarly, the thermoelectric conductivity of holes is twice as high in $\text{Nb}_3\text{O}_7(\text{OH})$ than in $\text{H-Nb}_2\text{O}_5$.

Experimental low-loss EEL spectra (energy losses between 0–50 eV) were recorded in the TEM for $\text{Nb}_3\text{O}_7(\text{OH})$ and $\text{H-Nb}_2\text{O}_5$. A good agreement between theory and experiment was discovered. These findings validate the results of the calculations and the model for hydrogen positioning. In addition the WIEN2k code[28] was applied to simulate the ELNES of the Nb-M₃ and O-K edge of $\text{Nb}_3\text{O}_7(\text{OH})$ revealing the contribution of inequivalent lattice sites of the Nb and O atoms.

The results of this study allow an interpretation of the applicability of the two niobium oxide phases orthorhombic $\text{Nb}_3\text{O}_7(\text{OH})$ and monoclinic $\text{H-Nb}_2\text{O}_5$ as photocatalysts or electrode materials. Both compounds exhibit suitable properties but $\text{Nb}_3\text{O}_7(\text{OH})$ exceeds $\text{H-Nb}_2\text{O}_5$ due to higher charge carrier mobility.

Bibliography

- [1] M. Grätzel, *J. Photochem. Photobio. C* 4, 145 (2003).
- [2] A. Kudo and Y. Miseki, *Chem. Soc. Rev.* 38, 253 (2009).
- [3] K. Maeda and K. Domen, *Journal of Physical Chemistry C* 111, 7851 (2007).
- [4] P. Cendula, S. D. Tilley, S. Gimenez, J. Bisquert, M. Schmid, M. Grtzel, and J. O. Schumacher, *J. Phys. Chem. C* 118, 29599 (2014).
- [5] Y. Matsumoto, *J. Solid State Chem.* 126, 227 (1996).
- [6] Y. Xu, and M. A. A. Schoonen, *Am. Mineral.* 85, 543 (2000).
- [7] I. E. Castelli, T. Olsen, S. Datta, D. D. Landis, S. Dahl, K. S. Thygesen, and K. W. Jacobsen, *Energy Environ. Sci.* 5, 5814 (2012).
- [8] L. Yang, H. Zhou, T. Fan, and D. Zhang, *Phys. Chem. Chem. Phys.* 16, 6810 (2014).
- [9] F. E. Osterloh, *Chem. Mater.* 20, 35 (2008).
- [10] H. Zhang, Y. Wang, D. Yang, Y. Li, H. Liu, P. Liu, B. Wood, H. Zhao. *Adv. Mater.* 24, 5198, (2012).
- [11] R. A. Rani, A. S. Zoolfakar, A. P. O'Mullane, M. W. Austin, K. Kalantar-Zadeh. *J. Mater. Chem. A* 2, 15683, (2014).
- [12] J. Wu, J. Wang, H. Li, D. Xue, *Thin Solid Films.* 544, 545 (2013).
- [13] M. Hmadeh, V. Hoepfner, E. Larios, K. Liao, J. Jia, M. Jose-Yacamán, G. A. Ozin, *ChemSusChem.* 7, 2104, (2014).
- [14] S. B. Betzler, A. Wisnet, B. Breitbach, C. Mitterbauer, J. Weickert, L. Schmidt-Mende, C. Scheu, *J. Mater. Chem. A* 2, 12005, (2014).
- [15] S. B. Betzler, T. Harzer, J. Ciston, U. Dahmen, G. Dehm, C. Scheu. *Crystal Growth & Design* 16, 4309-4317, (2016).
- [16] P. Hu, D. Hou, Y. Wen, B. Shan, C. Chen, Y. Huang, X. Hu. *Nanoscale* 7, 1963, (2015).

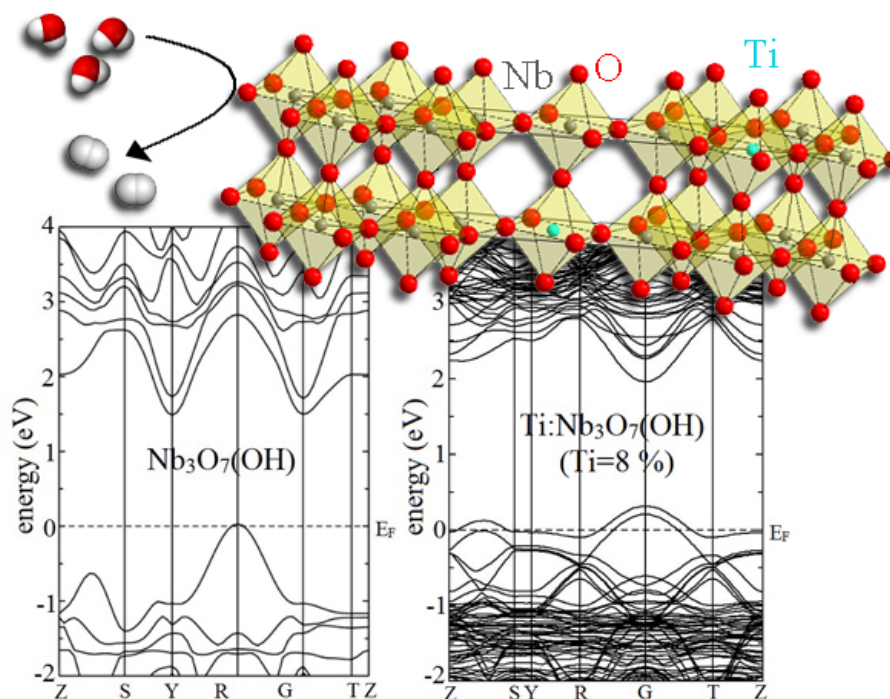
- [17] K. Sayama, H. Sugihara, H. Arakawa. *Chem. Mater.* 10, 7, (1998).
- [18] A. G. S. Prado, L. B. Bolzon, C. P. Pedroso, A. O. Moura, L. L. Costa. *Appl. Catal. B: Environ.* 82, 219, (2008).
- [19] R. Ghosh, M. K. Brennaman, T. Uher, M. R. Ok, E. T. Samulski, L. E. McNeil, T. J. Meyer, R. Lopez. *ACS Appl. Mater. Interfaces* 3, 3929, (2011).
- [20] H.-Y. Lin, H.-C. Yang, W.-L. Wang. *Catal. Today* 174, 106, (2011).
- [21] J. Z. Ou et al., *ACS Nano.* 6, 4045, (2012). PMID: 22512314
- [22] Y. Zhao, X. Zhou, L. Ye, S. C. E. Tsang. *Nano Rev.* 3, (2012).
- [23] H. Cui, G. Zhu, Y. Xie, W. Zhao, C. Yang, T. Lin, H. Gu, F. Huang. *J. Mater. Chem. A* 3, 11830, (2015).
- [24] H. Zhang, Y. Wang, P. Liu, S. L. Chou, J. Z. Wang, H. Liu, G. Wang, H. Zhao. *ACS Nano.* 10, 507, (2016).
- [25] R. Parr. *Density-Functional Theory of Atoms and Molecules; International Series of Monographs on Chemistry; Oxford University Press, USA, 1989.*
- [26] W. Kohn. *Rev. Mod. Phys.* 71, 1253, (1999).
- [27] J. P. Perdew, K. Burke, M. Ernzerhof. *Phys. Rev. Lett.* 77, 3865, (1996).
- [28] J. Heyd, J. E. Peralta, G. E. Scuseria, R. L. Martin. *J. Chem. Phys.* 123, (2005).
- [29] J. P. Perdew, *Phys. Rev. B* 45, 13244, (1992).
- [30] E. , S. H. Vosko. *Phys. Rev. B* 47, 13164, (1993).
- [31] F. Tran, P. Blaha. *Phys. Rev. Lett.* 102, 226401, (2009).
- [32] G. K. Madsen, D. J. Singh. *Computer Physics Communications* 175, 67, (2006).
- [33] P. Blaha, K. Schwarz, G. Madsen, D. Kvasnicka, J. Luitz. *WIEN2k: An Augmented Plane Wave plus Local Orbitals Program for Calculating Crystal Properties; Karlheinz Schwarz, Techn. Universitt Wien, Austria, 2001.*
- [34] C. Ambrosch-Draxl, J. O. Sofo. *Computer Physics Communications* 175, 1, (2006).
- [35] F. Wooten. *Optical Properties of Solids; Academic Press: New York, 1972.*
- [36] D. J. Singh, S. S. A. Seo, H. N. Lee, *Phys. Rev. B* 82, 180103, (2010).
- [37] D. Groh, R. Pandey, M. Sahariah, E. Amzallag, I. Baraille, M. Reart. *Journal of Physics and Chemistry of Solids* 70, 789, (2009).

- [38] K. Jorissen, J. J. Rehr. *Phys. Rev. B* 81, 245124, (2010).
- [39] N. Ashcroft, N. Mermin. *Solid State Physics*; HRW international editions; Holt, Rinehart and Winston, 1976.
- [40] J. M. Ziman, *Principles of the Theory of Solids*, 2nd ed.; Cambridge University Press, 1972; Cambridge Books Online.
- [41] J. Park, S. Heo, J. Chung, H. Kim, H. Lee, K. Kim, G. Park. *Ultramicroscopy* 109, 1183, (2009).
- [42] J. Tauc, R. Grigorovici, *A. physica status solidi (b)* 15, 627, (1966).
- [43] S. Andersson, *Acta Chem. Scand.* 18, 2339 (1964).
- [44] F. Izumi, H. Kodama. *Z. Anorg. Allg. Chem.* 441, 8, (1978).
- [45] Betzler, S. 3D Hierarchical Nb₃O₇(OH) superstructures: Synthesis, structural characterization and photophysical properties. Ph.D. thesis, Faculty of Chemistry and pharmacy, Ludwig-Maximilians-University of Munich, Munich, 2015.
- [46] B. Gatehouse, A. Wadsley. *Acta Cryst.* 17, 1545, (1964).
- [47] K. Kato. *Acta Crystallographica B* 32, 764, (1976).
- [48] D. O. Scanlon, C. W. Dunnill, J. Buckeridge, S. A. Shevlin, A. J. Logsdail, S. M. Woodley, R. A. Catlow, M. J. Powell, R. G. Palgrave, I. P. Parkin, et al. *Nat. Mater.* 2013, 12, 798801.
- [49] Penn, D. R. *Phys. Rev.* 128, 2093, (1962).
- [50] D. Bach, R. Schneider, D. Gerthsen, J. Verbeeck, W. AAAA. *Sigle. Microsc. Microanal.* 15, 505, (2009).
- [51] M. Rubio, L. Serrano-Andres, M. Merchan. *J. Chem. Phys.* 128, 104305, (2008).

Chapter 6

Tuning the electronic structure of $\text{Nb}_3\text{O}_7(\text{OH})$ by titanium doping for enhanced light-induced water splitting

This chapter is based on a manuscript by Wilayat Khan, Sophia B. Betzler, Christina Scheu, Ondřej Šipr and Ján Minár, which is to be submitted. In this chapter, we did the structural, optoelectronic and spectroscopic properties calculations, and the experimental EELS and ELNES were nicely reproduced by theory.



6.1 Introduction

The demand for fossil fuel from solar light is a continuously increasing scientific challenge [1]. Photocatalytic water-splitting is an alternative approach to accomplish the principles of conversion of solar light to chemical energy such as the splitting of water H_2O to produced H_2 fuel. This task required to accomplish at a mesoporous, nanostructural metal oxides under the illumination of light to produced clean and renewable energy [2]. The main challenges to the water splitting reaction lie in finding suitable photocatalytic materials that utilize maximum solar light and evaluate H_2 . Moreover, these materials should also fulfill some necessary requirements, e.g. they must be good photocatalysts and have chemical stability, efficient absorption of visible light, proper band structure with energetic valence band and conduction band position to fulfill the criteria of overall water splitting process. Electron-hole pair is created in semiconductor under solar light greater than band gap energy. Then the hole in the valence band and electron in the conduction band simultaneously take part in the production of O_2 : $\text{H}_2\text{O} + 2\text{h}^+ \rightarrow 1/2\text{O}_2 + 2\text{H}^+$ and H_2 : $2\text{H}^+ + 2\text{e}^- \rightarrow \text{H}_2$. The minimum band gap 1.23 eV (the free energy for water splitting) is required for these evaluation processes. Apart from the band gap, the photocatalytic materials acquire suitable band alignment. The first photoanode TiO_2 materials reported by the Fujishima and Honda [3], which is an effective material for water-splitting dye-sensitized photoelectrochemical solar cell. The efficiency of water splitting solar cell at common anatase TiO_2 is limited due to high electron-hole recombination rate and by low injection yields [4]. The injection yields in SnO_2 is reached to $\sim 100\%$ due to lower energy of the CB (0.5 V); on the other hand it has much higher recombination rate and oxides sensitizer [5].

The main goal of focusing on these research activities is to develop novel photoelectrodes materials that provide large surface area, improve the surface functionality and photocurrent transfer [6, 7]. It has been seen in the semiconductor-based heteronanostructures that explained the charge transfer from one component to the other component in the photocatalytic activity under solar light. Here the first component will be semiconductor and the other will be metal, transition metal oxide or some other semiconductor with suitable band edge [8, 9, 10].

It has been pointed out that Nb_2O_5 has many polymorphs, and it is a wide band gap (3.1 eV) semiconductor [11]. Numerous investigations have been carried out with emphasis on application to photocatalysis, lithium ion battery and DSSCs. The DSSC performance for monoclinic H- Nb_2O_5 reaches higher value of 3.05 % as compared to O- Nb_2O_5 /M- Nb_2O_5 photoanodes due to its high surface area [12]. Despite these developments, the solar conversion efficiencies of Nb_2O_5 are still very low ($\leq 5.0\%$) because of their insufficient area for dye loading. $\text{Nb}_3\text{O}_7(\text{OH})$ is another important photoelectrode material suitable with application in dye degradation and DSSCs. The $\text{Nb}_3\text{O}_7(\text{OH})$ is usually assembled by nanorods, and is able to produce

hydrogen effectively under solar light .

Currently, there is a small number of studies dedicated to the synthesis and investigation of the structural properties of the $\text{Nb}_3\text{O}_7(\text{OH})$ structure based on theory and experiment [12]. Recently, Betzler et. al, reported the preparation of 3D–heirarchical nanostructure $\text{Nb}_3\text{O}_7(\text{OH})$ *via* a template free, one–step hydrothermal strategy, and detailed structural and spectroscopic information were investigated in their study [13]. P. Hu et. al., [14] prepared 3D high-crystalline hierarchical nanostructures $\text{Nb}_3\text{O}_7(\text{OH})$ using a facile hydrothermal self–assembly strategy. The obtained nanostructure crystal possesses six–fold morphology i.e. sheaf–like nanoarchitectures. However, untill now there is only little research which focused on detailed density functional theory (DFT) study on the information about the optoelectronic and spectroscopic properties of this class of materials [15], and mentioned that $\text{Nb}_3\text{O}_7(\text{OH})$ imposed high electronic transport properties compared to Nb_2O_5 . Besides, enhancing the active lattice site and decreasing the probability of recombination of photogenerated carriers can further improve the photocatalytic activity, as indicated by an experimental study which uses Ti doping to generate $\text{Nb}_{3-x}\text{Ti}_x\text{O}_7(\text{OH})$.

This study aims to demonstrate the effect of the incorporated Ti atoms on the structural properties, optoelectronic and spectroscopic properties of $\text{Nb}_3\text{O}_7(\text{OH})$. We calculated the formation energy for the substitutional and interstitial doped titanium in $\text{Nb}_3\text{O}_7(\text{OH})$. The preferable position for Ti is the Nb site and investigate that the Ti changes the structural properties of $\text{Nb}_{3-x}\text{Ti}_x\text{O}_7(\text{OH})$. Based on the substitution Ti–doped systems, the linear optical properties were simulated at the level of TB–mBJ approach. We present the calculated data of electron energy loss spectra (EELS) and high energy loss spectra (Nb–M3 edge and O–K edge) of Ti–doped with experimental measured data with transmission electron microscope (TEM).

6.2 Computational and experimental methodology

6.2.1 Computational details

In this article, the structural, optical, spectroscopic properties of Ti–doped $\text{Nb}_3\text{O}_7(\text{OH})$ are investigated. The unit cell of $\text{Nb}_3\text{O}_7(\text{OH})$ has three Nb atoms, eight O atoms and three H atoms, respectively, as shown in Fig. 6.1a. In order to avoid the nearest impurity–impurity interaction in a cell, we used a $2 \times 2 \times 1$ supercell of $\text{Nb}_3\text{O}_7(\text{OH})$ to construct Ti (4.16 %)–doped and Ti (8.32 %)–doped compounds, where the Nb^{5+} atom is replaced by Ti^{4+} atom. To simplify the nomenclature, the compounds were given symbolic names as A1 (Ti (0.0 %): $\text{Nb}_3\text{O}_7(\text{OH})$), A2 (Ti (4.16 %): $\text{Nb}_3\text{O}_7(\text{OH})$), and A3 (Ti (8.32 %): $\text{Nb}_3\text{O}_7(\text{OH})$), respectively, because of Ti concentration. These

are displayed in Figs. 6.1(b, c).

All DFT calculations have been performed using the full potential linearized augmented plan wave method implemented in WIEN2k code [16]. The valence atomic configurations in all compounds are as follows: $5s^14p^64d^4$ for Nb, $4s^23p^63d^2$ for Ti and $2s^22p^4$ for O, respectively. After geometrical optimization, the accuracy of self-consistent convergence was set to 0.00001 and the forces convergence criteria was set to 0.0001 eV/Å. The structure optimization was done using generalized gradient approximation (GGA), while the electronic structure and optical properties were performed using TB-mBJ functional [17]. The TB-mBJ functional has an advantage over the available functionals (LDA [19], GGA [18], and EVGGA [20]) because it gives better band alignment. The Monkhorst-Pack k-meshes of $16 \times 16 \times 15$ and $12 \times 12 \times 4$ are used for A1, A2 and A3, respectively. The entire optical parameters like real and imaginary dielectric function, and electron energy loss function of pure and $\text{Nb}_{3-x}\text{Ti}_x\text{O}_7(\text{OH})$ from the OPTIC program interfaced in WIEN2k code [21]. Calculations of optical properties are based on the linear optical response theory.

The energy loss near edge (ELNES) fine structure of Nb-M₃ and O-K edges for A1, A2 and A3 systems, respectively, were calculated from the X-rays absorption program under WIEN2k code [16]. The ELNES of Nb-M₃ and O-K edges are based on Fermi's golden rule. To get better understanding with the experimental results we account for the core hole effect using the final state rule. The corresponding procedure were given in detail in the article of W. Khan et. al., [15]. All these calculations were performed for all inequivalent O atoms and Nb atoms/unit cell in $2 \times 2 \times 1$ supercell.

6.2.2 Experimental details

The samples investigated in this study were synthesized according to the hydrothermal synthesis procedure described elsewhere [13]. The titanium doping concentration was controlled by the amount of Ti(IV)-precursor added to the synthesis reaction. The dopant concentration in the $\text{Nb}_3\text{O}_7(\text{OH})$ nanostructures was determined by energy-dispersive X-ray spectroscopy performed in the transmission electron microscope using a *Bruker SuperX* spectrometer. Three different samples were investigated in this study. A titanium-free $\text{Nb}_3\text{O}_7(\text{OH})$ reference sample, a sample containing 6.1 ± 0.5 at% titanium relative to niobium and one containing XYZ at% titanium. The crystal structure of the different samples was determined to be $\text{Nb}_3\text{O}_7(\text{OH})$ by X-ray diffraction experiments performed using a STOE powder diffractometer equipped with a *Dectris Mythen K1* detector, *Seifert ID3003* generator and a *Seifert Long Fine Focus Dx-Cu12x0.4-S* X-ray tube. Small distortion of the crystal lattice were furthermore investigated by performing additional X-ray experiments on a XYZ diffractometer and Rietveld refinements.

The EELS experiments were performed using a *FEI Titan Themis* equipped

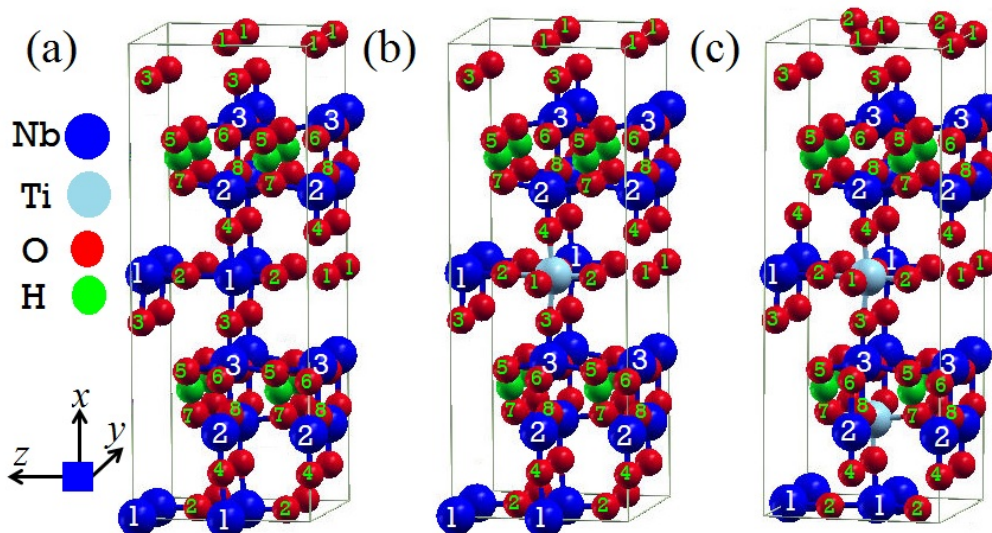


Figure 6.1: Crystal structures of (a) $\text{Nb}_3\text{O}_7(\text{OH})$, (b) Ti-doped $\text{Nb}_3\text{O}_7(\text{OH})$ (Ti=4.16 %) and (c) Ti-doped $\text{Nb}_3\text{O}_7(\text{OH})$ (Ti=8.32 %). These structures are based on $1 \times 2 \times 2$ supercell. The numbers assigned to different Nb and O atoms indicate that there are three inequivalent Nb atoms and eight inequivalent O atoms in these structures.

with a Cs-corrector for the probe operated at 300 kV. Using a monochromator to reduce the energy spread of the gun, an energy resolution of 0.18 – 0.20 eV was achieved, as determined from the full width of half maximum of the zero loss peak. The EEL spectra were collected with a XYZ spectrometer using a 5 mm spectrometer entrance aperture. The EELS experiments were carried out in the scanning transmission mode using featuring a convergence angle α of 23 mrad and collection angle β of XYZ mrad. The low-loss spectra were acquired using a dispersion of 0.025 eV/channel, while the element specific edges were acquired using a dispersion of 0.05 eV/channel. The energy loss of the edge onsets was determined with the *Dual EELS* technique.

6.3 Results and discussion

6.3.1 Structural properties

It is noted that the Ti incorporation at the octahedral lattice site of $\text{Nb}_3\text{O}_7(\text{OH})$ does not indicate significant changes of the crystal structure, but affects its crystallinity that reduces its growth rate. Experimental analysis exposed the reduction in the b - and c -directions, and an increase in the a -direction. It is claimed that the variations in the b - and c -directions are greater than in c -directions and that they might be caused by the doping of Ti in the crystal structure of $\text{Nb}_3\text{O}_7(\text{OH})$ [22].

Table 6.1: Calculated Interatomic Distances for $\text{Nb}_3\text{O}_7(\text{OH})$ (A1) and $\text{Ti:Nb}_3\text{O}_7(\text{OH})$ (A2, A3).

| Bond Lengths Å | sample A1 | sample A2 | Δ | sample A1 | sample A3 | Δ |
|----------------|-----------|-----------|----------|-------------|-------------|--------------|
| Nb/Ti–O | — | — | — | — | — | — |
| along x–axis | 2.211 | 2.184 | 0.0273 | 2.115/2.266 | 2.083/2.238 | 0.032/0.028 |
| along y–axis | 1.991 | 1.98 | 0.011 | 1.925/1.962 | 1.906/1.949 | 0.037/0.034 |
| along z–axis | 2.06 | 2.073 | –0.013 | 2.048/2.065 | 2.053/2.058 | –0.005/0.007 |

Pure $\text{Nb}_3\text{O}_7(\text{OH})$ has an orthorhombic crystal structure, which can be described as a combination of Nb, O and H atoms. In the crystal structure of $\text{Nb}_3\text{O}_7(\text{OH})$, each Nb atom is chemically bonded by six O atoms, forming a edge and corner sharing of ${}^1_\infty[\text{NbO}_6]$ octahedra, which are the key components of the mentioned crystal structure. An infinite chain of ${}^1_\infty[\text{NbO}_6]$ octahedra is produced due to common edge sharing. The $\text{Nb}_3\text{O}_7(\text{OH})$ was then modeled by doping Ti with different concentration. In order to see theoretically the impact imported by Ti on the structural properties, we calculated and analyzed the bond lengths.

The Nb–Nb bond lengths (3.80 Å→3.94 Å) in $\text{Nb}_3\text{O}_7(\text{OH})$ and $\text{Nb}_{3-x}\text{Ti}_x\text{O}_7(\text{OH})$ do not change significantly. Each Nb atom in the $\text{Nb}_3\text{O}_7(\text{OH})$ is connected to an O atom at a distance of 2.21 Å (along x –axis), 1.991 Å (along y –axis) and 2.06 Å, respectively. As we substitute one Nb by Ti in a sample of A2, we find that the calculated bond length along x –axis of Ti–O is 2.184 Å which is smaller by 0.0273 Å in $\text{Nb}_3\text{O}_7(\text{OH})$. The Ti–O (along y –axis) distance in A2 (1.98 Å) is close to the calculated bond length 1.991 Å (Nb–O). The bond lengths between Ti–O atoms decreased along x/y –axes. On the other hand, the distance between Ti and O atoms (2.073 Å) increases along z –axis by 0.013 Å against Nb–O distance. In A3 system, we have two ${}^1_\infty[\text{TiO}_6]$ octahedra which connect the ${}^1_\infty[\text{NbO}_6]$ chain. In this crystal structure, there is a strong decrease in the bond lengths along x/y –axes, the difference in the lengths are 0.032/0.028 Å, 0.037/0.034 Å, while still an increase in the distance between the atoms of Ti and O in z –direction. These modifications in the distances suggest that the Ti–doping distorts the structure of the entire crystallographic directions. The entire distances between Nb/Ti–O atoms are listed in Tab. 6.1. A decrease in the bond lengths along x/y –axis and an increase in the bond lengths along z –axis elucidate an agreement with the experimental data, in which the same trend in the lattice parameters (instead of crystallographic directions) was claimed .

Table 6.2: Ti dopant formation energies in $\text{Nb}_3\text{O}_7(\text{OH})$.

| E^{form} (eV) | Ti_{SUB} | Ti_{INS} | Δ |
|--|------------|------------|----------|
| Ti: $\text{Nb}_3\text{O}_7(\text{OH})$ | -1.415 | -0.238 | -1.177 |

6.3.2 Formation energy

In order to investigate the influence of single Ti dopant in $\text{Nb}_3\text{O}_7(\text{OH})$ and its relative stability for both substitutional (Ti_{SUB}) and interstitial doping (Ti_{INS}), the energy of formation for the relative dopant is calculated from the formulae [23];

$$E_{form} = E_{tot}(X : \text{Nb}_3\text{O}_7(\text{OH})) - E_{tot}(\text{Nb}_3\text{O}_7(\text{OH})) - m\mu_X + n\mu_{Nb} \quad (6.1)$$

and

$$E_{form} = E_{tot}(X : \text{Nb}_3\text{O}_7(\text{OH})) - E_{tot}(\text{Nb}_3\text{O}_7(\text{OH})) - m\mu_X \quad (6.2)$$

In Eqs. (1) and (2), the $E_{tot}(\text{Nb}_3\text{O}_7(\text{OH}))$ is the total energy of pristine $\text{Nb}_3\text{O}_7(\text{OH})$ and $E_{tot}(X:\text{Nb}_3\text{O}_7(\text{OH}))$ is the total energy of $\text{Nb}_3\text{O}_7(\text{OH})$ with dopant. The symbols μ_X and μ_{Nb} are the chemical potentials of dopant (here say Ti) and Nb atoms, while m and n are the number of the dopant and Nb atoms. These total energies of the $\text{Nb}_3\text{O}_7(\text{OH})$ and $\text{Ti}:\text{Nb}_3\text{O}_7(\text{OH})$ and chemical potentials of Ti/Nb atoms were calculated based on supercell crystal structures. Notify that Eq. (1) is used for single Ti (substitutional dopant) formation energy and Eq. (2) is used for single Ti (interstitial dopant) formation energy. The substitutional Ti atom in $\text{Nb}_3\text{O}_7(\text{OH})$ occupies the position of one Nb atom and the interstitial Ti sits close to the two Nb atoms. All Nb atoms are bound to six nearest neighbor oxygen atoms as shown in Fig. 6.1. Similarly the dopant Ti (substitutional) is coordinated by six oxygen atoms. The pristine $\text{Nb}_3\text{O}_7(\text{OH})$ contains the corner(one Nb)/edge(two Nb) sharing O octahedral sites. Thus, we calculated the formation energy for all possible Ti sites. The Ti dopant substitution at Nb site shows the lowest formation energy of -1.415 eV as compared to the value -0.238 eV for interstitial site of Ti (listed in Tab. 6.2). The difference between the formation energies between the Ti_{SUB} and Ti_{INS} is -1.177 eV. Thus, Ti most likely replaces niobium at its octahedral lattice sites. This is in good agreement to a recent experimental study [22] which also claims the replacement of niobium by titanium in Ti doped $\text{Nb}_3\text{O}_7(\text{OH})$ based on EELS data.

6.3.3 Band Structures and Density of States

The electronic band structures of the host and doped $\text{Nb}_3\text{O}_7(\text{OH})$ were calculated using TB-mBJ approximation and are displayed in Fig. 6.2. The calculated valence band (VB) and conduction band (CB) widths for the doped compounds are changed by Ti atoms, being in comparison to the host system.

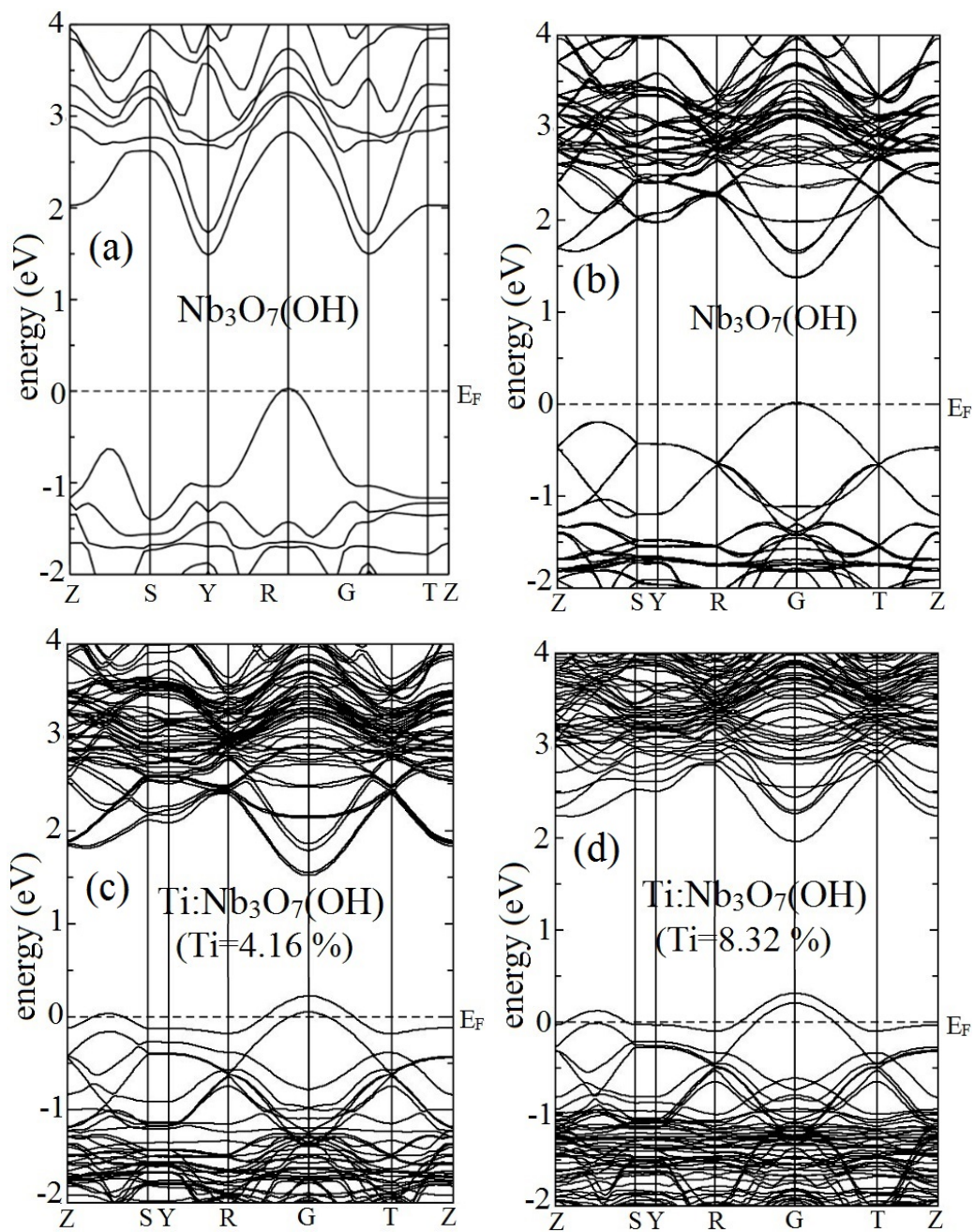


Figure 6.2: Overview of the band structure of nanostructure $\text{Nb}_3\text{O}_7(\text{OH})$ and Ti-doped $\text{Nb}_3\text{O}_7(\text{OH})$ as calculated from DFT. The Dispersion curves are taken along the Z-S-Y- Γ -T-Z lines in the BZ of $\text{Nb}_3\text{O}_7(\text{OH})$ (unit cell)/supercell (a)/(b) and c & d indicate the dispersion curve of Ti-doped $\text{Nb}_3\text{O}_7(\text{OH})$. This smearing of bands is related to the Ti contents.

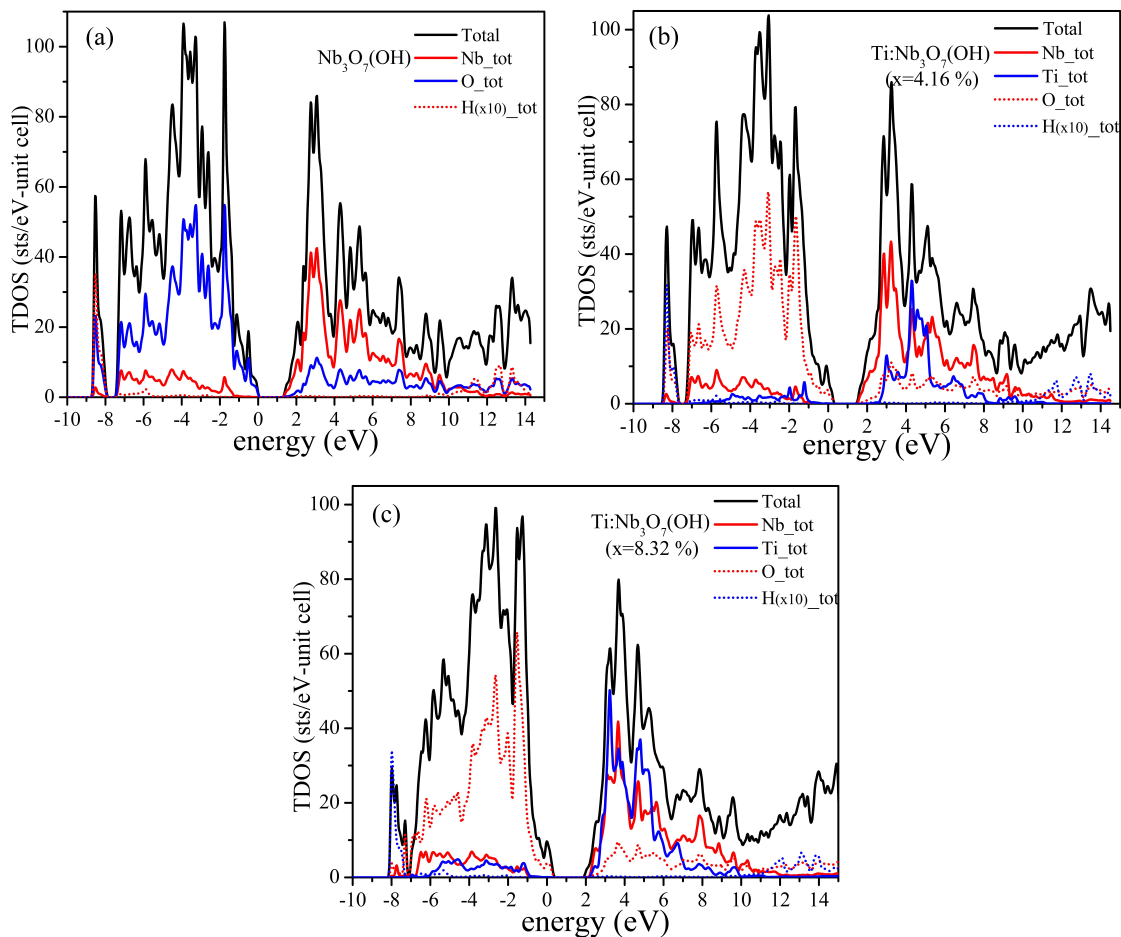


Figure 6.3: Calculated total and elemental resolved density of states for $\text{Nb}_3\text{O}_7(\text{OH})$ and Ti-doped $\text{Nb}_3\text{O}_7(\text{OH})$ as obtained from First principal calculations. (a) elemental resolved DOS for $\text{Nb}_3\text{O}_7(\text{OH})$, in which the black, red, blue (solid lines) and red (dotted line) represents total, Nb, O and H atoms. (b, c) elemental resolved DOS of Ti-doped systems, in which black, red, (solid lines) and blue/red (dotted lines) represents total, Nb, Ti, O and H atoms.

Our TB-mBJ [15] calculations conclude that pristine $\text{Nb}_3\text{O}_7(\text{OH})$ has an indirect band gap (R-Y) of 1.7 eV, as illustrated in Fig. 6.2a. This band gap is mainly donated O $2p^6$ -Nb $4d^4$ transitions. Doping the host material by Ti causes a band smearing over the Fermi level (see Figs. 6.2(b, c)). This smearing of bands is proportional to the Ti concentration such as that the smearing of bands increases with Ti contents. As Ti^{4+} substituted the Nb^{5+} in the $2 \times 2 \times 1$ supercell of $\text{Nb}_3\text{O}_7(\text{OH})$ and forms TiO_6 octahedra. The pair of electrons are attracted by O atom due to higher electronegativity, which corresponds to the bands smearing.

The total and atomic-resolved density of states (DOS) of pristine and Ti-doped $\text{Nb}_3\text{O}_7(\text{OH})$ systems were calculated using TB-mBJ approximation. The total density of states of the entire systems are described by black line in Figs. A.1(a, b, c). For pristine $\text{Nb}_3\text{O}_7(\text{OH})$, our electronic investigation has declared a width of the valence band within the 0-6.0 eV below the Fermi energy level (fixed to zero) and the conduction bandwidth is lying in the 0-8.0 eV range above the Fermi energy level. Fig. 6.3(a) presents the atomic resolved density of states, in which the red (solid line), blue (solid line) and red (dotted line) represent the total density of Nb, O and H atoms. It is clear that the O atoms make a significant contribution to the density in the VB, while density in the CB is robustly contributed by the Nb atoms. Red (solid line), blue (blue line), red (dotted line) and blue (dotted line) curves represent Nb, Ti, O and H atoms in Ti-doped systems. In Ti-doped systems (see Fig. 6.3(b, c)), we found in general the same description for VB but smearing of atomic resolved DOS come from O atom, while the CB differs due to the Ti atoms in addition to Nb atoms. However, it was observed that the contribution to the formation of CB moving from Nb to Ti (at Ti=8 %) or may constructed from the admixture of the atomic resolved DOS of Ti/Nb atoms. These results clearly indicate that there is no change in the occupancy of Nb states as it is positioned in pristine material.

Furthermore, we calculated the orbital resolved DOS of Nb, Ti, O and H atoms for the entire systems, respectively, look into the supplementary information. It has been shown in the Fig. A.1a that VB maxima are mainly consisted of O $2p$ orbitals with minor contribution of the s orbitals of Nb/H/O atoms and the CB is occupied by the empty Nb $5d$ orbitals.

Figs. A.1(c-f) represent the pDOS of orbital resolved density of states of Ti-doped $\text{Nb}_3\text{O}_7(\text{OH})$. The Ti atom in sample A2 is surrounded by a octahedron made up of six O atoms, with no big distortion of the octahedron in a specific direction. Analysis of pDOS represents that the states which smear over the E_F are solely constructed by the O $2p$ orbitals with a minor contribution of Ti p_x orbitals. This may be due to O atom attracting electron from the said orbitals towards itself because Ti has one less electron in the Ti-doped $\text{Nb}_3\text{O}_7(\text{OH})$. Moreover, the O $2p$ orbitals have some interplay with Ti $3d$ orbitals (at 1.20 eV). Deeper into VB, both O $2p$ and Ti $3d$ orbitals have strong interaction in addition to the hybridization with

Nb $4d$ orbitals. In the hybridization between O $2p$ and Ti $3d$ orbitals, the shared pair of electrons is attracted by the O atom, which registers the band smearing over the Fermi level in the band structure. The conduction band (CB) is mainly dominated by Nb $4d$ orbitals, and the only difference we found in the doped systems it is coupled with Ti $3d$ orbitals and positioning at higher energy than Nb $4d$ orbitals. As we seen a big change in the VBM but the CBM remain mostly unchanged by the doping the Ti in host material.

In case of system A3, we increased the concentration of Ti from 4.16 % to 8.32 % into $\text{Nb}_3\text{O}_7(\text{OH})$. It means that we have two less electrons in system A3. The pDOS analysis indicates that smearing as well as the intensity of O $2p$ orbitals increases in the VB, while in the conduction band the intensity of Ti $3d$ orbitals doubled compared to system A2. Here, in this case the Ti $3d$ orbitals are fully coupled with Nb $4d$ orbitals in the CBM. The remaining states have almost the same interaction with each other as in samples A1 and A2, respectively. The main advantage of Ti-doped $\text{Nb}_3\text{O}_7(\text{OH})$ is that these unoccupied states resulting an enhancement in the optical properties, through a reduced in the rate of electron-hole recombination. Consequently, the photoconversion efficiency is increased, which leads to higher photocatalytic activity in the Ti-doped $\text{Nb}_3\text{O}_7(\text{OH})$.

6.3.4 Optical properties

Regarding the linear optical properties, one of the most desired properties for photo-electrode material ($\text{Nb}_3\text{O}_7(\text{OH})$) is the extension of the absorption edge toward lower energy spectrum or to enhance photoabsorption. Doping with transition metals is one opportunity to enhance the optical absorption. Physically it can be identified by simulating the optoelectronic properties and seeing the excitonic effect as a function of incident photon. Therefore, a suitable OPTIC code implemented in all electron simulation computer program WIEN2k is used for calculating the complex dielectric function for pristine and Ti-doped $\text{Nb}_3\text{O}_7(\text{OH})$. For good agreement with the experimental optical band gap, we performed our calculations with TB-mBJ approximation, which is a more reliable tool. The calculated spectra dielectric function and other optical parameters are deduced from the dielectric function of pristine and Ti-doped $\text{Nb}_3\text{O}_7(\text{OH})$ systems.

Fig. 6.4 shows the real and imaginary part of the dielectric function as a function of energy for A1, A2 and A3 within the energy range of 0–20 eV. Comparing the absorption edge of doped systems with the pristine one, we found the same behavior throughout the spectra.

We plotted the $\varepsilon_1(\omega)$ and $\varepsilon_2(\omega)$ along x -axis and z -axis. All systems (A1, A2 and A3) have shown their absorption edge (λ_{max}) in the infra-red region (IR) (along z -axis, which is attributed to intraband transitions) and near ultra violet regions (along x -axis) both for real and imaginary dielectric function. It should

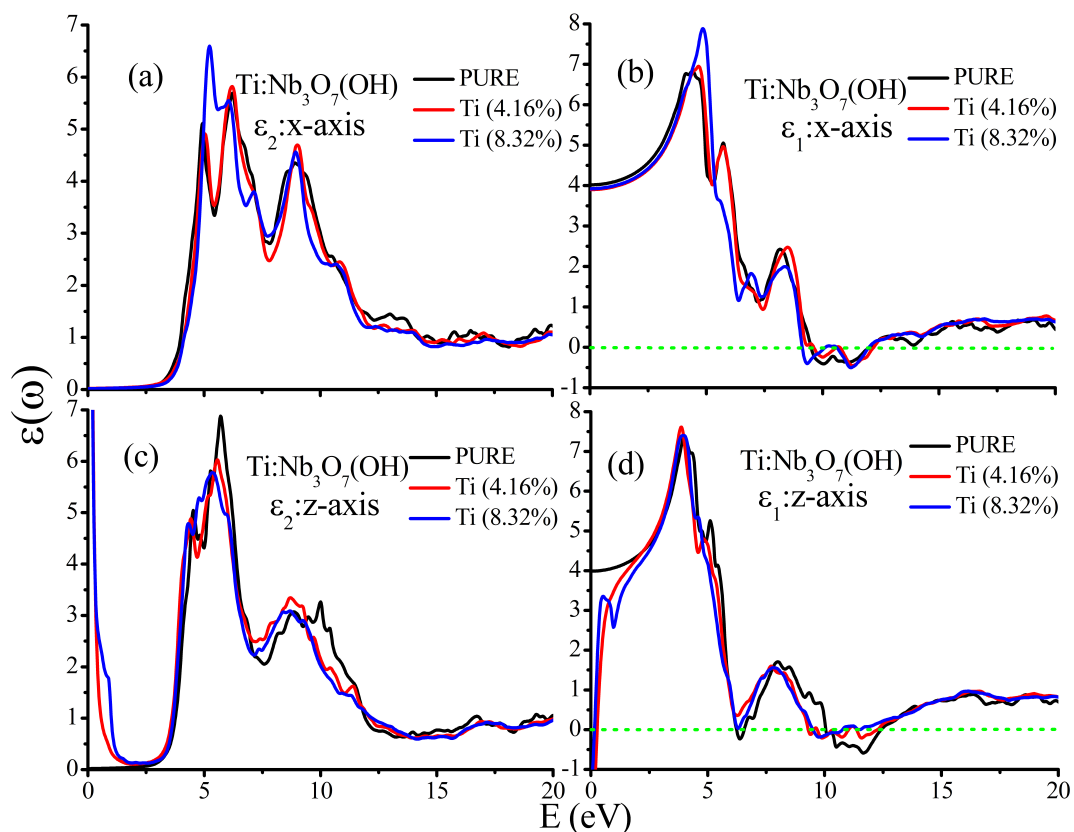


Figure 6.4: DFT calculated of optical properties. (a & b) the real and imaginary part of dielectric function of $\text{Nb}_3\text{O}_7(\text{OH})$ and $\text{Ti:Nb}_3\text{O}_7(\text{OH})$ along x-axis. Here Ti (8.32 %) show more absorption than Ti (0 % & 4.16 %). Fig c & d show the same optical parameter along z-axis which appear due to intraband transitions (due to smearing of orbitals) in the infrared region and interband transitions in the ultraviolet region.

be noted that in all cases, and because of the difference in the concentration of the dopant, the spectra are governed by the pronounced transitions from O $2p^6$ to Nb $4d^4$ orbitals, and other peaks exist due to other transitions of Nb $^{5+}$, O $^{2-}$ and H $^{1+}$ states from higher energy lying states. The simulated spectra of A2 and A3 indicate changes with Ti doping in Nb $_3$ O $_7$ (OH) as compared to A1, which can be explained as: the first peak appeared at 4.90 eV (in A1), 5.04 eV (in A2) and 5.24 eV (in A3), respectively. Quantitative investigation described that A3 explore highest absorption (6.6 a.u) than other systems (A1, A2). There are two more absorption peaks positioned at 5.42 eV/6.21 eV for A1, 5.42 eV/6.21 eV for A2 and 5.56 eV/6.11 eV for A3, but here the intensity is smaller (0.18 a.u) for A3 than other two systems. In addition, there are some valleys from 5.43 eV to 7.79 eV. But in between the first two absorption peaks A1 and A2, a valley is shown at 5.43 eV which is not visible in A3. This explore the absorption continuity in the spectrum of the A3 system imposed by Ti doping in Nb $_3$ O $_7$ (OH). The intensity in the peaks and some extra peaks in systems A2 and A3 appeared due the coupling of Ti $3d$ orbitals in addition to the Nb $4d$ orbitals.

We applied the Drude term to the spectra along z -axis which show two types of transitions; (1) intraband transitions and (2) interband transitions, as illustrated in Figs. 6.4(a, c). There are two sharp peaks observed (in systems A2 and A3) in the infrared region which are due to the intraband transitions. These transitions are based on the smearing of bands as displayed in the band structures of doped compounds. Comparison of the average spectra along z -axis of A2 and A3 exposes that the sharpness of the peaks depend on the Ti, where we see one small extra peak at 1.77 eV in A3 system. But apart from these peaks in the infrared region, there is an insulating region and then start the photon absorption at ~ 3.5 eV for A1, A2 and A3 systems. The optical absorption spectra show consistency in all systems with the same transition of electrons (O $2p^6$ to Nb $4d^d$) orbitals. Comparatively, A3 system has first absorption peak at 4.28 eV, which is also shifted towards lower energy (by 0.31 eV) as compared to A1 and A2, respectively. Fig. 6.4a shows that the $\epsilon_2(\omega)$ single main peak along z -axis as compared to the $\epsilon_2(\omega)$ along x -axis (which has three main peaks). In addition, A3 has two peaks located at 4.77 eV/5.40 eV (due to higher concentration of Ti atoms), while A1/A2 systems have only one peak at 5.70 eV/5.56 eV (lies in UV region), and only one main valley at 4.6 ± 1 eV. Additionally, the last small peaks signatures by all system around 9.0 eV but beyond this energy spectra decreases except the spectrum of A1 which still shows absorption around 10 eV. Finally, the spectra presents (see Fig. 6.4c) remarkable improvement in term of harvesting of solar light which is designated to higher concentration.

Figs. 6.4(b, d) show the real part of dielectric function, showing the electronic polarizability, of the A1, A2 and A3 systems along x -axis and z -axis directions, respectively. The static values in the spectra of $\epsilon_1(\omega)$ along x -axis were observed are 4.03 (3.90) for systems A1 (A2) and 3.93 for system A3. Then the spectra

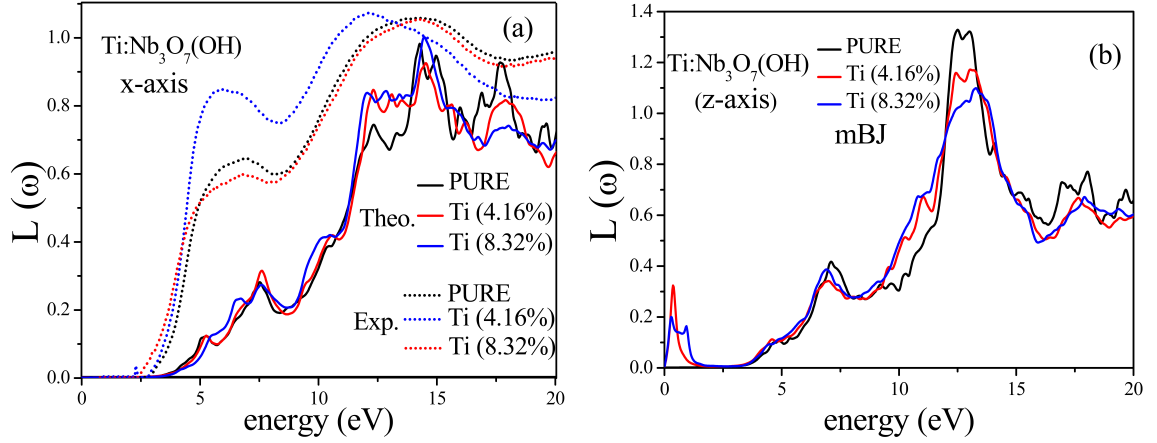


Figure 6.5: DFT simulated electron energy loss spectra (EELS) of $\text{Nb}_3\text{O}_7(\text{OH})$ (black), $\text{Ti: Nb}_3\text{O}_7(\text{OH})$ ($\text{Ti}= 4.16\%$) (red) and $\text{Ti: Nb}_3\text{O}_7(\text{OH})$ ($\text{Ti}= 8.32\%$) (blue), showing similar peaks except with the peak variations. (a) EELS spectra of the entire systems along x -axis and z -axis.

increases and a sharp peak in the spectra appeared at 4.39 eV for (A1), 4.69 eV for (A2) and 4.85 eV for (A3), which are well-defined as electronic polarizability of the corresponding interband transitions. For A3, the first sharp peaks in $\varepsilon_1(\omega)$ is more intense than one of the A1 and A2 due to the higher concentration of the dopant. The intensity of the peaks are directly related to the concentration of Ti i.e. $7.88 (\text{Ti}_{8.32}) > 6.83 (\text{Ti}_{4.16}) > 6.94$ (Pure), respectively. In the remaining two small peaks positioned at $\sim 5.6 \text{ eV}/8.18 \pm 0.4 \text{ eV}$ for all systems but the spectral intensity of A3 is smaller than A1 and A2 by a factor 1 (a.u). There are two valleys at energy points 7.1 ± 0.3 and $9.30 \rightarrow 11.33 \text{ eV}$ in the spectra, but the spectra of A3 reach more negative value. It explains that in A3 system electrons are rather more free when compared to A1 and A2, respectively. The spectra of $\varepsilon_1(\omega)$ for the doped systems along x -axis/ z -axis direction reveals greater anisotropy. Due to the smearing of bands, a Drude term is applied to the spectra (IR region, which comes from the interband transitions) in doped systems. Therefore, we find sharp valleys in the IR region at $0.1/0.2 \text{ eV}$ (A1,A3) and there is one other small valley at 1.0 eV for A3 system which is attributed to more smearing of bands. Comparatively, there is a shift of 0.25 eV in the spectra of $\varepsilon_1(\omega)$ in A3 toward lower energy i.e. the maximum peaks along z -axis are lying at 4.01 eV (A1), 3.87 eV (A2) and 3.76 eV (A3), respectively. For the $\varepsilon_1(\omega)$ in A1, A2 and A3 along z -axis, there are two deeper valleys in the spectra appearing at $6.27 \pm 0.08 \text{ eV}$ and $11.52 \pm 0.14 \text{ eV}$, respectively. The physics behind these valleys can be discussed later in this article in correlation with the electron energy loss function.

Owing to the different optical properties, we further investigate the electron energy loss (EEL) function ($L(\omega)$) for pristine and Ti-doped $\text{Nb}_3\text{O}_7(\text{OH})$, which describes the energy loss of electron traversing through the material. Figs. 6.5(a,

b) presents the calculated EEL spectra of $\text{Nb}_3\text{O}_7(\text{OH})$ as a function of energy. The calculated electron energy loss spectra along x -axis and z -axis indicate considerable anisotropy (see Figs. 6.5(a, b)). The experimental EELS measured using FEI Titan themis microscope is compared with the calculated spectra of the entire systems. The EELS of all systems A1, A2 and A3 provide a deep insight into the electronic structure and structural behavior of these compounds. The peaks in EELS appear due to the plasmon resonance. The $L(\omega)$ has a direct relation with $\varepsilon_1(\omega)$ i.e. at the energy points, where $\varepsilon_1(\omega)$ is equal to zero, plasma frequency is produced. The second reason of plasma frequency production can also be explained from the valleys in $\varepsilon_1(\omega)$, where the VB electrons behave like free particle and as a result produce plasma frequency. Fig. 6.5a shows greater energy loss for A3 as compared other systems (A1, A2), because it is deeper in valleys (see Fig. 6.4b). It means that in these energy points A3 has more free electrons in the VB with respect to energy and even shows the lowest absorption in the $\varepsilon_2(\omega)$. These plasma frequencies further impact of the spectra as plasmon resonance. From the qualitative peak to peak comparison between experimentally measured data and theoretically calculated data can be described as: the peaks in the experimental spectra are located around 5.7 eV 6.8 eV, 12.12 eV and 14.5 eV for the entire A1, A2 and A3 systems, while the peaks in the theoretical spectra are positioned at 5.31 eV, 7.1 eV, 12.12 eV and 14.4 eV for all samples, respectively, with a small difference of $\sim\pm 0.11$ eV among them. Thus, the agreement between Exp. and Theo. data shows that the experimentally measured spectra was nicely reproduced. In contrast to x -axis, the energy loss function of all systems along z -axis behaves differently because A3 shows less loss than A2, which shows less loss than A1. At the energy points around 7.0 eV and 12.0 eV, A3 exhibits photoabsorption a little higher than other systems. Doped-systems also expose some extra peaks due to zero loss corresponds to smearing of bands.

6.3.5 Spectroscopic properties

X-rays absorption module in the WIEN2k code is an efficient tool, to simulate the energy loss near edge fine structure of Nb-M₃ and O-K edges. These calculations were done to find better local surrounding of the Ti atom in $\text{Nb}_3\text{O}_7(\text{OH})$. The calculations are based on independent particle approach which is efficient to expose many body effects using Fermi's golden rule. Our findings on the WIEN2k calculations on the Nb-M₃ edge are displayed in Fig. 6.6 along with the experimental spectra, for the systems A1, A2 and A3, which describe the chemical states of Nb in $\text{Ti}:\text{Nb}_3\text{O}_7(\text{OH})$. Here we took only Nb-M₃ edge structure because both Nb-M_{2,3}, constructing from the spin orbit splitting of states, have the same spectral features. The ELNES of M₃ edge of Nb atoms are described by one white line and a shoulder. These results declare the signature of allowed atomic transitions from $4d^45p^6$ to $4d^52p^5$ orbitals. These peaks observed in $\text{Nb}_3\text{O}_7(\text{OH})$ and $\text{Ti}:\text{Nb}_3\text{O}_7(\text{OH})$ can be characterized by

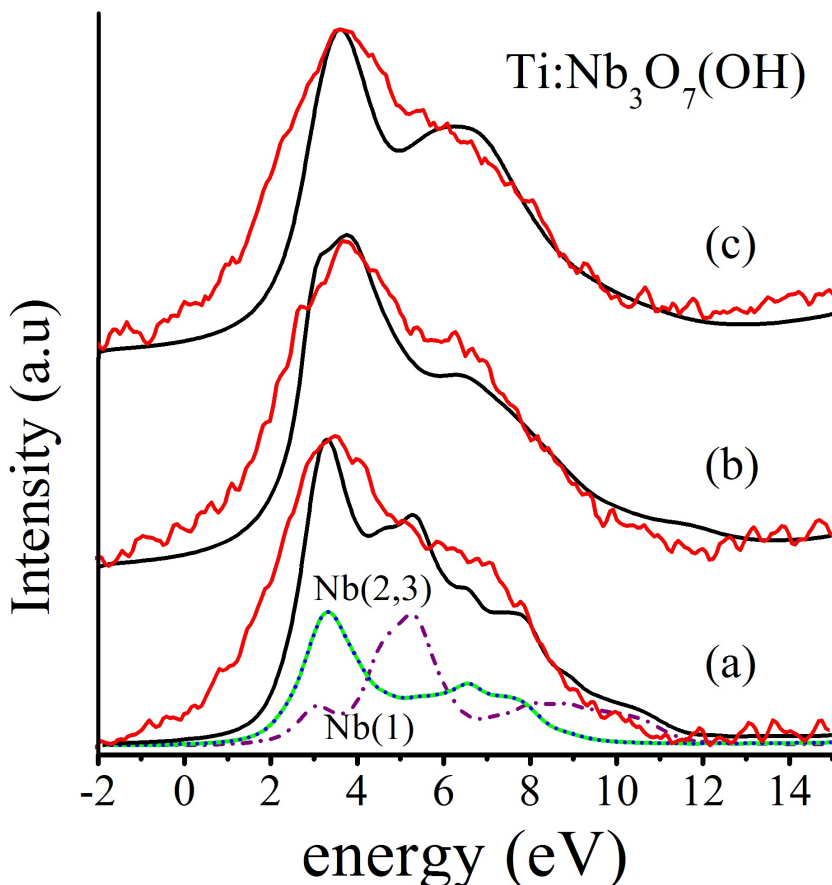


Figure 6.6: Calculated Nb-M₃ edges of Nb₃O₇(OH) and Ti:Nb₃O₇(OH) (Ti= 4.16 % and 8.32 %) along with the experimental data. (a) Different Nb atoms contribution to the spectra is also been shown. Schematic spectra of Nb-M₃ edges of the corresponding Ti concentrations along with the exp. data are also shown in b and c. The Black and red are designated to the calc. and exp. data of the Nb₃O₇(OH) and Ti:Nb₃O₇(OH), respectively.

the transitions from $5p \rightarrow 4d$, while the s character transitions are also present. Comparatively, $p \rightarrow s$ transition is much less intensive than $5p \rightarrow 4d$. The M₃ edge structures produced from the transition from $5p_{1/2} \rightarrow 4d_{3/2}$ range in the binding energy from -2 to 14 eV. In addition to the white line, the shoulder demonstrates the presence of pentavalent niobium element, while the increase in the shoulder at sample A3 suggests that the Ti contents in the octahedra of Nb₃O₇(OH). Regarding the atom specific contribution to the spectra of Nb-M₃, the white line is mainly contributed by the Nb(2) and Nb(3) (appearing at the corner sharing of octahedra in the crystal structure) and the shoulder is constructed by Nb(1) (positioned at the edge sharing octahedra). Both experimental and theoretical spectra have very nice agreement in shape with each other.

Fig. 6.7 presents theoretical study on near edge fine structure at O-K edge in

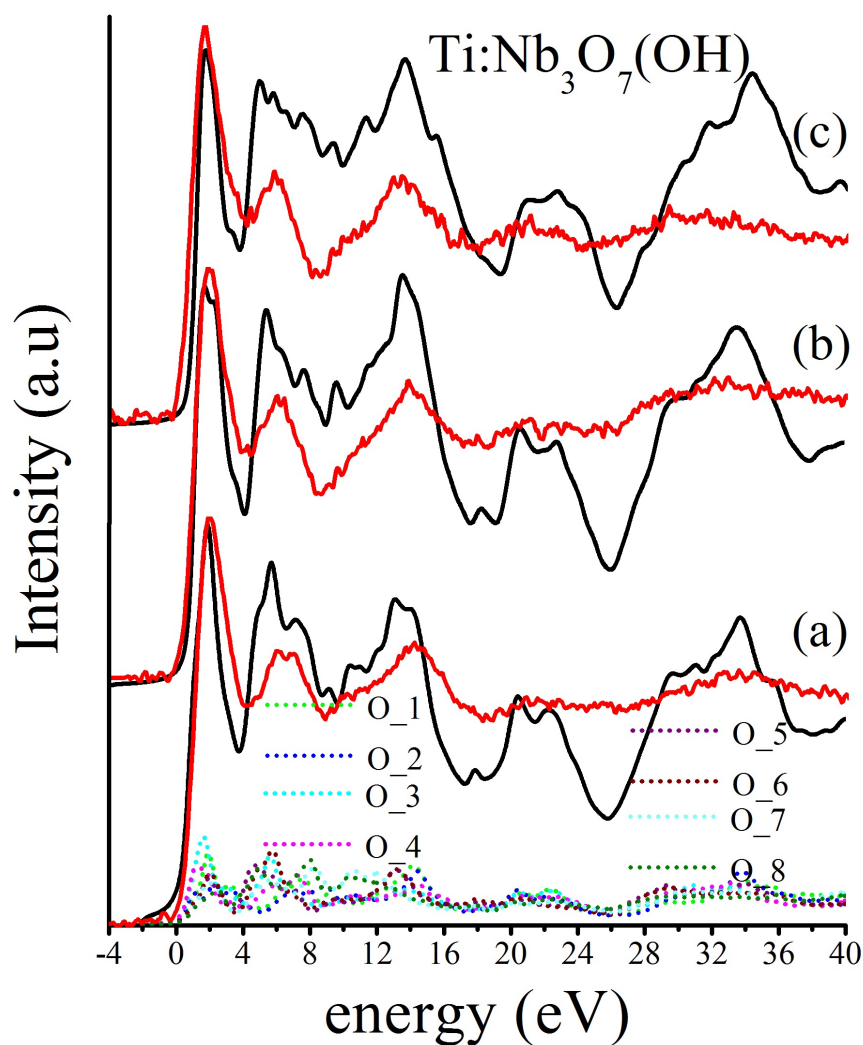


Figure 6.7: Calculated O–K edges of Nb₃O₇(OH) and Ti:Nb₃O₇(OH) (Ti= 4.16 % and 8.32 %) along with the experimental data. In (a), the calculated spectra constructed by different O atoms positioned at various lattice sites in the crystal structures. Fig b and c show the O–K edges of the corresponding Ti Nb₃O₇(OH) along with the exp. data. The Black and red are designated to the calc. and exp. data of the Nb₃O₇(OH) and Ti:Nb₃O₇(OH), respectively.

Ti:Nb₃O₇(OH) (A1, A2 and A3) along with the experimental data. The O–K edge is attributed to the allowed dipole transitions from $1s$ to p character of the states. The ELNES of the O–K edges for the pristine and Ti-doped Nb₃O₇(OH) were performed under WIEN2k code. The O–K edge near edge fine structure in Nb₃O₇(OH) and Ti:Nb₃O₇(OH) contains three main peaks in both theoretical and experimental spectra. Both experimental and theoretical O–K edges for the entire samples have the same features in shape. The quantitative difference between both experiment and theoretical spectra is due to the energy resolution limit (Exp.) and energy broadening limit (cal.). Different inequivalent O atoms in the crystal structures contribute to different peaks in the spectra. Therefore, for each case (A1, A2 and A3), we performed eight supercell calculations for each inequivalent O atoms. The contribution of each inequivalent O atom to each individual spectra for system A1 has been studied in detail in the previous study. The entire spectra of O K-edge for Nb₃O₇(OH) and Ti-doped Nb₃O₇(OH) were obtained as a weighted superposition of the mentioned O atoms. In comparison, there is no significant difference in the entire spectra of all samples (A1, A2 and A3), except some increment of small extra peaks at higher concentration of Ti in the Nb₃O₇(OH). These changes indicate the presence of TiO₆ octahedra in the doped samples.

Finally, we came to know that there is no significant difference into the ELNES of Nb–M₃ edge and O–K edge due to the substitution of Ti into the crystal structure of Nb₃O₇(OH) at different lattice sites.

6.4 Conclusion

In this study, we have focused on a series of Ti-doped Nb₃O₇(OH) photocatalytic materials with different concentrations of Ti (0–8%). We studied the structural, optoelectronic and spectroscopic properties of pure and doped Nb₃O₇(OH) using the TB–mBJ approach. The formation energy studies reveal that the Ti atom replaces the Nb atom in the lattice site of the crystal structure of host systems Nb₃O₇(OH). Calculated bond lengths expose that Ti incorporation in Nb₃O₇(OH) enhanced distances along z -axis and reduced them along x/y -axis and found same experimental trend about the crystallographic directions. The electronic structures of pure and doped Nb₃O₇(OH) with Ti contents revealed that the smearing of bands dedicated to the concentrations of Ti. Main peak in $\varepsilon_2(\omega)$ for the entire systems (A1, A2 and A3) demonstrated that it is constructed by the transitions of O– $2p^6$ states to Nb– $4d^4$ states with the coupling of Ti– $3d^2$ states. As the concentration of Ti increases, an increase in the intensity of optical spectra is observed. This is consistent with the calculated atomic resolved density of states of Nb₃O₇(OH) and Ti:Nb₃O₇(OH).

In the accord with our previous results from the WIEN2k code, the findings presented in this article suggest that Ti content has very small effect on the the EELS and O–K and Nb–M₃ edges spectra. This can be addressed in such a way that Ti

atoms do not change the structure of $\text{Nb}_3\text{O}_7(\text{OH})$ crystal within the doping limit (0–8%). Thus EELS and O–K and M_3 edges (including core hole effect for edges) for the entire systems were nicely produced and compared with the experimental spectra. High photoabsorption of the higher doped $\text{Nb}_3\text{O}_7(\text{OH})$ describes an enhancement in the photocatalytic activity.

Bibliography

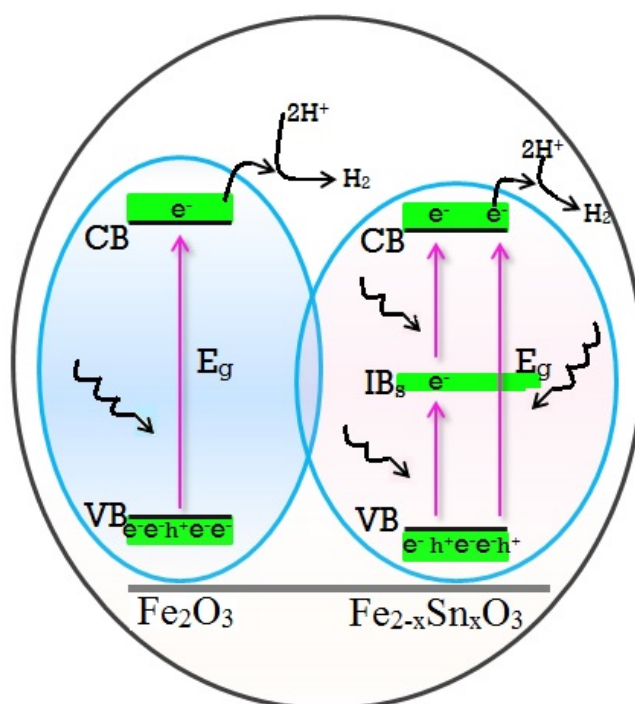
- [1] T. A. White, J. D. Knoll, S. M. Arachchige and K. J. Brewer *Materials*, 5, 27, (2012).
- [2] C. Chowdhury, S. Karmakar, and A. Datta. *J. Phys. Chem. C*, 121, 7615, (2017).
- [3] A. Fujishima, K. Honda, *Nature*, 238, 37, (1972).
- [4] J. R. Swierk, N. S. McCool, T. E. Mallouk, *J. Phys. Chem. C*, 119, 13858, (2015).
- [5] J. R. Swierk, N. S. McCool, C. T. Nemes, T. E. Mallouk, C. A. Schmuttenmaer, *J. Phys. Chem. C*, 120, 5940, (2016).
- [6] X. Fan, Z. Chu, F. Wang, C. Zhang, L. Chen, Y. Tang, D. Zou, *Adv. Mater.*, 20, 592, (2008).
- [7] F. Huang, D. Chen, L. Cao, R. A. Caruso, Y.-B. Cheng, *Energy Environ. Sci.*, 4, 2803, (2011).
- [8] I. E. Wachs, S. P. Phivilay, C. A. Roberts, *ACS Catal.*, 3, 2606, (2013).
- [9] L. Jing, W. Zhou, G. Tian, H. Fu, *Chem. Soc. Rev.*, 42, 9509, (2013).
- [10] S. Xie, Y. Wang, Q. Zhang, W. Fan, W. Deng, Y. Wang, *Chem. Commun.*, 49, 2451, (2013).
- [11] J. Wu, J. Wang, H. Li and D. Xue, *Thin Solid Films*, 544, 545, (2013).
- [12] H. Zhang, Y. Wang, D. Yang, Y. Li, H. Liu, P. Liu, B. J. Wood, H. Zhao, *Adv. Mater.*, 24, 1598, (2012).
- [13] S. B. Betzler, A. Wisnet, B. Breitbach, C. Mitterbauer, J. Weickert, L. Schmidt-Mended and C. Scheu *J. Mater. Chem. A*, 2, 12005, (2014).
- [14] P. Hu, D. Hou, Y. Wen, B. Shan, C. Chen, Y. Huang, X. Hu, *Nanoscale*. 77, 1963, (2015).
- [15] W. Khan, S. B. Betzler, O. Sipr, J. Ciston, P. Blaha, C. Scheu, and J. Minar *J. Phys. Chem. C*, 120, 23329, (2016).

-
- [16] P. Blaha, Schwarz, K.; Madsen, G.; Kvasnicka, D.; Luitz, J. WIEN2k: An Augmented Plane Wave plus Local Orbitals Program for Calculating Crystal Properties; Techn. Universitat Wien: Vienna, 2001.
- [17] F. Tran, Blaha, P. Accurate Band Gaps of Semiconductors and Insulators with a Semilocal Exchange-Correlation Potential. *Phys. Rev. Lett.*, 102, 226401, (2009).
- [18] J. P. Perdew, Burke, K.; Ernzerhof, M. Generalized Gradient Approximation Made Simple. *Phys. Rev. Lett.*, 77, 3865, (1996).
- [19] J. P. Perdew, Wang, Y. *Phys. Rev. B: Condens. Matter Mater. Phys.*, 45, 13244, (1992).
- [20] E. Engel, Vosko, S. H. *Phys. Rev. B: Condens. Matter Mater. Phys.*, 47, 13164, (1993).
- [21] C. Ambrosch-Draxl, Sofo, J. O. Linear Optical Properties of Solids within the Full-Potential Linearized Augmented Planewave Method. *Comput. Phys. Commun.*, 175, 1–14, (2006).
- [22] S. B. Betzler, F. Podjaski, K. Bader, M. Beetz, K. Hengge, A. Wisnet, M. Handloser, A. Hartschuh, B. V. Lotsch, and C. Scheu, *Chem. Mater.*, 28, 7666, (2016).
- [23] Y. Wang, R. Zhang, J. Li, L. Li and S. Lin *Nanoscale Research Letters*, 9, 46, (2014).

Chapter 7

Theoretical analysis of an Intermediate Band in Sn-doped Hematite with Wide-spectrum Solar Response

This chapter is based on a manuscript by Wilayat Khan, Christina Scheu, Ondřej Šipr and Ján Minár, which is to be submitted. In this chapter, we did the electronic structure, magnetic and optical properties calculations.



7.1 Introduction

Hematite (α -Fe₂O₃) is the most abundant and particularly the most attractive material for the photoelectrochemical (PEC) water splitting process on Earth. It can absorb solar light in the visible regime greater than its band gap (~ 2.2 eV) and hence report maximum efficiency of 12.9 % (theoretical) via harvesting of light [1]. Moreover, the photocatalytic efficiency of Fe₂O₃ extends to 40 % [2], because of its nontoxicity, low cost and stability under photocorrosion. In spite of these advantages, Fe₂O₃ offers very low conduction and a rapid recombination rate [3]. In order to improve the performance of Fe₂O₃ i.e. to enhance electrical conduction, different methods have been reported on the structure morphology that facilitates the dispersion of holes [3, 4]. Furthermore, many group IV elements are successfully doped in Fe₂O₃, resulting in an improvement in photocatalytic activity. Experimentally, it has been reported that Si and Sn are effective n-type dopants, enhancing the photocatalytic application of Fe₂O₃ [5, 6, 7].

In this regard, many theoretical calculations have been performed on the improvement of opto-electronic properties of Fe₂O₃ photoanode due to the doping of group IV elements. Electronic transport properties of Fe₂O₃ based on the incorporation of Ti, Zr, Si and Ge elements were simulated using cluster models at the level of Hartree-Fock [29]. The incorporation of these elements results in greater carrier concentration as well as carrier mobility. Finally, Ling et al., [9] prepared Sn-doping Fe₂O₃ nanostructures materials and confirmed its highly photocurrent density than other doping via characterizing by PEC and ultrafast laser spectroscopies. Hence, the knowledge of enhanced photocurrent density in Sn-doped Fe₂O₃ is not only responsible for exploring the photocatalytic activity but also is a step towards the development of novel photocatalytic materials.

At the same time, both theoretical as well as experimental studies on the analysis of the electronic structure of doped hematite have been reported in different articles [10, 11, 12, 13, 14]. However, in spite of our extensive, recent analyses on the hematite, it should be noticed that the intermediate band (I.B) in the electronic structure of Sn-doped Fe₂O₃ has not been reported in the previous work. The introduction of I.B's is the key feature of the solar cell materials that is able to absorb low energy photon to excite an electron from VB to I.B and then to CB. The main aim behind I.B's is that it produces extra excitons and hence enhances the photocurrent density lead high output quantum efficiency, with increase of output voltage of solar cells. Luque et al. [15] reported $\sim 63.2\%$ theoretical efficiency of a solar cell based on I.B. For I.B need to be efficient, it acquires some requirements: (1) small dispersion and (2) not to be discrete; while at the meantime, it should be narrow and is lying in between valence/conduction band. Unlike to natural photosynthesis, the notion of I.B allows a system to perform optical excitation by the absorption of two photons in the low energy scale (absorbed in the same system).

Linares et al., [16] introduced the notion of I.B for the first time in the quantum dots. Proceeding to this, many I.B materials have been proposed by the substitutional incorporation of proper amount of transition metals into semiconductors like Ti interstitial doped Si and N-doped Ga(As,P). Many experimental predictions have been placed about the structural properties by introducing Sn atom into the hematite along with a short theoretical description on the density of states (DOS), but direct theoretical evidence of the detail study on optoelectronic properties is still not available. In this article, several various concentrations of Sn were introduced into pristine Fe_2O_3 to greatly enhance the photocatalytic application. Interestingly, here in we introduce the concept of intermediate band for the first time in $\text{Fe}_{2-x}\text{Sn}_x\text{O}_3$ ($x=0\%$, 8% , and 12%), Sn-doping to enhance the photocurrent. Pristine and Sn-doped Fe_2O_3 nanostructures were studied by full potential linearized augmented plane wave (FP-LAPW) implemented in WIEN2k with density functional theory (DFT). We begin with the structure of $\alpha\text{-Fe}_2\text{O}_3$ having Fe atoms configuration $[(\uparrow\downarrow\uparrow)]$ that has minimum ground state energy and maximum energy band gap under spin polarized generalized gradient (GGA) function. Other properties like electronic structure and optical properties of $\alpha\text{-Fe}_2\text{O}_3$ and $\text{Fe}_{2-x}\text{Sn}_x\text{O}_3$ ($x=8\%$, and 12%) were studied using GGA+U approach. By electronic structure we obtained remarkably smaller band gap of 0.66 eV for 12% Sn and also introduce an I.B. By optical properties we found an enhancement in its optical performance that extended to infrared regime.

7.2 Theoretical details

We performed spin polarized calculations on pristine $\alpha\text{-Fe}_2\text{O}_3$ and $\text{Fe}_{2-x}\text{Sn}_x\text{O}_3$ ($x=8\%$ and 12%) with the full potential linearized augmented plane (FP-LAPW) method as employed in the WIEN2k package [28] within density functional theory (DFT) [18, 19, 20]. This methodology considers all electrons (core, semi-core and valence electrons), which freely participate in the spectroscopic properties, chemical bonding and optoelectronic properties. Plane wave cut-off or energy cut-off up to 7.0 was used to extend the electronic states that allow the convergence of energy to 0.00001 Ryd and $6\times 6\times 4$ Monkhorst-Pack [21] mesh of k-points was used to describe the reciprocal space for pristine and Sn-doped hematite. The iron (Fe) $4s$, $3p$ and $3d$ electrons, the oxygen (O) $2s$ and $2p$ electrons and the tin (Sn) $5s$, $5p$ and $4d$ electrons were deal as valence electrons.

The local density approximation (LDA) with the Ceperley Alder (CA) [22] exchange correlation potential and generalized gradient functional (GGA) [23] were used for the treatment of exchange correlation energy. A DFT with on-site Hubbard interaction (DFT+U) [24] was applied to Fe- d orbitals (highly localized state) to accurately assess the optical properties of doped highly correlated materials, particularly the band gap from the electronic structure. It can be seen that a plane DFT

cannot describe exactly the strong on-site Coulomb interaction of the corresponding orbitals. The values of U parameter in regard to DFT+U have been extensively described in the literature as dependent on the functionals used, but here in this study, we performed a series of scf-calculations for U=2–5 eV. The band gap values are: 0.925 eV (U=2 eV), 1.312 eV (U=3 eV), 1.675 eV (U=4 eV) and 2.17 eV (U=5 eV), respectively. From these findings we found that the effective U value applied to 3d localized orbitals of Fe is 5.0 eV. We clarified this value of U by the predicted band gap of O-2p and Fe-3d orbitals is 2.17 eV for GGA+U calculations, which has a nice concurrence with the experimental data and suit our purpose well.

We make a 2×2×1 supercell along the crystallographic directions (*x*, *y* and *z*-axis), and used the experimentally deduced lattice parameters of pristine α -Fe₂O₃ with rhombohedral symmetry in our calculations. We substituted a Sn atom that had acquired the 4+ ionization state as dopant element at the site of Fe atom (3+ ionization state) in this structure. All structures are optimized to get the stable position for each individual atom using generalized gradient functional (GGA) [23]. The concentration of Sn atoms was approximately equal to 8 % and 12%, respectively. Our calculations are based on antiferromagnetic spin configuration to achieve the accurate magnetic ground state.

As discussed, we had two different concentrations of Sn doping in hematite. For 8 % doping we adjust the Sn substitution at the lattice of Fe in such a way that one Sn lies in the spin up layer and the second atom in the spin down layer. Consequently, we get the total spin magnetic moment $\mu_s \sim 0$. In contrast, 12 % of Sn in hematite shows a total spin magnetic moment value corresponding to the value of the missing Fe atom. This is due to the enlarged μ_s at the sites where the entire spin donated by Fe atoms in the spin up or down layers depend on the Sn substitution. For the prevention of this large value of μ_s formation between the Sn doped Fe layers and undoped Fe layers, we followed our modeling (12 % doped Sn) as: (1) first we substituted two Fe atoms by Sn atoms in the up spin layers and one Fe atom by Sn atom in down layer and (2) then we reversed the same order/number of substitutions of the Sn atom in the Fe layers. Finally, we performed the calculations for both cases. The calculated total spin density arises from the doped Sn at different layer (Up/Down) in their respective antiferromagnetic Sn: Fe₂O₃ were statistically averaged to obtain zero spin density of states. Subsequently, the calculated results; μ_{tot} and optoelectronic properties for the corresponding doping profile were also statistically averaged.

7.3 Results and Discussion

7.3.1 Structural Properties

As the unit cell of pristine α -Fe₂O₃ [25] has four Fe atoms and six O atoms, we begin our calculations with the configuration ($\uparrow\downarrow\downarrow\uparrow$) which has the lowest total energy as illustrated in Fig. 7.1. The symbols \uparrow and \downarrow are used for spin up and spin down (Sandratskii et. al., [25] uses the symbols of + and -). It means that the two Fe atoms with spin up have opposite magnetic moment μ_B as compared to two Fe atoms with spin down, but have equal magnetic moment in magnitude. The findings obtained after the structure optimization of the unit cell using GGA functional are listed in Tab. 7.1.

Table 7.1: Results obtained for lattice parameters (a , c), volume (V_0) from calculations through the GGA method for α -Fe₂O₃. (in Å)

| Reference | a | c | c/a | V_0 |
|------------|-------|--------|-------|---------|
| Exp[26]. | 5.038 | 13.772 | 2.733 | 302.722 |
| This paper | 5.323 | 14.553 | 2.734 | 315.619 |

The antiferromagnetic behaviour of the α -Fe₂O₃ crystal structure along with the substitution of Sn at the different positions is illustrated in Fig. 7.1, where Fe atoms are coloured as royal blue. In order to know the effect of the Sn doping on the bond lengths, we presented a description of pristine and Sn-doped (substitutional) Fe₂O₃ structures from left to right (See Fig. 7.1). Following Fig. 7.1 Sn atom (dopant) is marked by magenta colour and the atoms (Fe/O) in the surrounding have royal blue/red colour, respectively.

We did the internal parameter optimization for the entire compounds using GGA functional and compared the calculated bond distances between Fe, O and Sn atoms. Herein, we compare the distances between Fe–O/Fe–Fe atoms (α -Fe₂O₃) with Sn–O and Fe–Sn atoms, respectively. These are exactly at the same positions in the crystal structure where Sn atom replaced the Fe atom. From the calculated data, it is clear that there is an increase in the bond lengths of Sn–O atoms than Fe and O atoms and the bond lengths tend to increase as a function of Sn content, resulting in a prominent distortion in the Fe layers. If $x=8$ %, there is an increase in bond lengths of 5.8 % (close to Sn) between Sn–O atoms, while there is a small increase in the bond lengths upto 1 % between Sn–Fe atom, respectively. The same trend we found in the bond lengths between Sn–Fe/O atoms i.e. the bond lengths between Sn–O atoms enhance upto 11.1 % and approximately the same displacement (10 %) in between Sn–Fe atoms. It is clear that one Sn⁺⁴ share three electrons with O

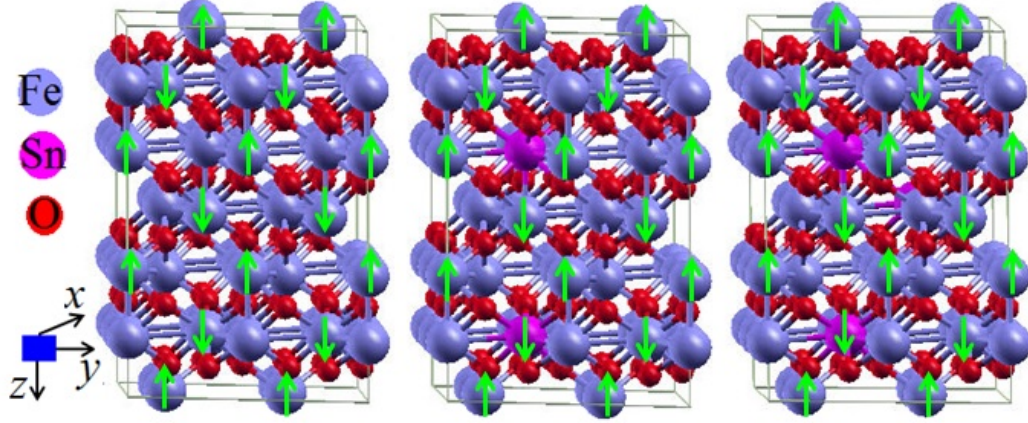


Figure 7.1: Schematic of of the unit cell of α - Fe_2O_3 with spin down Fe atoms and spin up Fe atoms, and Sn-doped with the same spin configuration, respectively.

atoms and one electron donate to Fe atom, [27] the bond length between Fe and O atom tends to increase due to the doping of Sn in all samples ($\text{Fe}_{2-x}\text{Sn}_x\text{O}_3$ ($x=0.0$, 8 % and 12 %)). One can see from these values of the bond lengths that Fe atoms show immediate interplay with O atoms.

7.3.2 Electronic structure

Figs. 7.2(a-c) presents the band structures of pristine α - Fe_2O_3 , $\text{Fe}_{1.92}\text{Sn}_{0.08}\text{O}_3$ and $\text{Fe}_{1.88}\text{Sn}_{0.12}\text{O}_3$, using GGA+U method. Here we review our results about the band gap character of α - Fe_2O_3 calculated at different functionals and compared with the literature findings. So, the band gap of α - Fe_2O_3 computed with LSDA (0.109 eV), GGA (0.33) and GGA+U (2.17 eV). After performing these calculations, it is clear that the gap value obtained through plan DFT is considerably smaller than the experimental gap. However, it is equal to the value obtained by Rollmann et. al., [13] using GGA with the projector augmented wave (PAW) within VASP code. While it is a bit smaller than the value of 0.51 eV (Punkkinen and co-workers) [28] using GGA in combination with the linear muffin-tin orbital (LMTO) method in atomic-sphere approximation (ASA) and value of 0.75 eV (Sandratskii et. al.,) [25] using LSDA with ASA method. The value of the band gap in our calculation (GGA+U) is very close to the experimental value of 2.20 eV [29].

So, we preferred the $U_{eff}=5.0$ eV on Fe- d orbitals for the electronic structure of pristine and Sn doped hematite to see the effect of Sn on the electronic structure and optoelectronic properties of α - Fe_2O_3 . From the simulated band structures, we understood that these findings are substantially dependent on the Sn-doped atoms and their concentration. In α - Fe_2O_3 , we found an indirect band gap of 2.17 eV similar to experimental value (2.20 eV) [29] at $U_{eff}=5.0$ eV. In Sn doped, the band structures are still indirect and the corresponding band gaps of 0.689

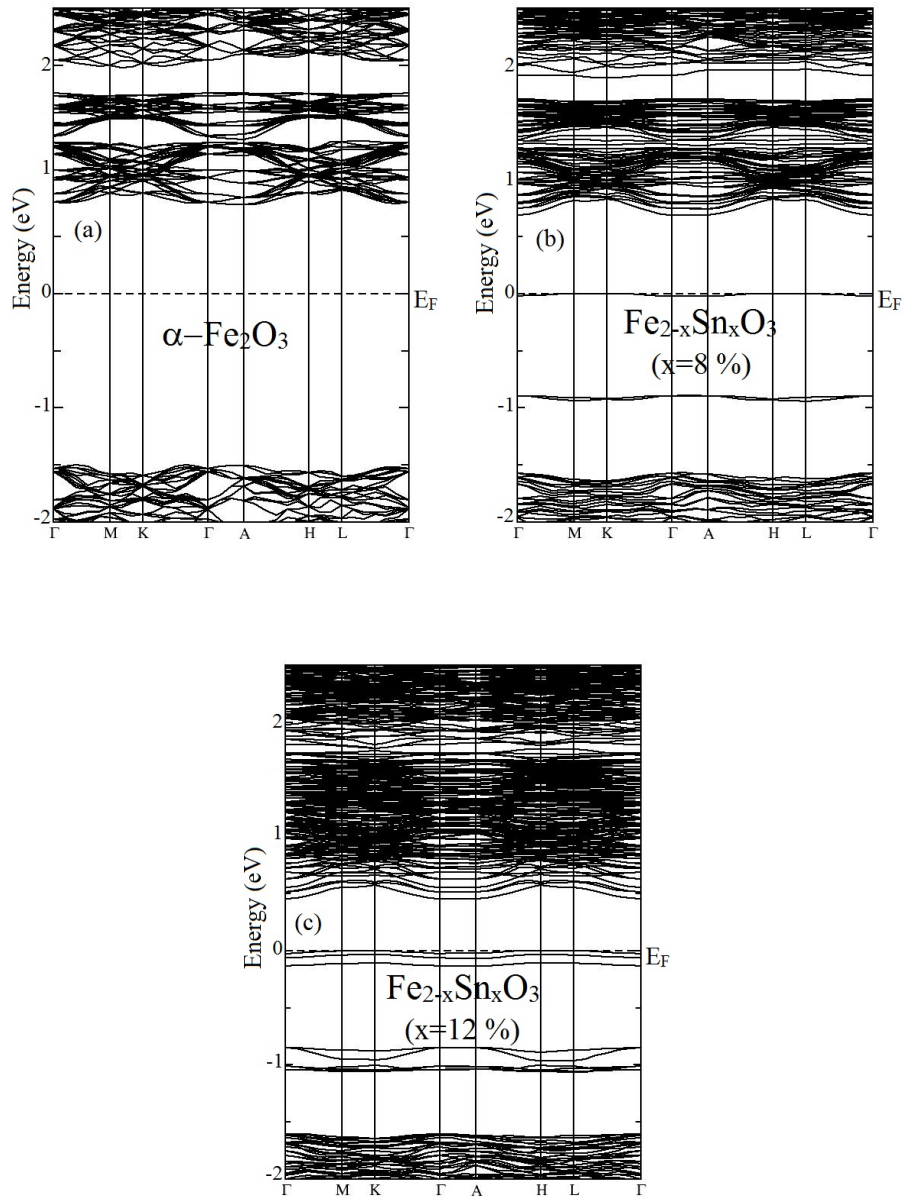


Figure 7.2: Band structures representation for $\alpha\text{-Fe}_2\text{O}_3$ and $\text{Fe}_{2-x}\text{Sn}_x\text{O}_3$ ($x = 8\%$ and 12%) under the GGA+U approach at $U_{eff} = 5.0$ eV.

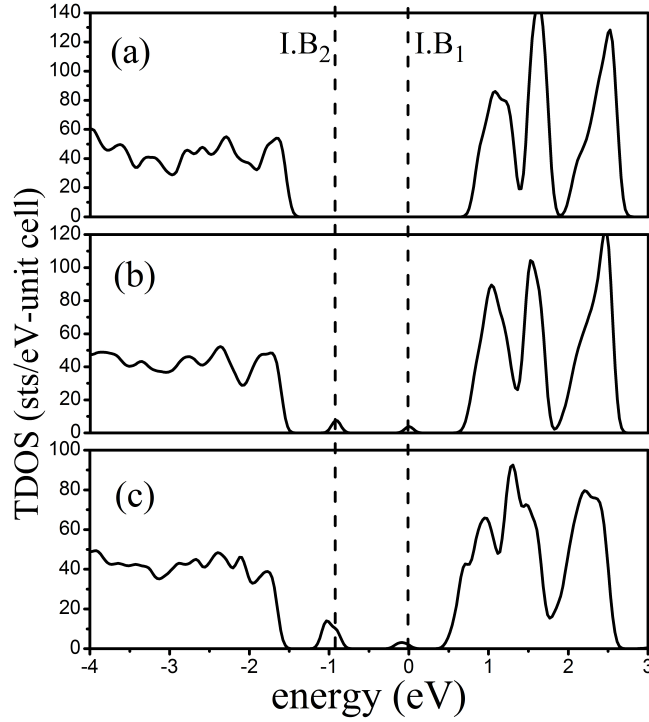


Figure 7.3: The calculated total density of states (TDOS) of α - Fe_2O_3 and $\text{Fe}_{2-x}\text{Sn}_x\text{O}_3$ ($x=8\%$ and 12%) under the GGA+U approach at $U_{eff}=5.0$ eV.

eV ($x=8\%$) and 0.66 eV ($x=12\%$), respectively. Those plots showed us that the U parameter influenced robustly the electronic spectra of the entire compounds. Following Fig. 7.2 we found three types of bands in valence band (VB) (1) Partially-filled intermediate bands (I.B₁) close to E_F , (2) filled intermediate bands (I.B₂) about a half-way between E_F and VBM, (3) band in the valence-band continuum which corresponds to bands in pristine hematite. The first two bands present an intermediate band constructed from Sn-4d/5s, Fe-3d and O-2p orbitals between VBM and CBM in Sn: Fe_2O_3 , which are compatible with the simulated density of states (DOS) mentioned in Figs. 7.3–6.

Band structures of dopant materials provide partially filled intermediate bands [30, 31] to expand the solar response to infrared region especially in case of Sn-doped hematite. The simulated electronic band structures indicate more flatness in $\text{Fe}_{2-x}\text{Sn}_x\text{O}_3$ with the increase in x . These flat bands are also used for the trapping of carriers. With respect to photocatalytic applications, Sn-doped hematite has interesting characteristics.

The total density of states (TDOS) and partial density of states (pDOS) of pristine and Sn-doped hematite were calculated using GGA+U ($U_{eff}=5.0$ eV). From the simulated DOS profiles (See Figs. 7.3–6), we came to know that these findings substantially depended on the Sn dope atoms and their concentration. A representative, band gap analysis was performed for the anti-ferromagnetic pristine

and Sn-doped hematite as exposed in Fig. 7.3. Starting with pristine hematite, one can see from Fig. 7.3a that the U parameter (on-site Coulomb interaction) breaks the covalency between $O-2p$ and $Fe-3d$ orbitals and move the $Fe-3d$ orbitals toward higher binding energies. There are some extra profile between VBM and CBM in the TDOS of Sn-doped Fe_2O_3 (in Figs. 7.3(b, c)). These profiles signature the contribution of the $Sn-5s$ and $Fe-3d/O-2p$ orbitals and contribute to $I.B_1$ and $I.B_2$, respectively. These profiles are discussed in detail with respect to atomic position of Fe atoms in angular momentum resolved density of states. The width of the I.B's is increased with Sn contents and reducing the insulation region.

The angular momentum resolved DOS are categorised into away Fe/O orbitals and close Fe/O orbitals (doped case) DOS from Sn atom compared to the Fe/O orbitals DOS of pristine hematite. The density of states (DOS) of Sn orbitals are plotted separately to see the effect/contribution of each individual Sn atoms (orbitals) to I.B's.

Figs. 7.4(a-c) illustrate the pDOS of $O-2p$ and $Fe-3d$ orbitals of pristine and doped hematite in the energy window (-4 to 3 eV), which is away from Sn atoms. In Fig. 7.4a, these are $Fe-3d$ and $O-2p$ orbitals pDOS in which both have the same profile and same contribution to the VBM and CBM as previously calculated data. In contrast to pristine hematite, the introduction of Sn onto the hematite structure (see Figs. 7.4(b, c) changes the story around the Fermi level. Accordingly, $x=8\%$ (b) produces the same profile for $Fe-3d/O-2p$ orbitals, but in $x=12\%$ (c), the width of the insulating region is reduced and introduce some extra texture of orbitals. This character of orbitals is not clear in the $x=8\%$ doping because these orbitals has negligibly small contribution. The peaks are the averaged profile of different Fe/O atoms, which is away from Sn atoms. The distances of Fe atoms from Sn atoms are varying from 4.0 Å to 6.0 Å and the distances of O atoms are varying from 3.78 Å to 6.09 Å in case of $x=8\%$. While, these distances are varying from 3.72 Å to 6.25 Å (for Fe atoms) and from 3.46 Å to 6.68 Å in case of $x=12\%$. It has been also confirmed that for all concentrations of Sn (8% and 12% in the hematite supercell), the I.B exist approximately at similar position between the VB and CB. It induces sub-band gaps between VB and CB; differ from the gap of the pristine hematite. At $x=12\%$, the $I.B_2$ is mainly contributed by the O atoms, while the spectral shape of $O-2p$ orbitals remain unchanged in all cases.

To check the influenced of the Fe/O atoms on the pDOS of doped hematite, which is closed to Sn atoms, we plotted the pDOS of $Fe-3d$ and $O-2p$ orbitals as illustrated in Figs. 7.5(a, b). These atoms are at a distance from Sn atoms varying from 2.68 Å to 3.59 Å (Fe atoms) and 2.09 Å to 2.14 Å (O atoms) in $x=8\%$, while they are varying from 2.84 Å and 3.59 Å (Fe atoms) and from 2.13 Å to 2.15 Å (O atoms) in case of $x=12\%$. Similar to $x=8\%$, we took the average profile of $Fe-3d/O-2p$ orbitals of the closest Fe and O atoms. As there are two intermediate bands ($I.B_1$ and $I.B_2$) need to analysis in term of these orbitals in different doping concentration.

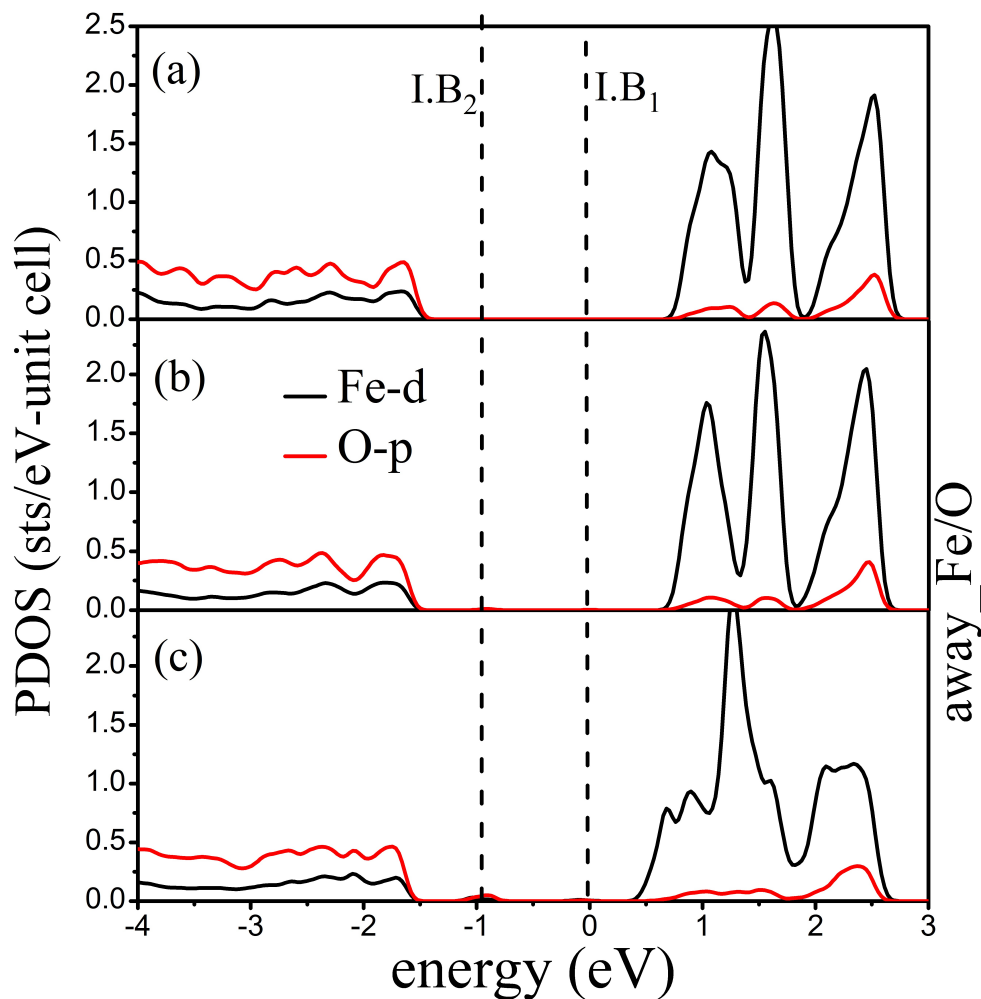


Figure 7.4: Averaged partial density of states (pDOS) images (a) α - Fe_2O_3 and in (b, c) $\text{Fe}_{2-x}\text{Sn}_x\text{O}_3$ ($x=8\%$, 12%) for those Fe atoms which are 4.0 \AA to 6.0 \AA ($x=8\%$)/ 3.72 \AA to 6.25 \AA ($x=12\%$) and for those O atoms which are 3.78 \AA to 6.25 \AA ($x=8\%$)/ 3.78 \AA to 6.6 \AA ($x=12\%$) away from Sn atoms. In (c), the pDOS of Fe- $3d$ orbitals show filled intermediate band at -0.8 eV under the GGA+U approach at $U_{eff}=5.0\text{ eV}$.

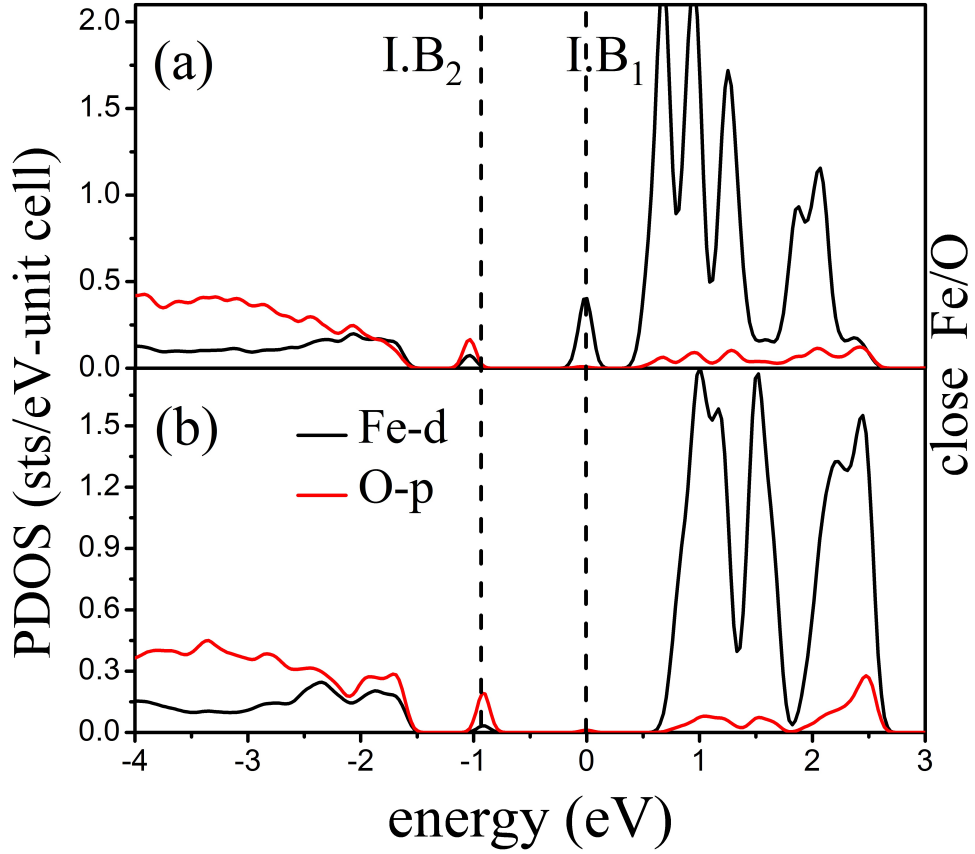


Figure 7.5: Averaged partial density of states (pDOS) images of (a, b) $\text{Fe}_{2-x}\text{Sn}_x\text{O}_3$ ($x=8\%$, 12%) for those Fe atoms which are 2.68 \AA to 3.59 \AA ($x=8\%$)/ 2.84 \AA to 3.59 \AA ($x=12\%$) and for those O atoms which are 2.09 \AA to 2.14 \AA ($x=8\%$)/ 2.13 \AA to 2.15 \AA ($x=12\%$) close to Sn atoms. In (a), the pDOS of Fe- $3d$ orbitals show partially filled intermediate band (I.B₁) and filled intermediate band (I.B₂) with O- $2p$ orbitals at -0.8 eV and in (b) O- $2p$ orbitals contribute to I.B₂ under the GGA+U approach at $U_{eff}=5.0\text{ eV}$.

Fig. 7.5b reveals that at lower concentration of Sn, the filled intermediate band is constructed by the O- $2p$ orbitals (0.29 sts/eV) with the minor contribution of Fe- $3d$ orbitals. While Fe- $3d$ /O- $2p$ orbitals have the same trend for I.B₂ as in $x=8\%$, but the partially filled I.B (I.B₁) is constructed from Fe- $3d$ orbitals (0.5 sts/eV). The increase in Sn concentrations (Fig. 7.5a) tend to move the occupied band to partially band which crosses the Fermi level and forms an I.B at the top of VB and also the conduction band edge is shifted down by 0.21 eV . Consequently, it reduces the band gap between VB and CB and enhances the width of sub-gaps between I.B and CB.

Now to introduce the pDOS of the main ingredient (Sn atom) which is responsible for the formation of the I.B's in hematite, which is presented in Fig. 7.6. Overall Sn atoms have quantitatively smaller contribution to the density of orbitals as compared to O/Fe atoms. Yet Sn has an important role in the topic of article. Both

intermediate bands (I.B₁, I.B₂) are constructed from the admixture of Sn-5s/5p/4d orbitals. Here we have two Sn atoms in the supercell of hematite ($x=8\%$), the I.B₁ crosses partially the E_F mainly constructed by Sn₂-4d orbitals (0.08 sts/eV) with the minor contribution of Sn₁-5s orbitals (0.00008 sts/eV) and the I.B₂ (filled one), around -0.8-1.0 eV, contributed by the Sn-4d orbitals (0.004 sts/eV), respectively. These can be visualized in the profile of Sn_{1,2}-5s/5p/4d orbitals, which is sketched in the left part of Figs. 7.6(a, b). Similar trend is also observed in Fe_{1.88}Sn_{0.12}O₃ with a slight difference as compared to Fe_{1.92}Sn_{0.08}O₃ as illustrated in the right part of Figs. 7.6(c-e). It can be explained as that the Sn₁-5s orbitals (0.00008 sts/eV) with small and same contribution of Sn₁-5p/4d orbitals (0.00002 sts/eV) to I.B₁, and Sn₁-4d orbitals contribute to I.B₂. Both I.B's are attributed by the same Sn₂-5p/4d orbitals. But Sn₃-5s/5p/Sn₃-5s (0.004 sts/eV) and Sn₃-5p orbitals constructed the partially filled intermediate band [32]. From the entire pDOS, one can notice that the *d* orbitals of Fe atoms and *p* orbitals of O atoms contributed mainly rather than the dopant atom (Sn) in Fe_{2-x}Sn_xO₃ construct an I.B. It is clarified from pDOS that the dopant (Sn) implies negligible effect on the band gap of the pristine compound. The partial DOS provides a clear evidence into the frontier of orbitals bonding behaviors, because here we deal with the intensity of orbitals in the given energy range.

Interestingly, our findings suggested that the I.B's around the E_F are partially filled featuring an enhancement in the efficiency of solar cell. The reason is that the probability of transitions from I.B's to CB is higher. To get the partially filled bands, it would be appreciated that we doped the hematite by *n*-type materials (e.g. Sn). At 8% (smallest concentrations), Sn introducing sub-gaps between partially filled I.B's and occupied band, due to addition of an extra electron to the unit cell. Larger Sn contents shift the occupied I.B's (at 0.8 eV in 8%) deeper into the VB and also the CB is shifted down towards the Fermi level. This large change of distances between partially occupied I.B at E_F and CBM or between the fully occupied I.B and VBM with doping and so on is in general possible in semiconductors.

7.3.3 Magnetic properties

To investigate the magnetic behaviour of Fe₂O₃, first we calculated magnetic moments for the corresponding anti-ferromagnetic configuration [(↑↓↑↑)] are 3.23 μ_B (LSDA), 3.49 μ_B (GGA) and 4.24 μ_B (GGA+U); at $U_{eff}=5.0$ eV), respectively. These values are about 1.64 μ_B , 1.10 μ_B , and 0.36 μ_B lower than the experimental value [25]. Then we doped Sn atoms and calculate the values of the magnetic moments that show a decrease in the magnetic moments of Fe atoms against Sn doping. These results indicate that each Sn atom has different interaction behavior and charge transfer respective to their positions. The numerical values of magnetic moments are 4.121 μ_B (Fe) in Fe₂O₃, 3.513 and 4.112-4.215 μ_B (Fe), 0.0142 μ_B (Sn)

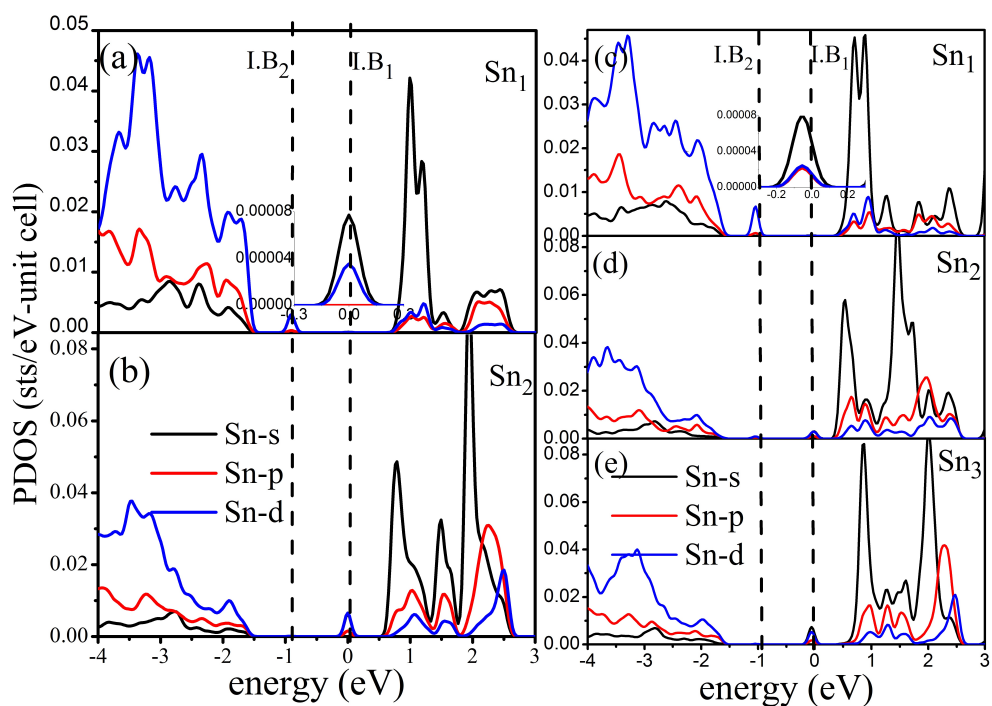


Figure 7.6: Partial density of states (pDOS) images of (a, b) $\text{Fe}_{2-x}\text{Sn}_x\text{O}_3$ ($x=8\%$) and (a, b, c) $\text{Fe}_{2-x}\text{Sn}_x\text{O}_3$ ($x=12\%$). Both shows the pDOS of Sn- $5s/5p/4d$ orbitals which contribute to the filled intermediate band (I.B₂) at -0.8 eV and partially filled intermediate band (I.B₁), under the GGA+U approach at $U_{eff}=5.0$ eV.

and 0.0266–0.0755 μ_B (O) in $\text{Fe}_{1.92}\text{Sn}_{0.08}\text{O}_3$, while the magnetic moment for Fe atoms varies from 3.515–3.99 and 4.11–4.124, 0.0138–0.0148 μ_B (Sn) and 0.0148–0.084 μ_B in $\text{Fe}_{1.88}\text{Sn}_{0.12}\text{O}_3$, respectively. These values suggest that the Fe atom is the origin of the entire magnetism and induces a negligible spin density in the Sn and O atoms. Overall, magnetism in each Fe atoms stems from the d orbitals. The decrease in the magnetic moments Fe atoms caused by the intra-atomic charge transfer within Sn and Fe/O atoms.

7.3.4 Optical properties

The linear optical properties for pristine and Sn-doped hematite achieve more interest in view of their high absorption of photon, giving rise to a high photocatalytic activity. Interestingly, in this paper, we predicted a strategy of intermediate band (I.B) in $\text{Fe}_{2-x}\text{Sn}_x\text{O}_3$ ($x=8\%$ and 12%) act as possible I.B material. The ability of I.B in a material as discussed in the band structure is to enhance effectively the efficiency of photovoltaics. In view of optical response, we will explain and compare the dielectric properties of these materials without and with I.B's prominent character in improving the ability of the desired compounds as photocatalyst.

Based on the calculated electronic structure, we are able to investigate the optical absorption in the infrared and visible region to obtain nice optoelectronic performance of Sn-doped hematite. Here, we mentioned the spectra of the pristine and $\text{Fe}_{2-x}\text{Sn}_x\text{O}_3$ only in the energy window 0.0–3.5eV, because our vision is to explore the optical response of the respective materials based on I.B's. We averaged both components, imaginary/real part ($\varepsilon_2/\varepsilon_1(\omega)$), of dielectric function, reflectivity and energy loss function for the entire compounds as presented in Figs. 7.7(a–d).

The optical spectra of the $\text{Fe}_{2-x}\text{Sn}_x\text{O}_3$ in the respective energy region are marked in different colours. It is also clear from the Fig. 7.7a that the presence of Sn^{+4} (four unpaired electron) cause an enormous shift in the absorption threshold and this deviation increases due to the presence of I.B simply enables some transitions which were not possible in pristine hematite. The $\varepsilon_2(\omega)$ spectra reveal \sim similar peaks at energy region from 2.8 eV and 3.25 eV for $\alpha\text{-Fe}_2\text{O}_3$ and $\text{Fe}_{2-x}\text{Sn}_x\text{O}_3$ ($x=8\%$ and 12%) (See Fig. 7.7a). But the first peak becomes smoother and shifted to higher energy in the doped hematite. Some extra peaks features in th infrared region from 0.5–2.2 eV for Sn-doped hematite ($\text{Fe}_{2-x}\text{Sn}_x\text{O}_3$) are also reported in this study, respectively, which can be correlated with the Sn contents in the hematite. Here, the maximum value of Sn ($x=12\%$) in $\text{Fe}_{2-x}\text{Sn}_x\text{O}_3$ shift the absorption edge to infrared region, which belongs to partially filled intermediate bands and is related to extra photon absorption. It describes that the inducing of Sn into hematite extend the light response to lower energy. Comparatively, the photocatalysis in $\alpha\text{-Fe}_2\text{O}_3$ is smaller than $\text{Fe}_{2-x}\text{Sn}_x\text{O}_3$ ($x=8\%$ and 12%) because $\alpha\text{-Fe}_2\text{O}_3$ absorb electromagnetic radiation greater than 2.2 eV to excite an electron from VB to

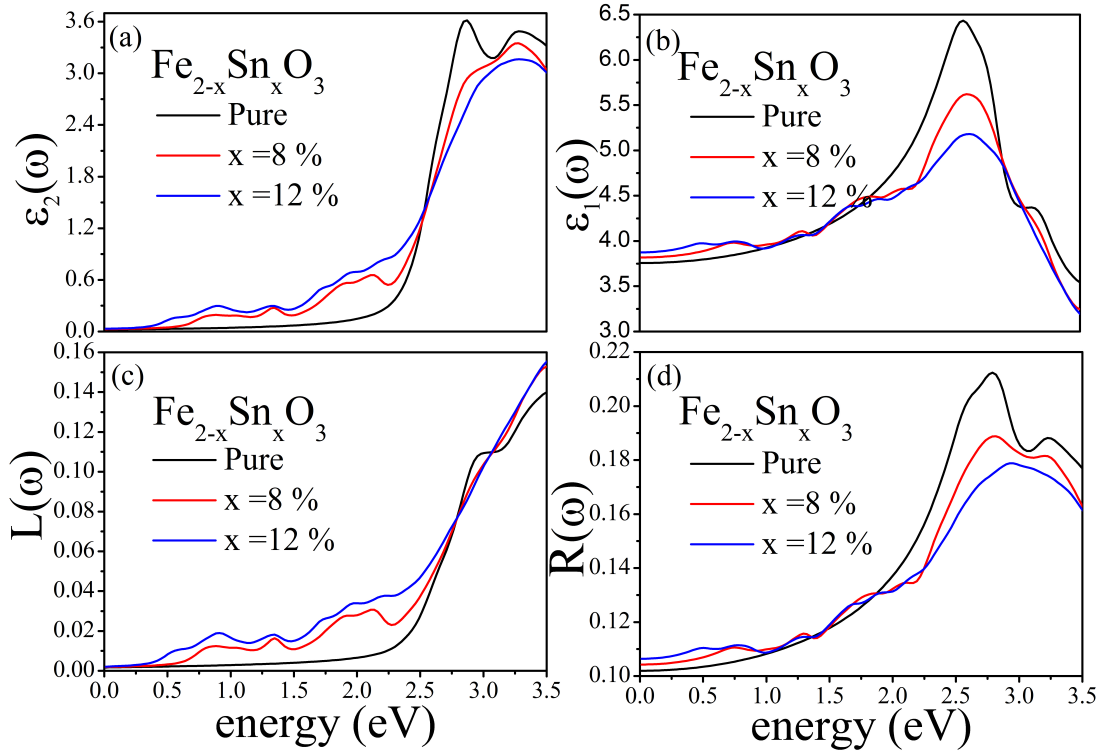


Figure 7.7: (a) Calculated optical spectra: (a) the imaginary and (b) the real part of dielectric function, (c) the electron energy loss function and (d) the reflectivity of α - Fe_2O_3 and $\text{Fe}_{2-x}\text{Sn}_x\text{O}_3$ ($x=8\%$ and 12%) in the energy window from 0.0 to 3.5 eV. The optical thresholds are compared to pure and different Sn concentration. The absorption edge of Fe_2O_3 with Sn-doped lies in IR region and maximum peaks related to the transition of I.B.

CB, while less exciton acquire less energy in $\text{Fe}_{2-x}\text{Sn}_x\text{O}_3$. The Sn doped hematite electronic structure features sub-gap that increases with the Sn contents. These sub-gaps are due to intermediate bands. They absorb more photons in such a way that one photon excites an electron from VB to intermediate band and second photon take it to CB from intermediate band.

The real part $\varepsilon_1(\omega)$ of dielectric function for pristine and Sn-doped Fe_2O_3 , showing the electronic polarizability, is plotted in Fig. 7.7b, based on the calculated electronic structures reported above (see Figs. 7.2–6). An inverse relationship has been reported in [33, 34] between ε_{elec} and E_g (band gap energy), whereas E_g has no effect ε_{ionic} . Here in the plot we see the ε_{tot} (comes from ε_{elec} and ε_{ionic}) in relation to E_g . Of more importance is the static value of $\varepsilon_1(\omega)$, which is 3.87 for $\text{Fe}_{2-x}\text{Sn}_x\text{O}_3$ ($x=12\%$) higher than the pristine and other Sn-doped compounds, and its origin can be seen in the imaginary spectra of the dielectric function. Similar to $\varepsilon_2(\omega)$, $\varepsilon_1(\omega)$ is also extended to IR regime in $\text{Fe}_{2-x}\text{Sn}_x\text{O}_3$ ($x=8\%$ and 12%) and shows maximum optical response in this region. The entire spectra in this energy range

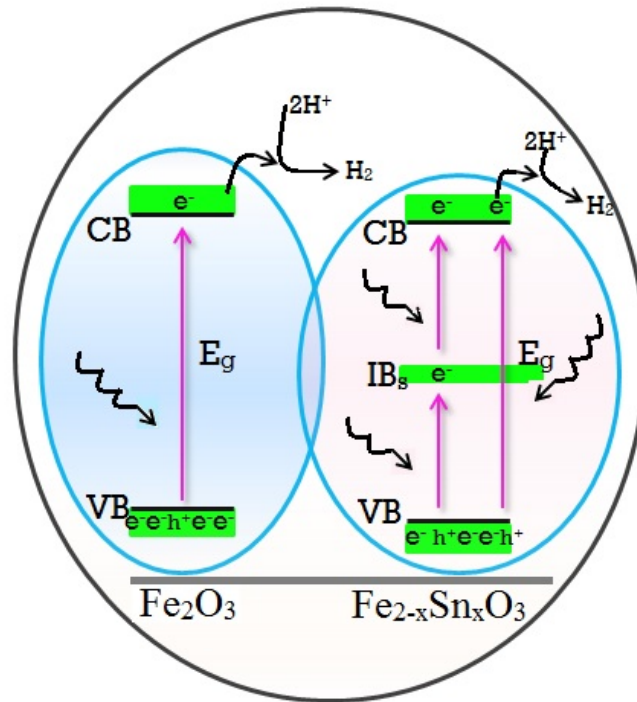


Figure 7.8: Visual representation of photocatalytic activity of α - Fe_2O_3 and $\text{Fe}_{2-x}\text{Sn}_x\text{O}_3$ in the UV region extended to Infrared region (left side) and on the right side the I.Bs photocatalysis of $\text{Fe}_{2-x}\text{Sn}_x\text{O}_3$.

(0.0–3.5 eV) are positive. The valley in $\varepsilon_1(\omega)$ corresponds to the first peak in the energy loss function demonstrated by plasmon resonance.

Figs. 7.7(c, d) show the energy loss function and reflectivity spectra of the series of hematite materials (pristine and Sn-doped) in the relative energy range of 0.0–3.5 eV to investigate the absorption characteristics of electromagnetic radiation. The reflectivity $R(\omega)$ and energy loss $L(\omega)$ spectra of the hematite are analyzed based on Sn concentration. There is a considerable variation between pristine and doped hematite that depends on the Sn concentration. The increase in the spectra of $L(\omega)$ can be attributed to the plasmon resonance because a structure modification occurred with substitutional doping in the hematite. However, the peaks extracted from calculated $L(\omega)$ spectra at 2.8 eV (pristine), 0.8 eV ($x=8\%$), and 0.6 eV ($x=12\%$) expose a similar optical profile as in $\varepsilon_2(\omega)$. Knowledge of the peak's positions of pristine and Sn-doped Fe_2O_3 obtained from the surface plasmon allows us to directly correlate it to $\varepsilon_1(\omega)$. In addition, the spectrum of 12% doping of Sn differs from other doping contents (Sn) due to more I.B's that provide a possible red shift in the peaks.

For further confirmation, the reflectivity $R(\omega)$ spectra are plotted in Fig. 7.7d. The $R(\omega)$ has minimal values (showing more transmittance) within the band gaps of the title compounds. The difference in the Sn concentration between Fe_2O_3 and $\text{Fe}_{2-x}\text{Sn}_x\text{O}_3$ causes the reflectivity to change producing desirable peaks on the

reflectivity spectra. The spectra of reflectivity at zero frequency show an increase due to Sn-contents in α -Fe₂O₃, and the same behavior is also noticed at higher reflectivity profiles. The characteristic peaks of the entire compound show that these materials exhibit high reflection. It should be remembered that both reflectivity and energy loss function are interrelated i.e. for maximum values of energy loss function, the $R(\omega)$ turns out to be minimal. Furthermore, the interrelationship between the calculated $L(\omega)$ and $R(\omega)$ spectra of pristine and Sn-doped hematite are called the mirror spectra of each other. In general, our investigation on the optical spectra of different parameters like $\varepsilon_2(\omega)$, $\varepsilon_1(\omega)$, $L(\omega)$ and $R(\omega)$ confirm optical shift from energy=2.38 eV (VIS region) to energy=0.4 eV (IR region), provides a new insight into the photocatalysis of hematite. Finally the analysis of our calculated findings confirmed that the photo-excitation in the infrared regime is attributed to the sub-band gaps absorption.

Further, to investigate the photocatalytic activity based on the above mentioned reason for α -Fe₂O₃ and Fe_{2-x}Sn_xO₃ ($x=8$ % and 12 %), which is attributed to the shift in the absorption edge from visible to infrared region as visualized in Fig. 7.8. Pristine α -Fe₂O₃ irradiated with energy greater than 2.17 eV evaluate very less hydrogen due to the excitation of electron to CB and left the hole in VB. The electronic structures of Fe₂O₃ and Fe_{2-x}Sn_xO₃ ($x=8$ % and 12 %) as shown in Figs. 7.2(a-c), indicate an obvious sub-band gaps compared to that of α -Fe₂O₃. The proposed photo-exciton separation model for pristine and Sn-doped Fe₂O₃ is illustrated in Fig. 7.8 that leads to improve the evaluation of H₂. As the band gap in 12 % Sn contents is narrower than Fe_{2-x}Sn_xO₃ ($x=8$ % and 12 %) as well as Fe₂O₃ absorbing higher energy and show superior photo-water splitting. Under the infrared light illumination, Fe_{1.88}Sn_{0.12}O₃ has suggested to have greater photocurrent density due to the influence of more intermediate band as compared Fe_{1.92}Sn_{0.08}O₃ and Fe₂O₃. Finally, the I.B enhances the photocurrent density under the illumination of light i.e. $VB+h\nu \rightarrow I.B's$ and $I.B's+h\nu \rightarrow CB$ and as a result improving remarkably the photocatalytic properties. It is known that Fe₂O₃ has the drawback of rapid recombination rate [35]. So for this reason, the compounds (Sn:Fe₂O₃) presented here have the I.B's lead as a model systems. However, these compounds enable us to obtain proper information about optoelectronic properties, which is based on I.B's, and also offering high photocurrent density.

7.4 Conclusion

The pristine and Sn-doped Hematite (Fe_{2-x}Sn_xO₃) have been shown to be efficient compounds for the water splitting process. The electronic properties of Fe_{2-x}Sn_xO₃ were calculated by full potential linearized augmented plane wave (FP-LAPW) method through DFT analysis. The electronic structures and density of states (DOS) of these compounds, reveal the insulating character, were performed un-

der the generalized gradient approximation plus Hubbard interaction (GGA+U), and the calculated band gap (2.17 eV) of the α -Fe₂O₃ ~similar to the experimental value. The calculated findings confirmed that the concentration of Sn⁺⁴ into the Fe₂O₃ (doped as substitution) leading to a decrease in the magnetic moments of Fe atoms, due to the intra-atomic charge transfer within Sn and Fe/O atoms. The calculated electronic band structures of pristine Fe₂O₃ (2.17 eV) and Fe_{2-x}Sn_xO₃ lead to a decrease in the band gaps (0.689 eV, 0.66 eV). The band structure calculations of Sn-doped hematite predicted partially filled intermediate band constructed from Fe-3*d*/Sn-4*d* orbitals with the minor contribution of Sn-5*s*/5*p* orbitals, which is also confirmed from the pDOS of the respective compound. A significant improvement has been highlighted in the imaginary part of the dielectric function extended to infrared from visible region due to this I.B. A schematic diagram was also plotted that shows an increase in the electrons excitation to conduction band under illumination of light in which Sn:Fe₂O₃ exposes a significant shift in the absorption of available light. We demonstrate theoretically that the pristine and Sn-doped hematite operating over a broad solar spectrum and our main vision of this study is to introduce the notion of I.B's in Fe_{2-x}Sn_xO₃ and extend it commercial applications.

Bibliography

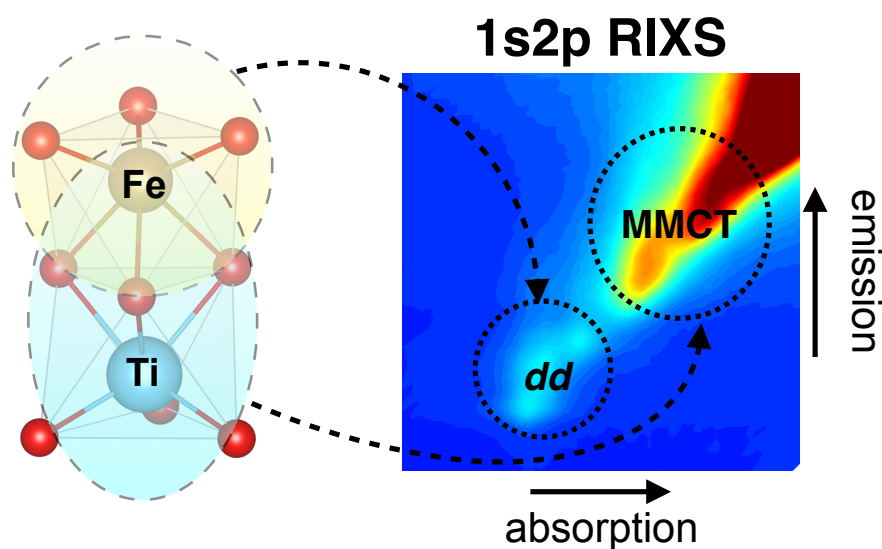
- [1] A. B. Murphy, P. R. F. Barnes, L. K. Randeniya, I. C. Plumb, I. E. Grey, M. D. Horne, and J. A. Glasscock, *Int. J. Hydrogen Energy*. 31, 1999, (2006).
- [2] X. Meng, G. Qin, W. A. Goddard, S. Li, H. Pan, X. Wen, Y. Qin, and L. Zuo, *J. Phys. Chem. C*. 117, 3779, (2013).
- [3] K. Sivula, F. Le Formal, and M. Gratzel, *Chem Sus Chem*. 04, 432, (2011).
- [4] C. X. Kronawitter, I. Zegkinoglou, S. H. Shen, P. Liao, I.S. Cho, O. Zandi, Y. S. Liu, K. Lashgari, G. Westin, J. H. Guo, et al., *Energy Environ. Sci.*, 07, 3100, (2014).
- [5] J. H. Kennedy, Menahem Anderman, and Ruth Shinar, *J. electrochem. Soc.:* 128, 2371, (1981).
- [6] N. T. Hahn and C. Buddie Mullins, *Chem. Mater*. 22, 6474, (2010).
- [7] M. Gaudon , N.Pailhe , J.Majimel,A.Wattiaux,J.Abel,A.Demourgues, *Journal of Solid State Chemistry*, 183 , 2101, (2010).
- [8] P. Liao, M. C. Toroker, E. A. Carter, *Nano Lett*. 11, 1775, (2011).
- [9] Y. C. Ling, G. M. Wang, D. A. Wheeler, J. Z. Zhang, Y. Li, *Nano Lett*. 11, 2119, (2011).
- [10] N. Iordanova, M. Dupuis, K. M. Rosso, *J. Chem. Phys*. 122, 144305, (2005).
- [11] X. Y. Meng, G. W. Qin, S. Li, X. H. Wen, Y. P. Ren, W. L. Pei, L. Zuo, *Appl. Phys. Lett*. 98, 112104, (2011).
- [12] M. N. Huda, A. Walsh, Y. F. Yan, S. H. Wei, M. M. A. Jassim, *J. Appl. Phys*. 107, 123712, (2010).
- [13] G. Rollmann, A. Rohrbach, P. Entel, J. Hafner, *Phys. Rev. B*. 69, 165107, (2004).
- [14] N. C. Wilson, S. P. Russo, *Phys. Rev. B*. 79, 094113, (2009).
- [15] A. Luque and A. Marti, *Phys. Rev. Lett*. 78, 5014, (1997).

- [16] I. Aguilera, Pablo Palacios, and P. Wahnou, *Phys. Rev. B.* 84, 115101, (2011).
- [17] P. Blaha, K. Schwarz, G. Madsen, D. Kvasnicka, and J. Luitz, WIEN2k: An Augmented Plane Wave plus Local Orbitals Program for Calculating Crystal Properties (Karlheinz Schwarz, Techn. Universitt Wien, Austria, 2001).
- [18] L. H. Thomas, *Proc. Cambridge Philos. Soc.* 23, 542, (1927).
- [19] E. Fermi, *Acta Chem. Scand.* 7, 73, (1928).
- [20] P. Hohenberg and W. Kohn, *Solid State Commun.* 136, 864, (1964).
- [21] H. J. Monkhorst and J. D. Pack, *Phys. Rev. B.* 16, 5188, (1976).
- [22] D. M. Ceperley and B. J. Alder, *Phys. Rev. Lett.* 45, 566, (1980).
- [23] J. P. Perdew, K. Burke, and M. Ernzerhof, *Phys. Rev. Lett.* 77, 3865, (1996).
- [24] A. I. Liechtenstein, V. I. Anisimov, and J. Zaanen, *Phys. Rev. B. Condens. Matter Mater. Phys.*, 52, 5467, (1995).
- [25] L. M. Sandratskii, M. Uhl, and J. Kbler, *J. Phys.: Condens. Matter*, 8, 983, (1996).
- [26] R. L. Blum, R. E. HrsBvrcx and Lenny W. FrNcm, *THE AMERICAN MINERALOGIST*, 51, 123, (1966).
- [27] Z. Zhou, and P. Huo, and L. Guo, and O. V. Prezhdo, *J. Phys. Chem. C.* 119, 26303, (2015).
- [28] M.P.J. Punkkinen, K. Kokko, W. Hergert, and I.J. Vayrynen, *J. Phys.: Condens. Matter*, 11, 2341, (1999).
- [29] P. L. Liao and E. A. Carter, *Phys. Chem. Chem. Phys.* 13, 15189, (2011).
- [30] A. M. Luque and C. A. Stanley, *Nat Photon.* 6, 146, (2012).
- [31] N. Lopez, L. A. Reichertz, K. M. Yu, K. Campman, and W. Walukiewicz, *Phys. Rev. Lett.* 106, 0287014, (2011).
- [32] M. Qin, Y. Wang, D. Wan, F. Huang, and J. Lin, *Sci. Rep.* 3, 1286, (2013).
- [33] V. Sharma, C. Wang, R. G. Lorenzini, R. Ma, Q. Zhu, D. W. Sinkovits, G. Pilania, A. R. Oganov, S. Kumar, G. A. Sotzing, S. A. Boggs, and R. Ramprasad, *Nature Commun.* 5, 4845, (2014).
- [34] L. M. Ghiringhelli, J. Vybiral, S. V. Levchenko, C. Draxl, and M. Scheffler, *Phys. Rev. Lett.* 114, 105503, (2015).
- [35] I. Kondofersky et al., *Appl. Mater. Interface.* 7, 4623, (2015).

Chapter 8

Local vs non-local states in FeTiO_3 probed with 1s2pRIXS: implications for photochemistry

This chapter is based on the on a manuscript by Myrtille O.J.Y. Hunault, Wilayat Khan, Ján Minár, Thomas Kroll, Dimosthenis Sokaras, Patric Zimmermann, Mario U. Delgado-Jaime and Frank M.F de Groot, published online in Inorganic Chemistry; DOI: 10.1021/acs.inorgchem.7b00938. In this chapter, we did the angular momentum resolved density of states and X-rays absorption spectra at the Fe-K edge based on electric dipole transitions, and analyzed all theoretical results.



8.1 Introduction

Hematite (α -Fe₂O₃) has been extensively considered for the development of photocatalysts as a low cost and non-toxic material [1]. Various dopings have been investigated to improve its low charge-carrier transport properties and to optimize its optical absorption, among which Ti-doping appeared as a promising solution [2]. Alternatively, efficient Fe-Ti associations have also been considered in various oxides [3] including heterojunction assemblies of iron and titanium oxides [4], in dye sensitized solar cells [5] and in heterobinuclear complexes [6]. In all of these, the photo-induced metal-metal charge transfer (MMCT) is expected to be the main mechanism that enables harvesting solar light energy with multivalent transition metal ions in both solid state and molecular complexes [7].

The present study focuses on ilmenite (FeTiO₃) as a model compound for the metal-metal charge transfer process in Ti-doped hematite. MMCT in FeTiO₃ has been first reported from optical absorption spectroscopy [8] by analogy with the optical absorption spectrum of blue sapphire (Fe and Ti doped Al₂O₃) [9]. Like hematite, ilmenite has a corundum structure (space group R $\bar{3}$) in which Ti and Fe occupy alternating layers of octahedrons along the *c* axis of the hexagonal unit cell (Fig. 8.1). As a result, the Fe and Ti neighboring octahedrons share a face. This particular linkage is expected to play a key role in the direct cation-cation interactions [10] and in particular to enable MMCT *via* the direct overlap of the Fe and Ti *z*² orbitals through the shared face. MMCT has also been observed with edge or corner bridged polyhedrons, in solids or heterobinuclear complexes, which questions the influence of the atomic structure and the nature of the anions in the MMCT efficiency [6d], [7a], [11, 12].

The valence states of iron and titanium cations in these compounds are also of great importance to determine the MMCT mechanism. While hematite is formally a high-spin Fe³⁺ oxide, the valence states of iron and titanium in ilmenite are suggested to be high-spin Fe²⁺ and Ti⁴⁺ respectively. The intermetallic charge transfer implies the transfer of an electron from Fe to Ti: Fe²⁺ + Ti⁴⁺ → Fe³⁺ + Ti³⁺. High-pressure induced Fe²⁺ to Fe³⁺ valence changes have been reported from Mossbauer and X-ray absorption (XAS) spectroscopies [13]. Therefore, the determination of the exact valence states of the metal cations in the ilmenite motivated several spectroscopic studies at the L_{2,3} edges of Ti and Fe and O K-edge. In an early resonant inelastic X-ray scattering (RIXS) study at the Ti L_{2,3}-edge, Butorin et al. suggested that low energy optical excited states (ca. 4eV) were due to Ti³⁺ [14]. Later, Radtke et al. confirmed using high-resolution electron energy loss spectroscopy (EELS) at the L_{2,3}-edges of Ti and Fe, their respective tetravalent and divalent oxidation states [15]. A second Ti L_{2,3}-edge RIXS study supported by Fe-Ti double cluster calculations assigned the low energy excitations observed in RIXS around 2.5 eV and 4 eV to MMCT [16].

In K-edge XAS, the weak $1s$ core-hole interaction with the valence electrons and the absence of orbital momentum of the s shell considerably decrease the influence of core-hole spin-orbit coupling compared to $L_{2,3}$ -edges XAS [17]. Both electric dipole (E1) and electric quadrupole (E2) transitions can contribute to the pre-edge features at the onset of the K-edge. Their analysis enables to derive precious information about the orbital hybridization of the absorbing cation. These pre-edge features arise from E2 transitions to $3d$ excited states splitted by multielectronic interactions and crystal field effects, and also E1 transitions to local and/or delocalized excited states with p character, which enhance the E2 pre-edge feature intensity and/or result in non-local features [18, 19, 20, 21]. To our knowledge, only one study of the Ti and Fe K-edge X-ray absorption near-edge structure (XANES) in FeTiO_3 was reported so far [22]. O K-edge results have revealed the overlap between the Ti $3d$ and O $2p$ orbitals [15], [22]. Despite these previous investigations, the particular role of oxygen and the contribution of Fe to the orbitals involved in the MMCT remains unclear and the picture of the Ti-Fe interaction is not yet fully determined. Furthermore, although not highlighted by the authors of Ref., [22] the K pre-edge of Fe^{2+} shows non-local features, occurring between the pre-edge transitions and the main edge. Unfortunately the data is measured in total fluorescence yield (TFY), yielding broad features, which are difficult to interpret. $K\alpha$ RIXS (or $1s2p$ RIXS) is a powerful technique to overcome this limitation as it enables to effectively suppress the core-hole lifetime broadening. [23], [24] This has already been demonstrated in the case of iron oxides and molecules, for which $1s2p$ RIXS has enabled to derive new insights into the valence and spin states and orbital hybridization [20], [25], [26].

Here we present the first $1s2p$ RIXS study of FeTiO_3 . The obtained HERFD-XANES (high energy resolution fluorescence detected X-ray absorption near edge structure) and RIXS two dimensional maps reveal five pre-edge distinct features. Comparison of experimental data with crystal field multiplet calculations and DFT calculated projected-density of states (pDOS) enables to decompose the electric dipole and quadrupole contributions and to determine the on-site and non-local orbital hybridization of the Fe orbitals in FeTiO_3 . We show how the two dimensional RIXS map is a powerful tool to discuss the nature of the pre-edge features and probe delocalization of the Fe $3d$ electrons over the two metal centers.

8.2 Materials and Methods

8.2.1 Samples

The ilmenite sample was a commercial synthetic black powder. The chemical composition and crystalline structure of the sample were characterized by XRD (Fig. B.1). The sample was finely ground and prepared as a pellet diluted in boron nitride down to a concentration of 1wt.% of Fe for the RIXS measurements. For compari-

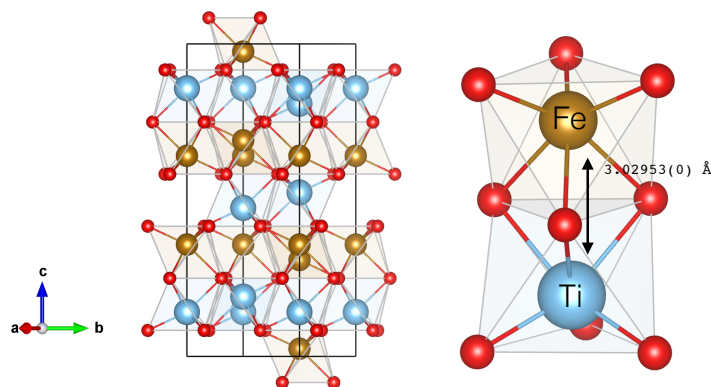


Figure 8.1: Crystal structure of ilmenite FeTiO_3 and zoom on the face sharing Fe and Ti octahedrons.

son we also measured hematite Fe_2O_3 , which is isostructural to FeTiO_3 but contains formally high-spin Fe^{3+} instead of high-spin Fe^{2+} .

8.2.2 RIXS measurements

The 1s2pRIXS measurements were performed at the wiggler end-station BL6-2 of the Stanford Synchrotron Radiation Lightsource (SSRL). The storage ring was operating in top-up mode with a electron current of 500 mA. The energy of the incident X-ray beam was selected using a liquid-nitrogen-cooled double-crystal monochromator Si(311) with an energy bandwidth of 0.2 eV at 7.1 keV. The incident energy was calibrated using a Fe foil and setting the energy position of the first inflection point of the K-edge to 7112.0 eV. The beamsize on the sample was $138 \mu\text{m} \times 395 \mu\text{m}$. Total fluorescence yield (TFY) absorption spectra were recorded using a Si photodiode. The emitted X-ray photons were collected and analyzed using a five-crystal spectrometer. We used the (440) reflection of spherically bent ($R = 1 \text{ m}$) Ge crystal analyzers. The sample was oriented 45° to the incident X-ray beam. The scattering angle was 90° and the analyzed x-rays were collected using a Silicon Drift Detector in Rowland geometry [27]. The energy of the emitted X-rays was calibrated through a series of elastic peaks in the Fe $K\alpha$ energy range (6300–6450 eV). The combined instrumental energy bandwidth was 0.66 eV full-width half-maximum (FWHM). Measurements were performed at room temperature with a helium chamber to minimize the absorption of the scattered X-rays.

8.3 Calculations

8.3.1 Density functional theory calculations

First-principles calculations of XANES and density of states (DOS) were performed using WIEN2k package based on linearized augmented plane-wave method within density functional theory [28]. We used the generalized gradient approximation (GGA) for the exchange correlation functional with the parametrisation of Perdew et al., [29] The electronic correlation of Fe $3d$ are treated by Hubbard interaction. No Hubbard interaction was used for the empty $3d$ bands of Ti. An energy cutoff of 7.0 eV was used for plane wave basis set. The unit cell parameters were set to the experimental values: $a=5.0875$ Å, $c=14.0827$ Å. [30] The magnetic order was set to the antiferromagnetic configuration, in which the Fe^{2+} spins are ferromagnetically aligned within a layer but antiferromagnetically coupled between layers in agreement with experimental evidences [31]. We included a core hole effect on one Fe atom and use the final state rule to calculate the K-edge XANES spectrum. A $1\times 1\times 2$ hexagonal supercell of 60 atoms was used to minimize the interaction between the core holes. The Fe K-edge absorption cross section was calculated in the electric dipole (E1) approximation. Finally, in order to interpret the pre-edge features, the projected-DOS are calculated on the supercell containing the core hole, with a $7\times 15\times 4$ Monkhorst-Pack k-points grid and a Gaussian broadening of 0.50 eV. The input files are given in the Supporting Information.

8.4 Crystal field multiplet calculations

The multielectronic interactions arising in the local excitations of the RIXS map of Fe^{2+} were calculated using the framework of crystal field multiplet theory (CFM), which is a multielectronic, semi-empirical approach initially developed by Thole et al. in the framework established by Cowan and Butler [32]. In this approach one considers an isolated Fe^{2+} ion embedded in a crystal field potential. It takes into account all the $3d-3d$ and $1s-3d$ electronic Coulomb interactions, as well as the spin-orbit coupling ζ on every open shell of the absorbing atom. Each of these many-body states is described by a linear combination of Slater determinants. More details on the method can be found in other references [17]. Calculations were performed using the quantum many-body script language QUANTY [33], based on second quantization and Lanczos recursion method to calculate Green functions [34], thus avoiding the explicit calculation of the intermediate and final states. The RIXS cross-section was calculated using the Kramers-Heisenberg equation [35]. In a first step, only the electric quadrupole contribution to the absorption process of the RIXS was considered. To account or the Fe point group in FeTiO_3 we describe the crystal field in C_{3v} symmetry. Because the trigonal distortion is small compared

to the energy resolution of RIXS, we use only the main crystal field parameter $10Dq$ set to 0.75 eV [15]. In first approximation, the multielectronic states will be described using the O_h point group irreps. The effect of bond covalency on the multielectronic interactions was described in the spherical approximation [36] by reducing homogeneously the Slater integrals by 64% of their Hartree–Fock value (corresponding to 80% of the atomic values). Spin–orbit coupling was kept to its Hartree–Fock calculated value.

The splitting of the lowest ${}^5T_{2g}$ (O_h) crystal–field term (ground state of the initial state of the RIXS) due to spin–orbit coupling was accounted using a Boltzmann weighting factor for each spectral contribution of the 15 micro–states. Calculations were performed for $T = 300$ K. We note that at this temperature, the first three states represent c.a. 60% of the total contribution to the spectra. The natural core–hole lifetime and experimental broadenings are described respectively by a Lorentzian function and a Gaussian function (see details in the Supporting Information). We investigated the contribution of the electric dipole transitions to the pre–edge features of the RIXS process by considering on–site p – d mixing allowed in the approximated C_{3v} point group symmetry (as well as the real C_3 point group). This is achieved by following the method described by Vercaemer et al. and considering a hybridization Hamiltonian that depends on three mixing parameters in C_{3v} point group [18]. All the parameters used for these calculations (Tab. B.1) and the input file for QUANTY are given in the the Supporting Information.

8.5 Results and discussions

8.5.1 Experimental 1s2pRIXS results

The Fe K–edge HERFD–XANES spectrum measured using the maximum energy of the $K\alpha_1$ emission line (setting the RIXS spectrometer at 6404.7 eV) is compared to the TFY spectrum of FeTiO_3 in Fig. 8.2a. The sharpening effect of the analyzer crystals becomes apparent mainly in the pre–edge region where several pre–edge features are more distinct in the HERFD–XANES spectrum than in the TFY spectrum. This is due to the effective reduction of the core–hole lifetime broadening obtained in RIXS [23], [24], [37]. The full RIXS map focuses on the pre–edge region (Fig. 8.2b) and shows the intensity of the emitted X–rays plotted in energy transfer as a function of the incident energy. We observe both $K\alpha_1$ and $K\alpha_2$ emission lines corresponding to the decay channels $2p_{3/2} \rightarrow 1s$ and $2p_{1/2} \rightarrow 1s$ respectively. The HERFD–XANES spectrum in Fig. 8.2a corresponds to a cut in the RIXS map along the diagonal red line plotted in Fig. 8.2b, which corresponds to the constant emitted energy 6404.7 eV from the non–resonant $K\alpha_1$ emission.

The RIXS map of ilmenite shows in total five features in the $K\alpha_1$ emission direction, labeled from (A) to (E) (Fig. 8.2b). Features (A), (B) and (C) in FeTiO_3

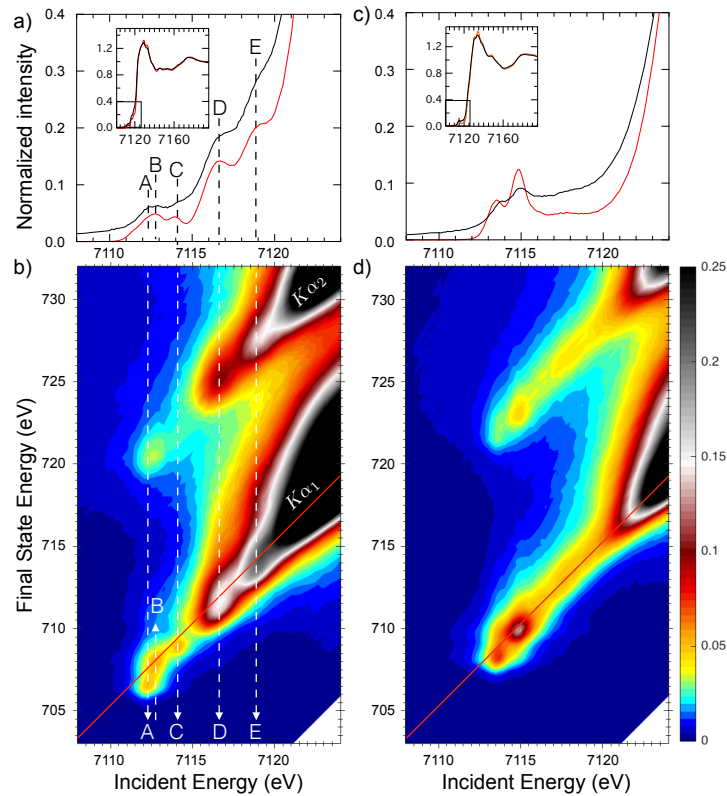


Figure 8.2: a) Fe K-edge XANES spectra of FeTiO₃ in TFY detection compared with K α_1 -HERFD detection (red line), inset: full energy range spectra; b) 1s2pRIXS map of FeTiO₃ showing the five features labeled from A to E; c) TFY and HERFD spectra of Fe₂O₃; d) 1s2pRIXS map of Fe₂O₃. The diagonal lines serve as guides for the eye to show the constant emitted energies for non-resonant K α_1 emission (RIXS map color scale is the intensity normalized to the edge jump of the K α_1 -HERFD spectrum).

are spread both incident and emission energy-wise similarly to previously reported RIXS maps of 6-fold coordinated high-spin Fe^{2+} in siderite [38] and fayalite [23]. They can be assigned to the absorption transitions from the core-shell $1s$ to the $3d$ states of the absorbing Fe atom, followed by the resonant emission transitions to the final states with a $2p$ core-hole. The energy transfer positions of these three peaks are out-of the diagonal corresponding to the non-resonant $K\alpha_1$ emission (red line on Fig. 8.2b). These peaks are assigned to the multielectronic final states and reflect the resonant emission process, which supports that the probed $3d$ states are localized on the absorbing Fe atom. Features (A), (B) and (C) are well separated from the edge rise due to the attraction by the $1s$ core-hole of the electron excited into the $3d$ orbitals [23], [38, 39, 40].

Figs. 8.2(c-d) show the HERFD-XANES and the RIXS map of Fe^{3+} of the isostructural hematite Fe_2O_3 , and are consistent with previous results [20],[26], [41]. The comparison with ilmenite shows that the main peak of the $3d$ resonances in the pre-edge of Fe^{3+} is observed at 7115 eV incident energy and 709 eV final state energy, which falls precisely between features (C) and (D) of the RIXS map of FeTiO_3 . This supports the previous conclusions that the oxidation state of Fe cations in ilmenite is Fe^{2+} [14].

Approximately 4.5 eV above peak (A), the HERFD-XANES spectrum and the $1s2p$ RIXS map show two distinct features (D) and (E) at the onset of the K-edge and separated by 2.5 eV. This confirms the presence of additional pre-edge features as suggested by previous K-edge TFY measurements [22] and highlights the advantage of HERFD-XANES and RIXS to identify peaks in the pre-edge otherwise buried in the rise of the Fe K-edge. Similar features have been observed in addition to the $1s \rightarrow 3d$ pre-edge excitations for other transition metal oxides. In the case of Fe^{3+} in hematite, the non-local features observed between 7116.5 and 7119 eV are assigned to electric dipole excitations into the delocalized $3d$ orbitals of the neighboring Fe, which contain some p character from the hybridization with the O $2p$ orbitals [20]. Non-local excitations have been reported for other transition metal cations in oxides such as Cr^{3+} in spinels [42], Ti^{4+} in rutile [21], [43], Ni^{2+} in NiO [44], Co^{3+} in LiCoO_3 [45]. Non-local features have also been observed in the Al K pre-edge in Fe-doped goethite and assigned to the Al^{3+} p states mixed with $3d$ states of the neighboring Fe^{3+} [46]. In these cases, the centrosymmetric point group (D_{2h} for Ti in rutile [21], D_{3d} for Co in LiCoO_3 [45] and Cr in spinel [42]) was used as an argument to rule out significant hybridization between the local $3d$ and the $4p$ orbitals of the absorbing atom. As a consequence, these additional features were assigned to electric dipole transitions to the $4p$ states of the absorbing atom mixed with the $3d$ states of the neighboring atom. Thus the non-local label means that the core-excited electron reaches delocalized states. More recently, HERFD-XANES results revealed non-local peaks in Fe-Mo and Fe-V cluster [12].

So far reported (HERFD-)XANES of high-spin Fe^{2+} in oxides, such as siderite or

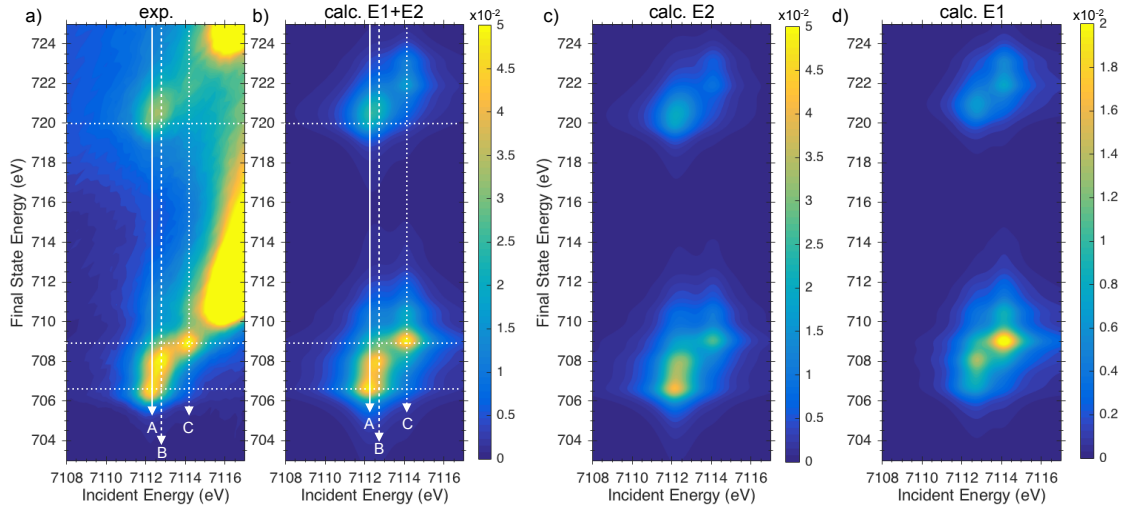


Figure 8.3: a) Experimental 1s2pRIXS plane of FeTiO_3 zoomed on features (A), (B) and (C); b) Calculated 1s2pRIXS plane of the local Fe^{2+} $1s \rightarrow 3d$ RIXS E2+E1 transitions.

staurolite, did not show non-local features and ruled out the presence of delocalized Fe $4p$ bands and strong orbital hybridization with neighboring atoms [38], [39]. The present observation suggests that the corundum structure and the presence of neighboring Ti^{4+} ions may play a role. In particular, we can already note that the 2.5 eV energy splitting between features (D) and (E) matches the $t_{2g}-e_g$ ligand field splitting reported for 6-fold coordinated Ti^{4+} in oxides such as rutile [21], [43]. Here, by analogy with Fe_2O_3 and other previously reported cases, the observed peaks (D) and (E) may arise from electric dipole transitions to the delocalized Ti $3d$ orbitals, with some p character from hybridization with O $2p$ and/or Fe $4p$ orbitals. To derive further information on the nature of the states involved in the five observed RIXS features, and confirm their assignment, we performed crystal field multiplet (CFM) and first-principle DFT calculations. They enabled to derive information about the orbital hybridization in ilmenite.

8.5.2 Crystal field multiplet analysis of the pre-edge features (A), (B) and (C)

The semi-empirical CFM model was used to account for multi-electronic interactions in the calculation of the multiplet features (A), (B) and (C) arising in the 1s2pRIXS spectra of high-spin Fe^{2+} (Fig. 8.3). We first describe the assignment of the multiplet features according to their energy and then we discuss the result of including the electric dipole (E1) contribution in the absorption process of the RIXS.

As shown in Fig. B.3, the energy positions of the calculated multiplet features

match with the experimental ones (A), (B) and (C). The calculated energy positions in the incident energy direction depend mainly (see Supporting Information, Fig. B.2) on the Slater integrals describing the multielectronic interactions in the $3d$ shell of the $1s^1 3d^7$ electronic configuration of the RIXS intermediate state. The best match was obtained for a reduction of the Slater integrals to 64% of the values calculated by a Hartree–Fock method. This is 80% of the free ion values (80% of the Hartree–Fock calculated values) previously used for $L_{2,3}$ edge calculation of Fe^{2+} in FeTiO_3 [15]. This reduction is interpreted as the nephelauxetic effect, due to the Fe–O chemical bonding, and agrees with other CFM calculations of K–edge XANES for Fe^{2+} in oxides [18], [19]. The incident energy positions of peaks (A), (B) and (C) do not vary significantly according to the incident energy resolution within 20% of the crystal field parameter $10Dq$ set to 0.75 eV (see Fig. B.2) [15]. As the energy positions of the peaks is well described within the experimental energy resolution by the crystal field parameter and Slater integrals reduction alone, we chose not to include the ligand field in order to minimize the number of parameters in the calculation.

The three observed features (A), (B) and (C) are assigned in Fig. 8.4 to the absorption from the ground state ${}^5T_{2g}$ of the initial electronic configuration $1s^2 3d^6$ to the multiplet states ${}^5T_{1g}$, ${}^5T_{2g}$ (from the 5F atomic term), and ${}^5T_{1g}$ (5P) of the intermediate electronic configuration $1s^1 3d^7$ (labels given in O_h point group for simplicity). In the HERFD–XANES spectrum, only the tail of the first ${}^5T_{1g}$ (5F) intermediate state is visible as a shoulder on the lower energy side. The ${}^5A_{2g}$ (5F) crystal field term from the intermediate $1s^1 3d^7$ configuration cannot be reached by electric quadrupole absorption from the ${}^5T_{2g}$ RIXS initial state because of the orbital momentum selection rules. Furthermore the spin-triplet states of $1s^1 3d^7$ electronic configuration cannot be reached within strict spin-selection rule $\Delta S = 0$. [47]

The experimental and calculated HERFD–XANES cuts through the RIXS maps (Fig. 8.4) enable to further compare the intensity of the features absorption-wise. The higher intensity of features (B) and (C) in the experimental HERFD–XANES spectrum compared to the calculated incident E2 contribution may arise from the tail of the non–local peak (D), which is partly supported by comparing with the tail–subtracted spectrum (see Fig. B.3 for further details on the fitting). It may also arise from an incident E1 absorption contribution to the RIXS signal. In a recent work, Vercamer et al. have estimated the influence of the site geometry and distortion on the relative contributions of electric quadrupole (E2) and electric dipole (E1) transitions to the absorption pre–edge of Fe^{2+} [18]. In the case of 6–fold coordinated sites, which only differ from a regular octahedron by small distortions, the E1 contribution to the pre–edge is weak but may affect the shape of the pre–edge. In ilmenite, the slightly higher intensity of peaks (B) and (C) may therefore also arise from local p – d mixing allowed by the trigonal distortion of the 6–fold coordinated Fe^{2+} site and the absence of inversion center in the point group (C_3).

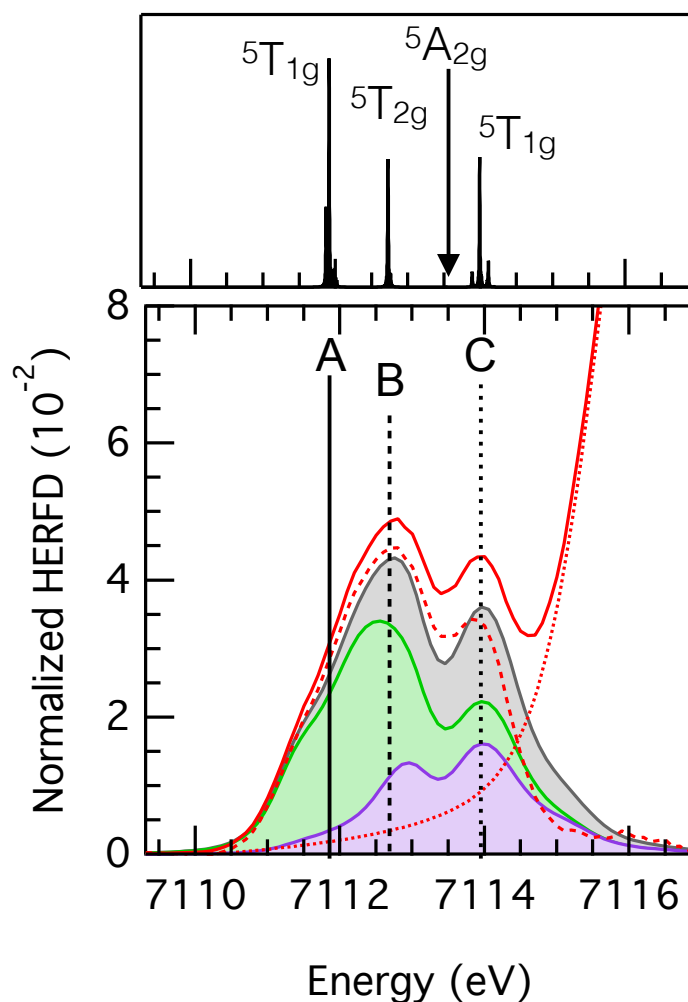


Figure 8.4: (Bottom) Calculated features (A), (B) and (C) of the Fe K-edge HERFD-XANES: E2+E1 sum (black) and individual E2 (green) and E1 (violet) contributions compared to the experimental (red -) spectrum and the corrected (- -) spectrum from the tail of feature (D) (...). (Top) Assignment of the $1s^1 3d^7$ multi-electronic states (in O_h symmetry for simplicity).

The p - d hybridization Hamiltonian accounts for hybridization of d and p orbitals of same symmetry (a_1 and e in C_{3v} approximated point group) via vibronic couplings within a given point group. In corundum, the A_1 vibration mode corresponds to the vibration along the c axis of the hexagonal unit cell. In order to estimate the dipole contribution to the local pre-edge, we have performed RIXS calculations including the local p - d hybridization with a_1 symmetry. For a mixing parameter $V_{pd}^{a_1} = 0.1$ eV, the fraction of $4p$ electrons mixed with the $3d$ is ca. 1%. The individual HERFD-XANES cuts (Fig. 8.4) and RIXS maps (Fig. B.4) of the incident E1 and E2 absorption contributions show that features (B) and (C) gain intensity from the E1 contribution. Overall, we estimate that the electric dipole absorption contribution to the pre-edge features (A), (B) and (C) represents 31% of the total pre-edge area integrated between 7110 and 7115 eV.

Fig. 8.5 compares the experimental and calculated RIXS constant incident energy (CIE) cuts at (A), (B) and (C). The calculated CIE cuts account for both incident E1 and E2 contributions and the detail of each is given in Fig. 8.5. Here again, we temporarily use the approximated O_h point group and ignore the incident E1 contribution to describe the spectral features. The essential difference between the CIE cuts at (A) and (B) relates to the involved intermediate state ${}^5T_{1g}$ and ${}^5T_{2g}$ respectively. The CIE cut at (B) is close to the 2pXAS spectrum because the intermediate state in the RIXS has the same symmetry (${}^5T_{2g}$) as the initial state of the 2pXAS. In both 1s2pRIXS and 2pXAS cases, the electric dipole transition (emission for RIXS and absorption for XAS) brings the ${}^5T_{2g}$ intermediate state (initial state for 2pXAS) to the same final states from $2p^53d^7$. The decay of the intermediate state ${}^5T_{1g}$ (feature A) reaches final states of different symmetries, which explains the different spectral shape. Because the intermediate states of the RIXS features (A) and (C) are identical (${}^5T_{1g}$), the electric dipole emission will lead to exactly the same final states. However, different matrix elements result in different spectral shapes. The shift of the CIE cut at (C) in final state energy, corresponds to the incident energy difference that is maintained in the decay process [26]. The small feature at 706.5 eV energy transfer in the CIE cut at (C) arises from the RIXS interference with the intermediate state of feature (A).

Altogether the CFM calculations support that the features (A), (B) and (C) arise from localized $Fe^* 3d$ states.

8.5.3 First-principle computed band-structure analysis of the non-local features (D) and (E)

According to the parity selection rule, electric dipole K-edge absorption is restrained to $1s \rightarrow 4p$ transitions. To determine the origin of the E1 contribution to the pre-edge features (D) and (E) and to deduce the origin of the p character of the probed orbitals, we performed the DFT calculations of the density of states (DOS) of $FeTiO_3$

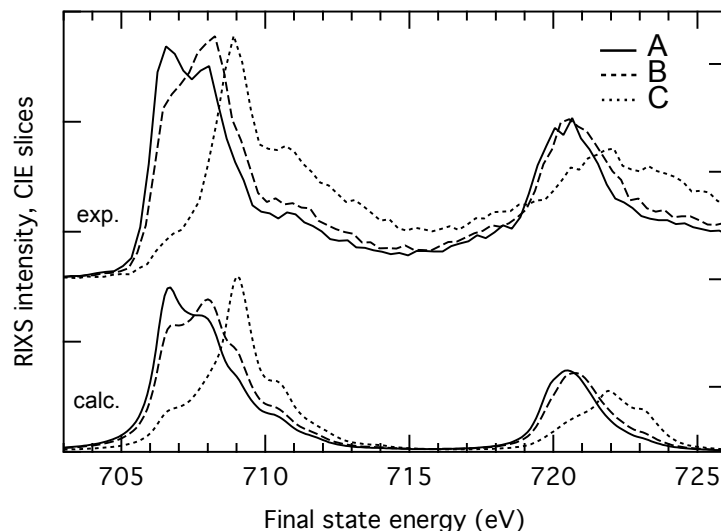


Figure 8.5: Experimental (top) and calculated (bottom) RIXS constant incident energy slices obtained at A (—) B (- -) and C (...), corresponding to the white lines drawn in Figure 3.

including the $1s$ core-hole on the absorbing Fe atom (herein after noted Fe^*) and computed the electric dipole absorption cross-section (Fig. 8.6). As will be discussed below the $1s$ core-hole mainly influences the Fe^* $3d$ electrons, therefore in Fig. 8.6, the projected DOS (pDOS) of Fe^* $4p$, Fe $3d$, Ti $3d$ and $4p$ and O $2p$ show little change with the core-hole compared to the ground state system. The exact results of the calculations without core-hole are given in Supporting Information (Fig. B.1).

The electronic structure of the ground state system (no core-hole) obtained with GGA-DFT and a Hubbard electronic correlation correction ($U = 5$ eV) is an insulator with a band gap of ca. 2 eV (Fig. 8.6 and Fig. B.1). The calculated pDOS shows that the upper part of the valence band is composed of Fe $3d$ majority spin (α spin) states and the occupied Fe $3d$ minority spin (β spin) state mixed with the occupied O $2p$ states. These pDOS agree with the previously calculated ones [22],[48]. The occupation of the $3d$ bands of Fe agrees with a high-spin Fe^{2+} : all α spin $3d$ bands are full, therefore the spin state is high-spin (for low-spin electronic configuration one would expect some empty α spin pDOS); the β spin $3d$ bands are partially filled, therefore iron is in the divalent oxidation state (for high-spin Fe^{3+} one would expect no electron in the β spin bands). This agrees with the interpretation of the features (A), (B) and (C) of the experimental $1s2p$ RIXS results.

Above the Fermi level, the bottom of the conduction band is split into two groups of bands centered around 3 and 5 eV. They correspond mainly to Fe $3d$ β spin, and Ti $3d$ bands. The Fe and Ti $4p$ and O $2p$ pDOS also contribute. The relative energy position of the Fe and Ti $3d$ empty pDOS depends on the Hubbard U correction used for Fe atoms, while the relative energy position of the other pDOS are not

affected (Fig. B.1). The Ti $3d$ pDOS is separated into two main groups by ca. 2 eV, in agreement with the order of magnitude of the crystal field splitting of the $3d$ orbitals of Ti^{4+} in 6-fold coordinated site.

Furthermore, in both the valence and conduction bands, the Fe and Ti $4p$ pDOS are mixed with the Fe and Ti $3d$ pDOS respectively. This mixing may arise from the noncentrosymmetric point group of the metal ion sites [18], [19], [47],[49],[50]. It is noteworthy that the pDOS calculations reveal that the empty Fe^* $3d$ states are also mixed with p states from Fe^* and O. This supports the existence of an additional small E1 contribution to the features (A), (B) and (C) in the $1s2p$ RIXS. The Fe^* $4p$ empty pDOS is 100 times smaller than the Fe^* $3d$ empty pDOS at the same energies, in agreement with the fraction of p -character derived from the p - d mixing Hamiltonian used in the CFM calculations. The contribution from the pDOS from Fe $4p$, Ti $4p$ and O $2p$ in the two main energy ranges of the Ti $3d$ pDOS supports the hybridization between the delocalized Ti $3d$ orbitals with the neighboring O and Fe p orbitals.

When including the $1s$ core-hole (Fig. 8.6), we observe that the Fe^* $3d$ empty pDOS is the most affected and shifts down to lower energies. The pDOS of the neighboring Fe and Ti cations are almost unchanged, and the Fe^* $4p$ and O $2p$ pDOS are only slightly influenced. The comparison between the relative energy positions of the occupied $3d$ pDOS of the Fe^* and Fe reveals the energy shift of 2 eV induced by the $1s$ core-hole. The shift is similar to previously reported experimental trends of ca. 2.5 eV for Ti in rutile [21], Cr spinels [42] and Fe in hematite [20]. Although the electric quadrupole (E2) absorption to the Fe^* $3d$ states was not calculated, the energy position of these states can be read from the pDOS. This energy is higher than the energy position of the E2 features (A), (B) and (C). This is a well understood limitation of the DFT GGA calculations, which overestimates the screening of the $1s$ core-hole. The capacity of alternative methods to better reproduce the $1s$ core-hole effect as been discussed in details elsewhere and goes beyond the scope of the present paper [21]. Assuming a similar energy shift induced by the $1s$ core-hole on the Fe^* $3d$ states of ilmenite, the empty $3d$ states of the non-excited Fe should lie approximately 2.5 eV above the pre-edge features (A), (B) and (C), just before the non-local features. This is lower than the calculated position of the Fe $3d$ states and suggests that the energy of the Fe $3d$ empty pDOS is too high with GGA+U. However, the decrease of the Hubbard U would decrease the gap energy in disagreement with the reported experimental gap of 2.75 eV. This shows that the electronic correlations are not fully accounted by the GGA+U method.

As indicated by the two vertical black dotted lines on Fig. 8.6, the calculated electric dipole (E1) XAS spectrum presents two features separated by ca. 2 eV. These two features before the main edge absorption agree with the experimental data. According to the pDOS, the central energy positions of these features match the two main empty pDOS of Ti $3d$. The p character of the excited states probed

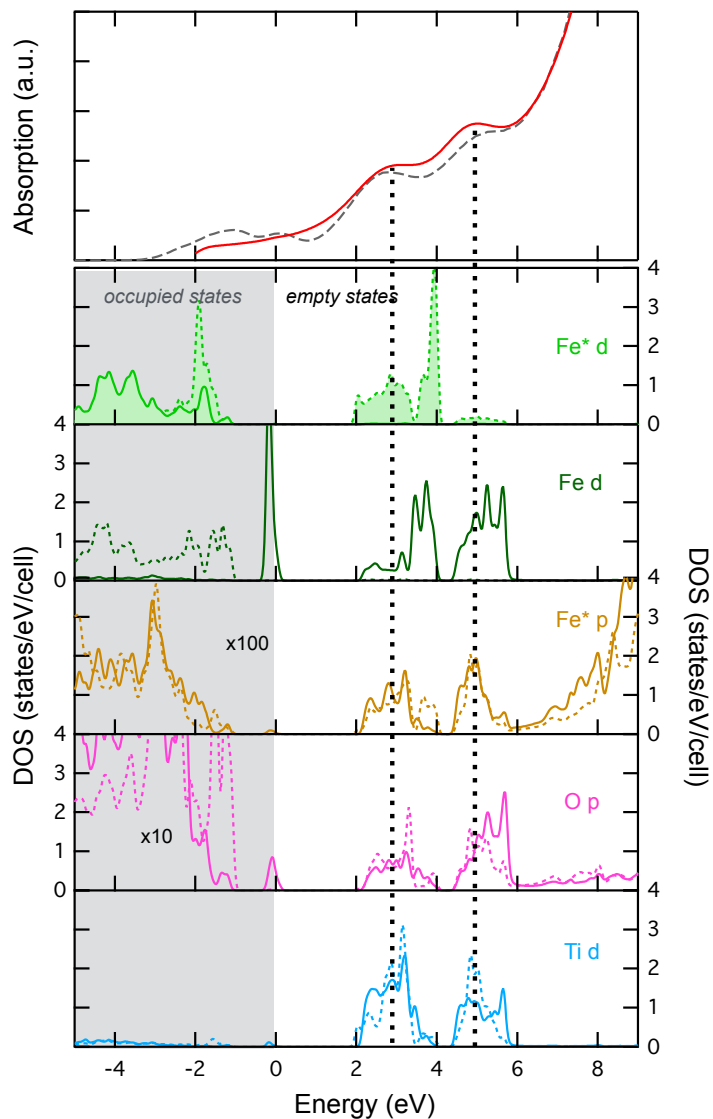


Figure 8.6: Calculated electric dipole absorption cross-section (red plain line) at the Fe K-edge (top panel) compared with the projected DOS (lower panels) on Fe, Ti and O (plain lines: β spin, dotted lines: α spin). The experimental HERFD-XANES is added for comparison (black dashed line, upper panel). Fe* denotes the Fe atom including the 1s core-hole

by the E1 absorption results from the contributions of Fe* $4p$, Ti $4p$ and O $2p$. The electric quadrupole (E2) transitions to the neighboring Fe $3d$ states are expected to be negligible by analogy with other transition metal oxides [21], [42], [44], [45]. These results confirm that the experimentally observed features (D) and (E) correspond to the E1 transitions to excited states of p character, which results from the hybridization between the neighboring Ti $3d$ delocalized orbitals and the Fe* $4p$ orbitals presumably via the O $2p$ orbitals.

8.5.4 Implications for photocatalysis

At the onset of the K-edge, the HERFD-XANES is a probe of the hybridization of the Fe* $3d$ and $4p$ orbitals via electric quadrupole and dipole absorption respectively. Our experimental and theoretical results show that Fe* $3d$ and $4p$ states are mixed (features (A), (B) and (C)) and that Fe* $4p$ are mixed with delocalized Ti $3d$ states.

Thus, the features (D) and (E), are indirect probes of respectively the Ti $3d$ t_{2g} orbitals (oriented in between the Ti–O bonds) and e_g orbitals (oriented along the Ti–O bonds) orbitals. In the present case, the trigonal distortion of the cation site induces the splitting of the e_g and t_{2g} orbitals into a_1 (z^2) and e (combination of xy , xz , xy and x^2-y^2). Note that here, the z Cartesian axis is along one of the C_3 symmetry axis of the octahedron [51]. The projected DOS on the $3d$ orbitals of Fe (Fig. B.2) shows that the occupied β spin orbital is mainly the a_1 orbital (z^2). The projected DOS on the d orbitals of Ti is in agreement with previous calculations (Fig. B.2) [22]. This leads to the a_1 orbital (z^2 orbital) pointing through the FeTi shared face as the occupied β spin orbital, in agreement with the measured polarization dependence of the MMCT optical (E1) absorption reported for (Fe–Ti):Al₂O₃ (blue sapphire) (Ref. 9.c). Altogether, our results of the orbital projection of the $3d$ bands of the cations agree with the early molecular orbital calculation of Sherman11 based on a (FeTiO₁₀)¹⁴⁻ edge-sharing cluster.

The two optical transitions to MMCT states are observed at 2.5 eV (500 nm) and 4.5 eV (275 nm) in optical spectroscopy [8] and Ti 2p3dRIXS [16]. In our DFT calculations, we find that the first Ti t_{2g} orbitals lie ca. 3 eV above the occupied β spin Fe $3d$ (t_{2g}) orbital and the Ti e_g orbitals lie ca. 5 eV above. Although these absolute energies are slightly higher than the energies of the excited MMCT states observed from experiment, their relative splitting in DFT and experimental 1s2pRIXS is in agreement with the splitting obtained in optical absorption spectroscopy. The Fe $4p$ /Ti $3d$ orbital hybridization demonstrated from our calculations supports that the electric dipole optical transitions to the MMCT states result from the Fe $4p$ character of these states. Previous O K-edge XAS results [22] have also confirmed the strong hybridization between O $2p$ and Ti $3d$ orbitals. Together with our DFT results, this strongly supports that the Fe $4p$ /Ti $3d$ orbital hybridization is mediated via the O $2p$ orbitals. Since no such hybridization has been reported so far

for divalent iron oxides, it highlights the particular role of Ti in the orbital overlap between Fe and Ti, despite the localized Fe^{2+} $3d$ states. This hybridization is favorable for the electron mobility in ilmenite and supports its observed photocatalytical activity.

HERFD–XANES appears to be a powerful tool to probe the Fe–Ti orbital hybridization involved in MMCT and the possibility to determine the mixing of the neighboring Ti states in the pre–edge of Fe K–edge will enable a better understanding of the role of Ti in the electronic structure of Ti–doped hematite. In particular, the micro–structure of hematite thin films has been used to enhance the charge carrier lifetime [1.a], [1.e], [1.d]. The influence of the preparation method and the crystallinity on the Fe–Ti orbital hybridization can thus be probed with the present approach, which benefits from the high penetration depth of hard X–rays and element selectivity combined with the high energy resolution provided by the HERFD–XANES.

In the case of mononuclear complexes, non–local peaks have been assigned to E1 transitions to anti–bonding π^* orbitals of the ligands (metal–to–ligand charge transfer states). Examples were reported for manganese complexes[52] and ferrous low spin model complex for cytochrome c [26], [53]. For binuclear complexes, such as for the Fe–Ti complexes reported by Turlington et al., [6.d], the present results suggest that the investigation of non–local peaks via $1s2p$ RIXS should provide key insights into the orbital overlap between the two metal centers, the influence of the geometry of the linkage between the two metal sites and the influence of the nature of the bridging ligands. Recently, Rees et al. have used a similar approach to compare the iron–heterometal bonds in nitrogenase enzymes (Fe–Mo and Fe–V) and assigned non–local peaks in the HERFD–XANES at Fe K–edge to MMCT peak [12].

Finally, these results open new perspectives for pump–probed experiments to investigate MMCT, with a specific focus on these non–local states at the Fe K–edge. Continuous laser excitation would enable to localize the optically excited photo–electron in steady state measurements as previously demonstrated for Au– TiO_2 [54]. Time–resolved experiments as available at synchrotrons (picosecond time scale) or X–ray free electron lasers (femtosecond time scale)[55] would enable to determine the excitation and decay lifetimes of the metal–to–metal charge transfer excited states.

8.6 Conclusion

We reports the first $1s2p$ RIXS results at the Fe K–edge of ilmenite, a model compound for MMCT, and the analysis of five pre–edge spectral features. The three first well distinct RIXS features are assigned mainly to electric quadrupole transitions to the localized Fe^* $3d$ states, shifted to lower energy by the $1s$ core–hole. CFM

calculations of these features confirm the dominating presence of Fe^{2+} . The small contribution of electric dipole absorption due to local p - d mixing allowed by the trigonal distortion of the cation site is supported by DFT and CFM calculations. Two other non-local features are assigned to electric dipole transitions to excited Fe^* $4p$ states mixed with the neighboring Ti $3d$ states. The comparison with calculations enables to demonstrate that MMCT in ilmenite is favored by the hybridization between the Fe $4p$ and Ti $3d$ orbitals *via* the O $2p$ orbitals. This work demonstrates the importance of the pre-edge energy region of transition metal K-edge where E1 and E2 transitions have equivalent intensities to probe the orbital hybridization between Fe and Ti in materials for photochemistry. It would be appealing in the next steps to use 1s2pRIXS to study the effect of Ti-doping in hematite in real photocatalyst systems. Furthermore the better understanding of the Fe K-edge provides the basis for future time-resolved spectroscopic investigations of the lifetime of MMCT excited states.

Bibliography

- [1] (a) K. Sivula, F. LeFormal, M. Grätzel, *ChemSusChem*, 4, 432, (2011); (b) M. J. Katz, S. C. Riha, N. C. Jeong, A. B. F. Martinson, O. K. Farha, J. T. Hupp, *Coordin. Chem. Rev.* 256, 2521, (2012); (c) M. S. Prévot, K. J. Sivula, *Phys. Chem. C*, 117, 17879, (2013); (d) F. Le Formal, S. R. Pendlebury, M. Cornuz, S. D. Tilley, M. Grätzel, J. R. Durrant, *J. Am. Chem. Soc.* 136, 2564, (2014); (e) P. S. Bassi, Gurudayal, L. H. Wong, Barber, *J. Phys. Chem. Chem. Phys.* 16, 11834, (2014); (f) A. G. Tamirat, J. Rick, A. A. Dubale, W.-N. Su, B.-J. Hwang, *Nanoscale Horiz.* 1, 243, (2016).
- [2] (a) K. T. Ranjit, B. J. Viswanathan, *Photochem. Photobiol.*, A 108, 79, (1997); (b) B. Pal, T. Hata, K. Goto, G. Nogami, *J. Mol. Catal. A: Chem.* 169, 147, (2001); (c) T. Droubay, K. M. Rosso, S. M. Heald, D. E. McCready, C. M. Wang, S. A. Chambers, *Phys. Rev. B* 75, (2007); (d) S. Kumari, A. P. Singh, Sonal, D. Deva, R. Shrivastav, S. Dass, V. R. Satsangi, *Int. J. Hydrogen Energy* 35, 3985, (2010); (e) P. Zhang, A. Kleiman-Shwarscstein, Y.-S. Hu, J. Lefton, S. Sharma, A. J. Forman, E. McFarland, *Energy Environ. Sci.* 4, 1020, (2011); (f) B. Zhao, T. C. Kaspar, T. C. Droubay, J. McCloy, M. E. Bowden, V. Shutthanandan, S. M. Heald, S. A. Chambers, *Phys. Rev. B* 84, (2011); (g) P. Liao, E. A. Carter, *J. Appl. Phys.* 112, 013701, (2012); (h) X. Lian, X. Yang, ; Liu, Y. Xu, C. Jiang, J. Chen, R. Wang, *Appl. Surf. Sci.* 258, 2307, (2012); (i) O. Zandi, B. M. Klahr, T. W. Hamann, *Energy Environ. Sci.* 6, 634, (2013); (j) Z. Fu, T. Jiang, Z. Liu, D. Wang, L. Wang, T. Xie, *Electrochim. Acta.* 129, 358, (2014); (k) A. Pu, J. Deng, M. Li, J. Gao, H. Zhang, Y. Hao, J. Zhong, X. Sun, *J. Mater. Chem. A* 2, 2491, (2014); (l) C. Andriamiadamanana, C. Laberty-Robert, M. T. Sougrati, S. Casale, C. Davoisne, S. Patra, F. Sauvage, *Inorg. Chem.* 53, 10129, (2014); (m) Y. Zeng, Y. Han, Y. Zhao, Y. Zeng, M. Yu, Y. Liu, H. Tang, Y. Tong, X. Lu, *Adv. Energy Mater.* 5, 1402176, (2015); (n) C. Toussaint, H. L. Le Tran, P. Colson, J. Dewalque, B. Vertruyen, B. Gilbert, N. D. Nguyen, R. Cloots, C. Henrist, *J. Phys. Chem. C* 119, 1642, (2015); (o) H. Ren, P. Koshy, F. Cao, C. C Sorrell, *Inorg. Chem.* 55, 8071, (2016).
- [3] (a) D. S. Ginley, M. A. Butler, *J. Appl. Phys.* 48, 2019, (1977); (b) W. Y. Teoh, R. Amal, L. Mädler, S. E. Pratsinis, *Cat. Today* 120, 203, (2007); (c) N. Rong, M. Chu, Y. Tang, C. Zhang, X. Cui, H. He, Y. Zhang, P. Xiao, *J. Mater. Sci.*

- 51, 5712, (2016); (d) P. García-Muñoz, G. Pliego, J. Zazo, A. Bahamonde, J. Casas, *J. Environ. Chem. Eng.* 4, 542, (2016); (e) M. E. Zarazúa-Morín, L. M. TorresMartínez, E. Moctezuma, I. Jurez-Ramírez, B. B. Zermeño, *Res. Chem. In-termed.* 42, 1029, (2016).
- [4] (a) D. Cordischi, N. Burriesci, F. D'Alba, M. Petrera, G. Polizzotti, M. J. Schiavello, *Solid State Chem.* 56, 182, (1985); (b) B. Gao, Y. J. Kim, A. K. Chakraborty, W. I. Lee, *Appl. Catal. B-Environ.* 83, 202, (2008); (c) Y. J. Kim, B. Gao, S. Y. Han, M. H. Jung, A. K. Chakraborty, T. Ko, C. Lee, W. I. Lee, *J. Phys. Chem. C* 113, 19179, (2009); (d) Q. D. Truong, J.-Y. Liu, C.-C. Chung, Y.-C. Ling, *Catal. Commun.* 19, 85, (2012); (e) Q. Liu, et al. *Nat. Commun.* 5, 5122, (2014); (f) X. Li, P. S. Bassi, P. P. Boix, Y. Fang, L. H. Wong, *ACS Appl. Mater. Interfaces* 7, 16960, (2015); (g) M. Wang, M. Pyeon, Y. Gönüllü, A. Kaouk, S. Shen, L. Guo, S. Mathur, *Nanoscale* 7, 10094, (2015).
- [5] (a) E. Vrachnou, N. Vlachopoulos, M. Grätzel, *J. Chem. Soc., Chem. Commun.* 868, (1987); (b) H. N. Ghosh, J. B. Asbury, Y. Weng, T. Lian, *J. Phys. Chem. B* 102, 10208, (1998); (c) M. Khoudiakov, A. R. Parise, B. S. Brunshwig, *J. Am. Chem. Soc.* 125, 4637, (2003); (d) K. Szacilowski, W. Macyk, M. Hebda, G. Stochel, *ChemPhysChem* 7, 2384, (2006).
- [6] (a) J. C. Curtis, T. J. Meyer, *Inorg. Chem.* 21, 1562, (1982); (b) C.-H. Yang, J. A. Ladd, V. L. J. Goedken, *Coord. Chem.* 19, 235, (1988); (c) A. Okamoto, R. Nakamura, H. Osawa, K. Hashimoto, *Langmuir* 24, 7011, (2008); (d) M. D. Turlington, J. A. Pienkos, E. S. Carlton, K. N. Wroblewski, A. R. Myers, C. O. Trindle, Z. Altun, J. J. Rack, P. S. Wagenknecht, *Inorg. Chem.* 55, 2200, (2016).
- [7] (a) G. Blasse, *Complex Chemistry*; Springer, 153, (1991); (b) D. M. D'Álessandro, F. R. Keene, *Chem. Soc. Rev.* (2006) (c) J. F. Endicott, Y.-J. Chen, *Coordin. Chem. Rev.* 257, 1676, (2013).
- [8] R. G. J. Strens, B. J. Wood, *Mineral. Mag.* 43, 347, (1979).
- [9] (a) J. Ferguson, P. E. Fielding, *Aust. J. Chem.* 25, 1371, (1972); (b) K. Eigenmann, H. H. Günthard, *Chem. Phys. Lett.* 13, 58, (1972); (c) M. G. Townsend, *Solid State Com.* 6, 81, (1968).
- [10] J. B. Goodenough, *Phys. Rev.* 117, 1442, (1960).
- [11] D. M. Sherman, *Phys. Chem. Miner.* 14, 355, (1987).
- [12] J. A. Rees, R. Bjornsson, J. K. Kowalska, F. A. Lima, J. Schlesier, D. Sippel, T. Weyhermüller, O. Einsle, J. A. Kovacs, S. DeBeer, *Dalton Transactions* 46, 2445, (2017).

- [13] (a) T. Seda, G. R. Hearne, *J. Phys.: Condens. Matter* 16, 2707, (2004); (b) X. Wu, G. Steinle-Neumann, O. Narygina, I. Kantor, C. McCammon, S. Pascarelli, G. Aquilanti, V. Prakapenka, L. Dubrovinsky, *Phys. Rev. B* 79, 094106, (2009).
- [14] S. M. Butorin, J.-H. Guo, M. Magnuson, J. Nordgren, *Phys. Rev. B* 55, 4242, (1997).
- [15] G. Radtke, S. Lazar, G. A. Botton, *Phys. Rev. B* 74, (2006).
- [16] (a) A. Agui, T. Uozumi, M. Mizumaki, T. Käämbre, *Phys. Rev. B* 79, (2009); (b) A. Agui, M. Mizumaki, T. Uozumi, *J. Electron Spectrosc. Relat. Phenom.* 205, 106, (2015).
- [17] F. d. Groot, A. Kotani, *Core level spectroscopy of solids*; CRC Press: Boca Raton, United States, (2008).
- [18] Vercamer, V. *Phys. Rev. B* 94, (2016).
- [19] M.-A. Arrio, S. Rossano, C. Brouder, L. Galois, G. Calas, *Europhys. Lett.* 51, 454, (2000).
- [20] P. Glatzel, A. Mirone, S. G. Eeckhout, M. Sikora, G. Giuli, *Phys. Rev. B* 77, (2008).
- [21] D. Cabaret, A. Bordage, A. Juhin, M. Arfaoui, E. Gaudry, *Phys. Chem. Chem. Phys.* 12, 5619, (2010).
- [22] S. W. Chen, M. J. Huang, P. A. Lin, H. T. Jeng, J. M. Lee, S. C. Haw, S. A. Chen, H. J. Lin, K. T. Lu, D. P. Chen, S. X. Dou, X. L. Wang, J. M. Chen, *Appl. Phys. Lett.* 102, 042107, (2013).
- [23] P. Glatzel, U. Bergmann, *Coordin. Chem. Rev.* 249, 65, (2005).
- [24] M. Bauer, *Phys. Chem. Chem. Phys.* 16, 13827, (2014).
- [25] T. Kroll, R. G. Hadt, S. A. Wilson, M. Lundberg, J. J. Yan, T.-C. Weng, D. Sokaras, R. Alonso-Mori, D. Casa, M. H. Upton, B. Hedman, K. O. Hodgson, E. I. Solomon, *J. Am. Ceram. Soc.* 136, 18087, (2014).
- [26] F. M. F. de Groot, P. Glatzel, U. Bergmann, P. A. van Aken, R. A. Barrea, S. Klemme, M. Hävecker, A. Knop-Gericke, W. M. Heijboer, B. M. Weckhuysen, *J. Phys. Chem. B* 109, 2075, (2005).
- [27] D. Sokaras, T.-C. Weng, D. Nordlund, R. Alonso-Mori, P. Velikov, D. Wenger, A. Garachtchenko, M. George, V. Borzenets, B. Johnson, T. Rabedeau, U. Bergmann, *Rev. Sci. Instrum.* 84, 053102, (2013).

- [28] P. Blaha, K. Schwarz, G. K. H. Madsen, D. Kvasnicka, J. Luitz, WIEN2K, An Augmented Plane Wave + Local Orbitals Program for Calculating Crystal Properties; Karlheinz Schwarz, Techn. Universitat Wien, Austria, (2001).
- [29] J. P. Perdew, K. Burke, M. Ernzerhof, Phys. Rev. Lett. 77, 3865, (1996).
- [30] B. A. Wechsler, C. T. Prewitt, Am. Mineral. 69, 176, (1984).
- [31] (a) J. B. Goodenough, J. J. Stickler, Phys. Rev. 164, 768, (1967); (b) P. F. McDonald, A. Parasiris, R. K. Pandey, B. L. Gries, W. P. Kirk, J. Appl. Phys. 69, 1104, (1991).
- [32] (a) R. D. Cowan, The Theory of Atomic Structure and Spectra; University of California Press: Berkeley, United States, (1981); (b) P. H. Butler, Point group symmetry applications: methods and tables; Plenum Press: New York, United States, (1981); (c) B. T. Thole, R. D. Cowan, G. A. Sawatzky, J. Fink, J. C. Fuggle, Phys. Rev. B 31, 6856, (1985).
- [33] M. W. Haverkort, J. Phys.: Conf. Ser. 712, 012001, (2016).
- [34] M. Taillefumier, D. Cabaret, A.-M. Flank, F. Mauri, Phys. Rev. B 66, (2002).
- [35] L. J. P. Ament, M. van Veenendaal, T. P. Devereaux, J. P. Hill, J. van den Brink, Rev. Mod. Phys. 83, 705, (2011).
- [36] H.-H. Schmidtke, In Optical Spectra and Chemical Bonding in Inorganic Compounds; Mingos, D. M. P., Schönherr, T., Eds.; Structure and Bonding 106; Springer Berlin Heidelberg, 19, (2004);, DOI: 10.1007/b11303.
- [37] J. P. Rueff, A. Shukla, J. Electron Spectrosc. Relat. Phenom. 188, 10, (2013).
- [38] J.-P. Rueff, L. Journel, P.-E. Petit, F. Farges, Phys. Rev. B 2004, 69, 235107.
- [39] M. Wilke, F. Farges, P.-E. Petit, G. E. Brown, F. Martin, Am. Miner. 86, 714, (2001).
- [40] L. Galois, G. Calas, M.-A. Arrio, Chem. Geol. 174, 307, (2001).
- [41] W. A. Caliebe, C.-C. Kao, J. B. Hastings, M. Taguchi, A. Kotani, T. Uozumi, F. de Groot, M. F. Phys. Rev. B 58, 13452, (1998).
- [42] L. Verger, O. Dargaud, G. Rousse, E. Rozsályi, A. Juhin, D. Cabaret, M. Cotte, P. Glatzel, L. Cormier, Phys. Chem. Miner. (2015).
- [43] J. Kas, J. Rehr, M. Tromp, R. J. Thomas, P. Glatzel, J. Phys.: Conf. Ser. 430, 012003, (2013).
- [44] C. Gougoussis, M. Calandra, A. Seitsonen, C. Brouder, A. Shukla, F. Mauri, Phys. Rev. B 79, (2009).

- [45] A. Juhin, F. de Groot, G. Vankó, M. Calandra, C. Brouder, *Phys. Rev. B* 81, 115115, (2010).
- [46] M. Ducher, M. Blanchard, D. Vantelon, R. Nemausat, D. Cabaret, *Phys. Chem. Miner.* (2015).
- [47] T. E. Westre, P. Kennepohl, J. G. DeWitt, B. Hedman, K. O. Hodgson, E. I. Solomon, *J. Am. Chem. Soc.* 119, 6297, (1997).
- [48] N. C. Wilson, J. Muscat, D. Mkhonto, P. E. Ngoepe, N. M. Harrison, *Phys. Rev. B* 71, (2005).
- [49] F. de Groot, G. Vankó, P. Glatzel, *J. Phys.: Condens. Matter* 21, 104207, (2009).
- [50] A. Bordage, E. Balan, J. P. R. Villiers, R. Cromarty, A. Juhin, C. Carvalho, G. Calas, P. V. Sunder Raju, P. Glatzel, *Phys. Chem. Miner.* 38, 449, (2011).
- [51] In the C₃ point group, with the C₃ axis along the z direction, the usual cubic Cartesian orbitals are not eigenstates of the single electron crystal field Hamiltonian. A detailed solution is given in¹⁸.
- [52] M. Roemelt, M. A. Beckwith, C. Duboc, M.-N. Collomb, F. Neese, S. DeBeer, *Inorg. Chem.* 51, 680, (2012).
- [53] M. Lundberg, T. Kroll, S. DeBeer, U. Bergmann, S. A. Wilson, P. Glatzel, D. Nordlund, B. Hedman, K. O. Hodgson, E. I. Solomon, *J. Am. Chem. Soc.* 135, 17121, (2013).
- [54] L. X. Chen, M. L. Shelby, P. J. Lestranger, N. E. Jackson, K. Haldrup, M. W. Mara, A. B. Stickrath, D. Zhu, H. Lemke, M. Chollet, B. M. Hoffman, X. Li, *Faraday Discuss.* 194, 639, (2016).
- [55] F. G. Santomauro, et al. *Sci. Rep.* 5, (2015).

Chapter 9

Summary and Conclusions

The water splitting process gained a wide attention to convert solar light to chemical energy. It uses semiconducting materials to produce electron-hole pair under illumination, which then takes part in the evaluation of hydrogen and oxygen. To achieve high efficiency, semiconductors need to have some important characteristics like high absorption, stability in aqueous solution, high charge transport etc. Following these criteria, it is very difficult to find suitable semiconductors for water splitting. At the beginning of thesis, we overviewed on the research of several ideal semiconductors. We specifically restrict ourselves to transition metal oxides, which are of low cost and offer stability in aqueous solutions. We began with nanostructure metal oxide semiconductors like $\text{Nb}_3\text{O}_7(\text{OH})/\text{Nb}_2\text{O}_5$ which have pronounced properties of hydrogen production and as electrode materials. Until now there is several studies devoted to the structural properties understanding of these compounds *via* experimental tools. That is why we attempted a theoretical study to provide a more deeper insight into some specific features of these materials, which were missing in the experimental study. We modeled $\text{Nb}_3\text{O}_7(\text{OH})$ and suggested proper position for H atom in the lattice site of the crystal, could not be possible from X-rays diffraction. To understand this, we performed theoretical calculations for $\text{Nb}_3\text{O}_7(\text{OH})$ and Nb_2O_5 using the linearized augmented plane wave method as employed in the WIEN2k code. By the introduction of H atom, we discovered the nature of the system (reference system Nb_3O_8) to semiconductor $\text{Nb}_3\text{O}_7(\text{OH})$. To analyze the performance of $\text{Nb}_3\text{O}_7(\text{OH})/\text{Nb}_2\text{O}_5$ as photoelectrodes materials, the band gap and energetic position of the bands found from the band structures. The calculated EELS of $\text{Nb}_3\text{O}_7(\text{OH})$ is similar to experimental data, suggesting the validity of our model. Investigation of optical properties in both systems showed identical optical band gap as well as identical optical absorption caused by the optical transition from oxygen p states to niobium d states. However, the mobility of charge carriers in $\text{Nb}_3\text{O}_7(\text{OH})$ is three times greater than Nb_2O_5 in the *p*-type region. Based on these analyses, we found that $\text{Nb}_3\text{O}_7(\text{OH})$ represents an improvement over Nb_2O_5 .

To enhance the photocatalytic activity, we modeled $\text{Nb}_3\text{O}_7(\text{OH})$ by doping Ti

with different concentrations. Titanium replaced the niobium atom in the octahedral site confirmed from the formation energy calculations. Ti also affected the internal parameters (bond distances) along different axes in the doped $\text{Nb}_3\text{O}_7(\text{OH})$. Ti imparted smearing of bands over the Fermi level in the electronic band structure. Due to the difference in states around the Fermi level, long wavelengths part of the solar spectrum (due to interband transition) is more pronounced in highly doped systems. Even, the optical spectral profile showed higher photoabsorption in highly doped system as compared to other systems. The local surrounding of Ti atoms in the crystal structures was confirmed from element-specific energy loss edge calculations.

A second photocatalytic material is hematite, which is doped by Sn atom to improve the photocatalysis. Optoelectronic properties of pure and doped $\alpha\text{-Fe}_2\text{O}_3$ are calculated using the generalized gradient approximation plus onsite-Hubbard potential. In this study, we have introduced the concept of intermediate bands in hematite by Sn doping for the first time. Importantly, we have found this intermediate bands can utilize solar light at a low energy regime which is important for application of solar light conversion. We discussed that these intermediate bands reduced the electron-hole recombination rate a main drawback of hematite. These results afford a theoretical background for designing highly efficient Fe_2O_3 based photocatalytic materials. Last but not the least, we studied ilmenite (FeTiO_3) a model compound for metal-metal charge transfer. We calculated 1s2pRIXS results at the Fe K-edge and five pre-edge spectral features for the first time. From the analysis of RIXS, it is confirmed that its non-local features were attributed to electric dipole transitions. This electric dipole absorption caused by the local p - d mixing calculated from DFT and crystal field calculations. Theoretical calculations confirmed that the mixing between $4p/3d$ orbitals of Fe/Ti atoms *via* the O $2p$ orbitals contributed to metal-metal charge transfer.

Studies on these systems open new perspective for the band gap engineering of $\text{Nb}_3\text{O}_7(\text{OH})/\text{Nb}_2\text{O}_5$ to extend the optical absorption towards the visible region. Doping of different classes of materials like transition metals, and some non-metals would enable the optical transitions within the visible light regime. Even, the doping materials could introduce high energetic position of CB and VB. Similarly, we could see some model scientific perspective in hematite ($\alpha\text{-Fe}_2\text{O}_3$) doping by different materials at bulk and at surface structures to enhance the capability of high optical absorption.

Appendix A

Tuning the electronic structure of $\text{Nb}_3\text{O}_7(\text{OH})$ by titanium doping for enhanced light-induced water splitting

This chapter is based on the supplementary information of a manuscript by Wilayat Khan, Sophia. B. Betzler, Christina Scheu, Ondrej Šipr and Ján Minár, which is to be submitted. In this chapter, we did orbitals resolved density of states of Nb, Ti, O and H atoms.

A.1 Detailed orbital resolved DOS of Nb-s/p/d orbitals Ti-s/p/d orbitals, O-s/p orbitals and H-s orbitals

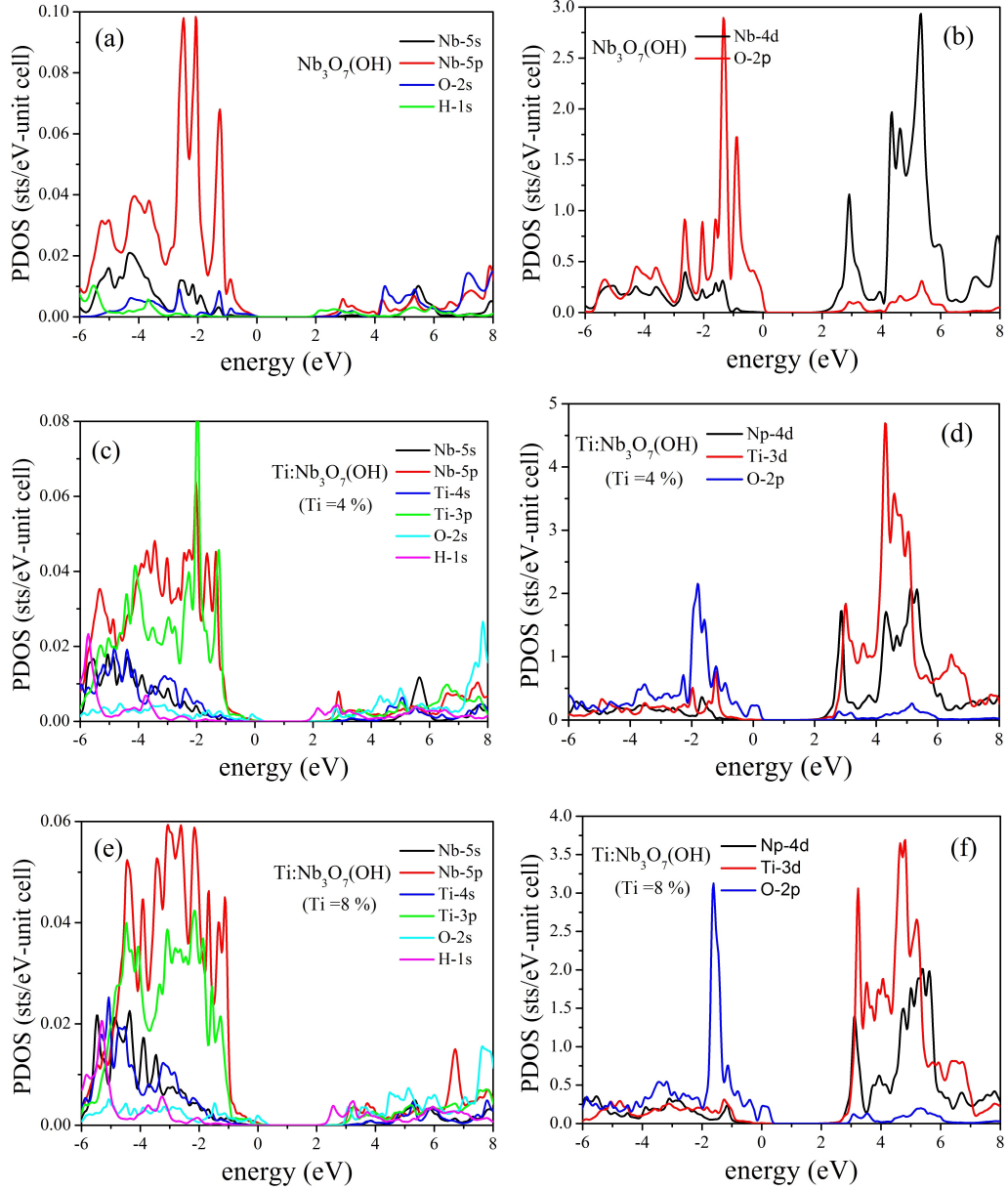


Figure A.1: Calculated orbital resolved DOS of (a, b) $\text{Nb}_3\text{O}_7(\text{OH})$ and (c-f) $\text{Ti}:\text{Nb}_3\text{O}_7(\text{OH})$. In all cases, the VBM are dominated by $\text{O}-2p$ orbitals and CBM are dominated by $\text{Nb}-4d$ orbitals. But due to the addition of Ti atom, the $\text{O}-2p/\text{Ti}-p$ orbitals smears over the Fermi level and $\text{Nb}-4d$ orbitals coupled with $\text{Ti}-3d$ orbitals.

Appendix B

Local vs non–local states in FeTiO₃ probed with 1s2pRIXS: implications for photochemistry

This chapter is based on the supplementary information on a manuscript by Myrtille O.J.Y. Hunault, Wilayat Khan, Ján Minár, Thomas Kroll, Dimosthenis Sokaras, Patric Zimmermann, Mario U. Delgado-Jaime and Frank M.F de Groot, published online DOI: [10.1021/acs.inorgchem.7b00938](https://doi.org/10.1021/acs.inorgchem.7b00938). In this chapter, we did the angular momentum resolved density of states calculations, and analyzed all theoretical results.

B.1 DFT calculation results

B.1.1 Effect of the Hubbard U

B.1.2 Detailed 3*d* orbitals pDOS

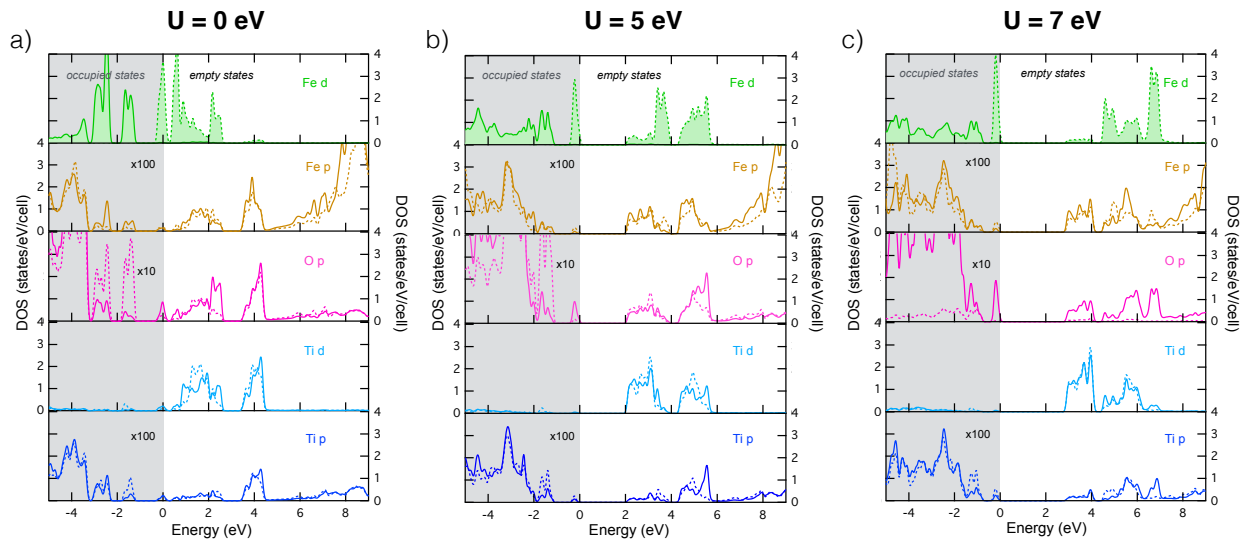


Figure B.1: Projected DOS of Fe, Ti and O atoms for various values of Hubbard U :

a) 0 eV, b) 5 eV, c) 7 eV.

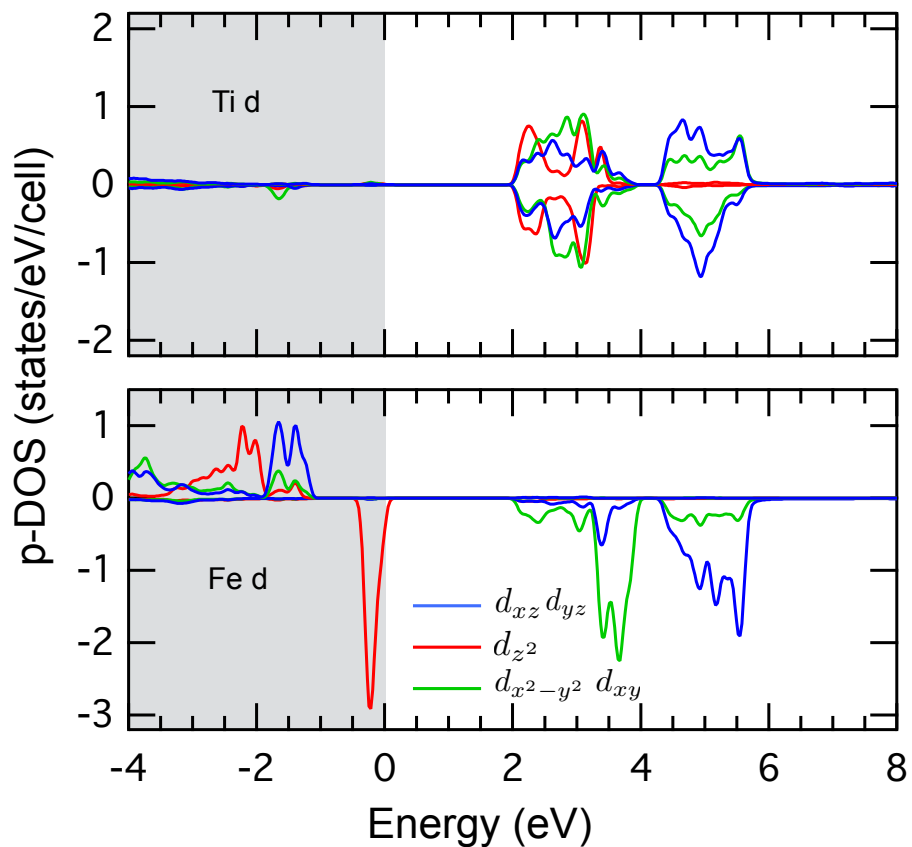


Figure B.2: Projected DOS on the 3d orbitals of Fe and Ti, calculated with DFT without core-hole.

ACKNOWLEDGMENTS

To begin with, millions of thanks could never express my deep gratitude to my late mother. Her absence has deprived me from being fully happy.

It is a hard job to include the names of all people who were involved directly or indirectly in the accomplishment of this study. However, I am very grateful to all my teachers since my school days, I think without being trained enough, I would have not been able to venture in the area of higher studies. First, I would like to express my greatest gratitude and sincere thanks to my research advisor and mentor Prof. Dr. Ján Minár for all his wonderful supervision during this PhD work. With my limited research experience in this field, he took me as his doctorate student and with his integrity, patience and guidance, encouraged me throughout the years. I pay homage to my great teacher, from whom I have learnt the research on water splitting materials. Besides providing the research facilities, he has always been available and accessible all the time to provide suggestions, ideas and pin pointed the loopholes for the amelioration/improvement of the work. I will always be thankful and grateful to have been supervised by him.

I express my heart-felt gratitude to Dr. Ondřej Šiper for his constant motivation and support during the course of my thesis. His scientific input, personal help and friendly nature have always made me feel at ease with him. The constant motivation and support from Dr. Salman Khan Safi, Dr. Muhammad Rahim and Dr. Faiq Jan is also gratefully acknowledged.

My acknowledgement will never be complete without the special mention of my lab seniors, Dr. Sikander Azam and Mr. Saleem Ayaz Khan who have taught me the lab culture and have lived by example to make me understand the hard facts of life. All the moments spent together during lab work, traveling for conferences, social gatherings and all other unforgettable memories.

I would like to acknowledge Dr. Zia-ur-Rehman Mashwani, Dr. Jamal Rafique, Dr. Anees Ahmad and Mr. Muhammad Arif for all their support and motivation during the initial days of my stay in the lab. I would like to acknowledge Mr. Amjad Ali, Mr. Motasim Billah Shah and Mr. Muhammad Ullah for their moral support and motivation, which drives me to give my best. I wish the best of luck to all in academic and scientific endeavors and hope the friendship established in 2012 will last in years to come.

I offer my cordial and profound thanks to Mr. Amjad Ali, Mr. Sir Faroosh Khan, Mr. Lal Zaman Khan and Mr. Azeem Ullah as their helping hands were always there for me whenever I need them. Their physical and moral support has always kept my courage high. It would take forever to list all the help I got from them. I would like to thank Dr. Christina Scheu and Dr. Sophia B. Betzler for their valuable support and collaboration in shaping up this thesis in its present form. I cannot imagine any better collaboration than what I had with them. A special

word of gratefulness to Mr. Martin Šafřánek,, who has gone out of way to help me with several technical and official matters. I am also grateful to Doc. Dr. RNDr Miroslav Holeček, Ex-Director NTC, and RNDr. Petr Martinec, Head of NTC for giving me an opportunity to work in this institute and making the facilities available for carrying out my research.

I would also acknowledge Computational and experimental design of advanced materials with new functionalities, This publication was supported by the project CEDAMNF, reg. no. CZ.02.1.01/0.0/0.0/15-003/0000358, co-funded by the ERDF and by GAČR (Proj. 17-1484OS). This work was also supported by project COST CZ LD15147 for providing me with the necessary funding and fellowship to pursue research at NTC.

Last but not the least; I am indebted from the core of my heart to all the sacrifices made by my family (Father, Brothers and Sisters). The more I would in honor of my parents the lesser it would be. I just say that I am proud of them. I am proud that I could make their dreams come true. I wish to express my deepest gratitude to my parents, siblings and to my other family members. Thank you all for the love, understanding, and support. It was not easy being so far away from you all, but do know deep and down, you are very proud of me.

To my daughters, thanks for always providing a refreshing break from the monotony of running my calculations. Last, but not least, I would like to thank my wife for her continued support and encouragement without which the making of this dissertation would never have been possible.

Wilayat Khan
Plzeň, Czech Republic
2nd October, 2017

Chapter 10

Curriculum vitae



WILAYAT KHAN

Date Of Birth: March 12th 1983

Email: wkhan@ntc.zcu.cz

PRESENT ADDRESS

New Technologies - Research Center,
University of West Bohemia,
Univerzitni 8, 306 14 Pilsen,
Czech Republic,
(+420) 775526684

PERMANENT ADDRESS

Village and post office Dagi,
District Swabi, 23430, Tehsil
Razar, Khyber Pakhtunkhwa,
Pakistan,
(+92) 9200235

RESEARCH AREA

First principle calculations of electronic structure, optic, spectroscopic and thermoelectric properties of technologically relative materials. Angle-resolved photo emission (ARPES) of topological insulator.

CURRENT RESEARCH INTEREST

- Theoretical and Experimental Study on the Optoelectronic Properties of $\text{Nb}_3\text{O}_7(\text{OH})$ and Nb_2O_5 Photoelectrodes.
- Tuning the electronic structure of $\text{Nb}_3\text{O}_7(\text{OH})$ by titanium doping for enhanced light-induced water splitting.
- Theoretical analysis of an Intermediate Band in Sn-doped Hematite with Wide-spectrum Solar Response.
- Local vs non-local states in FeTiO_3 probed with 1s2pRIXS: implications for photochemistry.

EDUCATION

| | | | |
|------|---------|-------------------------|--------------------------|
| 2012 | M.Phil. | Quaid e Azam University | I st Division |
| 2006 | M.Sc. | Malakand University | I st Division |
| 2004 | B.Sc. | Peshawar University | I st Division |
| 2001 | F.Sc. | BISE Peshawar | I st Division |
| 1999 | S.S.C. | BISE Peshawar | I st Division |

Master in Philosophy thesis title (M. Phil):

Preparation, Characterization and Dielectric Properties of Conducting Polymer-Carbon Nanotubes Composites.

EXPERIENCE

Teaching; Teaching experience in different graduate and undergraduate institutes during 2006-2010.

PROFICIENCIES

- Wien2k code
- BoltzTraP Code
- Elastic Code
- Gibbs Code
- SPRKKR Code
- CTM4XAS

SUBJECTS STUDIED (in M.phil and Master):

Quantum mechanics, Mathematical method of physics, Classical mechanics, Statistical mechanics, Plasma physics, Atomic and Molecular spectroscopy, Semiconductor physics, Solid state physics, Material Science, Modern physics, Electro dynamics, Magnetism, Electronics, Nuclear physics, Electro magnetic theory.

RESEARCH STAYS:

- Short term scientific visit (12 days) to Department of Chemistry, LMU, Germany , “to the group of Prof. Hubert Ebert and Dr. Jan Minár for the discussion SPR–KKR”, 2014.
- Autum School on dynamical mean field approach with predictive power for strongly correlated Electrons FZ, Jülich, Germany, 2014.

- Short term scientific visit (3 days) to Institute of Materials Chemistry, TU Vienna, Austria “Collaboration with Prof. Peter Blaha on X-rays spectra of $\text{Nb}_3\text{O}_7(\text{OH})$ and Nb_2O_5 nanostructures”, 2015.
- Hands-on course Introduction to the application of ab-initio methods in spectroscopy, New Technologies Research Centre, University of West Bohemia Czech Republic, 2015.
- Short term scientific visit (10 days) to Utrecht University, Netherland, “to the group of Prof. dr. Frank de Groot and Collaboration with the group members on spectroscopic properties on FeTiO_3 ”, 2016.
- Short term scientific visit (10 days) to LMU, Germany and Max Planks Institute Dusseldorf, Germany, “to the group of Prof. Hubert Ebert and Prof. Christina Scheu for the discussion of Exp. and Theo. ELNES”, 2015.
- Winter school on the fundamentals and applications of ab-initio methods in spectroscopy, Applied Physics Faculty of the University of Nova Gorica, Ajdovščina, Slovenia, 2016.
- The SUCCESS-2017 School on UV and Xray Spectroscopies of Correlated Electron Systems, held on Sept. 4th–15th, 2017 at the Centre de Physique des Houches, France.

Publications in 2014

1. W. Khan, A. H. Reshak: *Optoelectronic and thermoelectric properties of KAuX_5 ($X=\text{S}, \text{Se}$): a first principles study*. J. Mater Sci., 49, 1179–1192, (2014).
2. W. Khan, A. H. Reshak: *Thermoelectric properties of $\text{Li}_2\text{PbGeS}_4$ polar chalcopyrites single crystals as photovoltaic candidate*. Com. Mat. Sci., 89, 52–56, (2014).
3. W. Khan, J. Minar: *Theoretical study on optical and thermoelectric properties of the direct band gap α/β - Ca_2CdAs_2 pnictide semiconductors*. RSC Advances, 87, 46791–46799, (2014).
4. A. H. Reshak, W. Khan: *The density functional study of electronic structure, electronic charge density, linear and nonlinear optical properties of single crystal α - LiAlTe_2* . JALCOM, 592, 92–99, (2014).
5. W. Khan, A. H. Reshak: *A. Specific Features of $\text{Li}_5\text{La}_3\text{M}_2\text{O}_{12}$ ($M = \text{Nb}, \text{Ta}$) Single Crystals: Electrolyte for Solid States Batteries*. Sci. of Adv. Materials, 8, 1716–1726, (2014).

6. W. Khan, A. H. Reshak, K. R. Ahmad, Z. Alahmed: *Magnetic and thermoelectric properties of three different atomic ratio of Bi/Mn in BiMn_2O_5 : DFT approach*. JMMM, 369, 234–242, (2014).
7. A. H. Reshak, W. Khan: *Electronic structure, optical and thermoelectric transport properties of layered polyanionic hydrosulfate LiFeSO_4OH : Electrode for Li-ion batteries*. JALCOM, 591, 362–369, (2014).
8. A. H. Reshak, Y. Al-Douri, R. Khenata, W. Khan, S. A. Khan, S. Azam: *Electronic structure, Fermi surface topology and spectroscopic optical properties of $\text{LaBaCo}_2\text{O}_{5.5}$ compound*. JMMM, 363, 133–139, (2014).

Publications in 2015

1. A. H. Reshak, W. Khan: *Thermoelectric, electronic, optical and chemical bonding properties of Ba_2PrRuO_6 : At temperature 7 K and 150 K*. Mat. Res. Bulletin, 61, 551–559, (2015).
2. W. Khan, A. H. Reshak: *First principles treatment of structural, optical, and thermoelectric properties of Li_7MnN_4 as electrode for a Li secondary battery*. Mat. Res. Bulletin, 61, 306–314, (2015).
3. W. Khan, S. Goumri-Said: *Exploring optoelectronic structure and thermoelectricity of recent photoconductive chalcogenides compounds $CsCdInQ_3$ ($Q = Se, Te$)*. RSC Advances, 13, 9455–9461, (2015).
4. W. Khan, A. H. Reshak: *Electronic properties of orthorhombic $BaSn_2S_5$ single crystal*. Indian Journal of Phy., 5, 437–443, (2015).
5. S. Azam, S. A. Khan, W. Khan, S. Muhammad, H. Udin, G. Murtaza, R. Khenata, F. A. Shah, J. Minar, W. Ahmed: *Detailed DFT studies of the electronic structure and optical properties of $KBaMSe_3$ ($M = As, Sb$)*. JALCOM, 644, 91–96, (2015).
6. W. Khan, S. Azam, F. Shah, S. Goumri-Said: *DFT and modified Becke Johnson (mBJ) potential investigations of the optoelectronic properties of $SnGa_4Q_7$ ($Q = S, Se$) compounds. Transparent materials for large energy conversion*. Solid State Sci., 48, 244–250, (2015).
7. S. Azam, S. A. Khan, J. Minar, W. Khan, H. Udin, R. Khenata, G. Murtaza, S. Bin-Omran, S. Goumri-Said: *Coulomb interaction and spin-orbit coupling calculations of thermoelectric properties of the quaternary chalcogenides Tl_2PbXY_4 ($X = Zr, Hf$ and $Y = S, Se$)*. Semicond. Sci. Technol. 30 105018–105027, (2015).
8. W. Khan, S. Borek, J. Minar: *Correlation between the electronic structure, effective mass and thermoelectric properties of rare earth tellurides Ba_2MYTe_5 ($M = Ga, In$)*. RSC Advances, 64, 51461–51469, (2015).

Publications in 2016

1. W. Khan, S. Azam, M. B. Kanoun, S. Goumri-Said: *Optoelectronic structure and related transport properties of BiCuSeO based oxychalcogenides: First principle calculations*. Solid State Sci., 58, 86–93, (2016).
2. W. Khan, S. Goumri-Said: *Engel-Vosko generalized gradient approximation within DFT investigations of optoelectronic and thermoelectric properties of copper thioantimonates(III) and thioarsenate(III) for solar energy conversion*. Phy. Status Solidi B-Basic Solid State Phy., 253, 583–590, (2016).
3. W. Khan, G. Murtaza, T. Ouahrani, A. Mahmood, R. Khenata, M. Monir, H. Baltaceh: *Electronic, bonding, linear and non-linear optical properties of novel $Li_2Ga_2GeS_6$ compound*. JALCOM, 674, 109–115, (2016).
4. A. Yumak, S. Goumri-Said, W. Khan, K. Boubaker, P. Petkova: *Doping-induced stability in vanadium-doped ZnO quantum well wires (QWW): Combination of DFT calculations within experimental measurements*. Sol. State Sci., 57, 33–37, (2016).
5. Wilayat Khan, Sophia B. Betzler, Ondrej ipr, Jim Ciston, Peter Blaha, Christina Scheu, and Jan Minar: *Theoretical and Experimental Study on the Optoelectronic Properties of $Nb_3O_7(OH)$ and Nb_2O_5 Photoelectrodes*. J. Phys. Chem. C, 120, 23329–23338, (2016).

Publications in 2017

1. S. Ali, W. Khan, G. Murtaza, M. Yaseen, M. S. Ramay, A. Mahmood: *First principles study of magnetic and electronic properties of A_2BBO_6 ($A=Ba, Sr$) ($BB = FeRe, MnMo, and MnRe$) double perovskites.* JMMM, 441, 113–123, (2017).
2. W. Khan, S. Goumri-Said: *Magnetic and electronic properties of Neptunium chalcogenides from GGA plus U plus SOC and DFT investigations.* JMMM, 432, 574–580, (2017).
3. Myrtille O.J.Y. Hunault, Wilayat Khan, Ján Minár, Thomas Kroll, Dimosthenis Sokaras, Patric Zimmermann, Mario U. Delgado-Jaime and Frank M.F de Groot: *Local vs Nonlocal States in $FeTiO_3$ Probed with $1s2pRIXS$: Implications for Photochemistry.* Inorg. Chem., 56, 10882–10892, (2016).
4. K. M. Wong, Wilayat Khan, M. Shoaib, U. Shah, S. H. Khan, and G. Murtaza, *Ab Initio Investigation of the Structural, Electronic and Optical Properties of the $Li_2In_2XY_6$ ($X = Si, Ge; Y = S, Se$) Compounds.* J. of Elec. Mat., DOI: 10.1007/s11664-017-5805-1, (2017).
5. J. Krempaský, M. Fanciulli, N. Pilet, J. Minár, W. Khan, M. Muntwiler, F. Bertran, S. Muff, A.P. Weber, V.N. Strocov, V.V. Volobueiev, G. Springholz, J. H. Dil, *Spin-resolved electronic structure of ferroelectric α -GeTe and multi-ferroic $Ge_{1-x}Mn_xTe$.* arXiv:1708.04104v1 [cond-mat.mtrl-sci] 14 Aug 2017.
6. W. Khan, S. Hussain, J. Minár, S. Azam, *Electronic and thermoelectric properties of ternary chalcogenide semiconductors: First principles study,* J. of Elec. Mat., accepted, (2017).